



Numerical simulations for frequency prediction via mean flows

Yacine Bengana

► To cite this version:

Yacine Bengana. Numerical simulations for frequency prediction via mean flows. Mechanics [physics]. Université Paris sciences et lettres, 2018. English. NNT : 2018PSLET032 . tel-02170483v2

HAL Id: tel-02170483

<https://hal.science/tel-02170483v2>

Submitted on 19 Mar 2020

HAL is a multi-disciplinary open access archive for the deposit and dissemination of scientific research documents, whether they are published or not. The documents may come from teaching and research institutions in France or abroad, or from public or private research centers.

L'archive ouverte pluridisciplinaire **HAL**, est destinée au dépôt et à la diffusion de documents scientifiques de niveau recherche, publiés ou non, émanant des établissements d'enseignement et de recherche français ou étrangers, des laboratoires publics ou privés.

THÈSE DE DOCTORAT

de l'Université de recherche Paris Sciences et Lettres
PSL Research University

Préparée à l'École supérieure de Physique et de Chimie
Industrielles de la ville de Paris

Numerical simulations for frequency prediction via mean flows

École doctorale n°391

SCIENCES MÉCANIQUES, ACOUSTIQUE, ÉLECTRONIQUE ET ROBOTIQUE DE PARIS

Spécialité MÉCANIQUE

Soutenue par **Yacine Bengana**
le 17 décembre 2018

Dirigée par **Laurette Tuckerman**

COMPOSITION DU JURY :

M. Gallaire François
École Polytechnique Fédérale de Lausanne
Président

M. PIER Benoît
LMFA - CNRS
Rapporteur

M. SIPP Denis
ONERA-DAAA
Rapporteur

M. ALTMAYER Sebastian Andreas
Universitat Politècnica de Catalunya
Examineur

M. PASTUR Luc
IMSIA-ENSTA ParisTech
Examineur

M. LOISEAU Jean-Christophe
ENSAM
Invité

M. WESFREID José Eduardo
PMMH-ESPCI
Invité

Mme. TUCKERMAN Laurette
PMMH-ESPCI-UPMC-CNRS
Directrice de thèse

*À ma mère Nadia et à mon père Farid,
à qui je dois tout.*

Remerciement

Un sage a dit : "celui qui ne remercie pas d'abord les Hommes, ne peut pas remercier Dieu". Alors, je tiens à remercier en premier lieu ma directrice de thèse Laurette S. Tuckerman. Je lui serais toujours reconnaissant pour m'avoir soutenu pendant les moments intenses et difficiles et pour n'avoir jamais compté le temps passé avec moi à travailler mais aussi à échanger sur des sujets tout aussi passionnants. Son exigence, sa gentillesse et la liberté qu'elle m'a laissé m'ont permis de vivre trois années formidables. J'ai eu l'occasion de collaborer avec Jean-Christophe Loiseau et Jean-Christophe Robinet du laboratoire DynFluid à L'ENSAM. Travailler avec eux a été très enrichissant et particulièrement agréable. Je les remercie chaleureusement pour m'avoir offert cette chance. José Eduardo Wesfreid m'a permis de prendre part à ses travaux sur Henri Bénard et pour cela je lui adresse mes remerciements. Je tiens aussi à remercier Dwight Barkley pour ses suggestions toujours pertinentes à des moments clés de la thèse. Je remercie Damir Juric et Jalel Chergui du laboratoire LIMSI pour leur soutien et nos échanges au début de cette thèse. Merci à chaque membre du jury d'avoir accepté d'évaluer mon travail et pour les précieux échanges que nous avons eus pendant la soutenance.

J'ai trouvé au laboratoire PMMH un lieu où il fait bon travailler et c'est évidemment grâce à tous ses membres. Je tiens à remercier chaleureusement les doctorants et post-doctorants, Adeline, Adrien, Ashraf, Ali, Alex, Antonios, Benoît, Bill, Cesar, Charly, Clotilde, Eliott, Florence, Francesca, Gabi, Gaspard, Hadrien, Hector, Hugo, Jean, Lucie, Ludovic, Lukasz, Manon, Marine, Marion, PH, Piotr, Reda, Reinaldo, Salome, Tao, Vincent, Valentin, Yanan... pour qui je souhaite le meilleur pour la suite. Merci aux membres permanents et en particulier au directeur du laboratoire Philippe Petitjean et ses soutiens administratifs Claudette et Frédérique qui ont grandement contribué à cette atmosphère conviviale qui règne entre les murs du laboratoire. J'adresse naturellement de sincères remerciements aux nombreuses personnes que j'ai rencontrées dans mes pérégrinations scientifiques et qui ont participé à mon enrichissement intellectuel et personnel. Mes remerciements vont ensuite à mes amis pour les moments partagés ensemble. Merci donc à Abdel Adim, Ahmed, Anas, Amine, Antoine, Idir, Inès, Ilyesse, Julien, Mehdi, Mehmet, Mouna, Mounir, Nicolas, Rachid...et à tous ceux que je n'ai pas cités, qu'ils sachent qu'ils ne sont pas pour autant moins considérés.

Ma sérénité durant ces trois années intensives n'aurait pas été possible sans ma famille. Je prends ces quelques lignes pour exprimer ma profonde et indéfectible reconnaissance à mes parents, pour avoir toujours cru en moi et pour m'avoir tellement donné. Merci à mes frères et soeurs, Sabri, Nabil, Sofia, Massinissa et Sandra pour avoir toujours été à mes côtés. Je remercie également les autres membres de ma grande famille qui m'ont soutenu. Je remercie mes maîtres pour tout ce qu'ils m'ont apporté et merci à toi qui en ce moment est en train de lire cette thèse.

Contents

Remerciements	v
Chapitre 1 Introduction (en)	1
1.1 Linear stability analysis	2
1.1.1 Linear stability about the base flow	3
1.1.2 Mean flow analysis	4
1.2 Nonlinear dynamics	5
1.2.1 Self-consistent model	6
1.3 Present work	6
Bibliography	9
Chapitre 2 Introduction (fr)	10
2.1 Analyse de stabilité linéaire	11
2.1.1 Stabilité linéaire autour de l'écoulement de base	12
2.1.2 Analyse par écoulement moyen	13
2.2 Dynamique non linéaire	14
2.2.1 Modèle auto-consistant	15
2.3 Plan de la thèse	16
Bibliography	19
Chapitre 3 Bifurcation analysis and frequency matching in shear-driven cavity flow	20
3.1 Introduction	20
3.2 Governing equations and numerical methods	23
3.2.1 Problem definition	23
3.2.2 Base flow and linearization	24
3.2.3 Mean flow and linearization	25
3.2.4 Floquet analysis	27
3.2.5 Edge state technique for computing the unstable quasiperiodic state	27
3.2.6 Standard deviation	28
3.2.7 Hilbert transform	29
3.3 Bifurcation scenario	30
3.3.1 Overview	30
3.3.2 Linearization about the base flow	35
3.3.3 Spatial analysis and Hilbert transform	37
3.3.4 Quasiperiodic state and Floquet analysis	38

3.4	Frequency prediction	42
3.4.1	Linearization about the mean flow	42
3.4.2	RZIF and SCM	44
3.4.3	Cross-eigenvalues	47
3.4.4	Rossiter formula	48
3.5	Conclusion	49
Bibliography		56
Chapitre 4 Spirals and ribbons: frequencies from mean flows and heteroclinic orbits		57
4.1	Introduction	57
4.2	Methods	59
4.3	RZIF analysis	61
4.4	Heteroclinic orbits	65
4.5	Discussion	70
Bibliography		73
Chapitre 5 Frequency prediction from exact or self-consistent meanflows		74
5.1	Introduction	74
5.2	Definition of the problem	76
5.2.1	Thermosolutal convection	76
5.2.2	Numerical methods	78
5.2.3	Linear stability analysis	79
5.3	RZIF using fields from DNS	80
5.3.1	Overview	80
5.3.2	Fourier decomposition and eigenvectors	82
5.3.3	Approximating the mean flow	84
5.4	Self-consistent model	89
5.4.1	Decoupled model	89
5.4.2	Full Newton method for SCM	90
5.4.3	First-order SCM	92
5.4.4	Higher-order SCM	94
5.5	Discussion	97
5.6	Appendix	97
Bibliography		101
Chapitre 6 Preliminary studies		102
6.1	Lid-driven cavity flow	102
6.1.1	Problem	102
6.1.2	Numerical simulation and validation	103
6.1.3	Results	105
6.1.4	Conclusion	109
6.2	Stability analysis of the Bénard arrow	112
Bibliography		116

Chapter 1

Introduction (en)

Ancient civilizations have shown an intuitive and experimental knowledge of fluid mechanics, and used this knowledge in the fabrication of arrows, boats and the design of irrigation systems. Hydrostatic principles were investigated at least two thousand years ago in ancient Greece by Archimedes. Substantial progress in fluid mechanics began with the observations and experiments of Leonardo da Vinci: Evangelista Torricelli invented the barometer, Isaac Newton established the basis of classical mechanics and Daniel Bernoulli established the basis of fluid dynamics. During the nineteenth century, Claude-Louis Navier and George Stokes inferred the governing equations of fluid dynamics, known as the Navier-Stokes equations.

In addition to the beautiful structures that unsteady flows may exhibit (figure 2.1), their study plays an essential role in a large number of problems, from natural phenomena to industrial applications. For instance, the comprehension of such flows is helpful to suppress the unwanted vibrations of the vortical structures on bridges or to design vehicles with less energy consumption. Vortical structures could be also produced intentionally to enhance mixing in microfluidic devices for instance.

In this thesis we are interested in time-periodic flows also called oscillators which originate from a Hopf bifurcation. The Bénard-von Kármán vortex street observed in the cylinder wake (figure 2.1(b)) is a famous example of an unsteady flow produced through a Hopf bifurcation. Understanding the onset of the Hopf bifurcation as well as predicting the nonlinear frequency and the amplitude of the perturbation is essential to characterize such flows. The full Navier-Stokes equations solved by direct numerical simulation (DNS) and experiments give a good description of nonlinear flows. However, these methods are expensive. Moreover, these methods consider all the complexity of the flow which makes the study of the physical mechanisms difficult. In some cases, this complexity is not necessary to reproduce the main features of the full nonlinear problem.

Therefore many procedures have been developed to characterize such flows without solving the full Navier Stokes equations. The aim of this thesis is to show the limitations of some of these procedures, which will be described in the next sections.

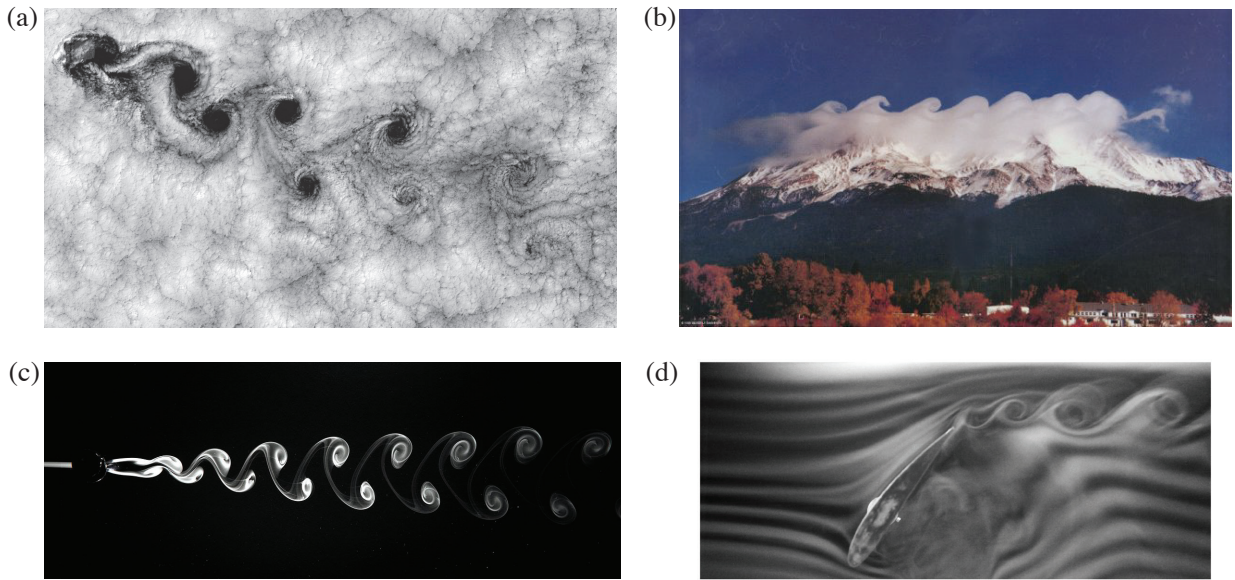


Figure 1.1 – (a) von-Kármán vortex street behind the Juan Fernandez Island, by Shannon [14]. (b) Kelvin-Helmholtz instability over Mount Shasta by Shannon [13]. (c) von-Kármán vortex street behind a cylinder by Wagner [18]. (d) Kelvin-Helmholtz instability around an airfoil by GmbH [4]

1.1 Linear stability analysis

The first statement about the concept of stability of physical systems was formulated in the nineteenth century by James Clerk Maxwell as reported by Campbell & Garnett [3] (p. 440) :

"When the state of things is such that an infinitely small variation of the present state will alter only by an infinitely small quantity the state at some future time, the condition of the system, whether at rest or in motion, is said to be stable ; but when an infinitely small variation in the present state may bring about a finite difference in the state of the system in a finite time, the condition of the system is said to be unstable..."

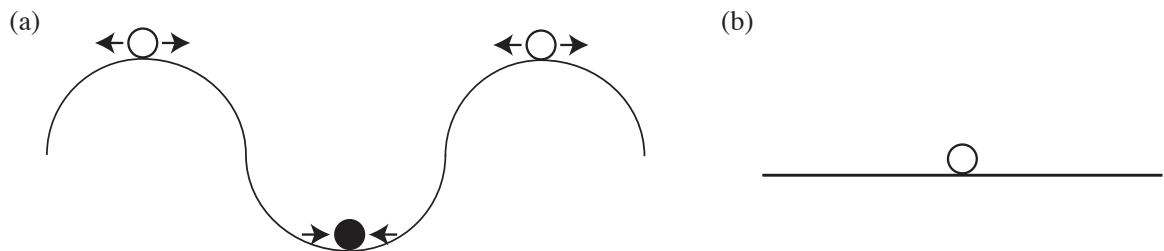


Figure 1.2 – Schematic illustration of the concept of stability. (a) The hollow balls are on the top of hills. These positions are unstable equilibrium states. The filled ball is in the valley, which is a stable equilibrium state. (b) The hollow ball positioned on a flat plate is marginally stable.

This stability concept is described by the schematic sketch in figure 2.2. For a small perturbation, the hollow balls will quit their positions permanently, which shows that these positions are unstable. In contrast, the filled ball subjected to an infinitesimal perturbation will stop at its original position after some oscillations, which indicates that this position is a stable equilibrium state. Figure 2.2(b) shows a hollow ball on a flat plate. This situation

corresponds to neutral stability. Indeed, all the positions on the flat plate are equivalent and the ball will remain wherever we place it.

1.1.1 Linear stability about the base flow

The equilibrium states or fixed points discussed in the previous section are the steady states about which we carry out a linear stability analysis. In fluid flow, the equilibrium state is a field of one, two or three dimensions and can be steady or periodic. This state is called the base flow. In the context of linear stability analysis, the base flow is the solution of the stationary Navier-Stokes equations. In experiments, an unstable base flow cannot be observed: experiment shows only the final periodic stable state. In numerical simulation, an unstable base flow can be obtained by various methods like the Newton-Raphson method, the selective frequency damping introduced by Åkervik *et al.* [1] or by imposing the symmetries of the base flow as was done by Barkley [2] for the cylinder wake. This last procedure is not always possible, because the base flow may not be symmetric in some configurations.

Linear stability analysis consists of analyzing the time evolution of a perturbation from the base state. This analysis was first carried out in two dimensions by Pierrehumbert & Widnall [12]. (In the 2000s a new terminology was introduced whereby linear stability analysis was called *global* linear stability analysis in contrast to the local stability analysis used for parallel and weakly parallel flows by researchers such as Huerre & Monkewitz [5].) Linear stability analysis is carried out by solving the linearized Navier-Stokes equations about the base flow

$$\partial_t \mathbf{u}' = \mathcal{L}_{\mathbf{U}_b} \mathbf{u}' \quad (1.1)$$

where \mathbf{u}' is the infinitesimal perturbation vector. $\mathcal{L}_{\mathbf{U}_b}$ is the operator linearized about the base flow \mathbf{U}_b , which corresponds to the Jacobian matrix. Solutions to (2.1) are of the form $\mathbf{u}' = \hat{\mathbf{u}} e^{(\sigma + i\omega)t}$. Therefore, equation (2.1) is reduced to the eigenvalue problem,

$$(\sigma + i\omega) \hat{\mathbf{u}} = \mathcal{L}_{\mathbf{U}_b} \hat{\mathbf{u}} \quad (1.2)$$

Equation (2.2) is characterized by the eigenvalues $\sigma + i\omega$ of the Jacobian matrix $\mathcal{L}_{\mathbf{U}_b}$. The stability of the base flow depends on the real part of the dominant eigenvalue:

- If $\sigma < 0$, then the base flow is stable
- If $\sigma = 0$, then the base flow is marginally stable
- If $\sigma > 0$, then the base flow is unstable

Figure 2.3 shows as a thin curve the result of the linear stability analysis about the base flow of the cylinder wake, reproduced from Barkley [2]. We observe the zero crossing of the growth rate σ shown in figure 2.3(b) at the critical Reynolds number $Re_c \approx 47$, which is the threshold of a supercritical Hopf bifurcation. The frequency ω obtained by linear stability analysis about the base flow shown in figure 2.3(a) matches the nonlinear frequency shown as a bold curve at $Re_c \approx 47$. However, this analysis fails to predict the frequency of the time-periodic solutions for $Re > Re_c$. This failure is due to the absence of the nonlinear term (Reynolds stress) from the linear stability analysis.

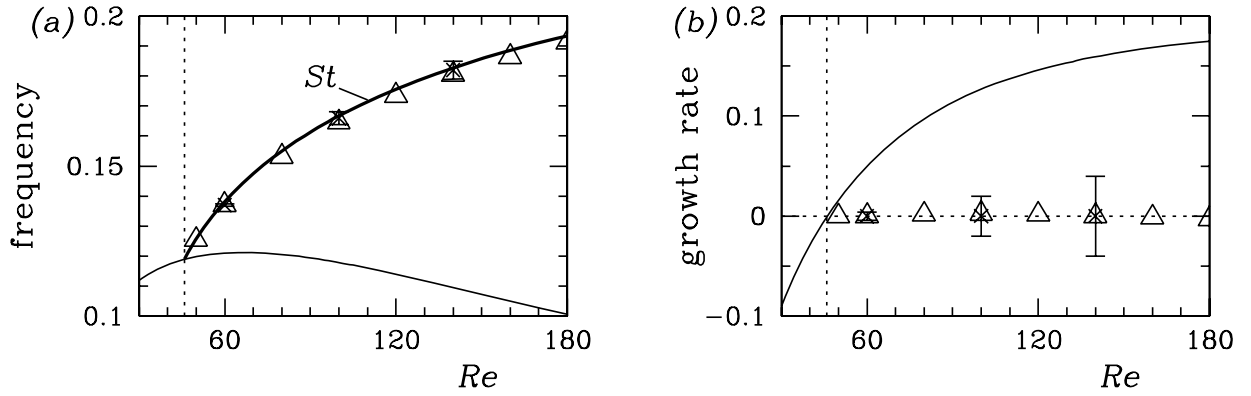


Figure 1.3 – (a) The imaginary part (frequency) and (b) the real part (growth rate) of the eigenvalue. The nonlinear frequency is shown as a bold curve, the thin curve shows the results predicted by linear stability analysis about the base flow and the triangles show the results obtained from linearization about the mean flow. From Barkley [2].

1.1.2 Mean flow analysis

The difference between the mean and base flow, called the distortion, is the result of the nonlinear interactions (Reynolds stress). Therefore, it is natural to think that the mean flow may receive information about the nonlinear dynamics (Maurel *et al.* [9], Zielinska & Wesfreid [19]). By following this idea, Barkley [2], Mittal [10], Pier [11] carried out linearization about the time-averaged flow for the cylinder wake and Turton *et al.* [17] in the thermosolutal convection, even though the mean flow is not a solution of the stationary Navier-Stokes equations. This procedure is identical to that presented in the previous section except that we replace the base flow by the mean flow in equations (2.1) and (2.2). The frequency (imaginary part of the eigenvalue) obtained by this procedure matches the nonlinear frequency over the entire range of Reynolds number as shown by the triangles in figure 2.3(a). Moreover, the growth rate (real part of the eigenvalue) is nearly zero as shown by figure 2.3(b), which means that the mean flow is neutrally stable. This property, named RZIF (Real Zero Imaginary Frequency) by Turton *et al.* [17], has been sometimes viewed as a prediction of the nonlinear frequency from the mean flow. This is not the case, because the mean flow must be obtained from a DNS or an experiment. However, this property emphasizes the relevance of the mean flow in the study of nonlinear systems.

The fact that the linear analysis about the base flow does not predict information about the full nonlinear system is not surprising, because in this analysis we neglect the nonlinear term. However, the fact that there are configurations, like the open shear-driven cavity flow, for which this analysis predicts fairly well the nonlinear frequency even at a high Reynolds number is intriguing. We suppose that this is because the distortion introduced via the Reynolds stress term is small. The frequency obtained by linearization about the mean flow remains closer, however, to the nonlinear frequency.

Linearization about the mean flow has also its limitations. Indeed, the RZIF property is not universal for all time-periodic flows. Thermosolutal convection presents two branches, one of traveling waves, another of standing waves. Turton *et al.* [17] have shown that only the traveling waves verify the RZIF property. Turton *et al.* [17] argued that the failure of the standing waves to satisfy the RZIF property, is due to their broad spectrum. The traveling waves, in contrast, show a peaked spectrum. They demonstrated that for

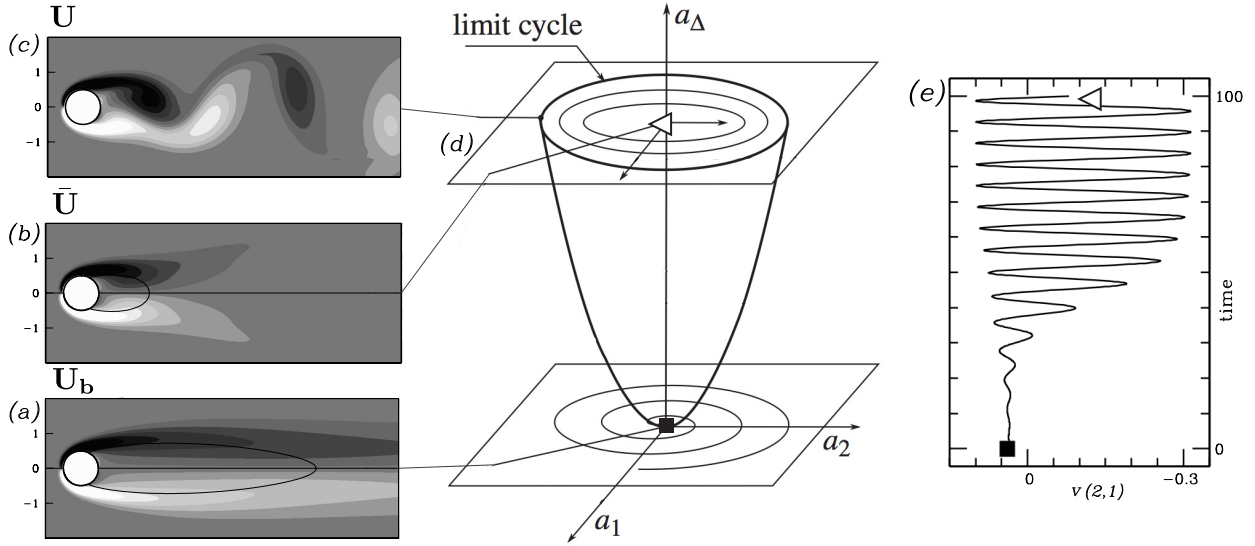


Figure 1.4 – Description of the saturation and mean flow distortion. (a) Base flow, (b) Temporal mean flow, (c) snapshot of the vortex shedding, (e) time evolution of the velocity at the point $(x_1 = 2, y = 1)$ from the base flow (black square) until saturation. From Barkley [2]. (d) Sketch of the transient wake dynamics (modified from Tadmor *et al.* [15]).

monochromatic oscillations the RZIF property is exactly satisfied.

1.2 Nonlinear dynamics

The nonlinear process from the bifurcation onset to the saturated state (Maurel *et al.* [9], Zielinska & Wesfreid [19]) is illustrated in figure 2.4. The schematic view in figure 2.4(d) describes the typical evolution of a Hopf bifurcation from the base flow (black square) until reaching the limit cycle, which corresponds to the time-periodic vortex shedding shown in figure 2.4(c). Near criticality (black square in figure 2.4(d,e)), the base flow (figure 2.4(a)) and the mean flow are almost the same and the nonlinear frequency measured at this stage of the bifurcation is nearly identical to that predicted by the linear stability about the base flow. During the growth of the perturbation, this frequency increases until reaching that of the vortex shedding and a continuous correction of the mean flow \bar{U} is introduced by the nonlinear interaction until saturation. The growth rate obtained by linearization about the instantaneous mean flow decreases until marginality as shown by Thiria *et al.* [16]. This process of amplitude saturation and mean flow distortion sheds light into the mechanisms leading to the RZIF property.

We have shown previously that linear stability analysis about the base flow has limitations. In most cases, linear stability analysis about the base flow is able to predict the frequency of the nonlinear system only near the onset of the bifurcation. On the other hand, linearization about the mean flow is not predictive as we need to carry out an experiment or DNS to compute the mean flow. Moreover, the linear analysis does not describe the amplitude saturation process. A self-consistent model (SCM) based on the RZIF property has been proposed by Mantić-Lugo *et al.* [7] to describe the amplitude saturation process. This model is described in the next section.

1.2.1 Self-consistent model

Mantič-Lugo *et al.* [7] developed the self-consistent model to describe the amplitude saturation process without time integration. This model is a coupled system consisting of the mean flow governing equation and linearized Navier-Stokes equations. Mantič-Lugo *et al.* [7] assumed that for supercritical flows satisfying the RZIF property, the leading mode suffices for the mean flow distortion. Therefore, the self-consistent model is written as

$$N(\bar{\mathbf{U}}) = -A_f \frac{\Re((\hat{\mathbf{u}}_{-1} \cdot \nabla) \hat{\mathbf{u}}_1)}{\|\Re((\hat{\mathbf{u}}_{-1} \cdot \nabla) \hat{\mathbf{u}}_1)\|_2} \quad (1.3a)$$

$$(\sigma + i\omega) \hat{\mathbf{u}}_1 = \mathcal{L}_{\bar{\mathbf{U}}} \hat{\mathbf{u}}_1 \quad (1.3b)$$

with $\hat{\mathbf{u}}_{-1} = \hat{\mathbf{u}}_1^*$ and $\mathcal{L}_{\bar{\mathbf{U}}}$ is the linear operator about $\bar{\mathbf{U}}$. The parameter A_f indicates the amplitude of the forcing term $\Re((\hat{\mathbf{u}}_{-1} \cdot \nabla) \hat{\mathbf{u}}_1)$. A_f is an external parameter, because the linear equation (2.3) does not determine the amplitude of the mode. The term $\Re((\hat{\mathbf{u}}_{-1} \cdot \nabla) \hat{\mathbf{u}}_1)$ is normalized by $\|\Re((\hat{\mathbf{u}}_{-1} \cdot \nabla) \hat{\mathbf{u}}_1)\|_2$, in order to ensure convergence of the system of equations (2.3) as described by Mantič-Lugo *et al.* [8]. This system is solved by Mantič-Lugo *et al.* [8] for a given A_f , by first solving the linear equation (2.3b) with the base flow as the initial guess. We obtain the solution σ , ω and the leading eigenmode $\hat{\mathbf{u}}_1$. Then, the forcing term $\Re((\hat{\mathbf{u}}_{-1} \cdot \nabla) \hat{\mathbf{u}}_1) / \|\Re((\hat{\mathbf{u}}_{-1} \cdot \nabla) \hat{\mathbf{u}}_1)\|_2$ is calculated with $\hat{\mathbf{u}}_1$ and a new mean flow is computed with equation (2.3a) by Newton method. This new mean flow $\bar{\mathbf{U}}$ is substituted into (2.3b) leading to new values for σ , ω and $\hat{\mathbf{u}}_1$. As long as the growth rate is greater than zero, $\sigma > 0$, the process is continued by increasing the amplitude A_f until convergence to the marginally stable solution $\sigma = 0$, ω , $\hat{\mathbf{u}}_1$ and $\bar{\mathbf{U}}$.

1.3 Present work

The aim of the present work is to characterize various flows undergoing a supercritical Hopf bifurcation using the procedures described previously. More specifically, we present in this manuscript three different configurations: the open shear-driven cavity flow, Taylor-Couette flow and finally thermosolutal convection.

Open shear-driven square cavity

The open shear-driven square cavity has been broadly used as a validation case for numerical and theoretical development. Despite the large number of studies based on this configuration, no detailed description of the first bifurcations has been given. This study is focused on a region of Reynolds number Re where two coexisting limit cycles are separated by an unstable quasiperiodic state. The first objective of this study is to describe in detail this bifurcation scenario by means of nonlinear direct numerical simulation, linear stability analysis, and Floquet analysis. The second objective concerns the prediction of the nonlinear frequency by linear stability analysis. The open cavity flow satisfies only partially the RZIF property. Indeed, the linear stability analysis about the mean flow computes a frequency that matches the nonlinear frequency but the mean flow is not marginally stable. Moreover, in this configuration, even linear stability analysis about the base flow predicts fairly well the nonlinear frequency. This case is a mild counterexample to the RZIF property, the first being the standing waves in thermosolutal convection of Turton *et al.* [17].

Taylor-Couette flow

The second part is devoted to the study of the RZIF property in a Taylor-Couette flow. The thermosolutal convection mentioned previously is driven by temperature and concentration differences. When these differences have opposite effects, a supercritical Hopf bifurcation occurs. In this case, the Hopf bifurcation leads to coexisting solutions, the traveling waves, and the standing waves, at most one of which can be stable as has been proven by Knobloch [6]. Turton *et al.* [17] showed that for the standing wave solution, the RZIF property is not satisfied: the frequency obtained by linearization about the mean flow is far from the nonlinear frequency and the growth rate is far from zero. This is the only known case in which the RZIF property is fully not satisfied. In the counter-rotating Taylor-Couette flow, there exists a range of Rayleigh number where a Hopf bifurcation leads to two solutions, the axially upwards and downwards moving spirals and the ribbons which are an equal superposition of these two kinds of spirals. The spirals are traveling waves and the ribbons are seen as standing waves. The primary objective of this study is to investigate the validity of the RZIF property on this pair of hydrodynamic traveling and standing waves. We have also discovered that the ribbon branch is followed by two types of successive heteroclinic cycles, connecting two pairs of axisymmetric vortices. The first heteroclinic orbit is non-axisymmetric, with excursions resembling ribbons, while the second has axisymmetric excursions. The analysis of these heteroclinic orbits is the second objective of this study.

Thermosolutal convection

The third part is devoted to better understanding the self-consistent model of Mantič-Lugo *et al.* [7]. This model has been assumed to be valid in all cases where the RZIF property is verified. We have tested the SCM on the traveling waves of the thermosolutal convection where the RZIF property holds (Turton *et al.* [17]). We have shown in this case that the SCM predicts the nonlinear frequencies only in the vicinity of the threshold. We have also implemented the SCM by considering higher orders in the Reynolds stress term, which greatly improved the prediction of the nonlinear frequency, the amplitude of the mode and the mean flow. This shows that when RZIF holds, the SCM is not necessarily valid. The SCM has been solved by mean of a full Newton method which avoids the convergence difficulties encountered in the algorithm proposed by Mantič-Lugo *et al.* [8].

Bibliography

- [1] ÅKERVIK, E., BRANDT, L., HENNINGSON, D. S., HØPFFNER, J., MARXEN, O. & SCHLATTER, P. 2006 Steady solutions of the Navier-Stokes equations by selective frequency damping. *Phys. Fluids* **18** (6), 068102. 3
- [2] BARKLEY, D 2006 Linear analysis of the cylinder wake mean flow. *EPL (Europhys. Lett.)* **75** (5), 750. 3, 4, 5
- [3] CAMPBELL, LEWIS & GARNETT, WILLIAM 1884 *The Life of James Clerk Maxwell: With Selections from His Correspondence and Occasional Writings*. Merchant Books. 2
- [4] GMBH 2010 Wind tunnel visualization of a naca 4412 airfoil at a low speed flow (re=20.000). *Wikimedia Commons* . 2
- [5] HUERRE, PATRICK & MONKEWITZ, PETER A 1990 Local and global instabilities in spatially developing flows. *Annu. Rev. Fluid Mech.* **22** (1), 473–537. 3
- [6] KNOBLOCH, E 1986 Oscillatory convection in binary mixtures. *Phys. Rev. A* **34** (2), 1538. 7
- [7] MANTIČ-LUGO, VLADISLAV, ARRATIA, CRISTÓBAL & GALLAIRE, FRANÇOIS 2014 Self-consistent mean flow description of the nonlinear saturation of the vortex shedding in the cylinder wake. *Phys. Rev. Lett.* **113** (8), 084501. 5, 6, 7
- [8] MANTIČ-LUGO, VLADISLAV, ARRATIA, CRISTÓBAL & GALLAIRE, FRANÇOIS 2015 A self-consistent model for the saturation dynamics of the vortex shedding around the mean flow in the unstable cylinder wake. *Phys. Fluids* **27** (7), 074103. 6, 7
- [9] MAUREL, A, PAGNEUX, V & WESFREID, JE 1995 Mean-flow correction as non-linear saturation mechanism. *Europhys. Lett.* **32** (3), 217. 4, 5
- [10] MITTAL, SANJAY 2008 Global linear stability analysis of time-averaged flows. *Int. J. Numer. Meth. Fluids* **58** (1), 111–118. 4
- [11] PIER, BENOÎT 2002 On the frequency selection of finite-amplitude vortex shedding in the cylinder wake. *J. Fluid Mech.* **458**, 407–417. 4
- [12] PIERREHUMBERT, RT & WIDNALL, SE 1982 The two-and three-dimensional instabilities of a spatially periodic shear layer. *J. Fluid Mech.* **114**, 59–82. 3
- [13] SHANNON 1999 From clouds over mount. <https://cnls.lanl.gov/petersen/header.html>. 2

- [14] SHANNON, B. 1999 Visualisation of the von Kármán vortex street behind the Juan Fernandez Islands. *NASA GSFC* . [2](#)
- [15] TADMOR, GILEAD, LEHMANN, OLIVER, NOACK, BERND R, CORDIER, LAURENT, DELVILLE, JOËL, BONNET, JEAN-PAUL & MORZYŃSKI, MAREK 2011 Reduced-order models for closed-loop wake control. *Phil. Trans. R. Soc. A* **369** (1940), 1513–1524. [5](#)
- [16] THIRIA, BENJAMIN, BOUCHET, GILLES & WESFREID, JOSÉ EDUARDO 2015 On the relation between linear stability analysis and mean flow properties in wakes. *arXiv preprint arXiv:1506.05948* . [5](#)
- [17] TURTON, SAM E, TUCKERMAN, LAURETTE S & BARKLEY, DWIGHT 2015 Prediction of frequencies in thermosolutal convection from mean flows. *Phys. Rev. E* **91** (4), 043009. [4](#), [6](#), [7](#)
- [18] WAGNER, J. 2014 Visualisation of the von Kármán vortex sheet behind a circular cylinder in air flow. *Wikimedia Commons* . [2](#)
- [19] ZIELINSKA, BJA & WESFREID, JE 1995 On the spatial structure of global modes in wake flow. *Phys. Fluids* **7** (6), 1418–1424. [4](#), [5](#)

Chapter 2

Introduction (fr)

La mécanique des fluides a été utilisée par les civilisations anciennes d’une façon intuitive et expérimentale, par exemple pour la fabrication de flèches, de bateaux ainsi que pour la mise en place de systèmes d’irrigation. Les principes de l’hydrostatique ont été étudiés depuis au moins deux mille ans par Archimède. Des progrès significatifs en mécanique des fluides ont commencé par les observations et expériences de Léonard de Vinci : Évangelista Torricelli a inventé le baromètre, Isaac Newton a instauré les bases de la mécanique classique et Daniel Bernoulli a mis en place les bases de la dynamique des fluides. Pendant le dix-neuvième siècle, Claude-Louis Navier et George Stokes ont déduit les équations de la dynamique des fluides, connues comme les équations de Navier-Stokes.

En plus de la beauté des structures que peuvent présenter les écoulements fluides instationnaires (figure 2.1), leur compréhension joue un rôle essentiel dans de nombreux problèmes, allant des phénomènes naturels aux applications industrielles. Par exemple, la compréhension de tels écoulements est utile pour la suppression des vibrations causées par les structures tourbillonnaires sur les ponts ou pour aider à concevoir des véhicules avec une faible consommation énergétique. Les structures tourbillonnaires peuvent aussi être produites volontairement pour améliorer le mélange dans les cellules microfluidiques par exemple.

Dans cette thèse nous sommes intéressés par les écoulements périodiques, aussi appelés oscillateurs, provenant de bifurcations de Hopf. La trainée tourbillonnaire de Bénard-von Kármán observée sur le sillage d’un cylindre (figure 2.1(b)) est un exemple très connu d’un écoulement instationnaire produit par une bifurcation de Hopf. La compréhension de la bifurcation ainsi que la prédiction de la fréquence non linéaire et l’amplitude des perturbations sont essentielles pour caractériser ce type d’écoulement. Les équations de Navier-Stokes résolues par moyen de simulation numérique directe (DNS) et d’expériences donnent une description précise de l’écoulement non linéaire. Cependant, ces méthodes sont coûteuses. De plus ces méthodes considèrent toute la complexité de l’écoulement ce qui rend l’étude des mécanismes physiques difficile. Dans certains cas, cette complexité n’est pas nécessaire pour reproduire les caractéristiques principales du problème non linéaire.

Par conséquent plusieurs procédures ont été développées pour caractériser de tels écoulements sans la résolution des équations de Navier-Stokes complètes. L’objet de cette thèse est de montrer la limitation de certaines de ces procédures, lesquelles seront décrites dans

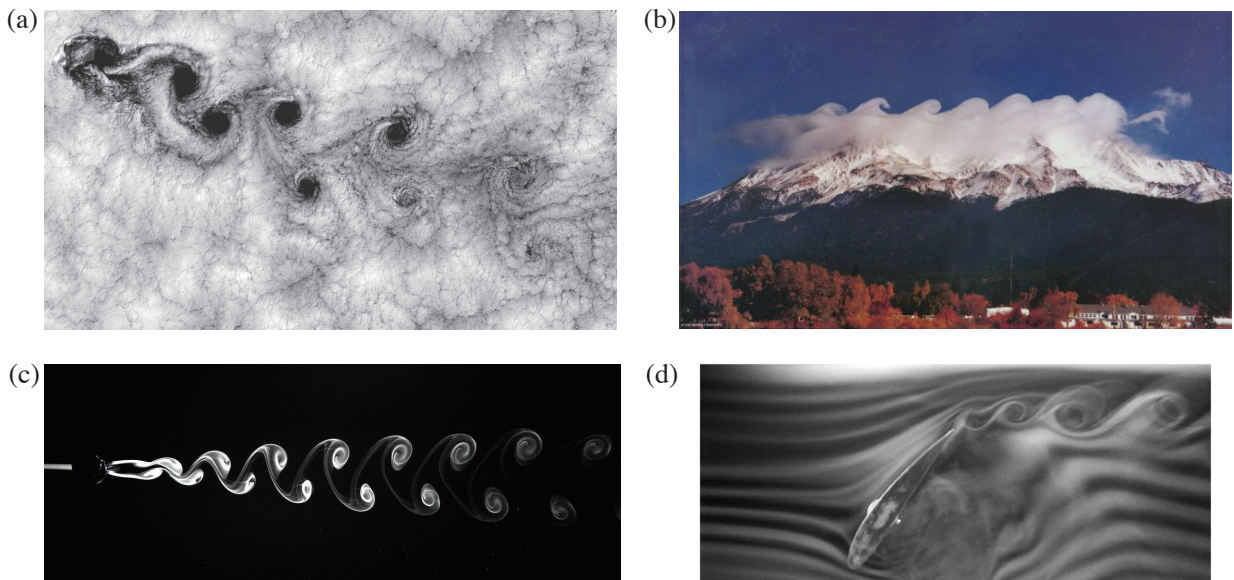


Figure 2.1 – (a) Trainée tourbillonnaire de von-Kármán observée derrière l'île Juan Fernandez, par Shannon [14]. (b) instabilité de Kelvin-Helmholtz observée au-dessus du mont Shasta, par Shannon [13]. (c) Trainée tourbillonnaire de von-Kármán observée derrière un cylindre par Wagner [18]. (d) Instabilité Kelvin-Helmholtz observée autour d'un profil d'aile, par GmbH [4]

les sections suivantes.

2.1 Analyse de stabilité linéaire

Le premier énoncé sur le concept de stabilité pour les systèmes physiques a été formulé pendant le dix-neuvième siècle par James Clerk Maxwell, cité par Campbell & Garnett [3] (p. 440) :

"When the state of things is such that an infinitely small variation of the present state will alter only by an infinitely small quantity the state at some future time, the condition of the system, whether at rest or in motion, is said to be stable; but when an infinitely small variation in the present state may bring about a finite difference in the state of the system in a finite time, the condition of the system is said to be unstable..."

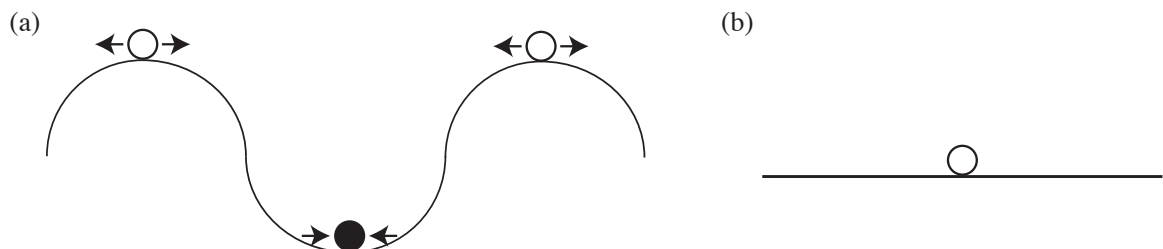


Figure 2.2 – Illustration schématique du concept de stabilité. (a) Les balles blanches sont positionnées au sommet des collines. Ces positions sont des points d'équilibre instables. La balle noire est positionnée dans la vallée, qui est une position d'équilibre stable. (b) La balle blanche positionnée sur une plaque plane est marginalement stable.

Ce concept de stabilité est décrit par le schéma présenté sur la figure 2.2. Pour une petite perturbation, les balles blanches quittent leur position définitivement, ce qui montre

que ces positions sont instables. Par contre, la balle noire soumise à une perturbation infinitésimale s'arrêtera sur sa position d'origine après quelques oscillations, ce qui indique que cette position est un état d'équilibre stable. La figure 2.2(b) montre une balle blanche sur une plaque plane. Cette situation correspond à une stabilité neutre. En effet, toutes les positions sur la plaque sont équivalentes et la balle restera sur n'importe laquelle de ces positions.

2.1.1 Stabilité linéaire autour de l'écoulement de base

Les états d'équilibre où points fixes discutés dans le paragraphe précédent sont les états stationnaires autour desquels nous appliquons l'analyse de stabilité linéaire. Dans les écoulements fluides, un état d'équilibre est un champ à une, deux ou trois dimensions et peut être stationnaire ou périodique. Cet état est nommé l'écoulement de base. Dans le contexte de l'analyse de stabilité linéaire, l'écoulement de base est la solution des équations stationnaires de Navier-Stokes.

Dans les expériences, l'écoulement de base instable ne peut pas être observé et seulement l'écoulement final périodique et stable est observé.

Dans une simulation numérique, l'écoulement de base instable peut être obtenu par plusieurs méthodes, telle que la méthode de Newton-Raphson, la *selective frequency damping* introduite par Åkervik *et al.* [1] ou en imposant les symétries de l'écoulements de base tels que cela avait été fait par Barkley [2] dans le cas du sillage d'un cylindre. Cette dernière procédure n'est souvent pas possible parce que l'écoulement de base n'a souvent pas de symétrie.

L'analyse de stabilité linéaire consiste à suivre l'évolution temporelle d'une perturbation à partir de l'état de base. Cette analyse a été initié en deux dimensions par Pierrehumbert & Widnall [12]. (Dans les années 2000s, l'analyse de stabilité linéaire a parfois été renommé "analyse de stabilité linéaire *globale*" en opposition avec l'analyse de stabilité linéaire locale utilisée dans le cas d'écoulements parallèles et quasi parallèles par des chercheurs tels que Huerre & Monkewitz [5].) L'analyse de stabilité linéaire est réalisée en résolvant les équations de Navier-Stokes linéarisées autour de l'écoulement de base.

$$\partial_t \mathbf{u}' = \mathcal{L}_{\mathbf{U}_b} \mathbf{u}' \quad (2.1)$$

où \mathbf{u}' est le vecteur des perturbations infinitésimales. $\mathcal{L}_{\mathbf{U}_b}$ est l'opérateur linéarisé autour de l'écoulement de base \mathbf{U}_b et correspond à la matrice Jacobienne. Les solutions de (2.1) sont de la forme $\mathbf{u}' = \hat{\mathbf{u}} e^{(\sigma + i\omega)t}$. Par conséquent, l'équation (2.1) est réduite à un problème aux valeurs propres,

$$(\sigma + i\omega) \hat{\mathbf{u}} = \mathcal{L}_{\mathbf{U}_b} \hat{\mathbf{u}} \quad (2.2)$$

L'équation (2.2) est caractérisée par les valeurs propres $\sigma + i\omega$ de la matrice Jacobienne $\mathcal{L}_{\mathbf{U}_b}$. La stabilité de l'écoulement de base dépend de la partie réelle de la valeur propre dominante:

- Si $\sigma < 0$, alors l'écoulement de base est stable

- Si $\sigma = 0$, alors l'écoulement de base est marginalement stable
- Si $\sigma > 0$, alors l'écoulement de base est instable

La courbe fine sur la figure 2.3 montre les résultats de l'analyse de stabilité linéaire autour de l'écoulement de base pour le sillage d'un cylindre. Nous observons sur la figure 2.3(b) le seuil de la bifurcation de Hopf supercritique au nombre de Reynolds critique $Re_c \approx 47$, indiqué par l'intersection du taux de croissance σ avec l'axe de stabilité marginale. La fréquence ω obtenue par l'analyse de stabilité linéaire autour de l'écoulement de base montrée sur la figure 2.3(a) est égale à la fréquence non linéaire à $Re = Re_c$, comme le montre par la courbe épaisse. Cependant, cette analyse échoue dans la prédiction de la fréquence non linéaire pour $Re > Re_c$. Cet échec est dû à l'absence des interactions non linéaires (contraintes de Reynolds) de l'analyse de stabilité linéaire.

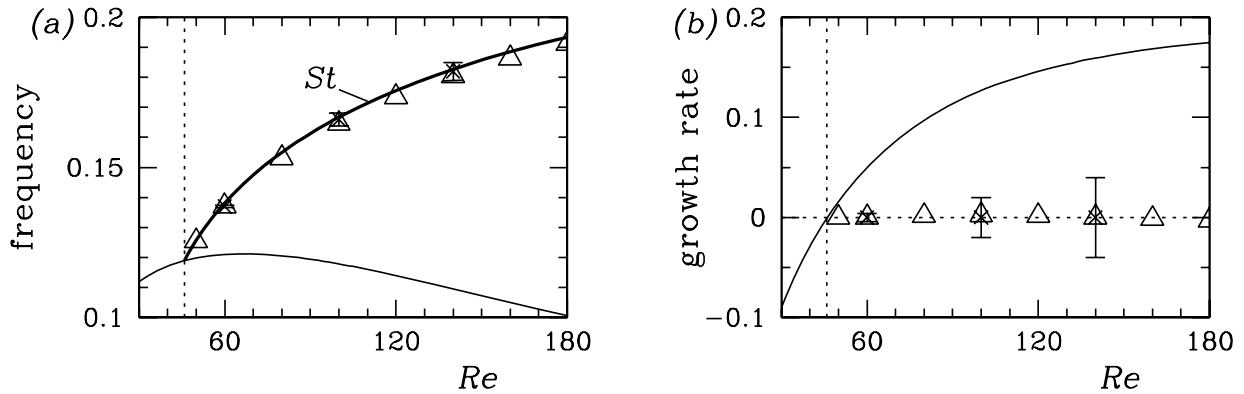


Figure 2.3 – (a) La partie imaginaire (fréquence) et (b) la partie réelle (taux de croissance) de la valeur propre. La fréquence non linéaire est montrée par la courbe en gras et la courbe fine montre les résultats prédits par l'analyse de stabilité linéaire autour de l'écoulement de base. Les triangles montrent les résultats obtenus à partir de la linéarisation autour de l'écoulement moyen. Barkley [2]

2.1.2 Analyse par écoulement moyen

La différence entre l'écoulement de base et moyen est nommée distorsion et elle est le résultat des interactions non linéaires (Reynolds stress). Par conséquent, il est naturel de penser que l'écoulement moyen peut capter des informations sur la dynamique non linéaire de l'écoulement (Maurel *et al.* [9], Zielinska & Wesfreid [19]). En suivant cette idée, Barkley [2], Mittal [10], Pier [11] ont réalisé la linéarisation autour de la moyenne temporelle de l'écoulement pour le sillage du cylindre et Turton *et al.* [17] pour la convection thermosolutale, même si l'écoulement moyen n'est pas solution des équations stationnaires de Navier-Stokes. Cette procédure est identique à celle présentée dans la section précédente mis à part que nous remplaçons l'écoulement de base par l'écoulement moyen dans les équations (2.1) et (2.2). La fréquence (partie imaginaire de la valeur propre) obtenue par cette procédure est égale à la fréquence non linéaire sur tout l'intervalle du nombre de Reynolds tels que le montrent les triangles sur la figure 2.3(a). De plus, le taux de croissance (partie réelle de la valeur propre) est presque égal à zéro tel que le montre la figure 2.3(b), ce qui indique que l'écoulement moyen est marginalement stable. Cette propriété, nommée RZIF (Real Zero Imaginary Frequency) par Turton *et al.* [17], a été vue comme une prédiction de la fréquence non linéaire à partir de l'écoulement moyen. Ceci n'est pas le cas, car l'écoulement moyen doit être obtenu à partir d'une DNS ou d'une expérience. Cependant, cette propriété souligne la pertinence de l'écoulement moyen dans

l'étude des systèmes non linéaires.

Le fait que l'analyse de stabilité linéaire autour de l'écoulement de base ne prédit pas d'information sur le système non linéaire complet n'est pas étonnant, car dans cette analyse nous négligeons les termes non linéaires. Cependant, le fait qu'il y ait des configurations, comme la cavité ouverte pour lesquelles cette analyse prédit relativement bien la fréquence non linéaire même à hauts nombres de Reynolds est surprenant. Nous supposons que cela est dû au fait que la distorsion introduite via le terme de contraintes de Reynolds est faible. Cependant, la fréquence obtenue par la linéarisation autour de l'écoulement moyen reste plus proche de la fréquence non linéaire.

La linéarisation autour de l'écoulement moyen possède également ses limitations. En effet, la propriété RZIF n'est pas universelle à tous les écoulements périodiques. La convection thermosolutal possède deux solutions, une d'ondes progressives et une autre d'ondes stationnaires. Turton *et al.* [17] ont montré que seuls les ondes progressives vérifient la propriété RZIF. Turton *et al.* [17] suggèrent que l'échec des ondes stationnaires pour satisfaire la propriété RZIF est dû à leur large spectre temporel. Les ondes progressives en revanche montrent un spectre piqué. Ils démontrent que pour des oscillations monochromatiques la propriété RZIF est exactement satisfaite.

2.2 Dynamique non linéaire

Le processus du début de la bifurcation jusqu'à l'état saturé (Maurel *et al.* [9], Zielinska & Wesfreid [19]) est illustré dans la figure 2.4. La vue schématique de la figure 2.4(d) décrit l'évolution typique de la bifurcation de Hopf à partir de l'écoulement de base (carrées noires) jusqu'à atteindre le cycle limite correspondant à la génération périodique des tourbillons montrés sur la figure 2.4(c). Proche du point critique (carré noir sur la figure 2.4(d,e)), l'écoulement de base (figure 2.4(a)) et l'écoulement moyen sont presque identiques et la fréquence non linéaire mesurée à ce stade de la bifurcation est presque identique à celle prédite par l'analyse de stabilité linéaire autour de l'écoulement de base. Pendant la croissance de la perturbation, cette fréquence augmente jusqu'à atteindre celle des émissions des tourbillons et une correction continue de l'écoulement moyen $\bar{\mathbf{U}}$ est introduite par les interactions non linéaires jusqu'à saturation. Le taux de croissance obtenu par la linéarisation autour de l'écoulement moyen instantané décroît jusqu'à la marginalité comme le montre Thiria *et al.* [16]. Ce processus de la saturation en amplitude et la distorsion de l'écoulement moyen apporte un éclairage sur les mécanismes conduisant à la propriété RZIF.

Nous avons montré précédemment que l'analyse de stabilité linéaire autour de l'écoulement de base a ses limitations. Dans la majeure partie des cas l'analyse de stabilité linéaire autour de l'écoulement de base est capable de prédire la fréquence du système non linéaire seulement proche du seuil de la bifurcation. D'un autre côté la linéarisation autour de l'écoulement moyen n'est pas prédictive puisque nous avons besoin des résultats d'une expérience ou d'une DNS pour calculer l'écoulement moyen. De plus, l'analyse linéaire ne décrit pas le processus de saturation de l'amplitude. Un modèle auto-consistant (SCM) basé sur la propriété RZIF a été proposé par Mantić-Lugo *et al.* [7] pour décrire le processus de saturation en amplitude. Ce modèle est décrit dans la section suivante.

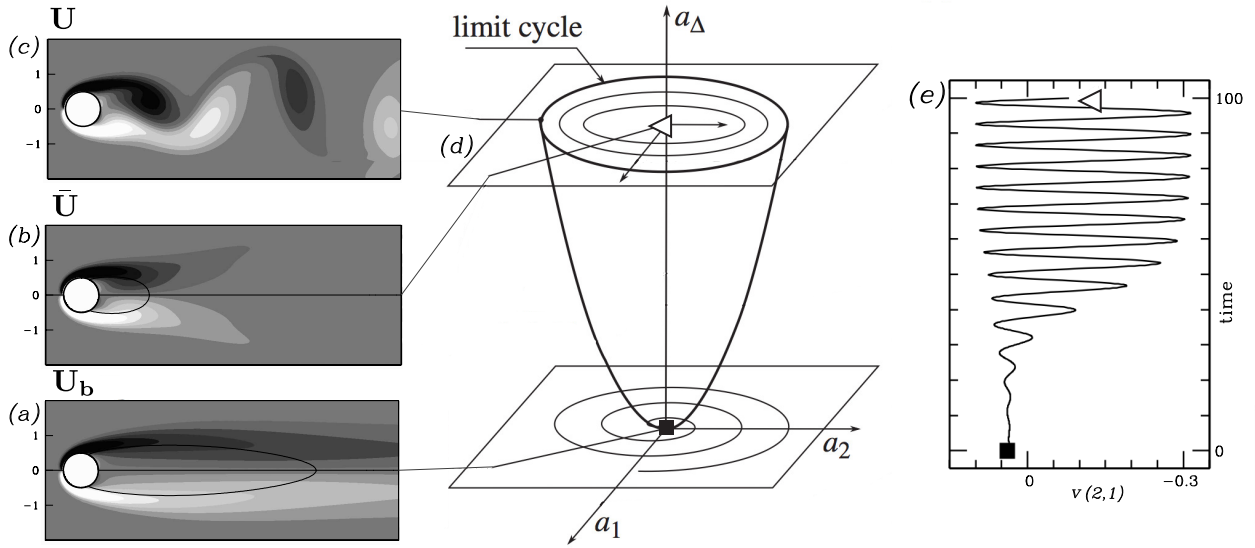


Figure 2.4 – Description de la saturation et distorsion de l'écoulement moyen. (a) écoulement de base, (b) écoulement moyenné dans le temps, (c) instantané de la trainée tourbillonnaire, (e) évolution temporelle de la vitesse au point de $(x_1 = 2, y = 1)$ de l'écoulement de base (carré noir) jusqu'à saturation. Barkley [2]. (d) Vision schématique de la transition du sillage dynamique (modifié à partir de la figure de (Tadmor *et al.* [15]))

2.2.1 Modèle auto-consistant

Mantič-Lugo *et al.* [7] ont développé un modèle auto-consistant pour décrire le processus de saturation en amplitude sans intégration temporelle. Ce modèle est un système couplé contenant l'équation gouvernant l'écoulement moyen et les équations de Navier-Stokes linéarisé. Mantič-Lugo *et al.* [7] supposent que pour les écoulements supercritiques satisfaisant la propriété RZIF, le mode principal est suffisant pour la distorsion de l'écoulement moyen. Par conséquent, le modèle auto-consistant est écrit comme

$$N(\bar{U}) = -A_f \frac{\Re((\hat{\mathbf{u}}_{-1} \cdot \nabla) \hat{\mathbf{u}}_1)}{\|\Re((\hat{\mathbf{u}}_{-1} \cdot \nabla) \hat{\mathbf{u}}_1)\|_2} \quad (2.3a)$$

$$(\sigma + i\omega) \hat{\mathbf{u}}_1 = \mathcal{L}_{\bar{U}} \hat{\mathbf{u}}_1 \quad (2.3b)$$

avec $\hat{\mathbf{u}}_{-1} = \hat{\mathbf{u}}_1^*$ et $\mathcal{L}_{\bar{U}}$ est l'opérateur linéaire autour de \bar{U} . Le paramètre A_f indique l'amplitude du terme de forçage $\Re((\hat{\mathbf{u}}_{-1} \cdot \nabla) \hat{\mathbf{u}}_1)$. A_f est un paramètre externe, car l'équation linéaire (2.3) ne permet pas de déterminer l'amplitude du mode. Le terme $\Re((\hat{\mathbf{u}}_{-1} \cdot \nabla) \hat{\mathbf{u}}_1)$ est normalisé par $\|\Re((\hat{\mathbf{u}}_{-1} \cdot \nabla) \hat{\mathbf{u}}_1)\|_2$ pour assurer la convergence du système d'équations (2.3) comme décrit par Mantič-Lugo *et al.* [8]. Ce système est résolu par Mantič-Lugo *et al.* [8] pour un A_f donnée, par premièrement la résolution de l'équation linéaire (2.3b) avec l'écoulement de base comme condition initiale. Nous obtenons la solution σ , ω et le mode propre principale $\hat{\mathbf{u}}_1$. Ensuite, le terme de forçage $\Re((\hat{\mathbf{u}}_{-1} \cdot \nabla) \hat{\mathbf{u}}_1) / \|\Re((\hat{\mathbf{u}}_{-1} \cdot \nabla) \hat{\mathbf{u}}_1)\|_2$ est calculé avec $\hat{\mathbf{u}}_1$ et un nouvel écoulement moyen est calculé via l'équation (2.3a) par une méthode de Newton. Ce nouvel écoulement moyen \bar{U} est substitué dans (2.3b) conduisant à une nouvelle solution pour σ , ω et $\hat{\mathbf{u}}_1$. Tant que le taux de croissance est plus grand que zéro, $\sigma > 0$, le processus est continué en augmentant l'amplitude A_f jusqu'à convergence vers la solution marginalement stable $\sigma = 0$, ω , $\hat{\mathbf{u}}_1$ et \bar{U} .

2.3 Plan de la thèse

L'objectif de ce présent travail est de caractériser plusieurs écoulements ayant une bifurcation de Hopf supercritique en utilisant les procédures décrites précédemment. Plus précisément, nous présentons dans ce manuscrit trois différentes configurations: l'écoulement dans une cavité ouverte entraînée par cisaillement, l'écoulement de Taylor-Couette et finalement la convection thermosolutal.

Cavité carrée ouverte et entraînée par cisaillement

L'écoulement dans une cavité carrée ouverte et entraînée par cisaillement a été largement utilisé comme cas de validation pour les développements numériques et théoriques. Malgré le nombre important d'études basées sur cette configuration, aucune description détaillée des premières bifurcations n'a été donnée. Cette étude concerne une plage du nombre de Re où deux cycles limites coexistent et sont séparés par un état quasi périodique. Le premier objectif de cette étude est de décrire en détail ce scénario de bifurcations via des simulations non linéaires directes, l'analyse de stabilité linéaire et l'analyse de Floquet. Le second objectif concerne la prédiction de la fréquence non linéaire par l'analyse de stabilité linéaire. L'écoulement dans une cavité ouverte satisfait partiellement la propriété RZIF. En effet, l'analyse de stabilité linéaire autour de l'écoulement moyen permet d'obtenir une fréquence qui est égale à la fréquence non linéaire mais l'écoulement moyen n'est pas marginalement stable. De plus, dans cette configuration, même l'analyse de stabilité linéaire autour de l'écoulement de base permet de prédire relativement bien la fréquence non linéaire. Ce cas est un léger contre exemple pour la propriété RZIF, la première étant les ondes stationnaires dans la convection thermosolutale de Turton *et al.* [17].

Écoulement de Taylor-Couette

La deuxième partie est dédiée à l'étude de la propriété RZIF dans l'écoulement de Taylor-Couette. La convection thermosolutale mentionnée précédemment est pilotée par une différence de température et de concentration. Lorsque ces différences ont des effets opposés, une bifurcation supercritique se produit. Dans ce cas, la bifurcation de Hopf conduit à deux solutions coexistantes : les ondes progressives et les ondes stationnaires avec au plus une solution stable comme cela a été prouvé par Knobloch [6]. Turton *et al.* [17] ont montré que pour les ondes stationnaires, la propriété RZIF n'est pas satisfaite: la fréquence obtenue par la linéarisation autour de l'écoulement moyen est différente de la fréquence non linéaire et le taux de croissance est loin de zéro. Ceci est le seul exemple connu pour lequel la propriété RZIF est pleinement non satisfaite.

Dans l'écoulement de Taylor-Couette contrarotatif, il existe un intervalle pour le nombre de Rayleigh pour lequel la bifurcation de Hopf conduit à deux solutions, les spirales montantes et descendantes dans la direction axiale et les rubans. Les rubans sont une superposition de ces deux types de spirales. Les spirales sont des ondes progressives et les rubans sont vus comme des ondes stationnaires. Le premier objectif de cette étude est d'investiguer la validité de la propriété RZIF sur cette paire d'ondes stationnaires et progressives. Nous avons aussi découvert que la branche des rubans est suivie successivement par deux types de cycles hétéroclines, connectant deux paires de tourbillons axisymétrique. La première orbite hétérocline est non-axisymétrique, avec des excursions ressemblant aux rubans, alors que la seconde a des excursions axisymétriques. L'analyse de ces orbites hétéroclines est le second objectif de cette étude.

Convection thermosolutal

La troisième partie est dédiée à une meilleure compréhension du modèle auto-consistant de Mantič-Lugo *et al.* [7]. Ce modèle est supposé être valide pour toutes les configurations où la propriété RZIF est vérifiée. Nous avons testé le SCM sur les ondes progressives de la convection thermosolutal pour lesquelles la propriété RZIF est satisfaite (Turton *et al.* [17]). Nous avons montré que pour cette solution le SCM prédit les fréquences non linéaires seulement au voisinage du seuil de bifurcation. Nous avons aussi implémenté le SCM en considérant les ordres supérieurs dans le terme des contraintes de Reynolds. Ceci a grandement amélioré la prédiction de la fréquence non linéaire, l'amplitude du mode ainsi que l'écoulement moyen. Ceci montre que lorsque RZIF est satisfaite, le SCM n'est pas nécessairement valide. Le SCM a été résolu au moyen d'une méthode de Newton complète. Cette méthode nous a permis d'éviter les difficultés de convergence rencontrées avec l'algorithme proposé par Mantič-Lugo *et al.* [8].

Bibliography

- [1] ÅKERVIK, E., BRANDT, L., HENNINGSON, D. S., HØPFFNER, J., MARXEN, O. & SCHLATTER, P. 2006 Steady solutions of the Navier-Stokes equations by selective frequency damping. *Phys. Fluids* **18** (6), 068102. [12](#)
- [2] BARKLEY, D 2006 Linear analysis of the cylinder wake mean flow. *EPL (Europhys. Lett.)* **75** (5), 750. [12](#), [13](#), [15](#)
- [3] CAMPBELL, LEWIS & GARNETT, WILLIAM 1884 *The Life of James Clerk Maxwell: With Selections from His Correspondence and Occasional Writings*. Merchant Books. [11](#)
- [4] GMBH 2010 Wind tunnel visualization of a naca 4412 airfoil at a low speed flow (re=20.000). *Wikimedia Commons* . [11](#)
- [5] HUERRE, PATRICK & MONKEWITZ, PETER A 1990 Local and global instabilities in spatially developing flows. *Annu. Rev. Fluid Mech.* **22** (1), 473–537. [12](#)
- [6] KNOBLOCH, E 1986 Oscillatory convection in binary mixtures. *Phys. Rev. A* **34** (2), 1538. [16](#)
- [7] MANTIČ-LUGO, VLADISLAV, ARRATIA, CRISTÓBAL & GALLAIRE, FRANÇOIS 2014 Self-consistent mean flow description of the nonlinear saturation of the vortex shedding in the cylinder wake. *Phys. Rev. Lett.* **113** (8), 084501. [14](#), [15](#), [17](#)
- [8] MANTIČ-LUGO, VLADISLAV, ARRATIA, CRISTÓBAL & GALLAIRE, FRANÇOIS 2015 A self-consistent model for the saturation dynamics of the vortex shedding around the mean flow in the unstable cylinder wake. *Phys. Fluids* **27** (7), 074103. [15](#), [17](#)
- [9] MAUREL, A, PAGNEUX, V & WESFREID, JE 1995 Mean-flow correction as non-linear saturation mechanism. *Europhys. Lett.* **32** (3), 217. [13](#), [14](#)
- [10] MITTAL, SANJAY 2008 Global linear stability analysis of time-averaged flows. *Int. J. Numer. Meth. Fluids* **58** (1), 111–118. [13](#)
- [11] PIER, BENOÎT 2002 On the frequency selection of finite-amplitude vortex shedding in the cylinder wake. *J. Fluid Mech.* **458**, 407–417. [13](#)
- [12] PIERREHUMBERT, RT & WIDNALL, SE 1982 The two-and three-dimensional instabilities of a spatially periodic shear layer. *J. Fluid Mech.* **114**, 59–82. [12](#)
- [13] SHANNON 1999 From clouds over mount. <https://cnls.lanl.gov/petersen/header.html>. [11](#)

- [14] SHANNON, B. 1999 Visualisation of the von Kármán vortex street behind the Juan Fernandez Islands. *NASA GSFC* . [11](#)
- [15] TADMOR, GILEAD, LEHMANN, OLIVER, NOACK, BERND R, CORDIER, LAURENT, DELVILLE, JOËL, BONNET, JEAN-PAUL & MORZYŃSKI, MAREK 2011 Reduced-order models for closed-loop wake control. *Phil. Trans. R. Soc. A* **369** (1940), 1513–1524. [15](#)
- [16] THIRIA, BENJAMIN, BOUCHET, GILLES & WESFREID, JOSÉ EDUARDO 2015 On the relation between linear stability analysis and mean flow properties in wakes. *arXiv preprint arXiv:1506.05948* . [14](#)
- [17] TURTON, SAM E, TUCKERMAN, LAURETTE S & BARKLEY, DWIGHT 2015 Prediction of frequencies in thermosolutal convection from mean flows. *Phys. Rev. E* **91** (4), 043009. [13](#), [14](#), [16](#), [17](#)
- [18] WAGNER, J. 2014 Visualisation of the von Kármán vortex sheet behind a circular cylinder in air flow. *Wikimedia Commons* . [11](#)
- [19] ZIELINSKA, BJA & WESFREID, JE 1995 On the spatial structure of global modes in wake flow. *Phys. Fluids* **7** (6), 1418–1424. [13](#), [14](#)

Chapter 3

Bifurcation analysis and frequency matching in shear-driven cavity flow

Y. Bengana¹, J.-Ch. Loiseau², J.-Ch. Robinet² and L. S. Tuckerman¹

¹Laboratoire de Physique et Mécanique des Milieux Hétérogènes (PMMH), CNRS; ESPCI Paris, PSL Research University; Sorbonne Université; Univ. Paris Diderot, France

²Laboratoire DynFluid, Arts et Métiers ParisTech, 75013 Paris, France

Submitted to *Journal of Fluid Mechanics*

A comprehensive study of the two-dimensional incompressible shear-driven flow in an open square cavity is carried out. Two successive bifurcations lead to two limit cycles with different frequencies and different numbers of structures which propagate along the top of the cavity and circulate in its interior. A branch of quasiperiodic states produced by secondary Hopf bifurcations transfers the stability from one limit cycle to the other. A full analysis of this scenario is obtained by means of nonlinear simulations, linear stability analysis, and Floquet analysis. We characterize the temporal behavior of the limit cycles and quasiperiodic state via Fourier transforms and their spatial behavior via the Hilbert transform. We address the relevance of linearization about the mean flow. Although here the nonlinear frequencies are not very far from those obtained by linearization about the base flow, the difference is substantially reduced when eigenvalues are obtained instead from linearization about the mean and in addition, the corresponding growth rate is small, a combination of properties called RZIF. Moreover growth rates obtained by linearization about the mean of one limit cycle are correlated with relative stability to the other limit cycle. Finally, we show that the frequencies of the successive modes are separated by a constant increment.

3.1 Introduction

We consider the incompressible shear-driven flow in a cavity, also known as open cavity flow. The first two-dimensional instability of the flow is localized along the shear layer delimiting the outer boundary layer above the cavity and also along the downstream side

of the cavity (Sipp & Lebedev [54], Sipp *et al.* [55]). This instability relies essentially on two mechanisms. First, the convectively unstable nature of the shear layer causes perturbations to grow as they travel downstream, essentially due to the Kelvin-Helmholtz mechanism. Once they impinge on the downstream corner of the cavity, the inner-cavity recirculating flow and the instantaneous pressure feedback provide the mechanisms by which these perturbations re-excite the upstream portion of the shear layer. At sufficiently high Reynolds numbers, the coupling of these mechanisms gives rise to a linearly unstable feedback loop. A similar unstable loop exists for compressible shear-driven cavity flows in which the instantaneous pressure feedback is replaced by upstream-propagating acoustic waves (Gloerfelt [22], Rockwell & Naudascher [49], Rossiter [50], Rowley *et al.* [51], Yamouni *et al.* [62]). The shear-driven open cavity flow has a number of applications in aeronautics (Yu [63]) and in industry, where it can serve as a mixing device (Chien *et al.* [11]).

Shear-driven instabilities in a cavity are often preceded by centrifugal instabilities as the Reynolds number is increased. The two are easy to distinguish since the shear-driven instabilities lead to streamwise traveling waves while the centrifugal instabilities lead to steady oscillations which are spanwise periodic (away from rigid boundaries if these are present). These spanwise oscillations are observed in simulations (Aidun *et al.* [1], Picella *et al.* [44], Theofilis *et al.* [59]) and in experiments (Douay *et al.* [13], Faure *et al.* [17, 18], Shankar & Deshpande [53]). This could make the two-dimensional (spanwise-independent) case seem academic. However, because the spanwise oscillations are of low amplitude and are mainly located inside the cavity, they have a minimal effect on the subsequent development of the flow for this range of Reynolds numbers. As the Reynolds number is further increased, shear-driven instabilities occur, leading to states resembling streamwise traveling waves (Basley *et al.* [7]). The resulting streamwise wavelengths and temporal frequencies are very similar to those observed in the spanwise-independent case, but the critical Reynolds numbers are different (Basley *et al.* [6, 7]). Experiments (Basley *et al.* [6, 7], Rockwell [47], Rockwell & Naudascher [49], Rossiter [50]) have shown that over a large range of aspect ratios, the frequency of the dominant mode is approximated quite well by a spanwise-independent approach. Rockwell [47], Rockwell & Naudascher [49] showed that in a square cavity with a short spanwise extent, the mode produced has a spatial wavelength which is approximately half the cavity length and a temporal period which is approximately one, in units of the cavity length and imposed velocity. This is consistent with our numerical results.

The two-dimensional shear-driven cavity has served multiple theoretical modeling purposes over the past decade, such as in optimal control, reduced-order modeling (Barbagallo *et al.* [3], Loiseau & Brunton [30]), and dynamic mode decomposition (Schmid [52]). Despite its use as a representative test case for complex nonlinear dynamics in fluid mechanics, an extensive analysis of the first few bifurcations experienced by the shear-driven cavity flow has never been carried out. The primary aim of the present work is to fill this gap. We have been able to determine the first primary and secondary bifurcations experienced by the flow and to draw the associated bifurcation diagram. The combined use of nonlinear direct numerical simulation, linear stability analysis and Floquet analysis then enabled us to investigate the stability of the various solution branches. More specifically, we have studied two limit cycles whose relative stability is mediated by an unstable quasiperiodic state. Our study is thus complementary to those of Sipp & Lebedev [54] and Meliga [40],

each of which treats one of the two limit cycles covered in this study. Another relevant numerical study is that of Tiesinga *et al.* [60], who conducted a bifurcation analysis of the two-dimensional lid-driven cavity which, in the parameter range of our study, behaves very similarly to the open cavity. Oscillations along the top of the cavity are, of course, ruled out, but the oscillations that travel down the downstream side of the cavity are quite similar in appearance and in behavior. As in our case, two limit cycles and an intermediate quasiperiodic state are found. Because of the viscous damping by the lid, the critical Reynolds numbers are about twice those for the open cavity (Fortin *et al.* [20], Poliashenko & Aidun [46]).

A second theme of our investigation, also previously addressed by Sipp & Lebedev [54] and Meliga [40], is the relevance of linearization about the mean flow. For a fully developed limit cycle, nonlinear interactions contribute to the mean flow, deviation from the base flow called the distortion. In this way, the mean flow inherits information from the nonlinearities (Maurel *et al.* [36], Zielinska *et al.* [64]). From this comes the idea to linearize about the mean flow, despite the fact that the mean flow is not a solution of the stationary Navier-Stokes equations. Although the empirical use of mean flows to study nonlinear dynamics is long-standing (Malkus [32], Morris [43], Stuart [57]), quantitative computations and comparisons are more recent, and primarily for the wake of a circular cylinder (Barkley [4], Hammond & Redekopp [24], Mittal [42], Pier [45]). When successful, this procedure leads to an eigenvalue whose imaginary part reproduces very well the frequency of the periodic orbit, even quite far from its threshold. Moreover, the real part of this eigenvalue is close to zero (Barkley [4]), which would be called marginal stability if the linearization were about the base flow. This property was named RZIF (a mnemonic for Real Zero Imaginary Frequency) by Turton *et al.* [61]. An extension of RZIF, called SCM (for Self-Consistent Model) has been proposed by Mantić-Lugo *et al.* [33, 34], in which the mean flow is computed, not as an average of the full time-dependent flow, but precisely so that the RZIF property is satisfied, i.e. such that the mean flow is marginally stable. Neither RZIF nor SCM are always valid; counterexamples have been found for regimes in thermosolutal convection by Turton *et al.* [61] and Bengana & Tuckerman [9]. Other flows for which these properties or models have been tested are the compressible flow in the wake of a cylinder (Fani *et al.* [16]) and counter-rotating Taylor-Couette flow (Bengana & Tuckerman [10]). Linearization about the mean flow has been applied to understanding the temporal spectra of turbulent flows (Beneddine *et al.* [8], Hwang & Cossu [25], McKeon & Sharma [37], Symon *et al.* [58]).

The paper is organized as follows: §3.2 introduces the configuration of the shear-driven cavity flow and the governing equations and the tools for the various analyses we have performed: linearization about the base and the mean flows, Floquet analysis, the temporal Fourier transform and the spatial Hilbert transform. Our results concerning the bifurcation scenario for this flow are presented in §3.3, more specifically two limit cycles produced by primary Hopf bifurcations and whose relative stability is mediated by an unstable quasiperiodic state produced by secondary bifurcations. In §3.4, we discuss linearization about the mean flow for both limit cycles, as well as the formula of Rossiter [50]. We summarize our conclusions in §3.5.

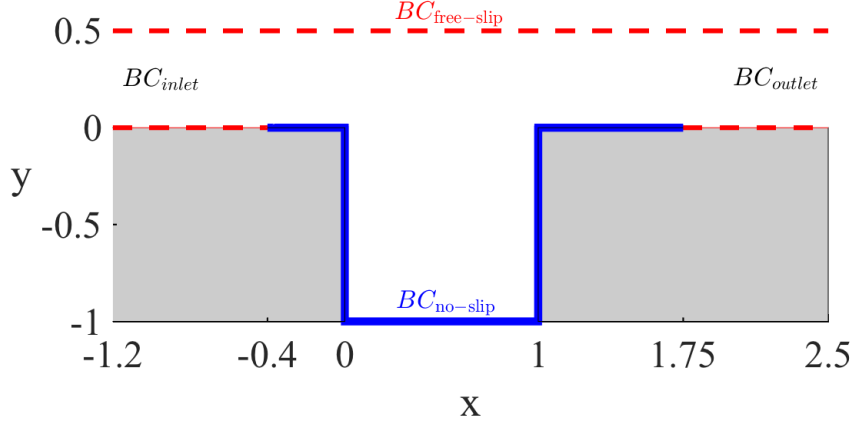


Figure 3.1 – Geometry of our study. At the inlet (BC_{inlet}) a uniform unit velocity ($u = 1$; $v = 0$) is imposed. Dashed red line: free-slip condition ($BC_{\text{free-slip}}$). Thick blue line: no-slip boundary condition ($BC_{\text{no-slip}}$). A free-outflow boundary condition is imposed at the outlet.

3.2 Governing equations and numerical methods

3.2.1 Problem definition

The configuration considered is the two-dimensional incompressible viscous shear-driven flow of a Newtonian fluid over an open cavity with equal length and depth shown in figure 3.1. This configuration is the same as that considered by Sipp & Lebedev [54] and Barbagallo *et al.* [3], or more recently by Meliga [40]. We use the unperturbed upstream velocity U_∞ , the cavity length L and the resulting advective time L/U_∞ to nondimensionalize the variables. The dynamics of the flow are governed by the incompressible Navier-Stokes equations

$$\begin{aligned} \frac{\partial \mathbf{U}}{\partial t} &= -\nabla P + \frac{1}{Re} \nabla^2 \mathbf{U} - \nabla \cdot (\mathbf{U} \otimes \mathbf{U}) \\ \nabla \cdot \mathbf{U} &= 0, \end{aligned} \quad (3.1)$$

where $\mathbf{U}(\mathbf{x}, t) = (U, V)^T$ and P are the velocity and pressure fields. The Reynolds number Re is defined as

$$Re = \frac{U_\infty L}{\nu},$$

where ν is the kinematic viscosity of the fluid. and will range between $Re = 4000$ and $Re = 5000$. The boundary conditions, illustrated in figure 3.1, are

$$\begin{aligned} \mathbf{U} &= \mathbf{e}_x \text{ on } BC_{\text{inlet}} \\ \mathbf{U} &= \mathbf{0} \text{ on } BC_{\text{no-slip}} \\ \partial_y U = V &= 0 \text{ on } BC_{\text{free-slip}} \\ \partial_x \mathbf{U} &= \mathbf{0} \text{ on } BC_{\text{outlet}} \end{aligned} \quad (3.2)$$

The boundary conditions at the inlet and along the wall are crucial. The flow is given a uniform profile at the inlet and develops a boundary layer structure as it advances

downstream. The instability occurs where the boundary layer reaches the upstream corner of the cavity and it is the thickness of the boundary layer at this point that controls the details of the transition. When free-slip conditions are imposed on the wall close to the inlet, then a boundary layer of an appropriate thickness develops over a shorter distance than would be the case if no-slip conditions were used over the entire wall. A shorter domain can be used, making the calculation more economical.

The Navier-Stokes equations are solved using the incompressible flow solver NEK5000 (Fischer *et al.* [19]) which is based on the spectral element method. A $\mathbb{P}_N - \mathbb{P}_{N-2}$ formulation has been used: the velocity field is discretized using N^{th} order Lagrange interpolants defined on the Gauss-Legendre-Lobatto quadrature points as basis and trial functions while the pressure field is discretized using Lagrange interpolants of degree $N-2$ defined on the Gauss-Legendre quadrature points. Finally, time integration is performed using the BDF3/EXT3 scheme: integration of the viscous term relies on backward differentiation while the convective terms are integrated explicitly using a third-order accurate extrapolation. In practice, the polynomial degree was set to $N = 6$ while the computational domain was discretized using 4000 spectral elements. The resulting mesh refinement is thus similar to that used in Sipp & Lebedev [54].

3.2.2 Base flow and linearization

A base flow $\mathbf{U}_b(\mathbf{x})$ is a solution of the stationary Navier-Stokes equations

$$\begin{aligned} 0 &= -\nabla P_b + \frac{1}{Re} \nabla^2 \mathbf{U}_b - \nabla \cdot (\mathbf{U}_b \otimes \mathbf{U}_b) \\ 0 &= \nabla \cdot \mathbf{U}_b. \end{aligned} \quad (3.3)$$

with the boundary conditions again given by (3.2). Various techniques can be used to compute the base flow $\mathbf{U}_b(\mathbf{x})$. Because of its simplicity, the selective frequency damping (SFD) technique initially proposed by Åkervik *et al.* [2] has been used; see also Cunha *et al.* [12], Jordi *et al.* [27, 28].

Once the equilibrium $\mathbf{U}_b(\mathbf{x})$ has been computed, we determine its linear stability. To do so, we consider an infinitesimal perturbation $\mathbf{u}(\mathbf{x}, t)$ to the base flow \mathbf{U}_b , whose dynamics are governed by the linearized Navier-Stokes equations

$$\begin{aligned} \frac{\partial \mathbf{u}}{\partial t} &= -\nabla p + \frac{1}{Re} \nabla^2 \mathbf{u} - \nabla \cdot (\mathbf{u} \otimes \mathbf{U}_b + \mathbf{U}_b \otimes \mathbf{u}) \\ \nabla \cdot \mathbf{u} &= 0. \end{aligned} \quad (3.4)$$

The boundary conditions are the homogeneous version of (3.2), i.e. we now prescribe a zero velocity profile at the inlet.

$$\begin{aligned} \mathbf{u} &= \mathbf{0} \text{ on } \text{BC}_{\text{inlet}} \\ \mathbf{u} &= \mathbf{0} \text{ on } \text{BC}_{\text{no-slip}} \\ \partial_y u = v = 0 &\text{ on } \text{BC}_{\text{free-slip}} \\ \partial_x \mathbf{u} &= \mathbf{0} \text{ on } \text{BC}_{\text{outlet}} \end{aligned} \quad (3.5)$$

Solutions to (3.4) are of the form $\mathbf{u}(\mathbf{x}, t) = \hat{\mathbf{u}}(\mathbf{x})e^{(\sigma+i\omega)t} + \text{c.c.}$, $p(\mathbf{x}, t) = \hat{p}(\mathbf{x})e^{(\sigma+i\omega)t} +$

c.c., we obtain the eigenvalue problem

$$\begin{aligned} (\sigma + i\omega) \hat{\mathbf{u}} &= \mathcal{L}_{\mathbf{U}_b} \hat{\mathbf{u}} \\ \nabla \cdot \hat{\mathbf{u}} &= 0, \end{aligned} \quad (3.6)$$

where $\mathcal{L}_{\mathbf{U}_b}$ is the Jacobian of the Navier-Stokes equations linearized around \mathbf{U}_b :

$$\mathcal{L}_{\mathbf{U}_b} \hat{\mathbf{u}} \equiv -\nabla \hat{p} + \frac{1}{Re} \nabla^2 \hat{\mathbf{u}} - \nabla \cdot (\mathbf{U}_b \otimes \hat{\mathbf{u}} + \hat{\mathbf{u}} \otimes \mathbf{U}_b) \quad (3.7)$$

The stability of the base flow is determined by the sign of the real part σ of the leading eigenvalue, which is the growth rate of the perturbation. If σ crosses zero for an eigenvalue with non-zero imaginary part ω , then a Hopf bifurcation leads to a limit cycle whose frequency at onset is ω . In our case, the base flow undergoes a first Hopf bifurcation at $Re_2 = 4126$, leading to a limit cycle LC_2 and a second Hopf bifurcation at $Re_3 = 4348$ gives rise to LC_3 .

We computed the leading eigenvalues and eigenvectors using a time-stepper approach; see, e.g., Edwards *et al.* [15]. Our stability calculation typically used a Krylov subspace of dimension $K = 256$ and a sampling period $\Delta T = 10^{-3}$ non-dimensional time units. Eigenvalues were considered to be converged if the residual obtained from the Arnoldi decomposition was below 10^{-6} .

3.2.3 Mean flow and linearization

At the threshold of a Hopf bifurcation, linearization about the base flow leads to an eigenvalue whose real part is zero and whose imaginary part is the frequency of the limit cycle which is produced. As the Reynolds number is increased and the limit cycle develops nonlinearly and deviates from the base flow, eigenvalues obtained by linearization about the base flow no longer correspond to the properties of the limit cycle. However, linearization about the mean flow often leads to an eigenvalue whose imaginary part is closer to the nonlinear frequency.

We consider a Reynolds decomposition of the instantaneous flow field, i.e.

$$\mathbf{U}(\mathbf{x}, t) = \overline{\mathbf{U}}(\mathbf{x}) + \mathbf{u}(\mathbf{x}, t)$$

where $\overline{\mathbf{U}}(\mathbf{x})$ is the mean flow and $\mathbf{u}(\mathbf{x}, t)$ is the zero-mean fluctuation. Introducing this decomposition into the Navier-Stokes equations and averaging shows that $\overline{\mathbf{U}}$ is governed by the Reynolds Averaged Navier-Stokes (RANS) equations

$$\begin{aligned} 0 &= -\nabla \overline{P} + \frac{1}{Re} \nabla^2 \overline{\mathbf{U}} - \nabla \cdot (\overline{\mathbf{U}} \otimes \overline{\mathbf{U}}) - \nabla \cdot (\overline{\mathbf{u} \otimes \mathbf{u}}) \\ 0 &= \nabla \cdot \overline{\mathbf{U}} \end{aligned} \quad (3.8)$$

with boundary conditions (3.2). The presence of the Reynolds stress tensor $\overline{\mathbf{u} \otimes \mathbf{u}}$ of the fluctuation means that these equations are not closed. We compute the mean flow $\overline{\mathbf{U}}(\mathbf{x})$ of a period- T limit cycle by carrying out a full nonlinear simulation via (3.1) and

time-averaging:

$$\bar{\mathbf{U}}(\mathbf{x}) = \frac{1}{T} \int_0^T \mathbf{U}(\mathbf{x}, t) dt.$$

The equations governing the dynamics of the fluctuation $\mathbf{u}(\mathbf{x}, t)$ are obtained by substituting $\bar{\mathbf{U}} + \mathbf{u}$ for \mathbf{U} into (3.1) and subtracting (3.8), leading to

$$\begin{aligned} \frac{\partial \mathbf{u}}{\partial t} &= -\nabla p + \frac{1}{Re} \nabla^2 \mathbf{u} - \nabla \cdot (\bar{\mathbf{U}} \otimes \mathbf{u} + \mathbf{u} \otimes \bar{\mathbf{U}}) - \underbrace{\nabla \cdot (\mathbf{u} \otimes \mathbf{u} - \bar{\mathbf{u}} \otimes \bar{\mathbf{u}})}_{\mathbf{f}} \\ 0 &= \nabla \cdot \mathbf{u} \end{aligned} \quad (3.9)$$

with homogeneous boundary conditions (3.5). The equations differ from the linearized Navier-Stokes equations by the presence of \mathbf{f} . The term $\nabla \cdot (\mathbf{u} \otimes \mathbf{u})$, is the usual quadratic interaction term neglected in base flow linear stability analyses. The term $\nabla \cdot (\bar{\mathbf{u}} \otimes \bar{\mathbf{u}})$ is the divergence of the Reynolds stress tensor of the fluctuation.

Studies carrying out mean flow stability analyses discard \mathbf{f} , leading to the linearized equations

$$\begin{aligned} \frac{\partial \mathbf{u}}{\partial t} &= -\nabla p + \frac{1}{Re} \nabla^2 \mathbf{u} - \nabla \cdot (\mathbf{u} \otimes \bar{\mathbf{U}} + \bar{\mathbf{U}} \otimes \mathbf{u}) \\ \nabla \cdot \mathbf{u} &= 0. \end{aligned} \quad (3.10)$$

Using once again a normal mode ansatz, this set of equations is reduced to the eigenvalue problem

$$\begin{aligned} (\sigma + i\omega) \hat{\mathbf{u}} &= \mathcal{L}_{\bar{\mathbf{U}}} \hat{\mathbf{u}} \\ \nabla \cdot \hat{\mathbf{u}} &= 0, \end{aligned} \quad (3.11)$$

where $\mathcal{L}_{\bar{\mathbf{U}}}$ is now the Navier-Stokes operator linearized around the mean flow, with $\bar{\mathbf{U}}$ substituted for \mathbf{U}_b in (3.7).

Although the mean flow is not an equilibrium solution of the Navier-Stokes solution, this approach has proved unexpectedly successful in characterizing the frequencies of the full nonlinear solutions of the Navier-Stokes equations. (For a counter-example, however, see Turton *et al.* [61].) Various theoretical overlapping justifications have been proposed for dropping or modeling \mathbf{f} in (3.9), such as:

1. The quadratic interaction of the fluctuation with itself is small and its temporal mean does not appear in a linear stability analysis (Barkley [4], Mantič-Lugo *et al.* [33, 34]).
2. The terms can be treated via an expansion in the distance from the threshold (Sipp & Lebedev [54]).
3. The instantaneous Reynolds stress tensor $\mathbf{u} \otimes \mathbf{u}$ is approximately equal to its temporal average $\bar{\mathbf{u}} \otimes \bar{\mathbf{u}}$ so that they almost cancel out (Turton *et al.* [61]); see also section 3.4.2.
4. The resolvent operator $(i\omega - \mathcal{L}_{\bar{\mathbf{U}}})^{-1}$ is sharply peaked or of low rank. This implies that its action on any vector, including \mathbf{f} , is approximately a projection onto the leading mode of the resolvent. The purpose of this procedure is not to eliminate \mathbf{f} , but to approximate it as a scalar multiple of the leading resolvent mode, and then to treat \mathbf{f} as a forcing input (Beneddine *et al.* [8], Hwang & Cossu [25], McKeon & Sharma

[37], Symon *et al.* [58]).

3.2.4 Floquet analysis

Our study of the shear-driven cavity focuses on two limit cycles, denoted by LC_2 and LC_3 , created by primary Hopf bifurcations and destabilized via secondary bifurcations. Floquet analysis will be used to characterize this destabilization. The dynamics of an infinitesimal perturbation $\mathbf{u}(\mathbf{x}, t)$ evolving in the vicinity of a T -periodic limit cycle $\mathbf{U}(\mathbf{x}, t)$ are governed by the linearized Navier-Stokes equations

$$\begin{aligned} \frac{\partial \mathbf{u}}{\partial t} &= \mathcal{L}_{\mathbf{U}(t)} \mathbf{u} \\ \nabla \cdot \mathbf{u} &= 0 \end{aligned} \tag{3.12}$$

with homogeneous boundary conditions (3.5). This set of equations is non-autonomous, as the operator $\mathcal{L}_{\mathbf{U}(t)}$ is T -periodic. Solutions to Eq. (3.12) are of the Floquet form

$$\mathbf{u}(\mathbf{x}, t) = \hat{\mathbf{u}}(\mathbf{x}, t) e^{(\sigma_F + i\omega_F)t} + \text{c.c.}$$

where $\hat{\mathbf{u}}(\mathbf{x}, t)$ are the T -periodic Floquet modes and $(\sigma_F + i\omega_F)$ the Floquet exponents. The stability of $\mathbf{U}(t)$ is determined by the Floquet multipliers

$$\mu = e^{(\sigma_F + i\omega_F)T}$$

If the moduli of the Floquet multipliers are smaller than one, perturbations will decay exponentially fast and the orbit is stable. On the other hand, if at least one of the Floquet multipliers has a modulus greater than one, then that perturbation will grow exponentially and the orbit is unstable; see, e.g. Barkley & Henderson [5] and Gioria *et al.* [21]. In our study the Floquet exponents are complex and the imaginary part ω_F of the Floquet exponent is the argument (angle) of the Floquet multiplier. The presence of an imaginary part leads to quasiperiodic behavior. More details and results are shown in §3.3.4.

3.2.5 Edge state technique for computing the unstable quasiperiodic state

As will be shown in §3.3, there is a range of Reynolds numbers over which limit cycles LC_2 and LC_3 co-exist. In phase space, on the boundary between the basins of attraction of these limit cycles, is an unstable quasi-periodic state QP . (More specifically, QP is an edge state, meaning that within the boundary, trajectories are attracted to it.) In order to compute QP , we use the same technique as in Itano & Toh [26] or Duguet *et al.* [14] for the laminar-turbulent edge state. In such cases, whether a trajectory evolves towards a turbulent or laminar state depends on the initial condition. Some initial conditions evolve directly to turbulence, others decay directly to the laminar state. By appropriately weighting turbulent and laminar solutions, an initial condition can be constructed so that the resulting trajectory converges to and remains a long time on the edge state before diverging towards one of these two attractors.

In our problem, a quasi-periodic state separates the two stable limit cycles LC_2 and LC_3 . Therefore we construct a weighted sum of the two, seeking an initial condition $\mathbf{U}(\mathbf{x}, 0)$ that

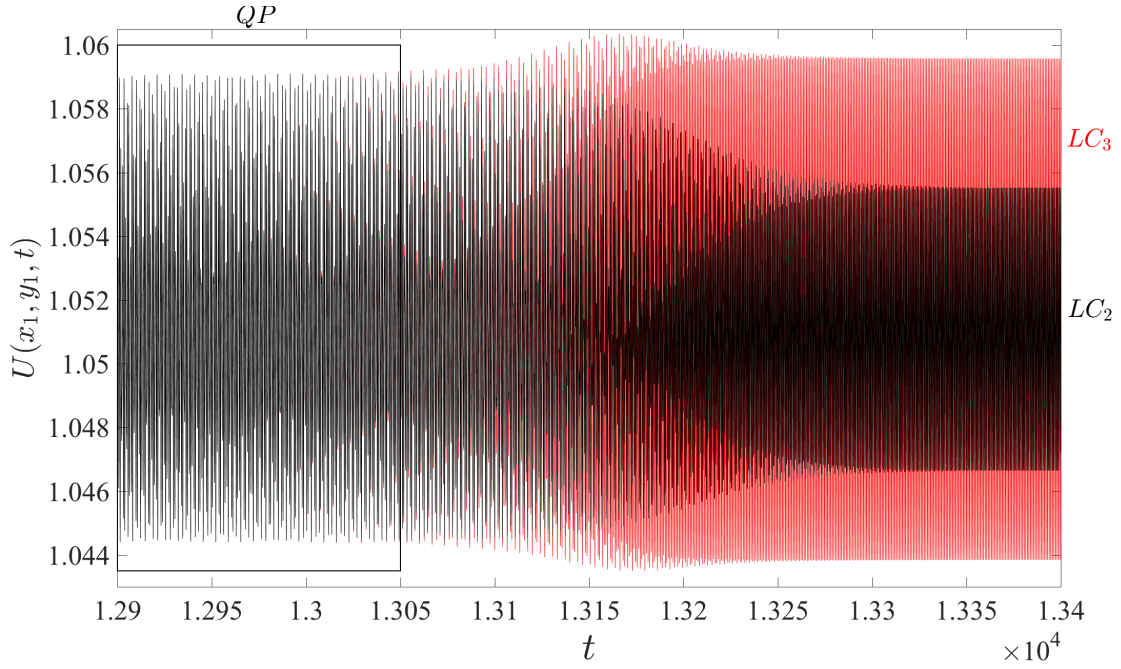


Figure 3.2 – Time traces of streamwise velocity at $Re = 4460$ for two simulations. The initial condition of the simulation is (3.13). For $\alpha = 0.47562027$ the system evolves towards LC_2 , shown as the black curve. For $\alpha = 0.47562256$ it evolves towards LC_3 , shown as the higher-amplitude red curve.

will evolve after some time to QP and then remain as long as possible before eventually converging to either limit cycle. Using the same bisection technique as in Lopez *et al.* [31], this initial condition is given by

$$\mathbf{U}(\mathbf{x}, t) = \alpha \mathbf{U}_{LC_2} + (1 - \alpha) \mathbf{U}_{LC_3}. \quad (3.13)$$

For $\alpha = 1$, the initial condition is LC_2 and for $\alpha = 0$, it is LC_3 . For each Reynolds number considered, we successively delimit an interval of α by bisection to capture the quasi-periodic state. As an illustration, we plot in figure 3.2 the time evolution of streamwise velocity recorded by a probe located at $(x_1, y_1) = (1.2, 0.2)$ for $\alpha = 0.47562027$ and 0.47562256 . A slight difference in α will bring the system after a long transient regime to either LC_2 or LC_3 .

3.2.6 Standard deviation

To construct the bifurcation diagram, we seek an appropriate measure of the oscillation amplitude as a function of Re . Time series from limit cycles LC_2 and LC_3 are shown in figures 3.2 and 3.3(c). Their amplitudes are easily obtained by measuring the maxima in a time series or the fundamental peak in the temporal Fourier spectrum. In contrast to these, which have maxima of constant amplitudes, the quasiperiodic state existing in the overlap region has maxima of varying heights as shown in figure 3.2 and in 3.3(b). To extract a single amplitude in their study of the cubic lid-driven cavity, Lopez *et al.* [31] used the standard deviation from the mean flow, defined as

$$\xi(U) = \left[\frac{1}{N} \sum_{n=0}^N (U(x_1, y_1, t_n) - \bar{U}(x_1, y_1))^2 \right]^{1/2} \quad (3.14)$$

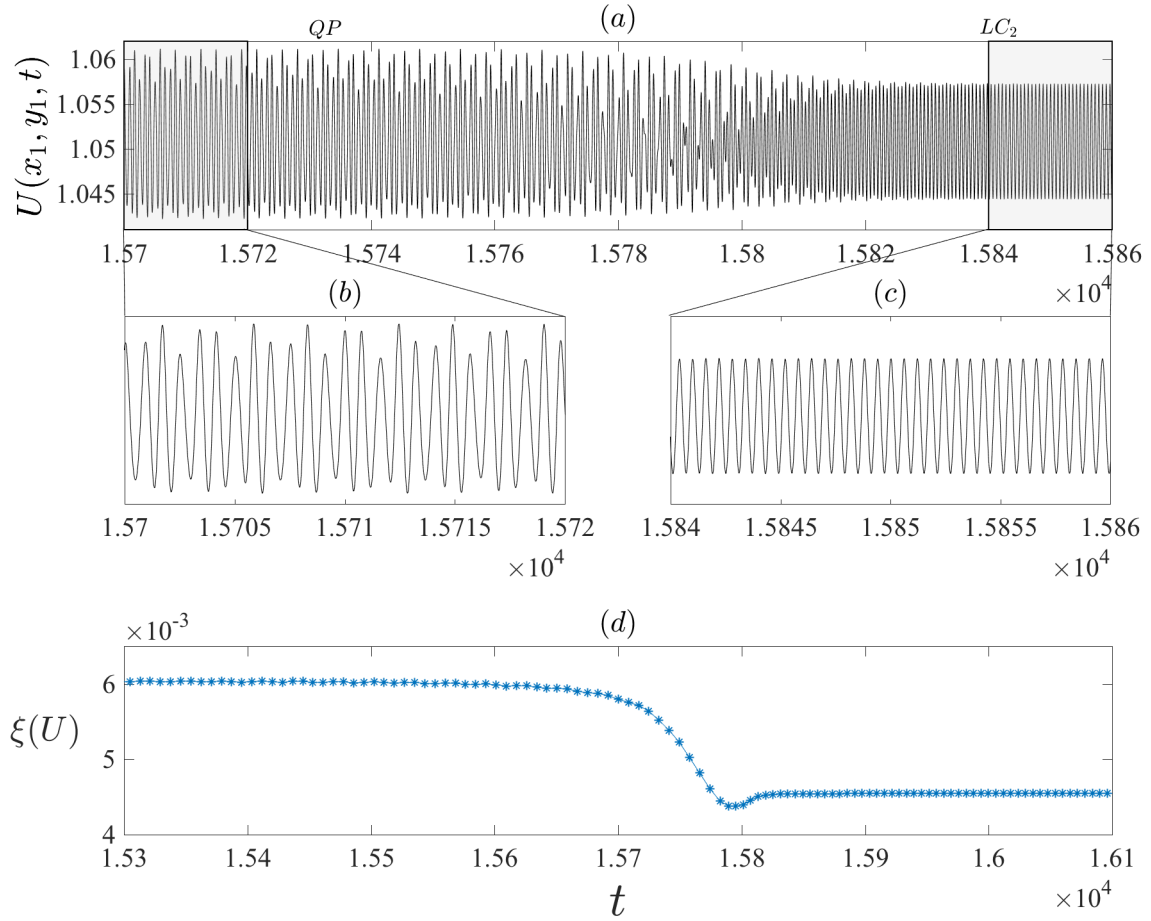


Figure 3.3 – (a) Time series of streamwise velocity at $(x_1, y_1) = (1.2, 0.2)$ and $Re = 4580$ for a simulation with $\alpha = 0.829630407714844$. The regimes corresponding to QP and to LC_3 are shown in (b-c). (d) The standard deviation is computed by a sliding window.

where $U(x_1, y_1, t_n)$ the streamwise velocity measured at $(x_1, y_1) = (1.2, 0.2)$ and at each instant t_n , N is the number of measurements in the time series, and $\bar{U}(x_1, y_1)$ is the temporal mean. We used the edge state technique described in §(3.2.5) to compute a time series in which the QP is maintained for a long time. In figure 3.3(d), we show the standard deviation of the time series plotted in figure 3.3(a). The standard deviation is computed over all times of a sliding window containing fifty peaks. Once the deviation is computed, the window is shifted by ten peaks and we compute the deviation again over fifty peaks. Figure 3.3(d) shows two regimes of constant $\xi(U)$ corresponding to QP and LC_2 , justifying the choice of $\xi(U)$ for the bifurcation diagram.

3.2.7 Hilbert transform

We use the Hilbert transform to obtain spatial characteristics of the flow. The Hilbert transform is a useful means of extracting the local amplitude and phase from a signal. A complex analytic signal $f_a(x)$ is constructed from real data $f(x)$. In contrast to a real signal that has negative and positive frequencies, f_a is complex and has only positive frequencies. This signal is obtained by

$$f_a(x) = f(x) + i\mathcal{H}(f(x)) \quad (3.15)$$

The imaginary part $\mathcal{H}(f(x))$ is its Hilbert transform, defined by phase shifting the positive and negative frequencies of the original real signal by $-\pi/2$ and $\pi/2$ respectively. More details about the Hilbert transform can be found in Smith [56]. Equation (3.15) is written in polar form

$$f_a(x) = A(x)e^{i\Phi(x)} \quad (3.16)$$

Thus we can extract the envelope (amplitude $A(x)$) and the phase $\Phi(x)$ from the analytic signal at each location, which is the main interest in using the Hilbert transform. We present the results in detail in §3.3.3.

3.3 Bifurcation scenario

3.3.1 Overview

The flow over a shear-driven cavity at low Reynolds number consists of a free laminar shear layer and one large recirculation within the cavity. As we increase the Reynolds number, the mixing layer is fed by the shear stress and its thickness develops over the cavity. As widely presented in several studies (Rockwell & Naudascher [49]), it is common to observe self-sustained oscillations in such configurations, in which the flow impacts on a wall. In figure 3.4(a) we show the bifurcation diagram over the range of Reynolds number $Re \in [4000, 5000]$. We represent the standard deviation from the mean of the streamwise velocity at a point as described in §3.2.6. The standard deviation is computed over all times t_n of the time series corresponding to LC_2 , LC_3 or QP . The line $\xi(U) = 0$ represents the solution of the stationary Navier-Stokes equations (base flow). We plot the stable and unstable states with bold and dashed curves respectively.

The base flow is stable for $Re < Re_2$ where $Re_2 \approx 4126$ is the critical Reynolds number of the first Hopf bifurcation. This threshold is obtained by quadratic interpolation of amplitudes and differs by only 0.34% from that found by Sipp & Lebedev [54]. Above this threshold, the base solution exists but is unstable. We observe a second Hopf bifurcation at $Re_3 \approx 4348$, also from quadratic interpolation of amplitudes, which agrees with the threshold measured by Meliga [40], differing only by 0.005%. These successive Hopf bifurcations lead after saturation by nonlinear interactions to two limit cycles which we name LC_2 and LC_3 because they display two or three maxima of the vertical velocity fluctuations, as will be shown in the next section.

Figure 3.4(b) shows the schematic phase portraits corresponding to the bifurcation diagram. The stable base flow (i) loses its stability through a primary Hopf bifurcation (ii) at Re_2 producing the limit cycle LC_2 . (iii) Another primary Hopf bifurcation at Re_3 produces the limit cycle LC_3 . (iv) A secondary subcritical Hopf bifurcation from LC_3 at Re'_3 produces the quasiperiodic state QP , which moves (v) in phase space towards LC_2 until it undergoes another secondary subcritical Hopf bifurcation (vi) at Re'_2 which destroys QP and destabilizes LC_2 . Above Re'_3 , LC_3 is stable at least until $Re = 5000$. Another Hopf bifurcation and interesting dynamics occur above $Re = 5000$ but these will not be discussed in this paper.

This bifurcation diagram is very similar to that seen in the related configuration of a

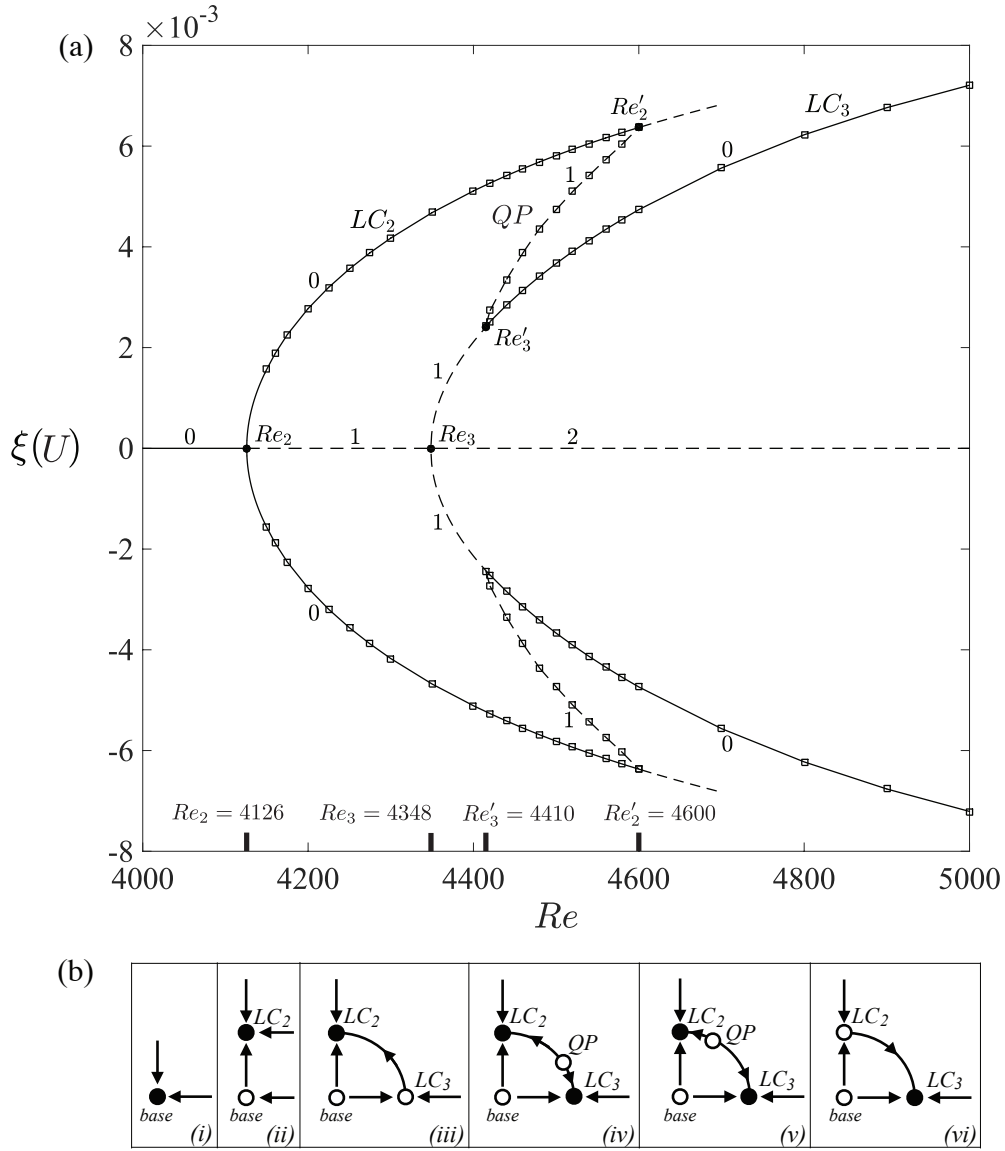


Figure 3.4 – (a) Bifurcation diagram of the shear-driven cavity flow for $Re \in [4000, 5000]$. On the x -axis, we show the Reynolds number Re and on the y -axis the standard deviation from the mean of the streamwise velocity at one point. The bold dots on the curves and the thick ticks on the x -axis show the critical Reynolds numbers. The integers show the number of unstable directions (counting a complex conjugate pair as a single direction). We represent stable states by bold curves and unstable ones by dashed curves. The line $\xi(U) = 0$ indicates the stationary base flow. The first Hopf bifurcation occurs at $Re_2 \approx 4126$ and the second at $Re_3 \approx 4348$. These two thresholds have been calculated by a quadratic interpolation from the amplitudes. The Hopf bifurcations give rise to limit cycles LC_2 and LC_3 . LC_2 is stable from its threshold until $Re'_2 \approx 4600$ where it loses stability to LC_3 . LC_3 is unstable from Re_3 to $Re'_3 \approx 4410$ and above this Reynolds number it becomes stable. Between LC_2 and LC_3 in the overlap region $Re \in [4400, 4600]$ there exists a quasiperiodic state QP , which has been computed by using $\alpha LC_2 + (1 - \alpha) LC_3$ as an initial condition for the full nonlinear simulation where $\alpha = \alpha(Re)$. (b) From left to right, the schematic phase portraits corresponding to the bifurcation diagram. The ordinate and abscissa can be considered to be projections onto the eigenmodes leading to LC_2 and LC_3 , respectively. The black dots and hollow circles show the stable and unstable states. (i) Stable base flow. (ii) Limit cycle LC_2 is shown as bifurcating in the vertical direction. (iii) LC_3 bifurcates in the horizontal direction. (iv, v) The circle moving on the orbit indicates the quasiperiodic state QP . (vi) QP has disappeared, stabilizing LC_3 .

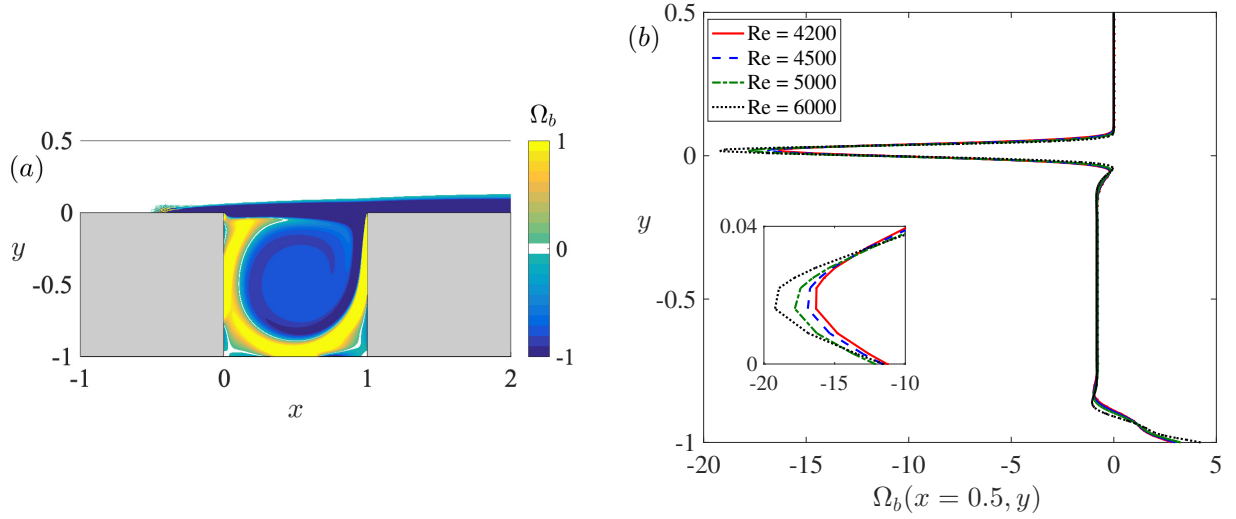


Figure 3.5 – Stationary solution (base flow). (a) Ω_b over the domain for $Re = 4500$. (b) Vorticity profiles $\Omega_b(x = 0.5, y)$ for $Re = 4200, 4500, 5000, 6000$. The major change in the base flow with Reynolds number is localised on the shear layer region and at the bottom of the cavity.

lid-driven cavity Tiesinga *et al.* [60]. These authors observed two successive primary Hopf bifurcations leading to branches with different spatial characteristics. Stability is transferred from the first branch to the second via a secondary branch, which is itself created and destroyed via subcritical secondary Hopf bifurcations. The Reynolds numbers they report for the lid-driven cavity are $Re_2 \approx 8375$, $Re_3 \approx 8600$, $Re'_3 = 8800$, $Re'_2 = 9150$, quite close to twice those we find for the shear-driven cavity. Indeed, this is a classic scenario which occurs in many hydrodynamic configurations; see Kuznetsov [29], Marques *et al.* [35], Meliga *et al.* [41]. Representing the dynamics by two complex amplitudes $r_2 e^{i\phi_2}$, $r_3 e^{i\phi_3}$, the dynamics are governed by the normal form:

$$\begin{aligned} \dot{r}_2 &= r_2(\mu_2 - a_{22}r_2^2 - a_{23}r_3^2) & \dot{\phi}_2 &= \omega_2 \\ \dot{r}_3 &= r_3(\mu_3 - a_{32}r_2^2 - a_{33}r_3^2) & \dot{\phi}_3 &= \omega_3 \end{aligned} \quad (3.17)$$

where coefficients μ_j , a_{ij} depend on Re and a_{22} and a_{33} are positive. The diagrams of figure 3.4(b) are projections of the dynamics onto the (r_2, r_3) plane.

The base flow is shown in figure 3.5. Figure 3.5(a) shows a visualisation of its spanwise vorticity $\Omega_b(x, y)$ over our domain for $Re = 4500$. The change in the mixing layer with increasing Re is not qualitatively visible on such a plot, so figure 3.5(b) presents profiles $\Omega_b(x = 0.5, y)$ at the midline for Reynolds numbers ranging from 4200 to 6000. These profiles show the increasing steepness of the shear layer at the top of the cavity.

In addition to base flows, we wish to show representations of the limit cycles LC_2 and LC_3 . For the flows in our study, the fluctuations are always dominated by the base or mean flow. In figure 3.6, we show visualisations of the vorticity Ω_2 , horizontal velocity u_2 and vertical velocity v_2 for an instantaneous flow from LC_2 . The left column shows the full fields and the right columns show the fluctuations obtained by subtracting the temporal mean of each field. The temporal means are not shown, since they are visually indistinguishable from the full fields. Although oscillations can be seen in Ω_2 in figure

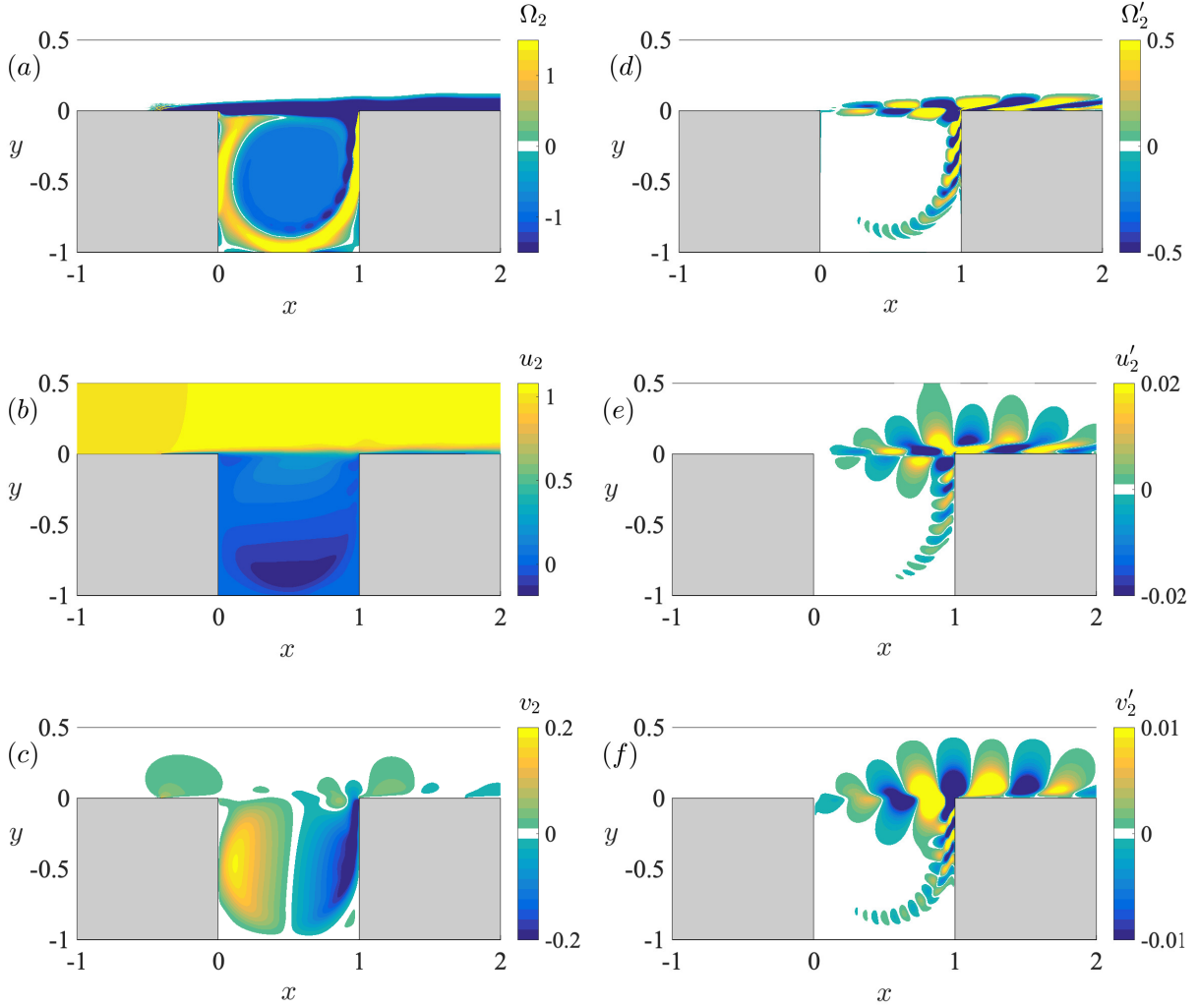


Figure 3.6 – Instantaneous visualisations of LC_2 at $Re = 4500$. The left column (a,b,c) shows the spanwise vorticity Ω_2 , the horizontal velocity u_2 , and the vertical velocity v_2 . The right column (d,e,f) shows the fluctuations, obtained by subtracting the mean, e.g. $\Omega'_2 = \Omega_2 - \bar{\Omega}_2$, where $\bar{\Omega}_2$ is the average over one temporal period. The mean fields $\bar{\Omega}_2$, \bar{u}_2 , \bar{v}_2 are almost identical to the instantaneous fields and are therefore not shown.

3.6(a), these are very weak, and even less visible in u_2 , v_2 in figures 3.6(b,c). Therefore to distinguish between LC_2 and LC_3 and the base flow, we examine the fluctuations, where the periodic structures along the top and downstream side of the cavity are quite visible. Both Ω'_2 and u'_2 in figures 3.6(d,e) display a two-layer structure with an abrupt vertical change of sign at the top of the cavity. Since we are interested primarily in the horizontal variation and propagation of structures along the top of the cavity, we choose to plot the quantity which most emphasizes this feature, namely the vertical velocity fluctuations v'_2 , as in figure 3.6(f).

In figures 3.7 and 3.8 we show the instantaneous vertical velocity fluctuations for LC_2 and LC_3 over one period. We observe four structures, i.e. two maxima and two minima of the vertical velocity fluctuations, in LC_2 and six structures, i.e. three maxima and three minima of the vertical velocity fluctuations, in LC_3 . Similar visualisations can be seen in calculations by Barbagallo *et al.* [3] and experiments by Basley *et al.* [6, 7].

The behavior resembles that of traveling waves. The structures, produced by a feedback mechanism, progress steadily to the right but the overall amplitude is not uniform. At

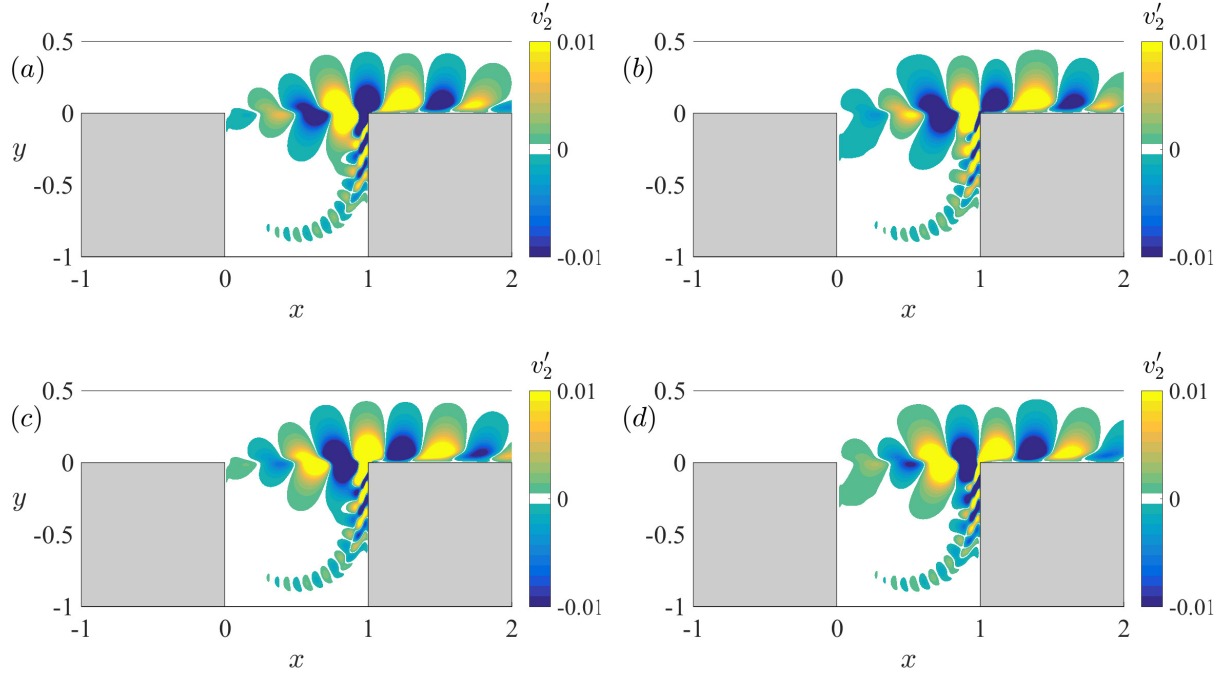


Figure 3.7 – Instantaneous vertical velocity fluctuations ($v' = v - \bar{v}$) for LC_2 over one period for $Re = 4500$. (a) $t = 0$ (b) $T/4$ (c) $T/2$ (d) $3T/4$. The structures are advected downstream, as they would be for a traveling wave. In the range of the cavity $x \in [0, 1]$ we count two maxima of the vertical velocity fluctuations. The velocity contours are deformed downstream for $x > 1.2$, due to the change to a free-slip boundary condition.

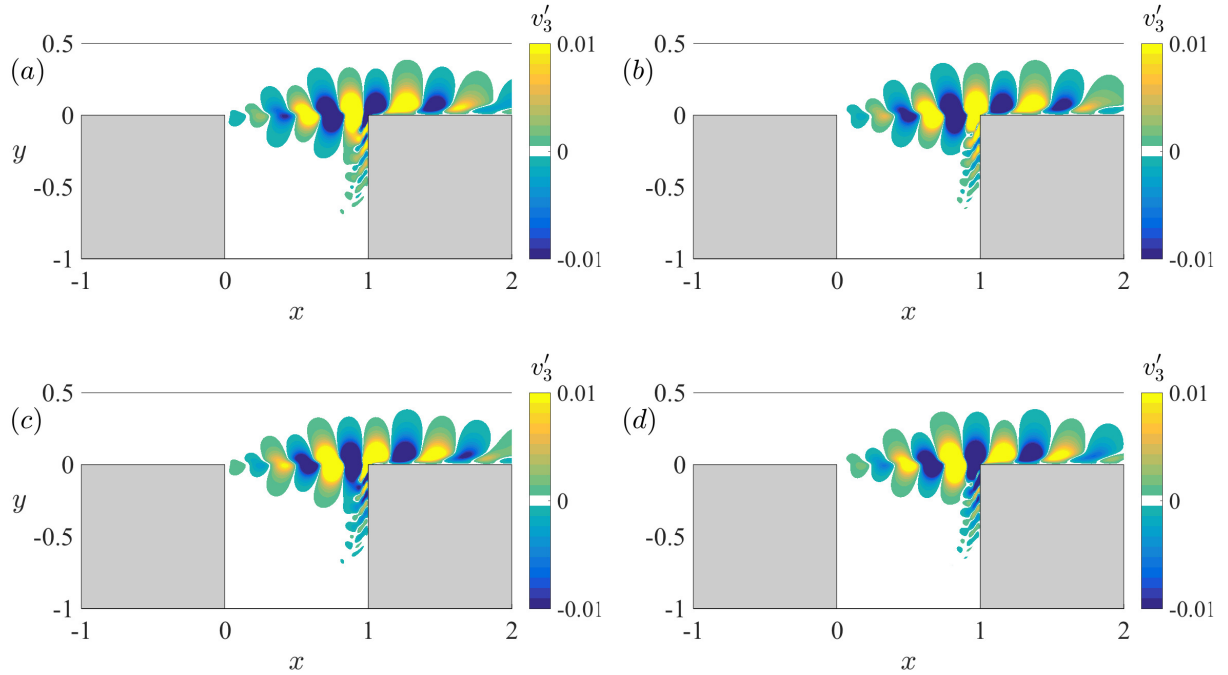


Figure 3.8 – Instantaneous vertical velocity fluctuations ($v' = v - \bar{v}$) for LC_3 over one period for $Re = 4500$. (a) $t = 0$ (b) $T/4$ (c) $T/2$ (d) $3T/4$. We observe the same dynamics as in LC_2 shown in figure 3.7. Over the range $x \in [0, 1]$ we count three maxima of the vertical velocity fluctuations.

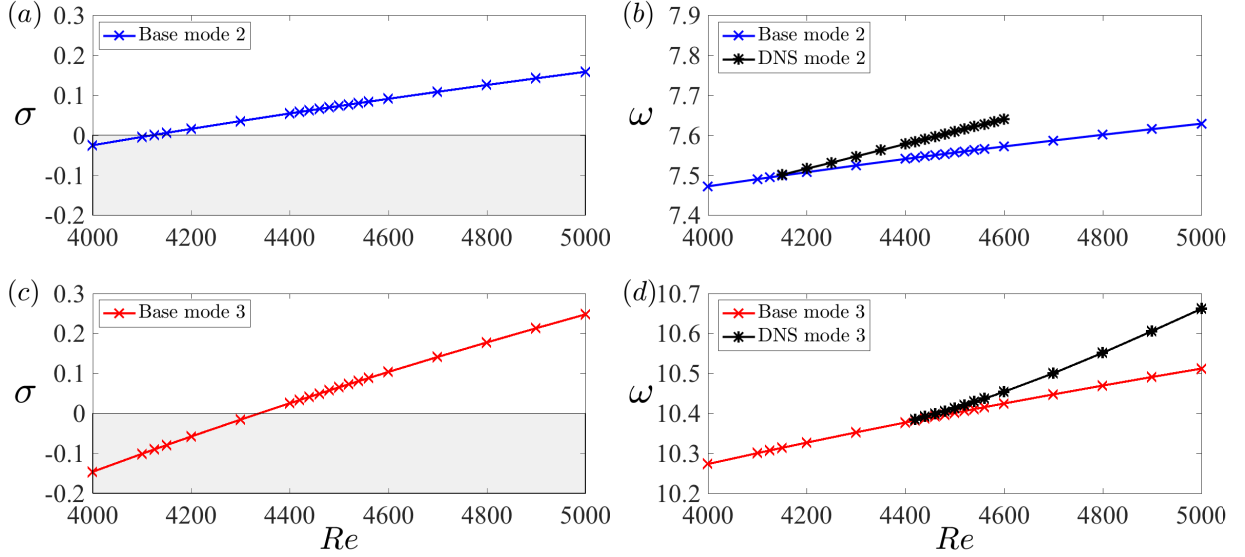


Figure 3.9 – Eigenvalues $\sigma + i\omega$ from linear stability analysis about the base solution with blue and red crosses, and nonlinear frequency from DNS simulation with black stars. (a,c): Growth rate σ of the most unstable eigenmode. In this range of Reynolds number, are two successive Hopf bifurcations as shown in the bifurcation diagram of figure 3.4. The growth rates for eigenvalues leading to LC_2 and LC_3 are shown with blue and red stars respectively. (b,d): Frequency ω of linear stability analysis about the base state and nonlinear simulation. The nonlinear and linear frequencies agree at onset, but when we increase the Reynolds number the nonlinear frequency deviates from that resulting from linear stability about the base flow.

the downstream corner, the structures split, as reported by Rockwell & Knisely [48]: one part follows the fluid downstream, while the other is entrained by the cavity recirculation and returns to feed the flow at the upstream corner, sustaining the vortex generation. The mechanism producing the oscillations is the same for both limit cycles LC_2 and LC_3 . The temporal frequency is near 7 for LC_2 and near 10 for LC_3 , as in Meliga [40], Sipp & Lebedev [54]. These modes are selected by the cavity length and the mean velocity of the mixing layer as described by Rossiter [50] and as will be discussed in §3.4.4.

3.3.2 Linearization about the base flow

In figure 3.9 we present the results of linear stability analysis about the base flow. We plot the growth rates σ in figure 3.9(a,c) and the frequencies ω in figure 3.9(b,d). As previously stated, two successive Hopf bifurcations correspond to two different modes. We plot in (a,b) the eigenvalue leading to LC_2 and (c,d) that corresponding to LC_3 . The zero crossing of the growth rate marks the Hopf bifurcation at which the base flow becomes unstable to that eigenmode. As presented in the bifurcation diagram in figure 3.4, the base flow acquires a first unstable direction at around $Re_2 \approx 4126$ and a second unstable direction at $Re_3 \approx 4348$. Figure 3.9(b,d) also shows the nonlinear frequencies for the two limit cycles. These agree with the eigenfrequencies at Re_2 and Re_3 , as is necessarily the case for a supercritical bifurcation, but as the Reynolds number increases, the frequencies diverge from one another. The frequency extracted at an early stage of a nonlinear simulation initialized by a small perturbation from the base flow will be equal to that given by linear analysis, but the nonlinear interactions will cause it to evolve with time to the nonlinear

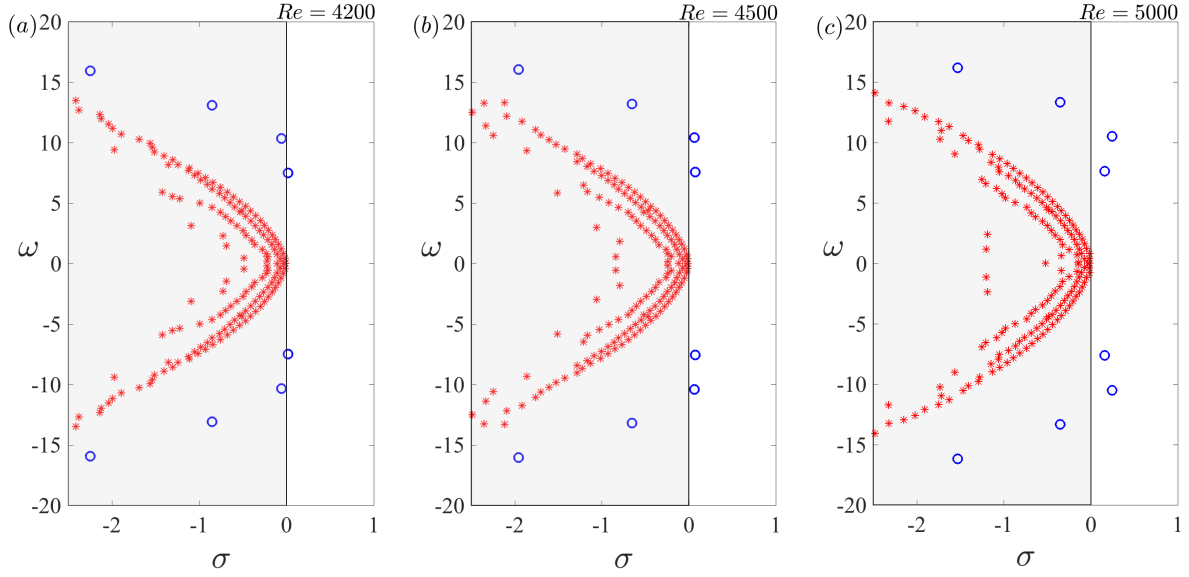


Figure 3.10 – Spectra of complex-conjugate eigenvalues of the base flow for (a) $Re = 4200$, (b) $Re = 4500$, (c) $Re = 5000$. Blue circles designate the converged eigenvalues and red stars the eigenvalues that did not converge. In these figures we observe the evolution of modes leading to LC_2 and LC_3 . The third converged mode, which is stable in this range of Reynolds number, crosses the imaginary axis for $Re \approx 6000$ (not shown).

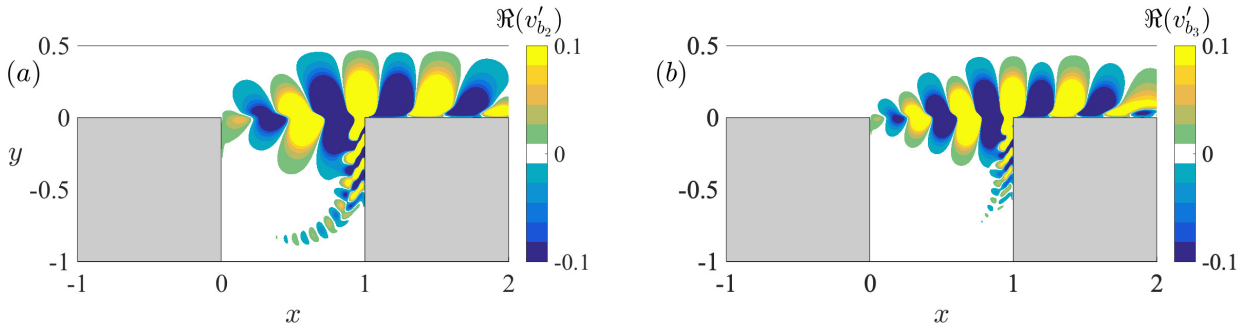


Figure 3.11 – Vertical velocity of the real parts of the leading unstable eigenmodes about the base flow at $Re = 4500$. (a,b) LC_2 and (c,d) LC_3 .

frequency. The frequencies leading to LC_2 and LC_3 cross at $Re = 4540$ (differing by only 0.6% from the value $Re = 4567$ reported by Meliga [40]). Below this value of Re , a simulation initialized with a small perturbation from the base flow will converge to LC_2 , while above, it will converge to LC_3 . In contrast, transition from LC_2 to LC_3 will take place when Re is increased above $Re'_2 \approx 4600$ and from LC_3 to LC_2 when Re is decreased below $Re'_3 \approx 4410$.

Figure 3.10 shows a portion of the eigenvalue spectra for $Re = 4200$, 4500, and 5000. We show in blue circles the eigenvalues that satisfied the convergence tolerance of 10^{-6} and in red stars those that did not converge. The first eigenvalue has crossed the $\sigma = 0$ axis by $Re = 4200$ and the second eigenvalue has crossed by $Re = 4500$. At this Re there are two unstable eigenvalues with almost the same growth rate. At $Re = 5000$ these two unstable eigenvalues have further increased and a third stable mode approaches the imaginary axis, becoming unstable at $Re \approx 6000$ (not shown).

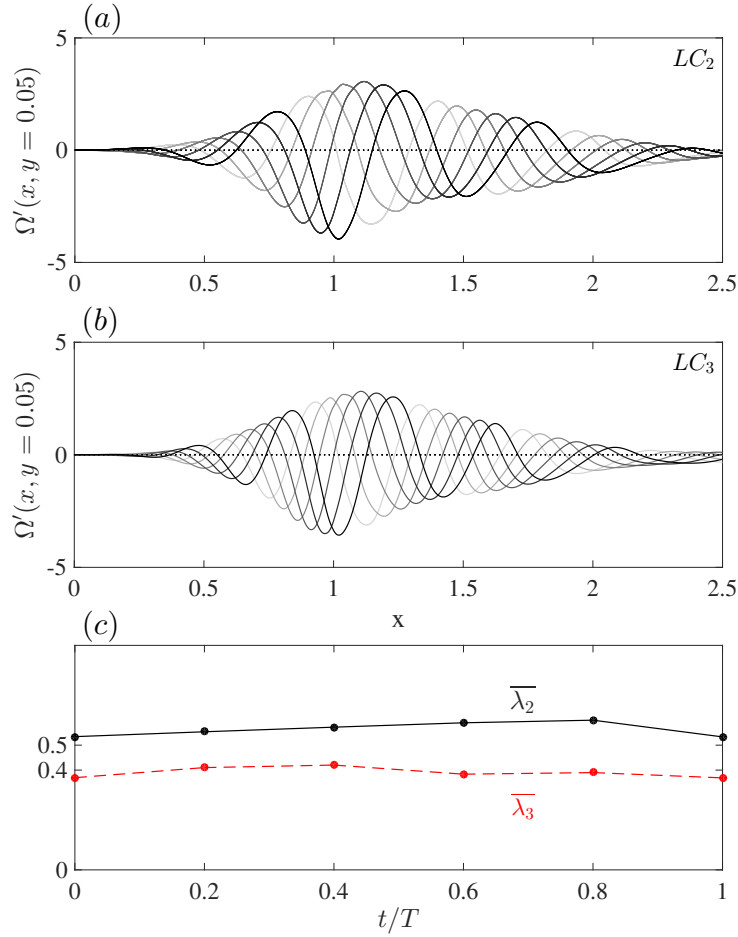


Figure 3.12 – Vorticity fluctuations above the cavity $\Omega'(x, y = 0.05)$ over one period. We observe the behavior of a traveling wave for (a) LC_2 and (b) LC_3 . Because the wavelength evolves in space, we calculate the average wavelength $\bar{\lambda}$ as shown in figure (c), in solid and dashed line for LC_2 and LC_3 respectively. The mean wavelength is near 0.5 for LC_2 and near 0.4 for LC_3 .

Figure 3.11(a,b) shows the real parts of the eigenvectors leading to LC_2 and to LC_3 . We observe two vertical velocity fluctuation maxima on LC_2 and three on LC_3 , as was mentioned in the discussion of figures 3.7 and 3.8.

3.3.3 Spatial analysis and Hilbert transform

We have shown in the previous sections that LC_2 and LC_3 have different numbers of structures across the cavity. Figure 3.12(a,b) shows the vorticity fluctuations Ω' slightly above the cavity like those shown in figure 3.6(d), at $y = 0.05$ and for $x \in [0, 2.5]$ for these limit cycles. Curves from light to dark show the vorticity fluctuations at various phases of the temporal period. These two figures show qualitatively the behavior of a traveling wave, but quantitatively the wavelength and amplitude are not constant. For this reason, at a fixed time, i.e for each curve shown in figure 3.12(a,b) we compute an average wavelength $\bar{\lambda}$. Averaging the wavelength over only $x \in [0, 1]$ is not possible because this range contains too few wavelengths. Figure 3.12(c) shows $\bar{\lambda}$ as the dashed and solid curves for LC_3 and LC_2 . The wavelengths vary little over time and have temporal averages $\langle \bar{\lambda}_2 \rangle = 0.56$ and $\langle \bar{\lambda}_3 \rangle = 0.39$.

We use the Hilbert transform presented in §3.2.7 to analyse in detail the final curve

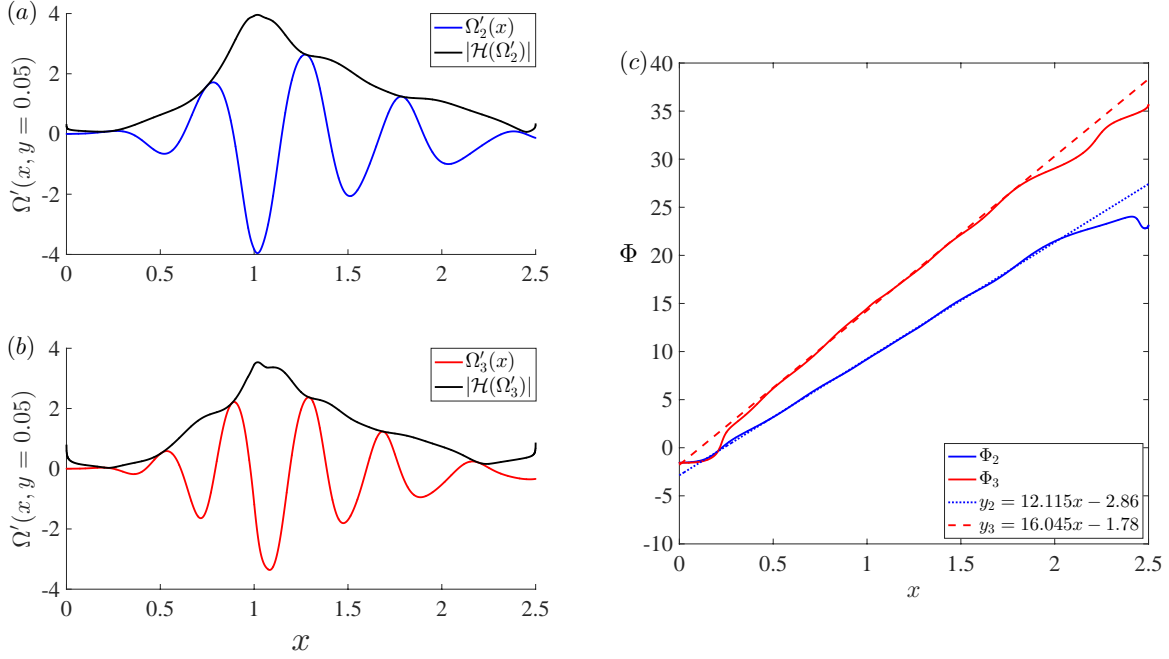


Figure 3.13 – Hilbert transform of vorticity fluctuations $\Omega'(x, y = 0.05)$. (a,b): vorticity fluctuation, its spline interpolation and the modulus of the Hilbert transform, which is the envelope of the signal. (c): The ratio between the real and imaginary parts of the Hilbert transform is the phase whose evolution is shown for LC_3 (red) and for LC_2 (blue). Linear fits to the phases Φ_i are shown by dashed and dotted curves

$\Omega'(x, y = 0.05)$ shown in figure 3.12a,b. We recall that the Hilbert transform produces from a real signal $f(x)$ a complex signal $f_a(x)$ which is written in polar form as $A(x)e^{i\Phi(x)}$. We show in figure 3.13(a,b) the vorticity fluctuations $\Omega'_2(x)$ and $\Omega'_3(x)$ for LC_2 and LC_3 with black curves. Because the Hilbert transform is very sensitive, we have interpolated the signals by cubic splines. The figure also shows the amplitudes $A(x)$ of the Hilbert transform of the signals. Over the range $x \in [0.5, 2.3]$, there are two influential locations: the downstream corner at $x = 1$, and the changeover of boundary condition at $x = 1.75$ from no-slip to free-slip. The amplitudes $A(x)$ show maxima at the downstream corner. Figure 3.13(c) shows the phase $\Phi(x)$ for LC_2 and LC_3 . The slope of $\Phi(x)$ is the wavenumber k . We show with dashed and dotted lines the linear regression calculated over $x \in [0.5, 1.5]$. The wavenumber for LC_2 obtained in this way is $k = 12.115$ and that for LC_3 is $k = 16.045$, leading to wavelengths $\lambda_2 = 0.519$ and $\lambda_3 = 0.392$. These values are fairly close to the values $\langle \bar{\lambda}_2 \rangle = 0.56$ and $\langle \bar{\lambda}_3 \rangle = 0.39$ obtained by measuring wavelengths, as shown in figure 3.12. The value $\lambda_2 \approx 0.5$ justifies our designation of LC_2 as containing two vertical velocity fluctuation maxima, since $L/\lambda_2 \approx 2$, but the value $\lambda_3 \approx 0.4$ leads to $L/\lambda_3 \approx 2.5$ rather than 3.

3.3.4 Quasiperiodic state and Floquet analysis

As presented in the previous sections, there is a range of Re over which two limit cycles coexist, separated by a quasiperiodic state. We mention here that this state is probably periodic rather than strictly quasiperiodic, because of the well-known nonlinear phenomenon of frequency locking, but its effective period is very long and we will continue to consider it to be quasiperiodic. Figures 3.2 and 3.3(b) show the time series corresponding to the

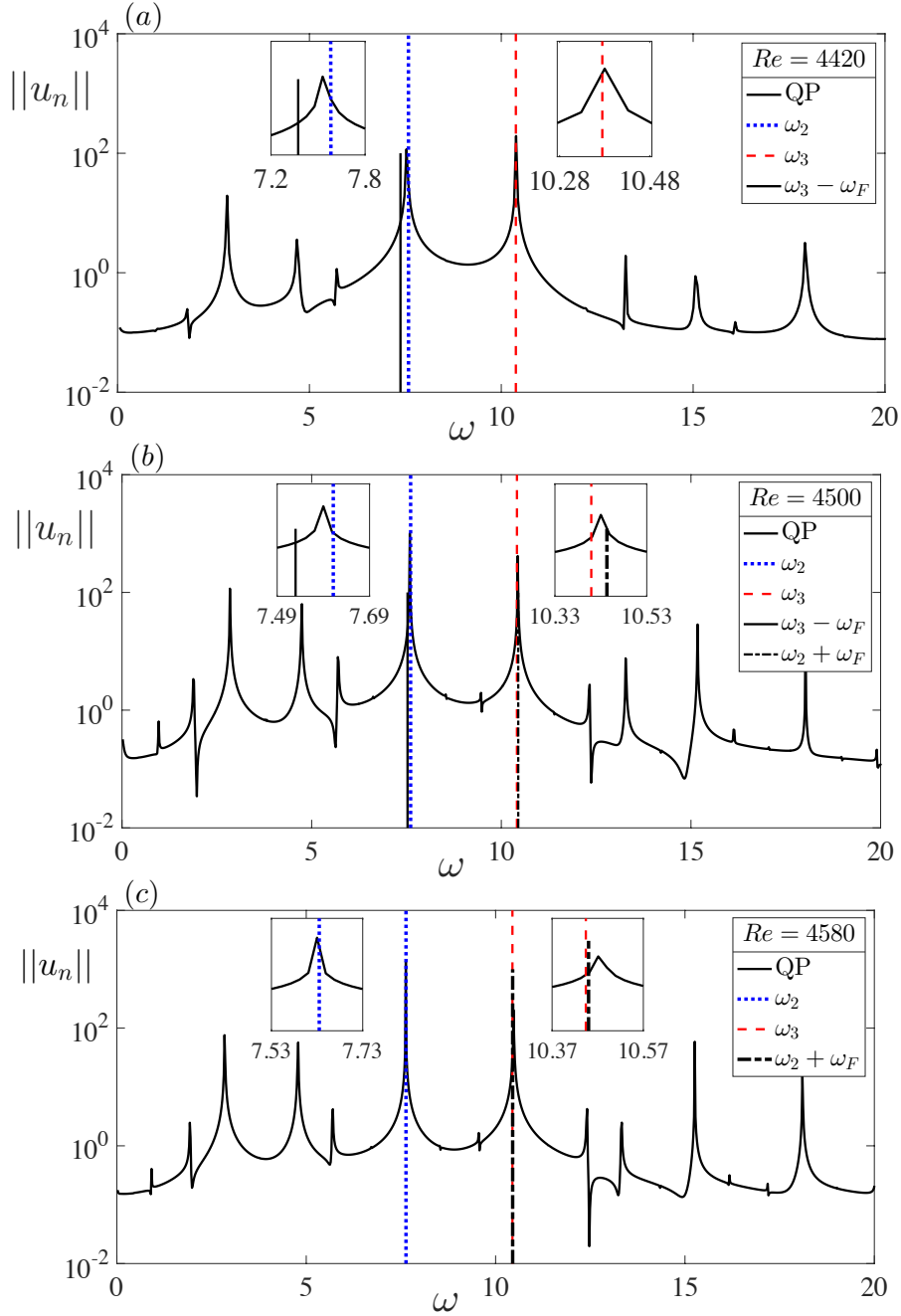


Figure 3.14 – Temporal Fourier spectra of the quasiperiodic state (black bold curves), computed with the edge state technique at (a) $Re = 4420$, near Re'_3 , (b) $Re = 4500$ and (c) $Re = 4580$, near Re'_2 . The vertical lines show the frequencies ω_2 (blue dotted lines) and ω_3 (red dashed lines) of LC_2 and LC_3 at the corresponding values of Re . (a) Near Re'_3 where QP is near LC_3 , the peak ω_{QP_3} of the QP spectrum matches its analogue ω_3 (red dashed line) on LC_3 , while ω_{QP_2} is slightly to the left of ω_2 (blue dotted line) of LC_2 . (c) Near Re'_2 , where QP is near LC_2 , the peak of ω_{QP_2} of the QP spectrum matches its analogue ω_2 (blue dotted line), while ω_{QP_3} is to the right of ω_3 (red dashed line) from LC_3 . (b) Away from Re'_2 and Re'_3 , both frequencies ω_{QP_2} and ω_{QP_3} are shifted slightly from their analogues on LC_2 and LC_3 . The vertical bold and dash-dotted lines show the frequencies calculated by Floquet analysis about LC_2 by $\omega = \omega_2 + \omega_F$ (dash-dotted line) and about LC_3 by $\omega = \omega_3 - \omega_F$ (bold line). Near the thresholds at (a) $Re = 4420$ and (c) $Re = 4580$, the frequency obtained by Floquet analysis about LC_3 and LC_2 are very close to ω_{QP_2} and ω_{QP_3} . At $Re = 4500$ in figure (b) the frequencies obtained by Floquet analysis about LC_2 and LC_3 are also close to their analogues in the quasiperiodic state even though the linear analysis is only valid at the vicinity of the thresholds.

quasiperiodic state. Figure 3.14 presents temporal Fourier spectra for three values of Re . The quasiperiodic state has two fundamental frequencies close to ω_2 and ω_3 as shown by the dotted and dashed lines in figures 3.14(a-c). QP can be viewed as a nonlinear superposition of LC_2 and LC_3

$$\mathbf{U}_{QP}(x, y, t) = \sum_n \sum_m c_{n,m} e^{i(n\omega_{QP_2} + m\omega_{QP_3})t} \quad (3.18)$$

where $n, m \in \mathbb{N}$, ω_{QP_2} and ω_{QP_3} are the fundamental frequencies of QP . The blue dotted lines show the nonlinear frequency of LC_2 and the red dashed lines that of LC_3 at the corresponding values of Re .

We now interpret the spectra of figure 3.14 in the context of the bifurcation diagram of figure 3.4. Because $Re = 4420$ is close to Re'_3 , the quasiperiodic state at $Re = 4420$ is close to the limit cycle LC_3 . In agreement with this, the peak at ω_{QP_3} matches almost exactly the nonlinear frequency $\omega_3 = 10.38$ of LC_3 indicated by the red dashed line in figure 3.14(a). In contrast QP is not close to LC_2 at this Reynolds number and so the peak at ω_{QP_2} is to the left of the the frequency $\omega_2 = 7.58$ of LC_2 (blue dotted line). At figure 3.14(c), corresponding to $Re = 4580$ near Re'_2 , the situation is naturally reversed. The peak at ω_{QP_2} matches almost exactly its analogue $\omega_2 = 7.634$ on LC_2 (blue dotted line) since it is close to LC_2 , while ω_{QP_3} is slightly to the right of $\omega_3 = 10.445$ of LC_3 . Away from LC_2 and LC_3 at $Re = 4500$, both frequencies $\omega_2 = 7.609$ and $\omega_3 = 10.412$ are slightly shifted from their analogues on the quasiperiodic state.

We have found from the nonlinear simulations that LC_2 loses stability towards LC_3 for $Re > Re'_2 \approx 4600$ and LC_3 gains stability for $Re > Re'_3 \approx 4420$. To shed light on the stability of these limit cycles, we carry out a Floquet analysis. In the Floquet framework, we decompose the velocity field as

$$\mathbf{U}(x, y, t) = \mathbf{U}_{LC}(x, y, t) + \epsilon e^{(\sigma_F + i\omega_F)t} \mathbf{u}_F(x, y, t) + c.c. \quad (3.19)$$

with \mathbf{U}_{LC} the periodic solution corresponding to the limit cycle about which the Floquet analysis is performed, \mathbf{u}_F the Floquet mode which is also periodic with period $T_b = 2\pi/\omega_b$ and $\sigma_F + i\omega_F$ the Floquet exponent. We rewrite (3.19) by expressing the Floquet mode as a Fourier series, leading to

$$\mathbf{U}(x, y, t) = \mathbf{U}_{LC}(x, y, t) + \epsilon e^{(\sigma_F + i\omega_F)t} \sum_n \mathbf{u}_{F,n}(x, y) e^{in\omega_b t} + c.c. \quad (3.20)$$

For $t = T_b$, we have $e^{in\omega_b T_b} = e^{in\omega_b (2\pi/\omega_b)} = e^{in2\pi} = 1$ and so (3.20) becomes

$$\mathbf{U}(x, y, T_b) = \mathbf{U}_{LC}(x, y, T_b) + \epsilon e^{\sigma_F 2\pi/\omega_b} e^{i2\pi\omega_F/\omega_b} \sum_n \mathbf{u}_{F,n}(x, y) + c.c. \quad (3.21)$$

with $\mu \equiv e^{\sigma_F 2\pi/\omega_b}$ the modulus and $\theta \equiv 2\pi\omega_F/\omega_b$ the argument of the Floquet multipliers.

Figure 3.15 shows the Floquet multipliers for both limit cycles in the complex plane. All Floquet multipliers (dots) are inside the unit circle, meaning that the corresponding limit cycles are stable at these Reynolds numbers. Figures 3.15(a,b) show the results for LC_2

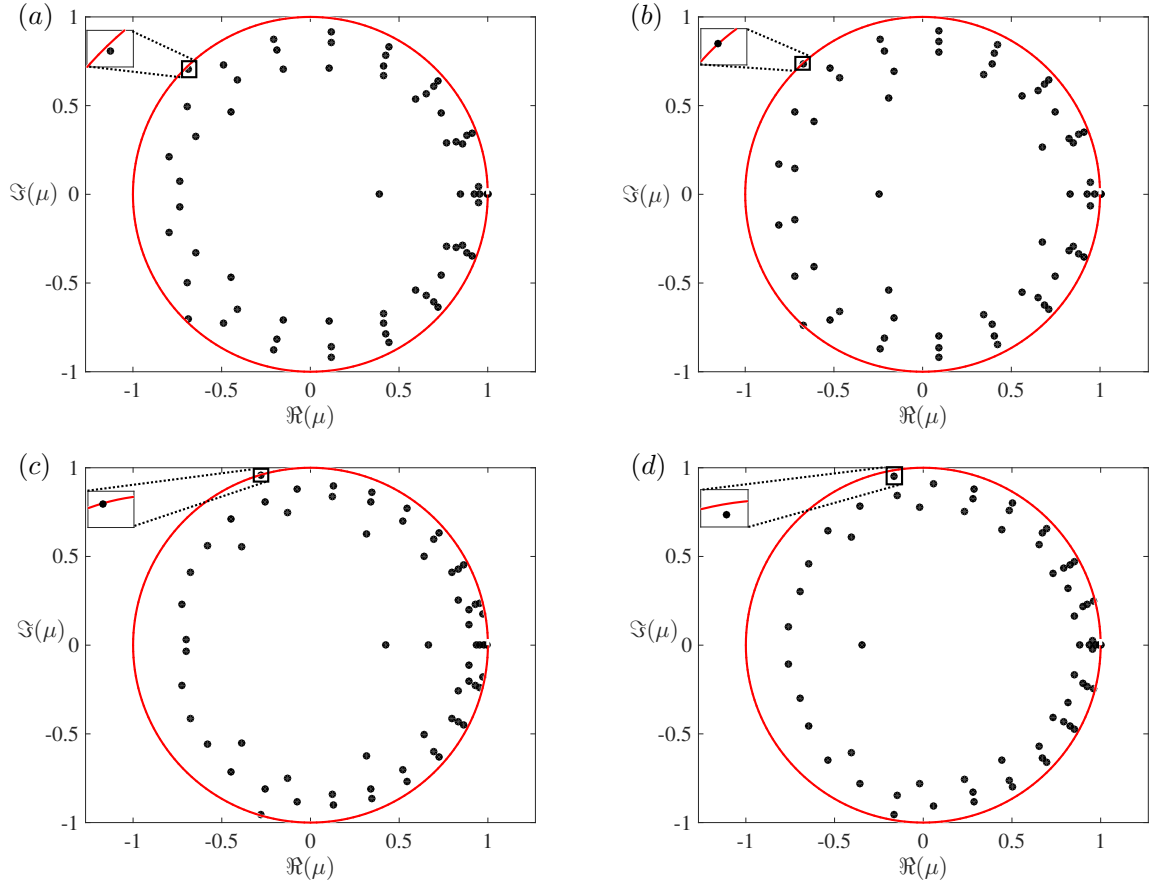


Figure 3.15 – Floquet multipliers for LC_2 : (a) $Re = 4500$, (b) $Re = 4600$, and LC_3 : (c) $Re = 4420$, (d) $Re = 4500$. The small boxes are enlargements of the region surrounding the dominant Floquet multiplier.

at $Re = 4500$ and 4600 respectively. In figure 3.15a at $Re = 4500$, the dominant Floquet multiplier modulus is $|\mu| = 0.981$. On figure 3.15b, by $Re = 4600 \lesssim Re'_2$, this multiplier has moved closer to the unit circle, with $|\mu| = 0.999$. Figures 3.15(c,d) show that the moduli of the dominant Floquet multipliers for LC_3 at $Re = 4420 \gtrsim Re'_3$ and at $Re = 4500$ are $|\mu| = 0.995$ and $|\mu| = 0.967$. Thus the results shown by the Floquet analysis confirm the nonlinear observations. The results of this Floquet analysis resemble those found for the lid-driven cavity by Tiesinga *et al.* [60].

We now turn to the argument of the Floquet multipliers. If the Floquet exponent is real ($\omega_F = 0$) then the Floquet multiplier is one and the bifurcating state has the same frequency as the base limit cycle. If $\omega_F/\omega_b = 1/2$ then the Floquet multiplier is -1 , which corresponds to a subharmonic mode. In our problem the dominant Floquet multiplier is complex, and so the bifurcation is a secondary Hopf bifurcation and the solution near the threshold of QP is described by equation (3.20). The spectrum of QP near the threshold contains ω_b and its multiples as well as the frequencies introduced by the secondary Hopf bifurcation, namely $\pm\omega_F \pm n\omega_b$, with a dominant contribution from $n = \pm 1$. Indeed, near Re'_2 , the spectrum of QP contains frequencies ω_2 and $\omega_2 + \omega_F = \omega_2(1 + \frac{\theta}{2\pi}) = 10.45$ while near Re'_3 , QP contains frequencies ω_3 and $\omega_3 - \omega_F = \omega_3(1 - \frac{\theta}{2\pi}) = 7.37$

These calculations are confirmed by figures 3.14(a,c). For (a) $Re = 4420 \gtrsim Re'_3$, the Floquet analysis about LC_3 yields a frequency $\omega_3 - \omega_F$ (solid vertical black line) comparable to the peak at ω_{QP_2} . For (c) $Re = 4580 \lesssim Re'_2$, the Floquet analysis about LC_2 yields the

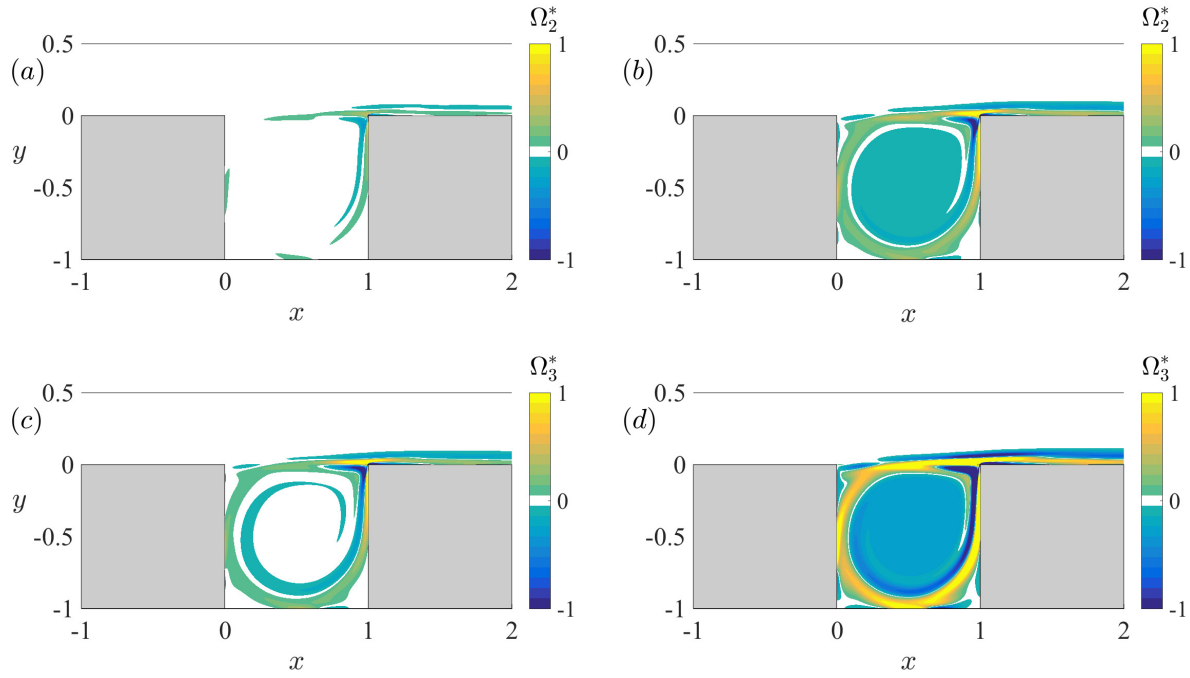


Figure 3.16 – Distortion of the mean flow ($\Omega^* = \bar{\Omega} - \Omega_b$). For LC_2 at (a) $Re = 4200$ and (b) $Re = 4500$. For LC_3 at (c) $Re = 4500$ and (d) $Re = 5000$. The distortion measures the deviation of the mean flow from the base flow due to nonlinear interaction and increases with Reynolds number.

frequency $\omega_2 + \omega_F$ (dashed vertical black line) which is very close to ω_{QP_3} .

3.4 Frequency prediction

3.4.1 Linearization about the mean flow

Linear stability analysis – i.e. linearizing about the base flow and solving the resulting eigenproblem – is a classic tool in hydrodynamics. Bifurcations which create new branches are determined unambiguously by linear stability analysis and, if the bifurcation is supercritical, the spatial and temporal behaviors of the new states near threshold are similar to those of the eigenvector and eigenvalue responsible for the instability. Further from the threshold, these properties evolve and may well differ substantially from those of the bifurcating eigenvector and eigenvalue. In some cases, it has been shown that linearization about the mean flow of a limit cycle can yield more accurate approximations of the nonlinear states. We have carried out a linear analysis about the temporal mean for both limit cycles LC_2 and LC_3 and compared the resulting frequencies with those obtained from linearization about the base flow and with the nonlinear frequencies of these cycles. This procedure has been carried out for LC_3 by Meliga [40]; here we carry out the same procedure for LC_2 and compare the two regimes.

The mean flow greatly resembles the base flow shown in figure 3.5, and therefore we plot instead their difference, the distortion $\bar{\Omega}^* \equiv \bar{\Omega} - \Omega_b$, which is shown for LC_2 at $Re = 4200$ and 4500 in figure 3.16(a,b) and for LC_3 at $Re = 4500$ and 5000 in figure 3.16(c,d). Nor do we show the eigenmodes obtained by linearizing about the mean flow, since they resemble those obtained from linearizing about the base flow (figure 3.11) as well as the nonlinear vertical velocity fluctuations (figures 3.7 and 3.8).

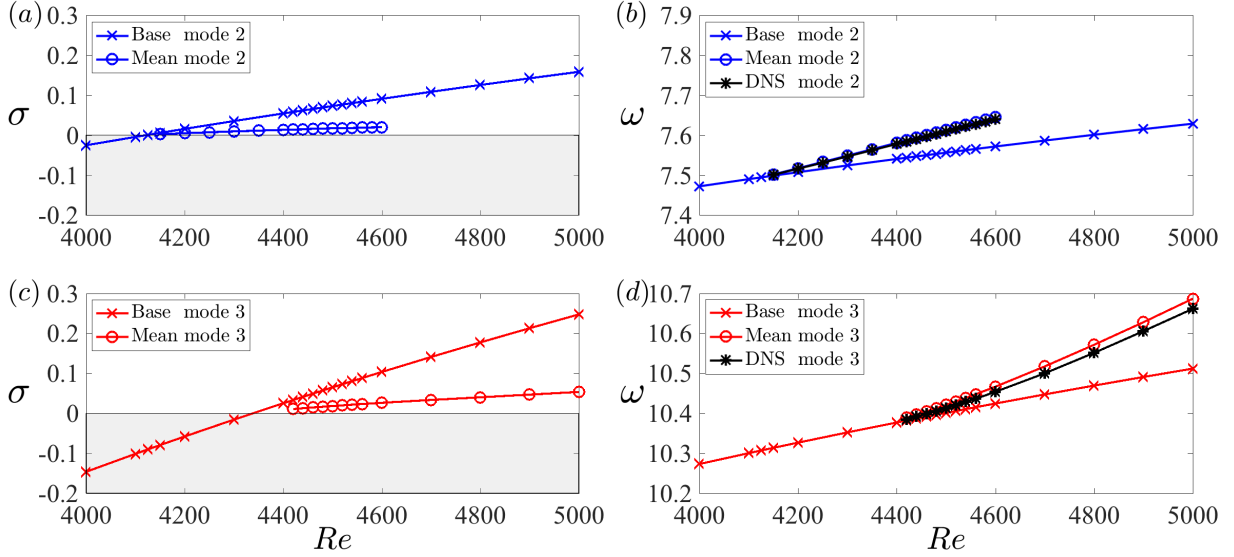


Figure 3.17 – Eigenvalues $\sigma + i\omega$ from linear stability analysis about the base and mean flows of LC_2 and LC_3 . The eigenvalues about the base flow are plotted with crosses. Linear stability about the mean flow is shown with circles. The nonlinear frequency from DNS is plotted with black stars. (a,c): The growth rate σ for LC_2 for the mean flow is nearly zero but that of LC_3 is smaller than that about the base flow, but not enough to be considered to be neutrally stable. (b,d): The imaginary parts of the eigenvalues are almost exactly equal to the nonlinear frequencies, especially for LC_2 . For LC_3 , although the imaginary part of the eigenvalue and the nonlinear frequency are necessarily equal at onset, the two diverge slightly as Re increases.

Figure 3.17 and Table 3.1 compare the eigenvalues resulting from linearization about the base flow and the mean flow and those of the nonlinear simulation. Figure 3.17 plots the frequencies and growth rates over the Reynolds number range $[4000, 5000]$ that we have studied, while Table 3.1 shows numerical data extracted from these figures for three representative Reynolds numbers, 4200, 4500 and 5000. We note that unlike for the cylinder wake (Barkley [4]), the frequencies obtained from the usual linear stability analysis are already not very far from those of the nonlinear limit cycles. Table 3.1 shows a deviation of less than 0.6% for the frequencies in LC_2 and of less than 1.4% for LC_3 over this Reynolds number range. In contrast, for the cylinder wake (Barkley [4]), the difference between the nonlinear frequencies and those obtained by linear stability analysis reaches 15% by $Re = 60$, a Reynolds number comparable to the distance above criticality studied here and reaches 100% by $Re = 180$, a frequent upper limit of such studies. This difference will be discussed further in sections §3.4.4 and §3.5.

Figure 3.17(b) for LC_2 (circles) shows that the frequency obtained by linearization about the mean flow is nonetheless much closer to the nonlinear temporal frequency (stars) than that given by linear stability about the base flow (crosses). Quantitatively, table 3.1 shows the relative difference at $Re = 4500$ between the nonlinear frequency and the frequency obtained from the base flow to be 0.7%; this difference is reduced to 0.04% when the linearization is performed about the mean flow. Moreover, the growth rate obtained about the mean flow (circles) in figure 3.17(a) is nearly zero, as found by Barkley [4] for the cylinder wake. Table 3.1 shows a growth rate at $Re = 4500$ of 0.073 for linearization about the base flow; this is reduced by a factor of 5 to 0.017 for the linearization about the mean.

	linearize about base			linearize about mean			nonlinear			$\Delta\omega$	Δf
Re	4200	4500	5000	4200	4500	5000	4200	4500	5000		
ω_2	7.502	7.556	7.629	7.517	7.612		7.516	7.609		2.8	0.45
diff	0.014	0.053		0.001	0.003						
σ_2	0.016	0.073	0.158	0.005	0.017						
ω_3	10.327	10.401	10.512		10.421	10.686		10.412	10.661	2.8	0.45
diff		0.011	0.149		0.009	0.025					
σ_3	-0.058	0.065	0.247		0.018	0.053					
ω_4	13.099	13.188	13.321							2.8	0.45
ω_5	15.931	16.029	16.183								

Table 3.1 – Linear and nonlinear frequencies for cavity modes. The first row shows frequencies from linearization about the base and from linearization about the mean and nonlinear simulations, where available. Second row for ω_2 and ω_3 shows deviation from frequencies from nonlinear simulations. When the RZIF property is satisfied, linearization about the nonlinear mean yields frequencies close to nonlinear frequencies. The third row for ω_2 and ω_3 shows linear growth rates for cavity modes. Linearization about base yields growth rates which cross zero transversely as the bifurcation threshold is crossed. When the RZIF property is satisfied, linearization about the nonlinear mean yields growth rates near zero, i.e. the mean flow is nearly marginally stable. Last columns show the frequency increment from one row to the next row, which is constant to two digits, regardless of the Reynolds number or which type of frequency is used.

For LC_3 , the frequency obtained by linearizing about the mean presented in figure 3.17(d) (circles) agrees well with the nonlinear frequency (stars). The curves begin to diverge slightly for $Re \geq 4600$, and although the agreement is not as good as it is for LC_2 , the frequencies are still very close. Quantitatively, table 3.1 shows the relative difference at $Re = 5000$ between the nonlinear frequency and the frequency obtained from the base flow to be 1.4%; this difference is reduced to 0.02% when the linearization is performed about the mean flow. Table 3.1 shows a growth rate at $Re = 5000$ of 0.247 for linearization about the base flow; this is again reduced by a factor of 5 to 0.053 for the linearization about the mean.

3.4.2 RZIF and SCM

We now present an argument for the validity of linearization about the mean flow. The derivation is closely related to the idea called harmonic balance in the aerodynamic literature (Hall *et al.* [23], McMullen *et al.* [38], McMullen & Jameson [39]). Turton *et al.* [61] argued that the RZIF property holds exactly if the time dependence is monochromatic, meaning that higher harmonics are negligible compared to the fundamental frequency. Consider the evolution equation

$$\partial_t \mathbf{U} = \mathcal{L}\mathbf{U} + \mathcal{N}(\mathbf{U}, \mathbf{U}) \quad (3.22)$$

where \mathcal{L} is linear and $\mathcal{N}(\cdot, \cdot)$ is a quadratic nonlinearity. Let

$$\mathbf{U} = \bar{\mathbf{U}} + \sum_{n \neq 0} \mathbf{u}_n e^{in\omega t} \quad (3.23)$$

(with $\mathbf{u}_{-n} = \mathbf{u}_n^*$) be the temporal Fourier decomposition of a periodic solution to (3.22) with mean $\bar{\mathbf{U}}$ and frequency ω . In (3.23) and throughout this subsection, subscripts refer

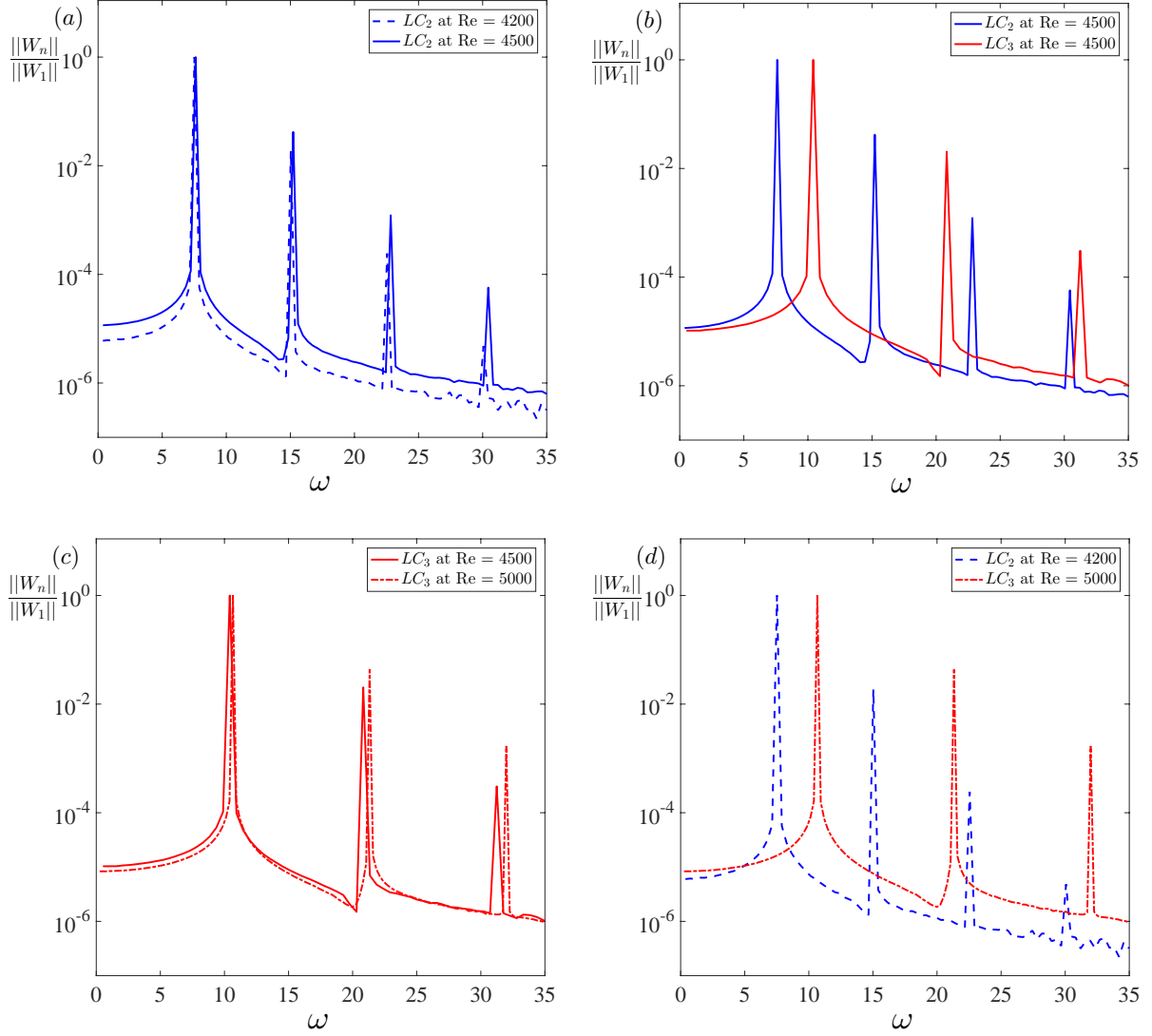


Figure 3.18 – Temporal spectra of streamwise velocity normalized by the fundamental frequency for LC_2 and LC_3 . (a) Spectra of LC_2 at $Re = 4200$ and $Re = 4500$. (b) At $Re = 4500$ for LC_2 and LC_3 . (c) At $Re = 4500$ and $Re = 5000$ for LC_3 . (d) Spectra of LC_2 and LC_3 at $Re = 4200$ and $Re = 5000$ respectively.

to temporal harmonics of a single limit cycle, rather than serving to distinguish between LC_2 and LC_3 .

The $n = 0$ (mean) component of (3.22) is

$$0 = \mathcal{L}\bar{\mathbf{U}} + \mathcal{N}(\mathbf{u}_1, \mathbf{u}_{-1}) + \mathcal{N}(\mathbf{u}_{-1}, \mathbf{u}_1) + \mathcal{N}(\mathbf{u}_2, \mathbf{u}_{-2}) + \mathcal{N}(\mathbf{u}_{-2}, \mathbf{u}_2) + \dots \quad (3.24)$$

while the $n = 1$ component is

$$\begin{aligned} i\omega \mathbf{u}_1 = & \underbrace{\mathcal{L}\mathbf{u}_1 + \mathcal{N}(\bar{\mathbf{U}}, \mathbf{u}_1) + \mathcal{N}(\mathbf{u}_1, \bar{\mathbf{U}})}_{\mathcal{L}_{\bar{\mathbf{U}}}\mathbf{u}_1} \\ & + \underbrace{\mathcal{N}(\mathbf{u}_2, \mathbf{u}_{-1}) + \mathcal{N}(\mathbf{u}_{-1}, \mathbf{u}_2) + \mathcal{N}(\mathbf{u}_3, \mathbf{u}_{-2}) + \mathcal{N}(\mathbf{u}_{-2}, \mathbf{u}_3) + \dots}_{\mathcal{N}_1} \end{aligned} \quad (3.25)$$

If, as is often the case, $\|u_n\| \sim \epsilon^{|n|}$, then $\mathcal{N}_1 = O(\epsilon^3)$ may be neglected and RZIF is satisfied:

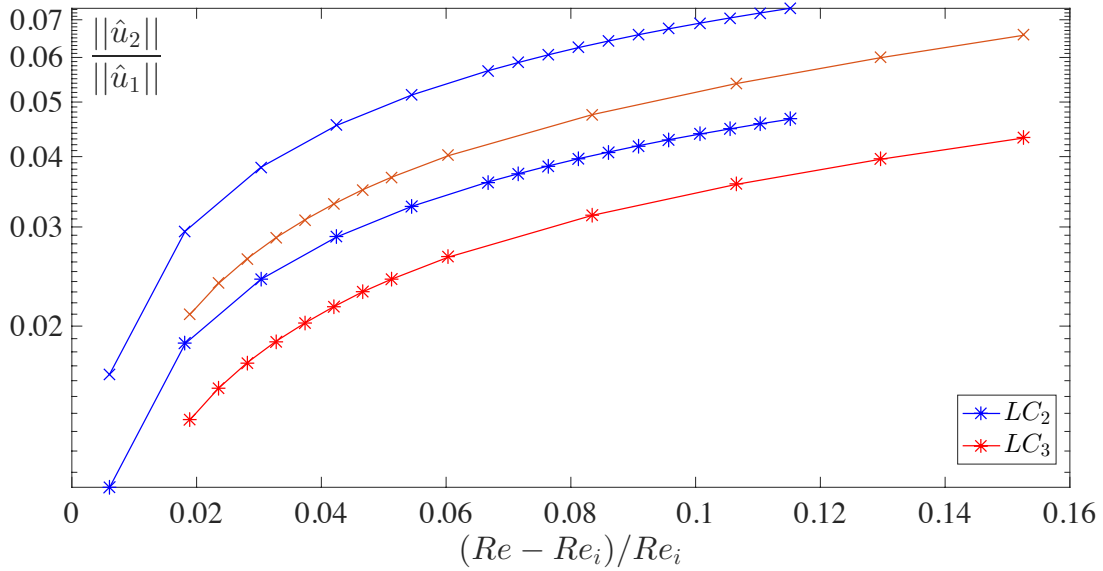


Figure 3.19 – Amplitude of second harmonic (stars) and the sum of the amplitudes of the three lowest harmonics (crosses) normalized by the amplitude of the fundamental frequency as a function of relative Reynolds number for LC_2 and LC_3 . As in figure 3.18, the fundamental frequency dominates the second harmonic. These ratios are always below 10^{-1} and are slightly higher for LC_2 than that for LC_3 .

the linear operator $\mathcal{L}_{\bar{U}}$ in (3.25) has the pure imaginary eigenvalue $i\omega$, corresponding to the frequency of the periodic solution. Hence the RZIF property is satisfied for near-monochromatic oscillations in a system with quadratic nonlinearity.

We mention here that RZIF is not predictive, since it requires a full nonlinear direct numerical simulation to be carried out in order to compute the temporal mean \bar{U} . An approach which is actually predictive, i.e. which does not require a DNS, has been proposed by Mantič-Lugo *et al.* [33, 34], who called it the Self-Consistent Model (SCM). The SCM truncates the mean flow equation (3.24) as well as the $n = 1$ equation (3.25), leading to the closed system

$$\begin{aligned} 0 &= \mathcal{L}\bar{U} + \mathcal{N}(\mathbf{u}_1, \mathbf{u}_{-1}) + \mathcal{N}(\mathbf{u}_{-1}, \mathbf{u}_1) \\ i\omega\mathbf{u}_1 &= \mathcal{L}\mathbf{u}_1 + \mathcal{N}(\bar{U}, \mathbf{u}_1) + \mathcal{N}(\mathbf{u}_1, \bar{U}) \end{aligned} \quad (3.26)$$

This system is then solved for \bar{U} and \mathbf{u}_1 by various iterative methods; see Mantič-Lugo *et al.* [33, 34]. The next higher truncation, i.e. retaining \bar{U} , \mathbf{u}_1 , and \mathbf{u}_2 , has been studied by Meliga [40]. It may happen, however, that RZIF is satisfied, while SCM is not, i.e. that while higher-order modes may be neglected in (3.25), they are essential to forming the correct mean flow and cannot be neglected in (3.24); see Bengana & Tuckerman [9].

For thermosolutal convection, Turton *et al.* [61] showed that for traveling waves, the RZIF property is satisfied and the spectrum is highly peaked, while for standing waves the spectrum is broad and the RZIF property is not satisfied. We now wish to see if the temporal spectra of LC_2 and LC_3 also explain the fact that the RZIF property is better satisfied for LC_2 than for LC_3 . We show in figure 3.18 the temporal spectra of streamwise velocity normalized by the fundamental frequency for LC_2 and LC_3 , for various values of Reynolds number. In figure 3.19 we plot the ratio of the second harmonic to the fundamental frequency. The ratio $||\hat{u}_2||/||\hat{u}_1||$ is consistently less than 0.05 for both

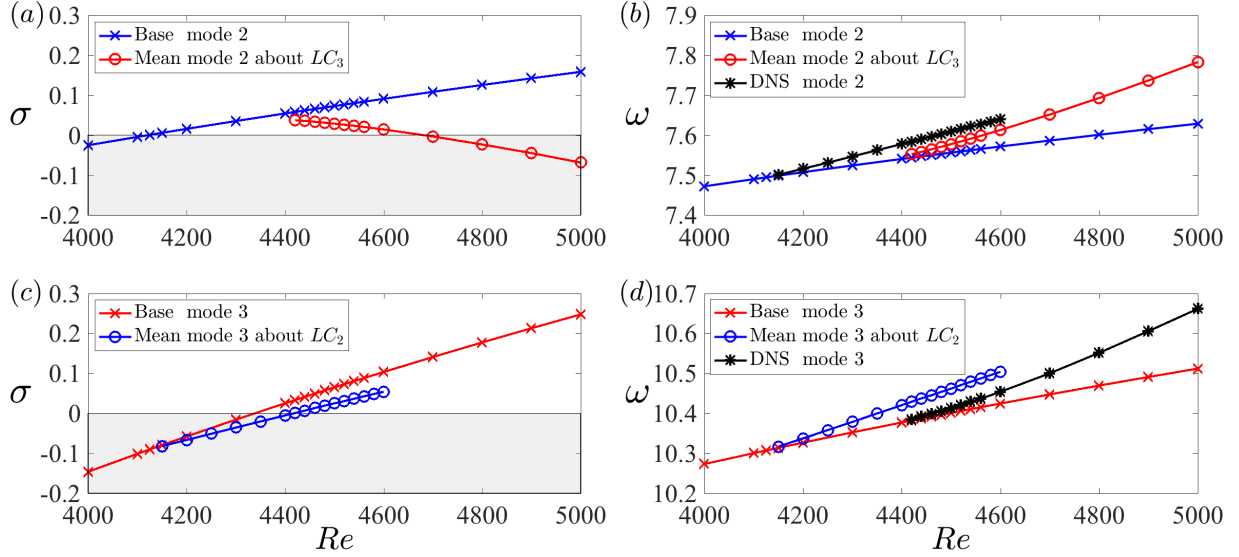


Figure 3.20 – Eigenvalues $\sigma + i\omega$ from linearization about the base and mean flows. Here the spatial form of the eigenvector does not correspond to that of the mean flow. The eigenvalues about the base flow are plotted with crosses, blue for LC_2 and red for LC_3 . The eigenvalues of mode two about the mean flow of LC_3 are shown with red circles and that of mode three about the mean flow of LC_2 with blue circles. The nonlinear frequencies from DNS are plotted with black stars for LC_2 and LC_3 . (a) The growth rate of mode two about the mean of LC_3 (red circles) decreases from the threshold $Re_3 \approx 4348$ of LC_3 and becomes negative at $Re \approx 4681$. This may correspond qualitatively to the fact that LC_3 is unstable to mode 2 perturbations when it is created at Re_3 and becomes stable at $Re'_3 \approx 4410$. (c) The growth rate of mode three about the mean of LC_2 (blue circles) increases from the threshold $Re_2 \approx 4126$ of LC_2 and becomes positive at $Re \approx 4418$. This may correspond qualitatively to the fact that LC_2 is stable when created at Re_2 and becomes unstable at $Re'_2 \approx 4600$.

flows over the range of our investigation, while $(\|\hat{u}_2\| + \|\hat{u}_3\| + \|\hat{u}_4\|)/\|\hat{u}_1\|$ remains below 0.07, consistent with the fact that RZIF is satisfied. We observed that RZIF is closer to being valid for LC_2 than for LC_3 , but the ratios in figure 3.19 follow the opposite tendency. Thus, the explanation proposed by Turton *et al.* [61] in terms of the temporal Fourier amplitudes does not explain this difference.

3.4.3 Cross-eigenvalues

Like the base flow, the mean flow has a full spectrum of eigenvalues and eigenvectors. Thus, the mean flow of LC_2 has not only eigenvectors with two vertical velocity fluctuation maxima with corresponding eigenvalues shown in figures 3.17(a,b), like those which lead to LC_2 , but it also has also eigenvectors with three maxima like those which lead to LC_3 and their corresponding eigenvalues. Similarly, the mean flow of LC_3 has eigenvectors containing two maxima. We refer to these as cross-eigenvalues. Figure 3.20 shows the cross-eigenvalues corresponding to mode two, obtained by linearization about the mean flow of LC_3 (circles, figure 3.20(a,b)) and those of mode three about the mean flow of LC_2 (circles, figure 3.20(c,d)). The eigenvalues obtained from the base and from the mean necessarily agree at Re_2 for LC_2 and at Re_3 for LC_3 , since when the limit cycles are created, the base and mean flows are equal.

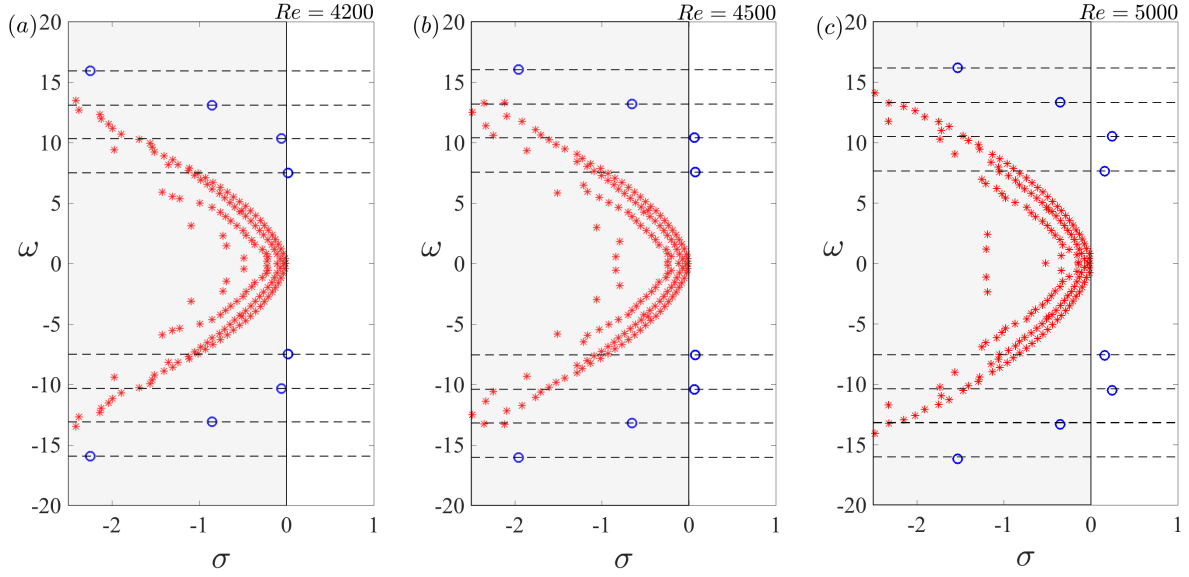


Figure 3.21 – Spectra of the base flow for (a) $Re = 4200$, (b) $Re = 4500$, (c) $Re = 5000$. Blue circles designate the converged eigenvalues and red stars the eigenvalues that did not converge. Horizontal lines emphasize the fact that the frequencies are equally spaced.

Focusing on figure 3.20(a), we recall that LC_3 is created at $Re_3 \approx 4348$ and is unstable to eigenmodes of type 2 until $Re'_3 \approx 4410$, i.e. there is a Floquet mode with positive Floquet exponent for $Re \in [4348, 4410]$. This is qualitatively the behavior that is seen in figure 3.20(a), although here the cross-eigenvalue σ is positive over a higher range, for $Re \in [4348, 4681]$. Focusing now on figure 3.20(c), we recall that LC_2 is created at $Re_2 \approx 4126$ and becomes unstable to eigenmodes of type 3 at $Re'_2 \approx 4600$. This is again qualitatively close to the behavior is seen in figure 3.20(c), except that here the cross-eigenvalue σ becomes positive at the lower value of $Re \approx 4418$.

These results indicate that for a limit cycle, linearization about its mean flow may be able to convey information about the growth rate, frequency, and spatial characteristics of its stability to secondary bifurcations. Referring back to figure 3.4(b), these phase portraits represent the limit cycles as fixed points, whose existence and stability are governed by the dynamics of the two-dimensional normal form (3.17), (3.17). Stability or instability of LC_2 to LC_3 or vice versa is represented by the horizontal arrows emanating to or from LC_2 , located on the vertical axis, and the vertical arrows emanating to or from LC_3 , located on the horizontal axis. The temporal mean would then be interpreted as a fixed point approximation to a limit cycle, and the cross-eigenvalues would then correspond to their relative stability. Although this is plausible, we emphasize that there exists at present no mathematical framework for this interpretation. Moreover, although the trends seen in figure 3.20 support this interpretation, the agreement is only qualitative.

3.4.4 Rossiter formula

We return to Table 3.1, the last column of which shows that the frequencies of successive modes increase by a constant interval. (For a given mode, the various versions of its frequency differ by at most 1%-2%.) We emphasize this again by reproducing the

eigenspectra in figure 3.21, adding horizontal lines which emphasize visually the constant difference between the frequencies. Spectra similar to those in figure 3.21 are also seen for the lid-driven cavity in Tiesinga *et al.* [60]. In flows over shear-driven cavities, Rossiter [50] observed that the temporal frequencies for self-sustained oscillations were quantized and proposed the following empirical formula:

$$f_n = \frac{U_\infty}{L} \frac{n - \gamma}{M + 1/\kappa} \implies \frac{U_\infty}{L} \kappa (n - \gamma) \text{ for } M = 0 \quad (3.27)$$

where U_∞ and L are the free-stream speed away from the cavity and the length of the cavity, and M is the Mach number, here set to zero. The phenomenological constant γ is a phase lag, while the increment κ will be discussed below. The essence of (3.27) is not only that the temporal frequencies f_n observed are quantized (which is to be expected in a finite cavity) but that they are separated by a fixed increment Δf . Heuristically, if the limit cycle consists of n structures advected horizontally at velocity U_{adv} , then the average structure occupies a length L/n and strikes the cavity corner with frequency $U_{\text{adv}}/(L/n)$. Since the frequencies in table 3.1 are nondimensionalized by U_∞/L , we have

$$\Delta f = \frac{U_\infty}{L} \kappa = \frac{U_{\text{adv}}}{L} = 0.45 \implies \kappa = \frac{U_{\text{adv}}}{U_\infty} = 0.45 \quad (3.28)$$

Thus, the frequency is seen to be determined primarily by the geometry and the free-stream velocity.

3.5 Conclusion

We have carried out a detailed study of the dynamics of shear-driven square cavity flow over the Reynolds number range 4000 to 5000. An original result of the study is the detailed description of two solution branches, which are limit cycles with different numbers of structures, i.e. vertical velocity fluctuation extrema, across the cavity. These appear via successive primary supercritical Hopf bifurcations. Stability is transferred from the first to the second limit cycle via an unstable quasiperiodic state which is created and destroyed via subcritical secondary Hopf bifurcations from the limit cycles. The primary and secondary Reynolds numbers are such that there exists a region of bistability. Transition from one limit cycle to the other is hysteretic and is characterized by a sudden change in frequency from $\omega \sim 7$ to $\omega \sim 10$ and a change in the number of structures along the shear layer of the cavity. By using edge state tracking, we have been able to produce an approximation to the quasiperiodic state and to measure its temporal Fourier spectrum, which corresponds well to the frequencies computed by a Floquet analysis of the two limit cycles. The Hilbert transform is used to extract spatial envelopes and wavenumbers for representatives of these limit cycles.

A possible extension of our study is to the range $Re > 5000$. Although the next two eigenvalue pairs seen in figure 3.21 cross the imaginary axis, time-dependent simulations do not exhibit these frequencies, as has also been observed by Tiesinga *et al.* [60] for the lid-driven cavity. Preliminary simulations also show that limit cycle LC_3 may undergo a secondary Hopf bifurcation between $Re = 6000$ and $Re = 7500$. At these Reynolds numbers, the temporal Fourier spectrum shows low-frequency components whose associated spatial characteristics are localized inside the cavity.

Our second focus has been to apply the technique of linearization about the temporal mean of the limit cycles, an approach which has been shown to describe nonlinear properties in many cases. More specifically, in many cases the real part of the leading eigenvalue is near zero (a property which would be described as marginal stability in the context of linearization about the base) and the imaginary part is near the nonlinear frequency of the limit cycles. The combination of these properties is called RZIF.

Based on this study and preceding ones, we can classify hydrodynamic configurations into three categories with respect to the RZIF property. The first is those for which the nonlinear frequencies deviate substantially from those resulting from linearization about the base flow, but are close to those resulting from linearization about the mean flow, and the mean flow growth rate is also very small. This category includes the cylinder wake (Barkley [4], Mantič-Lugo *et al.* [33], Mittal [42]), for which RZIF has been studied most extensively, as well as the traveling waves of thermosolutal convection (Turton *et al.* [61]), and the ribbons and spirals of counter-rotating Taylor-Couette flow (Bengana & Tuckerman [10]). In the second category, the nonlinear, base flow and mean flow frequencies are all different and the mean flow growth rate is not small, such as the standing waves of thermosolutal convection (Turton *et al.* [61]). In the third category, the difference between the nonlinear and the base flow frequencies and the base flow growth rate is already fairly low. This is what we find for the shear-driven cavity flow at the parameter values we have studied. The frequencies are primarily set by the geometry and the convection velocity. The nonlinear self-sustained mechanism distorts the base flow only slightly, leaving the convection velocity and hence the frequency almost unchanged. Linearization about the mean flow further and substantially reduces these already small differences. It would be useful to know a priori into which category a hydrodynamic configuration falls. Explanations in terms of traveling or standing waves (Bengana & Tuckerman [10], Turton *et al.* [61]) have not yet proved satisfactory or complete.

Because the shear-driven cavity flow in our Reynolds number range has two limit cycles, we can take the further step of computing other eigenmodes of the mean, which do not correspond to the limit cycle. We find that these eigenmodes mimic qualitatively the behavior of the limit cycles with respect to one other: as the Reynolds number is increased, the real part of one eigenvalue decreases from positive to negative for a limit cycle which undergoes stabilization via a secondary bifurcation, and increases from negative to positive for a cycle which undergoes destabilization. Further investigation, in the form of simulations of other hydrodynamic configurations, and more theoretical understanding, would be necessary to verify whether and when this is a systematic tendency. Another possible direction would be to generalize this type of analysis to quasiperiodic regimes, linearizing about the full temporal mean or else about some other quantity.

In summary, the existence of two competing limit cycles for shear-driven cavity flow has yielded both an interesting bifurcation diagram, containing features such as subcritical bifurcations, hysteresis and a quasiperiodic state. At the same time, the existence of two cycles has also extended the application and interpretation of linearization about the mean flow.

Acknowledgments

This work was performed using high performance computing resources provided by the Institut du Développement et des Ressources en Informatique Scientifique (IDRIS) of the Centre National de la Recherche Scientifique (CNRS), coordinated by GENCI (Grand Équipement National de Calcul Intensif), grants A0032A06362 and A0042A01119.

Bibliography

- [1] AIDUN, CYRUS K, TRIANTAFILLOPOULOS, NG & BENSON, JD 1991 Global stability of a lid-driven cavity with throughflow: Flow visualization studies. *Phys. Fluids A* **3** (9), 2081–2091. [21](#)
- [2] ÅKERVIK, E., BRANDT, L., HENNINGSON, D. S., HØEPFFNER, J., MARXEN, O. & SCHLATTER, P. 2006 Steady solutions of the Navier-Stokes equations by selective frequency damping. *Phys. Fluids* **18** (6), 068102. [24](#)
- [3] BARBAGALLO, ALEXANDRE, SIPP, DENIS & SCHMID, PETER J 2009 Closed-loop control of an open cavity flow using reduced-order models. *J. Fluid Mech.* **641**, 1–50. [21](#), [23](#), [33](#)
- [4] BARKLEY, D 2006 Linear analysis of the cylinder wake mean flow. *EPL (Europhys. Lett.)* **75** (5), 750. [22](#), [26](#), [43](#), [50](#)
- [5] BARKLEY, DWIGHT & HENDERSON, RONALD D 1996 Three-dimensional Floquet stability analysis of the wake of a circular cylinder. *J. Fluid Mech.* **322**, 215–241. [27](#)
- [6] BASLEY, JÉRÉMY, PASTUR, LR, LUSSEYRAN, FRANÇOIS, FAURE, TH M & DELPRAT, NATHALIE 2011 Experimental investigation of global structures in an incompressible cavity flow using time-resolved piv. *Exp. Fluids* **50** (4), 905–918. [21](#), [33](#)
- [7] BASLEY, J., PASTUR, L. R., DELPRAT, N. & LUSSEYRAN, F. 2013 Space-time aspects of a three-dimensional multi-modulated open cavity flow. *Phys. Fluids* **25**, 064105. [21](#), [33](#)
- [8] BENEDDINE, SAMIR, SIPP, DENIS, ARNAULT, ANTHONY, DANDOIS, JULIEN & LESSHAFFT, LUTZ 2016 Conditions for validity of mean flow stability analysis. *J. Fluid Mech.* **798**, 485–504. [22](#), [26](#)
- [9] BENGANA, Y. & TUCKERMAN, L.S. 2019 The self-consistent model and thermosolutal convection. *in preparation* . [22](#), [46](#)
- [10] BENGANA, Y. & TUCKERMAN, L.S. 2019 Spirals and ribbons in counter-rotating taylor-couette flow: frequencies from mean flows and heteroclinic orbits. *submitted* . [22](#), [50](#)
- [11] CHIEN, W-L, RISING, H & OTTINO, JM 1986 Laminar mixing and chaotic mixing in several cavity flows. *J. Fluid Mech.* **170**, 355–377. [21](#)

- [12] CUNHA, G, PASSAGGIA, P-Y & LAZAREFF, M 2015 Optimization of the selective frequency damping parameters using model reduction. *Phys. Fluids* **27** (9), 094103. [24](#)
- [13] DOUAY, CL, PASTUR, LR & LUSSEYRAN, FRANÇOIS 2016 Centrifugal instabilities in an experimental open cavity flow. *J. Fluid Mech.* **788**, 670–694. [21](#)
- [14] DUGUET, YOHANN, WILLIS, ASHLEY P & KERSWELL, RICH R 2008 Transition in pipe flow: the saddle structure on the boundary of turbulence. *J. Fluid Mech.* **613**, 255–274. [27](#)
- [15] EDWARDS, WS, TUCKERMAN, LAURETTE S, FRIESNER, RICHARD A & SORESENSEN, DC 1994 Krylov methods for the incompressible Navier-Stokes equations. *J. Comput. Phys.* **110** (1), 82–102. [25](#)
- [16] FANI, A, CITRO, V, GIANNETTI, F & AUTERI, F 2018 Computation of the bluff-body sound generation by a self-consistent mean flow formulation. *Phys. Fluids* **30** (3), 036102. [22](#)
- [17] FAURE, THIERRY M, ADRIANOS, PANAYOTIS, LUSSEYRAN, FRANÇOIS & PASTUR, LUC 2007 Visualizations of the flow inside an open cavity at medium range reynolds numbers. *Exp. Fluids* **42** (2), 169–184. [21](#)
- [18] FAURE, THIERRY M, PASTUR, LUC, LUSSEYRAN, FRANÇOIS, FRAIGNEAU, YANN & BISCH, DANIEL 2009 Three-dimensional centrifugal instabilities development inside a parallelepipedic open cavity of various shape. *Exp. Fluids* **47** (3), 395–410. [21](#)
- [19] FISCHER, P.F., LOTTES, J.W. & KERKEMEIR, S.G. 2008 Nek5000 Web pages. [Http://nek5000.mcs.anl.gov](http://nek5000.mcs.anl.gov). [24](#)
- [20] FORTIN, A, JARDAK, M, GERVAIS, JJ & PIERRE, R 1997 Localization of hopf bifurcations in fluid flow problems. *Int. J. Numer. Meth. Fluids* **24** (11), 1185–1210. [22](#)
- [21] GIORIA, RAFAEL DOS SANTOS, JABARDO, PAULO JOSÉ SAIZ, CARMO, BRUNO SOUZA & MENEGHINI, JULIO ROMANO 2009 Floquet stability analysis of the flow around an oscillating cylinder. *J. Fluids Struct.* **25** (4), 676–686. [27](#)
- [22] GLOERFELT, XAVIER 2009 Cavity noise. *VKI lecture series* **3**. [21](#)
- [23] HALL, KENNETH C, THOMAS, JEFFREY P & CLARK, WILLIAM S 2002 Computation of unsteady nonlinear flows in cascades using a harmonic balance technique. *AIAA J.* **40** (5), 879–886. [44](#)
- [24] HAMMOND, DA & REDEKOPP, LG 1997 Global dynamics of symmetric and asymmetric wakes. *J. Fluid Mech.* **331**, 231–260. [22](#)
- [25] HWANG, YONGYUN & COSSU, CARLO 2010 Linear non-normal energy amplification of harmonic and stochastic forcing in the turbulent channel flow. *J. Fluid Mech.* **664**, 51–73. [22](#), [26](#)

- [26] ITANO, TOMOAKI & TOH, SADAYOSHI 2001 The dynamics of bursting process in wall turbulence. *JPSJ* **70** (3), 703–716. [27](#)
- [27] JORDI, B E, COTTER, C J & SHERWIN, S J 2014 Encapsulated formulation of the selective frequency damping method. *Phys. Fluids* **26** (3), 034101. [24](#)
- [28] JORDI, B E, COTTER, C J & SHERWIN, S J 2015 An adaptive selective frequency damping method. *Phys. Fluids* **27** (9), 094104. [24](#)
- [29] KUZNETSOV, YU A 1998 *Elements of Applied Bifurcation Theory, Applied Mathematical Sciences*, vol. 112. New York: Springer. [32](#)
- [30] LOISEAU, J-CH & BRUNTON, S L 2018 Constrained sparse Galerkin regression. *J. Fluid Mech.* **838**, 42–67. [21](#)
- [31] LOPEZ, JUAN M, WELFERT, BRUNO D, WU, KE & YALIM, JASON 2017 Transition to complex dynamics in the cubic lid-driven cavity. *Phys. Rev. Fluids* **2** (7), 074401. [28](#)
- [32] MALKUS, W. V. R. 1956 Outline of a theory of turbulent shear flow. *J. Fluid Mech.* **1** (5), 521–539. [22](#)
- [33] MANTIČ-LUGO, VLADISLAV, ARRATIA, CRISTÓBAL & GALLAIRE, FRANÇOIS 2014 Self-consistent mean flow description of the nonlinear saturation of the vortex shedding in the cylinder wake. *Phys. Rev. Lett.* **113** (8), 084501. [22](#), [26](#), [46](#), [50](#)
- [34] MANTIČ-LUGO, VLADISLAV, ARRATIA, CRISTÓBAL & GALLAIRE, FRANÇOIS 2015 A self-consistent model for the saturation dynamics of the vortex shedding around the mean flow in the unstable cylinder wake. *Phys. Fluids* **27** (7), 074103. [22](#), [26](#), [46](#)
- [35] MARQUES, F, LOPEZ, JM & SHEN, J 2002 Mode interactions in an enclosed swirling flow: a double hopf bifurcation between azimuthal wavenumbers 0 and 2. *J. Fluid Mech.* **455**, 263–281. [32](#)
- [36] MAUREL, A, PAGNEUX, V & WESFREID, JE 1995 Mean-flow correction as non-linear saturation mechanism. *Europhys. Lett.* **32** (3), 217. [22](#)
- [37] MCKEON, BJ & SHARMA, AS 2010 A critical-layer framework for turbulent pipe flow. *J. Fluid Mech.* **658**, 336–382. [22](#), [27](#)
- [38] MCMULLEN, MATTHEW, JAMESON, ANTONY & ALONSO, JUAN 2006 Demonstration of nonlinear frequency domain methods. *AIAA J.* **44** (7), 1428–1435. [44](#)
- [39] MCMULLEN, MATTHEW S & JAMESON, ANTONY 2006 The computational efficiency of non-linear frequency domain methods. *J. Comput. Phys.* **212** (2), 637–661. [44](#)
- [40] MELIGA, PHILIPPE 2017 Harmonics generation and the mechanics of saturation in flow over an open cavity: a second-order self-consistent description. *J. Fluid Mech.* **826**, 503–521. [21](#), [22](#), [23](#), [30](#), [35](#), [36](#), [42](#), [46](#)
- [41] MELIGA, PHILIPPE, GALLAIRE, FRANÇOIS & CHOMAZ, JEAN-MARC 2012 A weakly nonlinear mechanism for mode selection in swirling jets. *J. Fluid Mech.* **699**, 216–262. [32](#)

- [42] MITTAL, SANJAY 2008 Global linear stability analysis of time-averaged flows. *Int. J. Numer. Meth. Fluids* **58** (1), 111–118. [22](#), [50](#)
- [43] MORRIS, P. J. 1976 The spatial viscous instability of axisymmetric jets. *J. Fluid Mech.* **77** (3), 511–529. [22](#)
- [44] PICELLA, F., LOISEAU, J.-CH., LUSSEYRAN, F, ROBINET, J.-CH., CHERUBINI, S. & PASTUR, L. 2018 Successive bifurcations in a fully three-dimensional open cavity flow. *J. Fluid Mech.* **844**, 855–877. [21](#)
- [45] PIER, BENOÎT 2002 On the frequency selection of finite-amplitude vortex shedding in the cylinder wake. *J. Fluid Mech.* **458**, 407–417. [22](#)
- [46] POLIASHENKO, MAXIM & AIDUN, CYRUS K 1995 A direct method for computation of simple bifurcations. *J. Comput. Phys.* **121** (2), 246–260. [22](#)
- [47] ROCKWELL, D 1977 Prediction of oscillation frequencies for unstable flow past cavities. *J. Fluids Eng.* **99** (2), 294–299. [21](#)
- [48] ROCKWELL, D & KNISELY, C 1980 Vortex-edge interaction: Mechanisms for generating low frequency components. *Phys. Fluids* **23** (2), 239–240. [35](#)
- [49] ROCKWELL, D & NAUDASCHER, ET 1978 Self-sustaining oscillations of flow past cavities. *J. Fluids Eng.* **100** (2), 152–165. [21](#), [30](#)
- [50] ROSSITER, JE 1964 Wind tunnel experiments on the flow over rectangular cavities at subsonic and transonic speeds. *Tech. Rep.*. Ministry of Aviation; Royal Aircraft Establishment; RAE Farnborough. [21](#), [22](#), [35](#), [49](#)
- [51] ROWLEY, CLARENCE W, COLONIUS, TIM & BASU, AMIT J 2002 On self-sustained oscillations in two-dimensional compressible flow over rectangular cavities. *J. Fluid Mech.* **455**, 315–346. [21](#)
- [52] SCHMID, P. J. 2010 Dynamic mode decomposition of numerical and experimental data. *J. Fluid Mech.* **656**, 5–28. [21](#)
- [53] SHANKAR, PN & DESHPANDE, MD 2000 Fluid mechanics in the driven cavity. *Annual review of fluid mechanics* **32** (1), 93–136. [21](#)
- [54] SIPP, DENIS & LEBEDEV, ANTON 2007 Global stability of base and mean flows: a general approach and its applications to cylinder and open cavity flows. *J. Fluid Mech.* **593**, 333–358. [21](#), [22](#), [23](#), [24](#), [26](#), [30](#), [35](#)
- [55] SIPP, DENIS, MARQUET, OLIVIER, MELIGA, PHILIPPE & BARBAGALLO, ALEXANDRE 2010 Dynamics and control of global instabilities in open-flows: a linearized approach. *Appl. Mech. Rev.* **63** (3), 030801. [21](#)
- [56] SMITH, JULIUS O. 2007 *Mathematics of the Discrete Fourier Transform (DFT)*. W3K Publishing. [30](#)
- [57] STUART, J. T. 1958 On the non-linear mechanics of hydrodynamic stability. *J. Fluid Mech.* **4** (1), 1–21. [22](#)

- [58] SYMON, SEAN, ROSENBERG, KEVIN, DAWSON, SCOTT TM & MCKEON, BEVERLEY J 2018 Non-normality and classification of amplification mechanisms in stability and resolvent analysis. *Phys. Rev. Fluids* **3** (5), 053902. [22](#), [27](#)
- [59] THEOFILIS, V, DUCK, PW & OWEN, J 2004 Viscous linear stability analysis of rectangular duct and cavity flows. *J. Fluid Mech.* **505**, 249–286. [21](#)
- [60] TIESINGA, G, WUBS, FW & VELDMAN, AEP 2002 Bifurcation analysis of incompressible flow in a driven cavity by the newton–picard method. *J. Comput. Appl. Math.* **140** (1-2), 751–772. [22](#), [32](#), [41](#), [49](#)
- [61] TURTON, SAM E, TUCKERMAN, LAURETTE S & BARKLEY, DWIGHT 2015 Prediction of frequencies in thermosolutal convection from mean flows. *Phys. Rev. E* **91** (4), 043009. [22](#), [26](#), [44](#), [46](#), [47](#), [50](#)
- [62] YAMOUNI, S., SIPP, D. & JACQUIN, L. 2013 Interaction between feedback aeroacoustic and acoustic resonance mechanisms in a cavity flow: a global stability analysis. *J. Fluid Mech.* **717**, 134–165. [21](#)
- [63] YU, YUNG H 1977 Measurements of sound radiation from cavities at subsonic speeds. *J. Aircr* **14** (9), 838–843. [21](#)
- [64] ZIELINSKA, BJA, GOUJON-DURAND, S, DUSEK, J & WESFREID, JE 1997 Strongly nonlinear effect in unstable wakes. *Phys. Rev. Lett.* **79** (20), 3893. [22](#)

Chapter 4

Spirals and ribbons: frequencies from mean flows and heteroclinic orbits

Yacine Bengana¹ and Laurette S. Tuckerman¹

¹Laboratoire de Physique et Mécanique des Milieux Hétérogènes (PMMH), CNRS; ESPCI Paris, PSL Research University; Sorbonne Université; Univ. Paris Diderot, France

Submitted to *Physical Review Fluids*

A number of time-periodic flows have been found to have a property called RZIF: when a linear stability analysis is carried out about the temporal mean (rather than the usual steady state), an eigenvalue is obtained whose **Real** part is **Zero** and whose **Imaginary** part is the nonlinear **Frequency**. For two-dimensional thermosolutal convection, a Hopf bifurcation leads to traveling waves which satisfy the RZIF property and standing waves which do not. We have investigated this property numerically for counter-rotating Couette-Taylor flow, in which a Hopf bifurcation gives rise to branches of upwards and downwards traveling spirals and ribbons which are an equal superposition of the two. In the regime that we have studied, we find that both spirals and ribbons satisfy the RZIF property. As the outer Reynolds number is increased, the ribbon branch is succeeded by two types of heteroclinic orbits, both of which connect saddle states containing two axially stacked pairs of axisymmetric vortices. One heteroclinic orbit is non-axisymmetric, with excursions that resemble the ribbons, while the other remains axisymmetric.

4.1 Introduction

A number of time-periodic flows have been found to have the following property: when a linear stability analysis is carried out about the temporal mean (rather than the usual steady state from which they bifurcate), an eigenvalue emerges whose imaginary part reproduces the frequency of the nonlinear oscillation and whose real part is near zero. This property was first discovered by Barkley [5] and extensively studied [16, 17, 19, 20, 22, 26] for the cylinder wake (for which it is strongly verified) and then for an open cavity [6, 18, 26] (for which it holds quite well, though not exactly). In these two-dimensional flows, a

horizontal velocity imposed at infinity is deviated as it encounters objects (a cylinder) or openings (a cavity) and, for sufficiently high Reynolds number, undergoes a Hopf bifurcation.

In Turton, Tuckerman & Barkley [28], this property was named RZIF – a mnemonic for the fact that the eigenvalue obtained by linearizing about the mean flow has a **Real** part of **Zero** and an **Imaginary** part which is the nonlinear **Frequency** – and was studied for a quite different kind of flow. Thermosolutal convection is driven by a vertical density gradient in a fluid mixture between two horizontal plates, which in turn is caused by imposed temperature and concentration differences at the two bounding plates. When the temperature and concentration have opposing effects on the density, instability is manifested as a Hopf bifurcation. In a two-dimensional domain with horizontally periodic boundary conditions, this is a classic case of the breaking of $O(2)$ symmetry (translations and reflection) and leads to the simultaneous formation of traveling and standing wave branches, at most one of which can be stable [13]. Turton et al. [28] discovered that the traveling waves in thermosolutal convection provide another clear realisation of the RZIF property, while the standing waves provide an equally clear counterexample: the real part of the eigenvalue obtained by linearizing about the mean part of the standing waves is far from zero and its imaginary part is far from the nonlinear frequency.

We have sought to continue this investigation on another pair of hydrodynamic traveling and standing waves. In Taylor-Couette flow, when only the inner cylinder rotates, a steady bifurcation leads to the classic Taylor vortices. In counter-rotating Taylor-Couette flow, however, these vortices are inclined to the rotation axis, and hence non-axisymmetric. A Hopf bifurcation then gives rise to branches of the well-known spirals [2, 14, 15] and the somewhat lesser-known ribbons [1, 7, 8, 9, 12, 23, 24, 25, 27], which, like standing waves, are an equal superposition of spirals moving axially upwards and downwards. As in [13, 28], this is a consequence of the breaking of $O(2)$ symmetry, here in the axial direction, when end effects are disregarded. Figure 4.1 shows the appearance of these two types of flows.

Counter-rotating Taylor-Couette flow has an additional symmetry when compared to the two-dimensional thermosolutal cases studied in [13, 28]. Along with the $O(2)$ axial z symmetry, the Taylor-Couette configuration has $SO(2)$ symmetry, consisting of rotations (not reflection) in the azimuthal θ direction. The tilted spirals or azimuthally tiled ribbons are not axisymmetric, and hence they break $SO(2)$ symmetry. In such cases, bifurcations always lead to states which rotate in the azimuthal direction; see e.g. [11]. Thus, although ribbons are standing waves in the axial direction, i.e. equal superpositions of axially-upwards and axially-downwards traveling waves, they rotate in the azimuthal direction, as do the spirals.

As the rotation velocity of the outer cylinder is varied, the ribbon branch is succeeded by two types of heteroclinic orbits, both of which connect saddle states consisting of two pairs of axisymmetric vortices. One heteroclinic orbit is non-axisymmetric, with excursions that resemble the ribbons, while the other remains axisymmetric.

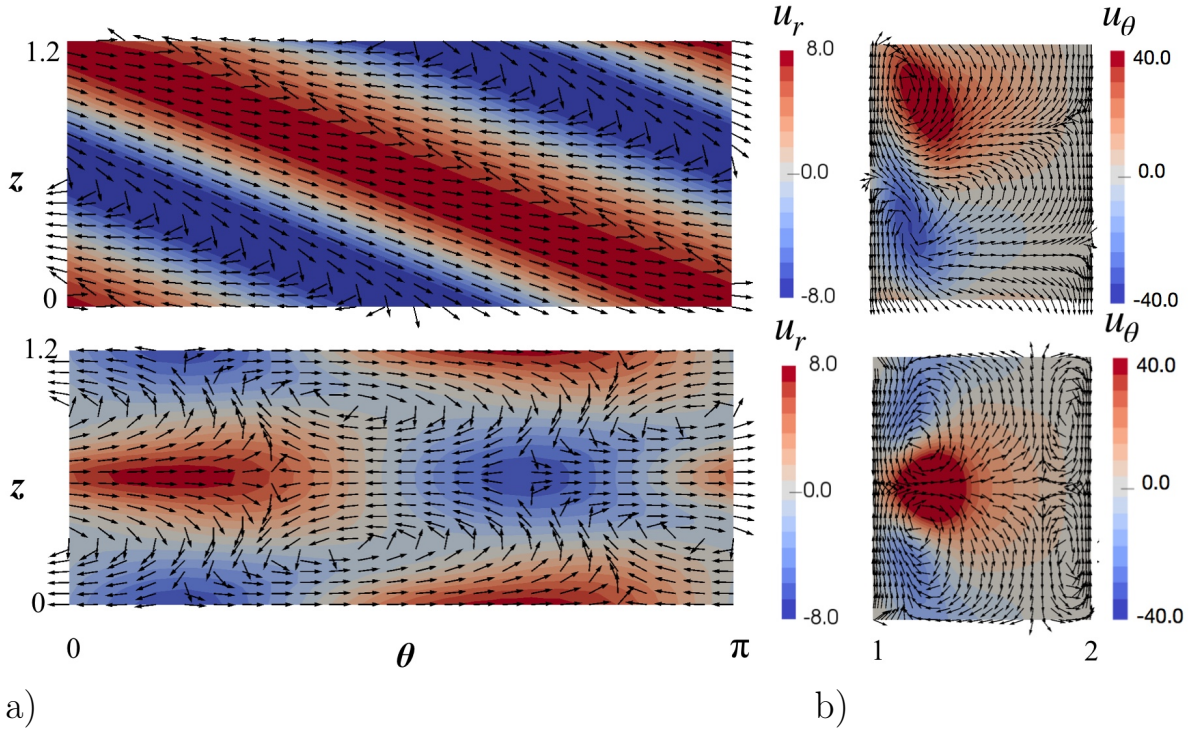


Figure 4.1 – Nonlinear spirals (top) and ribbons (bottom) at $Re = -550$. The deviation from laminar Couette flow is shown. Spirals of the opposite helicity exist and have identical properties but are not shown. a) (θ, z) velocity (arrows) with u_r (colors) at $r = 1.26$, near the maximum of the deviation from laminar Couette flow. b) (r, z) velocity (arrows) with u_θ (colors).

4.2 Methods

To investigate this problem numerically, we have used the spectral finite-difference code of Willis [10] to solve the Navier-Stokes equations in a cylindrical annulus,

$$\partial_t \mathbf{U} = -(\mathbf{U} \cdot \nabla) \mathbf{U} - \nabla P + \nabla^2 \mathbf{U} \quad (4.1a)$$

$$\nabla \cdot \mathbf{U} = 0 \quad (4.1b)$$

$$\mathbf{U} = \mathbf{e}_\theta Re_{\text{in}}, \mathbf{e}_\theta Re_{\text{out}} \quad \text{at } r_{\text{in}}, r_{\text{out}} \quad (4.1c)$$

where the length scale is $d \equiv r_{\text{out}} - r_{\text{in}}$ and the time scale is d^2/ν , where ν is the kinematic viscosity. The radius ratio is $\eta \equiv r_{\text{in}}/r_{\text{out}}$, the two Reynolds numbers are defined as $Re_j \equiv r_j \Omega_j d/\nu$ where $j = \text{in, out}$, and the numerical resolution is $(N_r, N_\theta, N_z) = (33, 16, 16)$.

We use the parameters in Pinter et al. [23, 24, 25], namely radius ratio $\eta \equiv r_{\text{in}}/r_{\text{out}} = 0.5$, inner Reynolds number $Re_{\text{in}} = 240$ and azimuthal wavenumber $M_0 = 2$ (azimuthal wavelength $2\pi/M_0 = \pi$). We have chosen the axial wavelength $\lambda_z = 1.2$, slightly less than the value studied intensively by [23, 24, 25] to avoid a secondary bifurcation they describe near the onset of spirals and ribbons for $\lambda_z = 1.3$. Because counter-rotating Taylor-Couette flow is centrifugally unstable only near the inner cylinder, here for $r \in [1, 1.24]$, the preferred axial wavelength is correspondingly less than that which would be expected if the vortices filled the gap. Because Re_{in} remains fixed and we will vary Re_{out} , we will simplify the notation by using Re instead of Re_{out} to designate the outer Reynolds number.

We have modified the Taylor-Couette code [10] in order to timestep the equations linearized

about a velocity field \mathbf{U} :

$$\partial_t \mathbf{u} = -(\mathbf{U} \cdot \nabla) \mathbf{u} - (\mathbf{u} \cdot \nabla) \mathbf{U} - \nabla p + \nabla^2 \mathbf{u} \quad (4.2a)$$

$$\nabla \cdot \mathbf{u} = 0 \quad (4.2b)$$

$$\mathbf{u} = 0 \quad \text{at } r_{\text{in}}, r_{\text{out}} \quad (4.2c)$$

Time-integration of the linearized equations (4.2) about a steady solution \mathbf{U} converges to the leading eigenvector, i.e. that whose corresponding eigenvalue has the most positive or least negative real part or growth rate. It is a means of carrying out the power method on the exponential of the right-hand-side of (4.2). Integration of (4.2) does not generally lead to a steady or periodic state, since the nonlinear terms which would otherwise saturate the amplitude is absent. Instead, it leads to states whose amplitude increases or decreases, but with a constant growth rate and frequency, in the case of a complex eigenvalue.

We first use the linearized code to compute the Hopf bifurcation threshold from laminar Couette flow. For various timesteps Δt , we calculate the growth rate σ as a function of Re and then use linear extrapolation or interpolation to find Re_c such that $\sigma(Re_c) = 0$. (This procedure circumvents critical slowing down and so finds bifurcation thresholds faster and more accurately than could be done with nonlinear simulations.) The bifurcation thresholds calculated using $\Delta t = 10^{-4}$, 10^{-5} , and 10^{-6} are, respectively, $Re_c = -595.23$, $Re_c = -586.65$, $Re_c = -585.42$, the last of which we consider to be the converged value. (For greater legibility and simplicity, in what follows we cite its truncated value -585 .)

The branches of spirals and ribbons illustrated in figure 4.1 bifurcate at $Re \approx -585$ towards increasing Re . Their functional form is:

$$\begin{aligned} u^{\text{SPI}\pm}(r, \theta, z, t) &= \sum_m \hat{\mathbf{u}}_m(r) e^{im(z/\lambda_z \pm M_0\theta - \omega_{\text{SPI}}t)} \\ u^{\text{RIB}}(r, \theta, z, t) &= \sum_{k,m} \left\{ \begin{array}{l} \hat{u}_{km,r}(r) \mathbf{e}_r \sin(kz/\lambda_z) \\ \hat{u}_{km,\theta}(r) \mathbf{e}_\theta \sin(kz/\lambda_z) \\ \hat{u}_{km,z}(r) \mathbf{e}_z \cos(kz/\lambda_z) \end{array} \right\} e^{im(M_0\theta - \omega_{\text{RIB}}t)} \end{aligned} \quad (4.3)$$

The spirals are traveling waves: they depend on z , θ , and t only via the single combination $z/\lambda_z + M_0\theta - \omega_{\text{SPI}}t$. The ribbons have fixed axial nodal lines and are reflection symmetric; the axis of symmetry is $z = \lambda_z/2$ in equation (4.3) and in figure 4.1. The ribbons are traveling waves in θ : they depend on θ and t via $M_0\theta - \omega_{\text{RIB}}t$. Many other complex and esthetic symmetry-breaking flows have been observed in numerical simulations of this configuration [1, 8, 12, 23, 24, 25], including cross-spirals, oscillating cross spirals, mixed cross spirals and mixed ribbons.

We will use numerical simulations of the nonlinear and linearized equations (4.1) and (4.2) to investigate the RZIF phenomenon mentioned in the introduction, in which linearization about the mean flow of a periodic solution yields an eigenvalue whose **Real** is **Zero** and whose **Imaginary** part which is the nonlinear **Frequency**. To do so, we will calculate the spirals and ribbons by time integrating the nonlinear equations (4.1) until an asymptotic state is reached. Because the spirals and ribbons are both azimuthally traveling waves, their temporal means are identical with their azimuthal means which are, in turn, the axisymmetric ($m = 0$) components of (4.3). We will then find the eigenvalues and

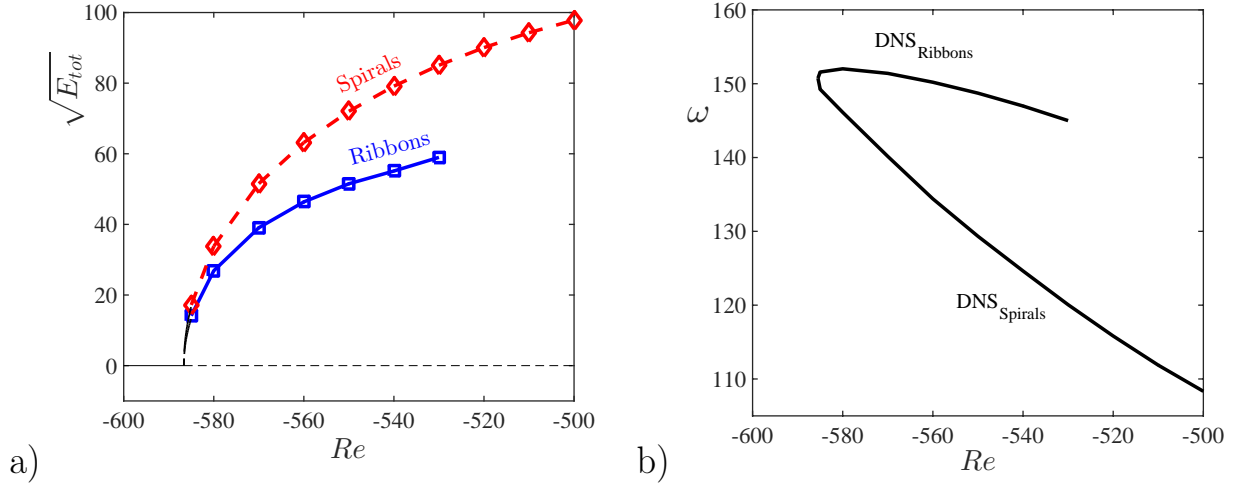


Figure 4.2 – a) Bifurcation diagram for spirals and ribbons. Square root of kinetic energy of the deviation from laminar Couette flow is shown as a function of Re . The ribbons are stable where shown, while the spirals are calculated by using a spiral initial condition. b) Frequencies of spiral and ribbon states as a function of Re .

eigenvectors about the resulting mean flows by integrating equations (4.2).

4.3 RZIF analysis

We begin by showing the bifurcation diagram for spirals and ribbons. Their common threshold is $Re \approx -585$. On figure 4.2a, we represent the square root of kinetic energy of the two branches. In this parameter range, the spirals are unstable to ribbons, but can be computed by including only $k = m$ modes or, like [23], by setting the $m = 0$ component of u_r to zero. The ribbons themselves become unstable for $Re \gtrsim -530$. Figure 4.2b shows the frequency of the nonlinear spirals and ribbons (symbols), as well as those obtained by linearizing about laminar Couette flow (dashed line). Linearization about the laminar flow leads to the same set of eigenvalues for spirals or ribbons, since the eigenvectors corresponding to upgoing and downgoing spirals are related by symmetry, with their superposition leading to ribbons. For a supercritical Hopf bifurcation, these necessarily match the frequency of the nonlinear branches at the threshold. As Re is increased, the frequencies of the nonlinear spirals deviate greatly from those derived from the laminar flow, but the frequencies of the nonlinear ribbons remain close. This was also true of the standing waves of thermosolutal convection [28], which inspired this study: the frequencies of the nonlinear standing waves were much closer to those obtained by linearization about the laminar (conductive) flow than were the frequencies of the nonlinear traveling waves.

Figure 4.3 shows the temporal means of the nonlinear spiral and ribbon states shown in figure 4.1 at $Re = -550$. Since spirals are traveling waves in both the θ and the z direction, their temporal means are equivalent to their spatial means and have no dependence on either direction. Ribbons are traveling waves in the θ direction and so their means have no θ dependence. We set \mathbf{U} in the linearized equations (4.2) to the mean flows of spirals or ribbons shown in figure 4.3 and initialize \mathbf{u} with fields of the spiral or ribbon form, respectively. We then integrate until the growth rate and the frequency are constant. The resulting field $\mathbf{u}(t)$ then cycles between the real and imaginary parts of the eigenvector

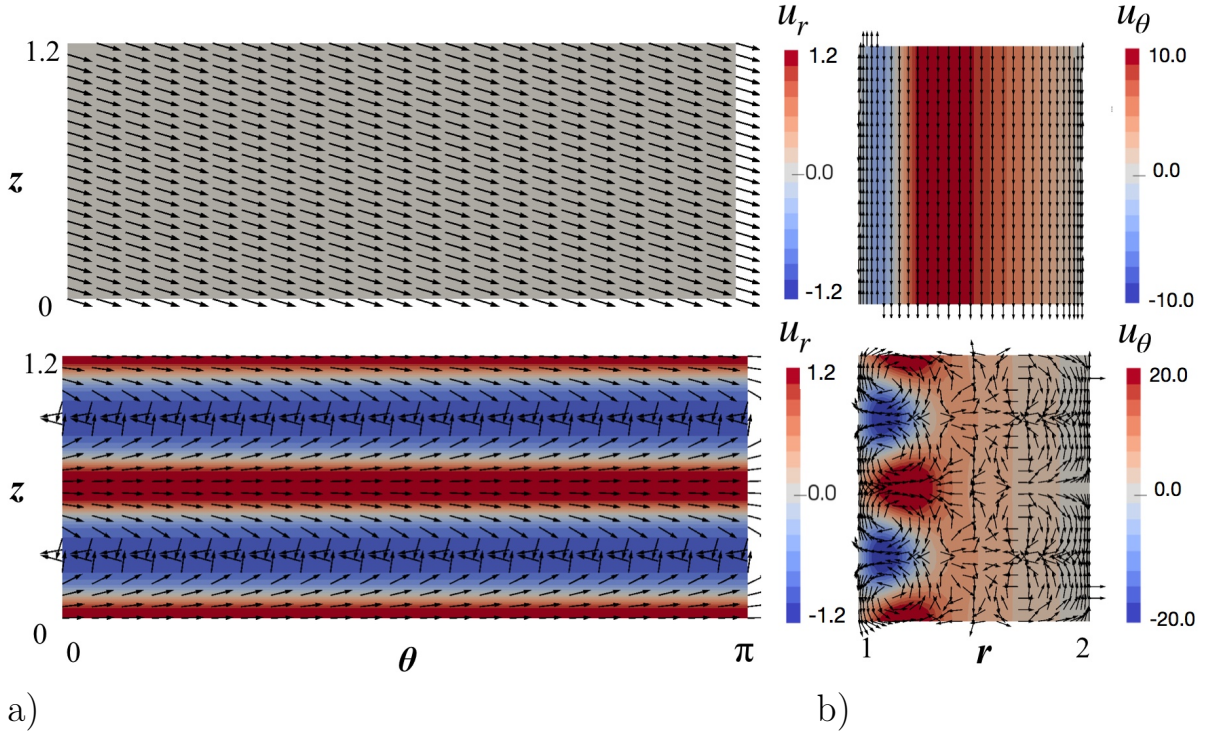


Figure 4.3 – Mean flow of spirals (top) and ribbons (bottom) at $Re = -550$. The deviation from laminar Couette flow is shown. a) (θ, z) velocity (arrows) with u_r (colors) at $r = 1.26$, near the maximum of the deviation from laminar Couette flow. b) (r, z) velocity (arrows) with u_θ (colors). Since the spirals are traveling waves in the θ and z directions, their means have no dependence on either. The ribbons are traveling waves in θ and hence their mean is axisymmetric.

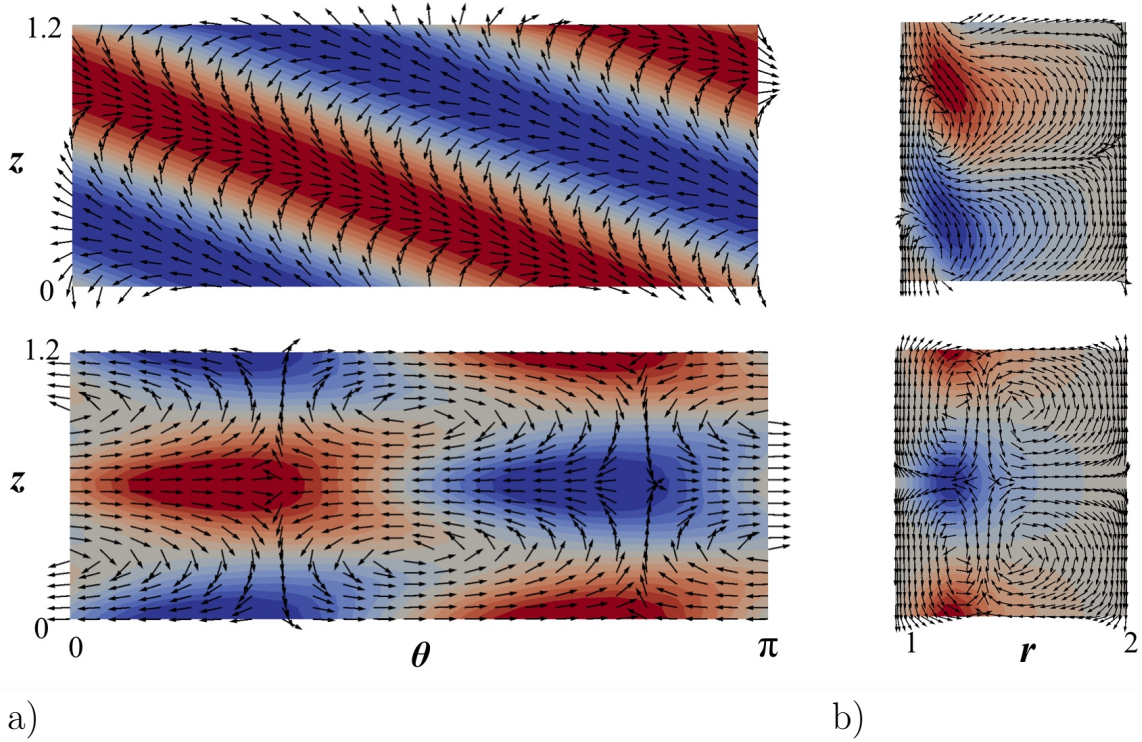


Figure 4.4 – Eigenvectors resulting from linearization about mean flow of spirals (top) and ribbons (bottom) at $Re = -550$. a) (θ, z) velocity (arrows) with u_r (colors) at $r = 1.26$. b) (r, z) velocity (arrows) with u_θ (colors). These eigenvectors resemble the deviation of nonlinear spirals and ribbons from the laminar Couette flow as well as the eigenvectors of spiral and ribbon form obtained from linearizing about the laminar flow.

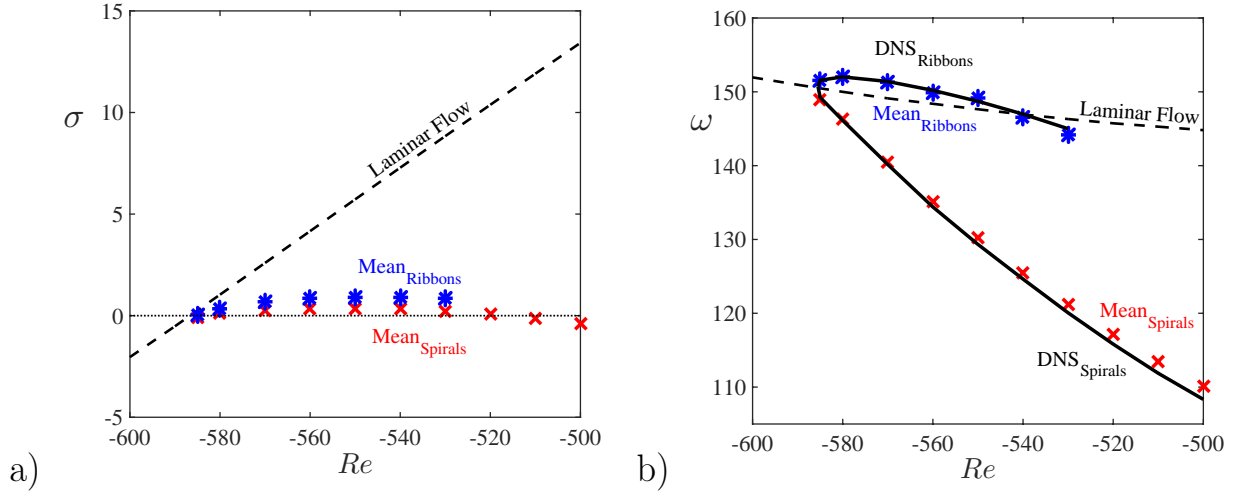


Figure 4.5 – Growth rates (a) and frequencies (b). Results from nonlinear numerical simulations (black curves) and from Navier-Stokes equations linearized about the laminar flow (dashed lines), about the mean flow of spirals (red crosses), and about the mean flow of ribbons (blue stars). Satisfaction of the RZIF property for the frequencies is demonstrated by the agreement between the red crosses and the black curve for spirals and between the blue stars and the black curve for ribbons. Satisfaction of the RZIF property for the growth rates is demonstrated by the fact that the blue stars and the red crosses are near zero.

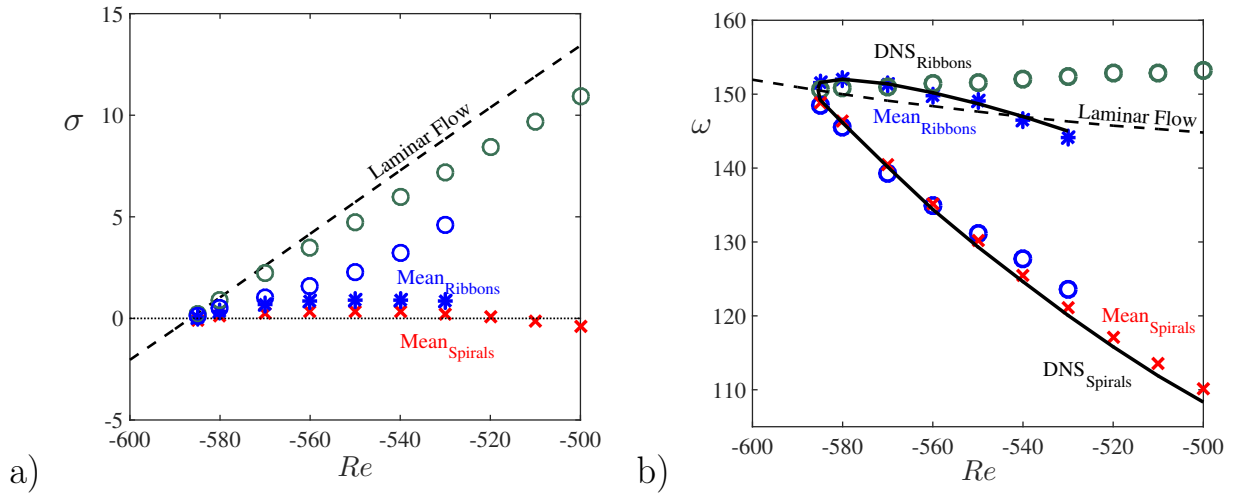


Figure 4.6 – Same as figure 4.5 with additional eigenvalues. The hollow circles are eigenvalues corresponding to spiral eigenvectors. The dark green circles (upper set) are obtained by linearizing around a mean spiral flow whose orientation is opposite to that of the eigenvector while the blue ones (lower set) are obtained by linearizing around the mean flow of a ribbon.

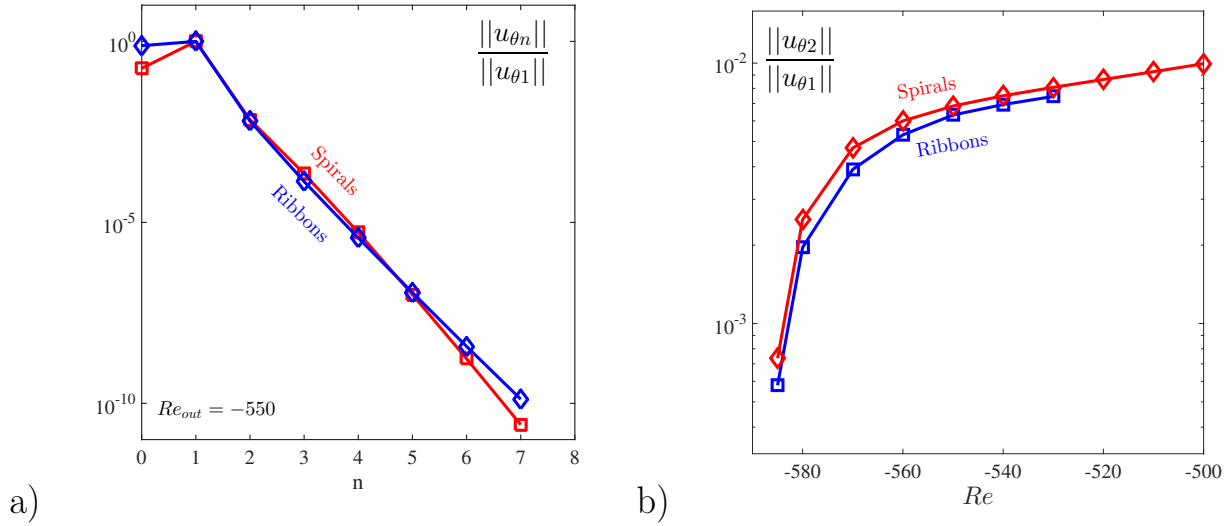


Figure 4.7 – Spectra of spirals and ribbon states. a) Full spectrum for states at $Re = -550$, normalized by amplitude of fundamental frequency. b) Ratio of second harmonic to fundamental frequency.

which here are related by a spatial shift. Figure 4.4 shows samples of these eigenvectors. These greatly resemble the deviations of the corresponding nonlinear flows from laminar Couette flow shown in figure 4.1 and resemble even more the usual eigenvectors of spiral and ribbon form resulting from linearization about laminar Couette flow.

Figure 4.5 presents the main result of this section, namely that both the spirals and the ribbons satisfy the RZIF property. The growth rates or real parts of eigenvalues are shown in figure 4.5a and the frequencies or imaginary parts are shown in figure 4.5b. The solid curves show the frequencies obtained from nonlinear simulations. Linearization about the mean flows of spirals (red crosses) or of ribbons (blue stars) lead to eigenvalues whose imaginary parts agree with the nonlinear frequencies. The corresponding growth rates are seen to be near zero, i.e. the mean flows are nearly marginally stable. (This has no relation to the marginal stability of the full spirals or ribbons to shifted versions of themselves, which arises from their θ or z dependence in a homogeneous domain.) Thus, both the spirals and the ribbons satisfy the RZIF property. This contrasts with the thermosolutal case, in which the traveling waves satisfied the RZIF property, while the standing waves did not.

Additional eigenvalues are shown in figure 4.6, which are not related to the basic RZIF property. Both correspond to spiral eigenvectors and have positive growth rates. These show the frequency and growth rate of spiral eigenvectors superposed on the mean flow of spirals of opposite helicity (dark green circles) or of ribbons (blue circle). The positive growth rate for the spirals of opposite chirality could be related to the linear instability of the spirals to ribbons; such a transition would take place via the addition of spirals of opposite chirality until equal amplitudes are reached. However, for these parameter values, ribbons show no tendency to make a transition to spirals, and yet the growth rates from the mean flow of ribbons to spirals are also positive (although less so than the growth rates from the mean flow of spirals). More understanding of the meaning of linearization about mean flows would be necessary to interpret these eigenvalues.

The RZIF property is implied by a near-monochromatic spectrum, as shown in [28] as follows. Consider the evolution equation

$$\partial_t \mathbf{U} = \mathcal{L}\mathbf{U} + \mathcal{N}(\mathbf{U}, \mathbf{U}) \quad (4.4)$$

where \mathcal{L} is linear and $\mathcal{N}(\cdot, \cdot)$ is a quadratic nonlinearity. Let

$$\mathbf{U} = \bar{\mathbf{U}} + \sum_{n \neq 0} \mathbf{u}_n e^{in\omega t} \quad (4.5)$$

(with $\mathbf{u}_{-n} = \mathbf{u}_n^*$) be the temporal Fourier decomposition of a periodic solution to (4.4) with mean $\bar{\mathbf{U}}$ and frequency ω . The $n = 1$ component of (4.4) is

$$\begin{aligned} i\omega \mathbf{u}_1 = & \underbrace{\mathcal{L}\mathbf{u}_1 + \mathcal{N}(\bar{\mathbf{U}}, \mathbf{u}_1) + \mathcal{N}(\mathbf{u}_1, \bar{\mathbf{U}})}_{\mathcal{L}_{\bar{\mathbf{U}}}\mathbf{u}_1} \\ & + \underbrace{\mathcal{N}(\mathbf{u}_2, \mathbf{u}_{-1}) + \mathcal{N}(\mathbf{u}_{-1}, \mathbf{u}_2) + \mathcal{N}(\mathbf{u}_3, \mathbf{u}_{-2}) + \mathcal{N}(\mathbf{u}_{-2}, \mathbf{u}_3) + \dots}_{\mathcal{N}_1} \end{aligned} \quad (4.6)$$

If, as is often the case, $\|\mathbf{u}_n\| \sim \epsilon^{|n|}$, then $\mathcal{N}_1 = O(\epsilon^3)$ may be neglected and RZIF is satisfied: the linear operator $\mathcal{L}_{\bar{\mathbf{U}}}$ in (4.6) has the pure imaginary eigenvalue $i\omega$, corresponding to the frequency of the periodic solution. Hence the RZIF property is satisfied for near-monochromatic oscillations in any system with a quadratic nonlinearity.

It remains to verify whether these periodic solutions are near-monochromatic. Figure 4.7 shows the temporal Fourier spectra of the azimuthal velocity for the spirals and the ribbons. For the thermosolutal case of [28], the ratio $\|u_2\|/\|u_1\|$ was found to be much higher for the standing waves (greater than about 10^{-1}) than for the traveling wave branch (between 10^{-3} and about 10^{-1}), explaining the satisfaction of RZIF for the traveling waves and not for the standing waves. In contrast, for this counter-rotating Taylor-Couette case, figure 4.7 shows that the temporal spectra for spirals and ribbons are quite similar. The ratio $\|u_2\|/\|u_1\|$ is consistently less than 10^{-2} for both flows over the range of our investigation. This is consistent with the fact that RZIF is satisfied for both flows.

4.4 Heteroclinic orbits

Pinter et al. [23, 24, 25] observed that the ribbon branch became unstable and was succeeded by oscillating cross-spirals as Re was increased. We observe this as well, near $Re \approx -525$. As Re is further increased, however, the oscillating cross-spirals are themselves succeeded by a near-heteroclinic orbit, in which the system spends the overwhelming majority of its time in one of two saddles containing two pairs of axisymmetric vortices. The two saddles differ by a quarter of an axial period (one vortex). The system passes from one to the other via rapid non-axisymmetric excursions resembling the ribbon states. Snapshots of the phases of an excursion taken from a heteroclinic cycle at $Re = -502$ are shown in figure 4.8.

Figure 4.9a shows timeseries from this heteroclinic orbit. Time spent at the two saddles are seen as two plateaus. The approaches to and departures from the saddles are oscillatory; this appears clearly in the enlarged timeseries as well as in the spirals of the phase portrait

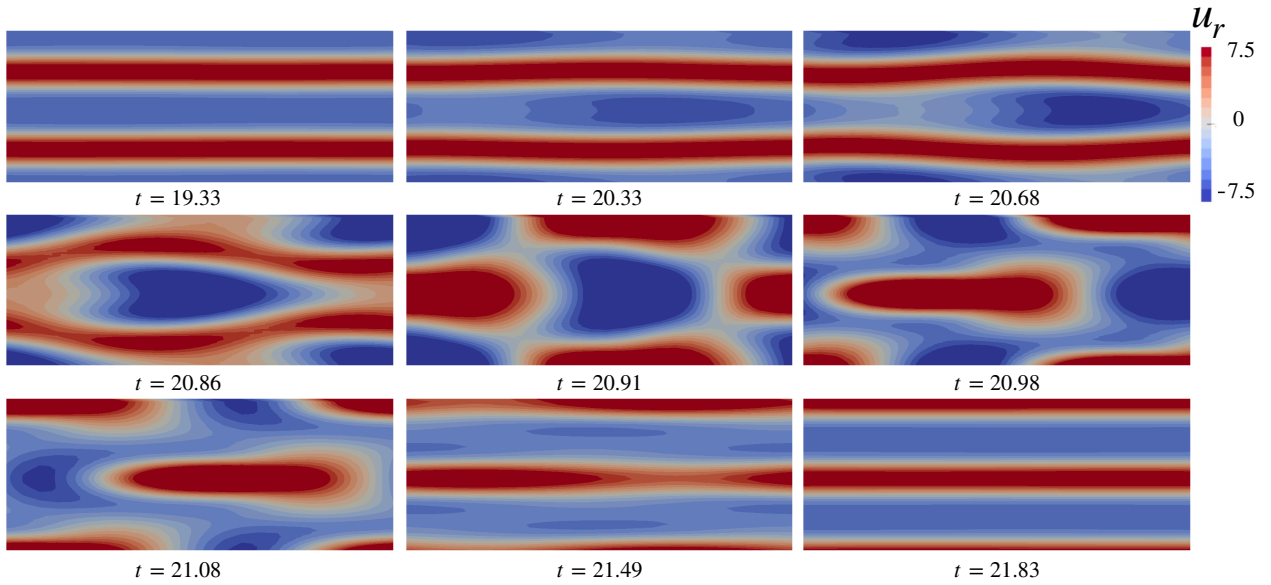


Figure 4.8 – Non-axisymmetric heteroclinic cycle at $Re = -502$. Colors show the radial velocity in a (θ, z) slice at $r = 1.26$. The first (top left) and last (bottom right) visualizations show the saddles which anchor the heteroclinic cycles. These contain two pairs of axisymmetric vortices and differ by an axial phase shift of a single vortex. The visualizations between the two illustrate the excursion or rapid transition between the two saddles, via states which resemble ribbons.

of figure 4.10a. In the phase portrait, the two saddles are distinguished, and the spiraling approaches to them are approximately perpendicular to one another. In the timeseries at the bottom of figure 4.9, the energy in the non-axisymmetric modes is seen to increase and to decrease logarithmically.

As Re is further increased, this regime is succeeded by another type of heteroclinic orbit, visualized in figure 4.11. Timeseries for this cycle are shown in figure 4.9b for $Re = -490$. The two plateaus are the same as for the previous heteroclinic cycle, but the approaches to and departures from the saddles are not oscillatory. These approaches and departures differ from excursion to excursion, as highlighted in the enlargements. The difference between the excursions is also seen in the phase portraits in figure 4.10b, which begins with a transient oscillatory phase. The black dots in the phase portrait are equally spaced in time and so accumulate on the saddles. Trajectories are seen approaching and leaving the saddles along different paths at different angles. Turning to the logarithmic energy timeseries, after an initial transient (corresponding to the oscillatory transient in the phase portrait), the energy in the non-axisymmetric modes becomes and remains very small. Instead, it is the energy in the odd axial wavenumber modes which tracks the heteroclinic cycle. Since the saddles contain two stacked pairs of vortices, their axial Fourier spectrum contain only even multiples of the fundamental wavenumber $2\pi/\lambda_z$. Excursions are manifested by the logarithmic increase and decrease of the energy contained in odd multiples of $2\pi/\lambda_z$ in the axial spectrum. The variation from cycle to cycle is also seen in the logarithmic timeseries.

The axisymmetric heteroclinic cycle is very similar to that observed in the 1:2 mode-interaction [3, 21]. An erratic alternation between a few different types of excursions is also seen in the cycles of [21]. As explained in these references, this cycle is a consequence of the interaction of axial modes with wavenumbers $2\pi/\lambda_z$ and $4\pi/\lambda_z$. Furthermore, the heteroclinic orbits can be characterized quantitatively by calculating the rates of approach

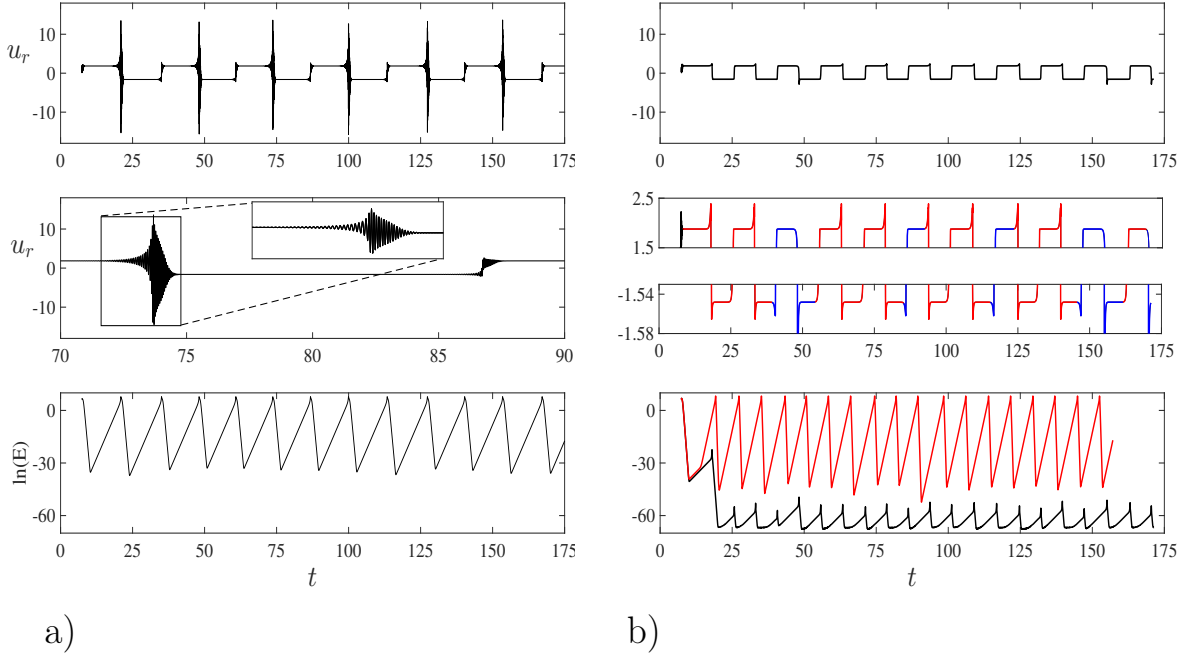


Figure 4.9 – Timeseries for a) oscillatory and non-axisymmetric heteroclinic cycle at $Re = -502$ and for b) non-oscillatory and axisymmetric heteroclinic cycle at $Re = -490$. Top: complete timeseries alternating between two plateaus. Middle: enlargements of timeseries. a) enlargement of a single period from a non-axisymmetric cycle, with further enlargement around the excursion. The differences between the growth/decay rates and frequencies during the spiralling approach and departure are clear. b) enlargements near the peaks of the excursions, highlighting their variation. Bottom: Logarithmic plot of energy, which grows and decays exponentially. The non-axisymmetric energy is shown in black and, for the axisymmetric heteroclinic cycle, the energy corresponding to axisymmetric but axially antisymmetric modes is shown in red. Both types of heteroclinic cycles have the same plateaus, up to numerical roundoff.

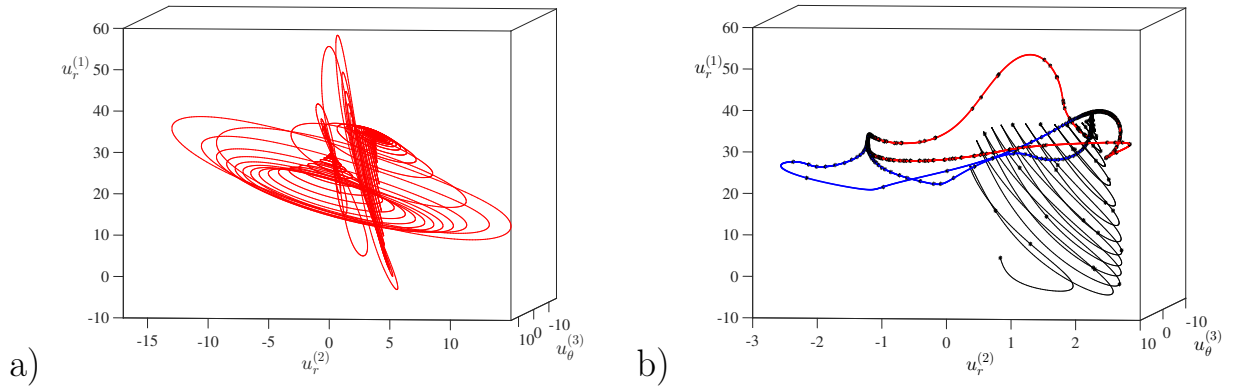


Figure 4.10 – a) Phase portraits for a) oscillatory heteroclinic cycle at $Re = -502$ and for b) non-oscillatory heteroclinic cycle at $Re = -490$ using $u_r(r = 1.2, \theta = 0, z = 0)$, $u_r(r = 1.2, \theta = \pi/3, z = \lambda_z/3)$, and $u_\theta(r = 1.2, \theta = 2\pi/3, z = 2\lambda_z/3)$ corresponding to timeseries in figure 4.9. The trajectory in the oscillatory heteroclinic cycle spirals inwards along one curved surface and outwards along a perpendicular curved surface. Non-oscillatory phase portrait begins with a spiralling transient, then follows different paths into and out of the saddles. The color coding (blue and red) of these paths matches that in the timeseries, where can be seen subtle differences between the excursions. The saddles for the two cycles are the same; note the different scale for $u_r^{(2)}$ between (a) and (b).

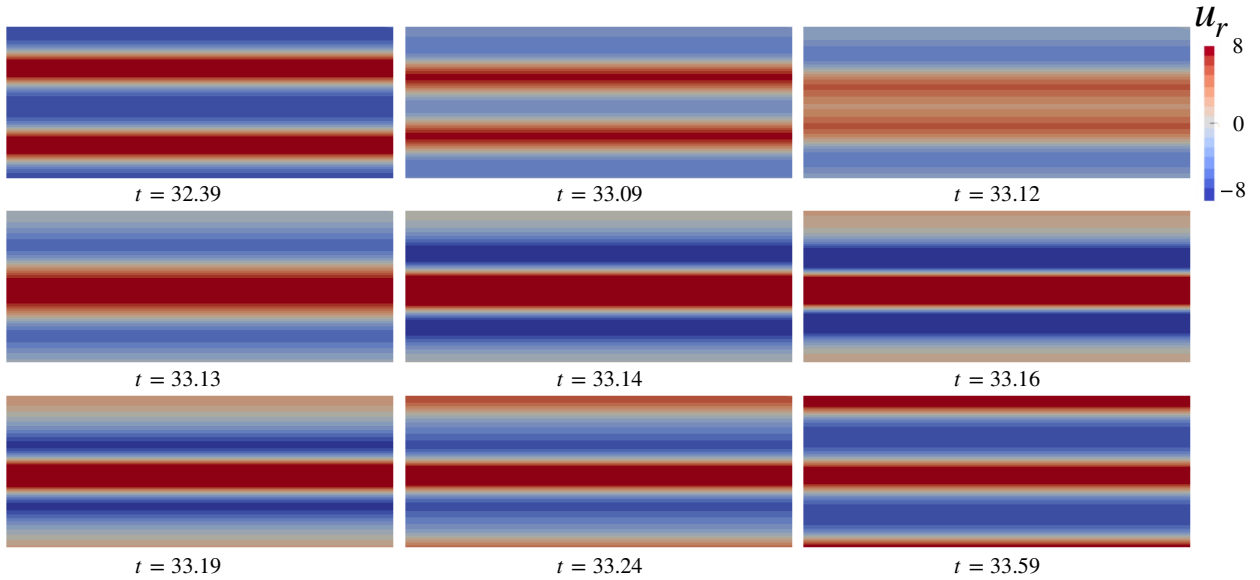


Figure 4.11 – Axisymmetric heteroclinic cycle at $Re = -490$. Colors show the radial velocity in a (θ, z) slice at $r = 1.26$. The first (top left) and last (bottom right) visualizations show the saddles which anchor the heteroclinic cycles. These contain two pairs of axisymmetric vortices and differ by an axial phase shift of a single vortex. For this heteroclinic cycle, the states remain axisymmetric throughout the rapid transition between the two saddles.

and departure from the saddles which anchor the heteroclinic orbits. These are the two leading eigenvalues (in the axisymmetric subspace) of the saddles and are seen as the slopes of the black curve in the logarithmic timeseries in figure 4.9b. We plot these as a function of Re in figure 4.12b. The existence of the heteroclinic cycle requires eigenvalues of opposite signs; thus, the axisymmetric cycle exists for $Re > -502$, where one of the leading eigenvalues becomes positive while the other remains negative. Stability of the cycle requires that the rate of departure be no greater than the rate of approach, i.e. the absolute value of the negative eigenvalue must exceed the positive eigenvalue. This occurs for $Re < -482$. Hence the axisymmetric cycle exists and is stable within this axisymmetric subspace in the range $Re \in [-502, -482]$.

The theory in [3, 21] does not concern oscillatory heteroclinic cycles or complex eigenmodes. However, assuming that the analysis of the oscillatory cycles is similar to that of the non-oscillatory cycles, we plot the slopes (or real parts of the eigenvalues) seen in the logarithmic timeseries of figure 4.9a as a function of Re . We also plot the frequencies associated with these eigenvalues in figure 4.13a, associated with the oscillations in the timeseries in figure 4.9a and the spiraling in and out in the phase portraits of figure 4.10a. Using the same criteria as for the non-oscillatory cycles, figure 4.12a shows that the oscillatory heteroclinic cycle exists and is stable within the subspace of these eigendirections for $Re \in [-522, -476]$.

The theory in [3, 21] also does not address the relative stability of two kinds of heteroclinic cycles. The transition that we observe when Re is reduced from -502 to -490 implies that the non-axisymmetric heteroclinic cycles is unstable to the axisymmetric one at this value of Re . In fact, we observe non-axisymmetric heteroclinic cycles for $Re < -496$ and axisymmetric cycles for $Re > -496$, separated by the point at which axisymmetric and non-axisymmetric departure rates cross, as seen in figure 4.13b. This supports the idea that the cycle whose departure rate from the saddles is smaller is unstable to the cycle

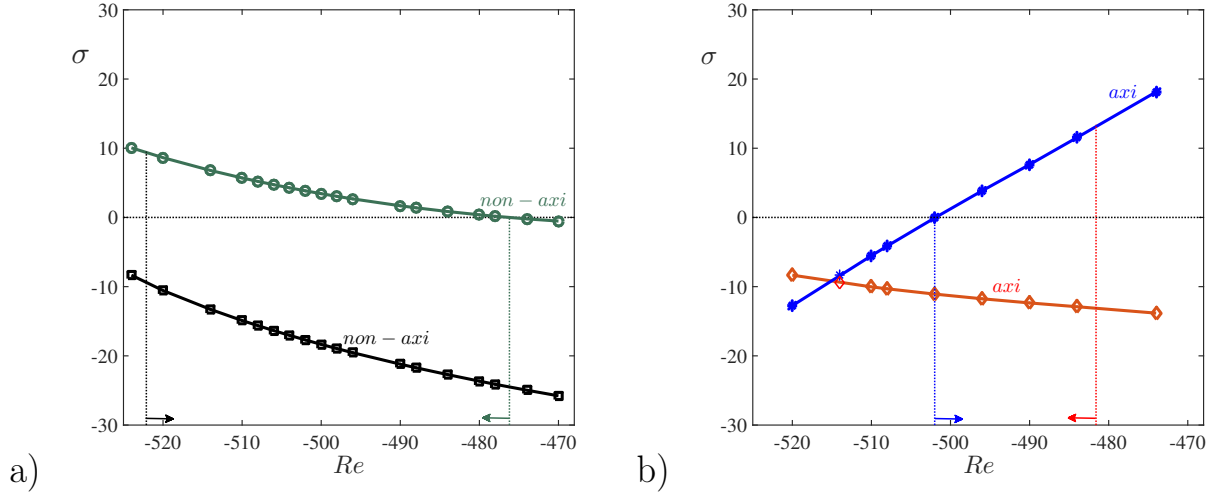


Figure 4.12 – Rate of approach to and departure from saddles as a function of Re . These are the slopes of the logarithmic plots of figure 4.9 and also the real parts of the leading eigenvalues. a) Non-axisymmetric oscillatory heteroclinic cycle. The cycle exists when the eigenvalues are of opposite sign, here for $Re < -476$. The cycle is stable within the space of these eigenmodes when the rate of approach exceeds the rate of departure, here for $Re > -522$. b) Axisymmetric non-oscillatory heteroclinic cycle. The cycle exists when the eigenvalues are of opposite sign, here for $Re > -502$. The cycle is stable within the space of these eigenmodes when the rate of approach exceeds the rate of departure, here for $Re < -482$.

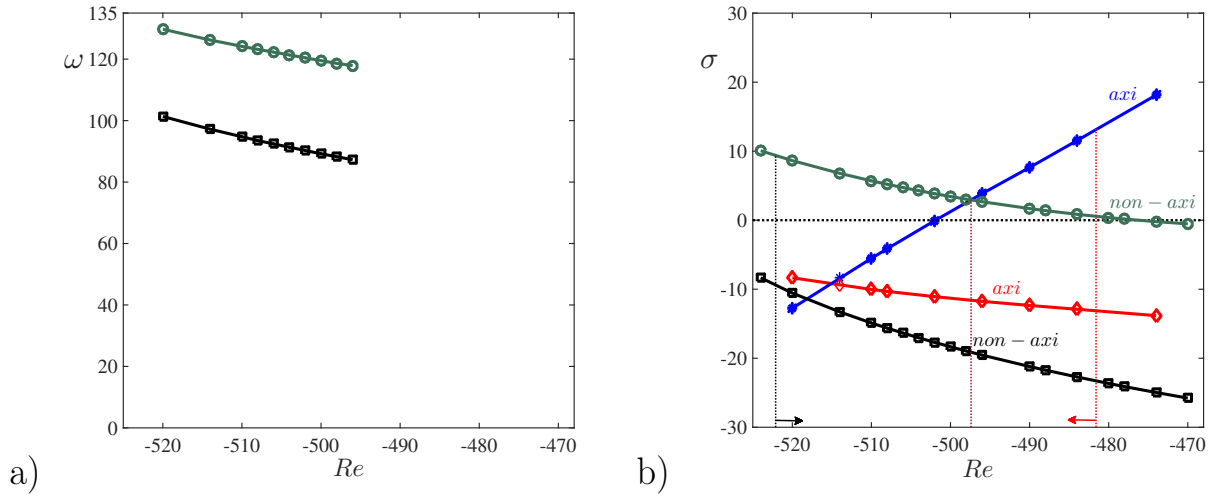


Figure 4.13 – a) Imaginary parts of eigenvalues involved in non-axisymmetric oscillatory heteroclinic cycle. b) Real parts of eigenvalues involved in both heteroclinic cycles, axisymmetric and non-axisymmetric. Non-axisymmetric cycles are observed for $Re < -496$, when the largest eigenvalue (departure rate, dark green circles) corresponds to a non-axisymmetric eigenpair. Axisymmetric cycles are observed for $Re > -496$, when the largest eigenvalue (blue stars) corresponds to an axisymmetric eigenvector. The other endpoints of the stability ranges, shown as the black rightwards and red leftwards arrows, involve the next-to-largest eigenvalues (rates of approach, red diamonds and black squares); see figure 4.12 and its caption. Summarizing, the stability range of the non-axisymmetric cycle is $Re \in [-522, -496]$, while that of the axisymmetric cycle is $Re \in [-496, -482]$, which matches our observations.

whose departure rate is greater [4]. Combining all of the criteria, the stability range of the non-axisymmetric cycle is $Re \in [-522, -496]$, while that of the axisymmetric cycle is $Re \in [-496, -482]$.

4.5 Discussion

The problem of characterizing the nonlinear frequency of a periodic flow away from the threshold has led to one proposed solution: when a linear stability analysis is carried out about the temporal mean, an eigenvalue is obtained whose **Real** part is **Zero** and whose **Imaginary** part is the nonlinear **Frequency**. This RZIF property has heretofore been studied for the cylinder wake, an open cavity, and thermosolutal convection. It is strongly satisfied for the cylinder wake and the traveling waves of thermosolutal convection with oppositely directed density gradients, weakly satisfied for the open cavity, and not at all satisfied for the standing waves of thermosolutal convection. Although the RZIF property is a natural outcome of a near-monochromatic temporal spectrum, it is not entirely clear when this occurs.

We have investigated RZIF in another configuration, counter-rotating Taylor-Couette flow, which, like the thermosolutal convective case, has a Hopf bifurcation leading to branches of traveling and standing waves, here manifested as spirals and ribbons. In the thermosolutal case, the traveling waves display the RZIF property and have a temporal Fourier spectrum which is highly peaked, while the standing waves do not. Here, both the spirals and the ribbons display the RZIF property and both have temporal spectra which are equally peaked. However, the ribbons are standing waves only in the axial direction and are traveling waves in the azimuthal direction. This may be the cause of the difference between the Taylor-Couette and thermosolutal cases. The search for another counter-example to RZIF, especially in a purely hydrodynamic flow without additional fields, remains open.

During the course of our investigation, we discovered two heteroclinic cycles, one non-axisymmetric and the other axisymmetric. Both cycles are anchored by the same saddles: axisymmetric states containing two axially stacked pairs of vortices. The axisymmetric heteroclinic cycle is a manifestation of the classic 1:2 mode interaction, here the interaction between axisymmetric states with one and two pairs of vortices. The non-axisymmetric heteroclinic cycle is not of this type, since the approach to and from the saddles is oscillatory via transients resembling ribbons. However, it is anchored by the same axisymmetric saddles. The existence of two qualitatively different heteroclinic cycles connecting the same saddles is an unusual and intriguing feature. These cycles will be studied in more detail in a later investigation.

Bibliography

- [1] ALTMAYER, S & HOFFMANN, C. 2010 Secondary bifurcation of mixed-cross-spirals connecting travelling wave solutions. *New J. Phys.* **12** (11), 113035. 58, 60
- [2] ANTONIJOAN, J, MARQUES, F & SANCHEZ, J 1998 Non-linear spirals in the Taylor–Couette problem. *Phys. Fluids* **10** (4), 829–838. 58
- [3] ARMBRUSTER, DIETER, GUCKENHEIMER, JOHN & HOLMES, PHILIP 1988 Heteroclinic cycles and modulated travelling waves in systems with $O(2)$ symmetry. *Physica D* **29** (3), 257–282. 66, 68
- [4] ASHWIN, PETER & CHOSSAT, PASCAL 1998 Attractors for robust heteroclinic cycles with continua of connections. *J. Nonlinear Sci.* **8** (2), 103–129. 70
- [5] BARKLEY, D 2006 Linear analysis of the cylinder wake mean flow. *Europhys. Lett.* **75** (5), 750. 57
- [6] BENGANA, Y, LOISEAU, J.-C., ROBINET, J.-C. & TUCKERMAN, L.S. 2019 Bifurcation analysis and frequency prediction for open cavity flow. *submitted to J. Fluid. Mech.* . 57
- [7] CHOSSAT, PASCAL & IOOSS, GÉRARD 2012 *The Couette-Taylor Problem*. Springer. 58
- [8] DEGUCHI, KENGO & ALTMAYER, S 2013 Fully nonlinear mode competitions of nearly bicritical spiral or Taylor vortices in Taylor-Couette flow. *Phys. Rev. E* **87** (4), 043017. 58, 60
- [9] DEMAY, Y & IOOSS, G. 1984 Calcul des solutions bifurquées pour le problème de Couette-Taylor avec les 2 cylindres en rotation. *J. Mec. Théor. Appl.* pp. 193–216, special issue. 58
- [10] DESSUP, T., TUCKERMAN, L. S., WESFREID, J. E., BARKLEY, D. & WILLIS, A. 2018 The self-sustaining process in Taylor-Couette flow. *Phys. Rev. Fluids* **3**, 123902. 59
- [11] ECKE, R. E., ZHONG, FANG & KNOBLOCH, E 1992 Hopf bifurcation with broken reflection symmetry in rotating Rayleigh–Bénard convection. *Europhys. Lett.* **19** (3), 177. 58
- [12] HOFFMANN, C, ALTMAYER, S, PINTER, A & LÜCKE, M 2009 Transitions between Taylor vortices and spirals via wavy Taylor vortices and wavy spirals. *New J. Phys.* **11** (5), 053002. 58, 60

- [13] KNOBLOCH, E 1986 Oscillatory convection in binary mixtures. *Phys. Rev. A* **34** (2), 1538. [58](#)
- [14] KRUEGER, E. R., GROSS, A. & DI PRIMA, R. C. 1966 On the relative importance of Taylor-vortex and non-axisymmetric modes in flow between rotating cylinders. *J. Fluid Mech.* **24** (3), 521–538. [58](#)
- [15] LANGFORD, W. F., TAGG, RANDALL, KOSTELICH, E. J., SWINNEY, H. L. & GOLUBITSKY, M. 1988 Primary instabilities and bicriticality in flow between counter-rotating cylinders. *Phys. Fluids* **31** (4), 776–785. [58](#)
- [16] MANTIČ-LUGO, VLADISLAV, ARRATIA, CRISTÓBAL & GALLAIRE, FRANÇOIS 2014 Self-consistent mean flow description of the nonlinear saturation of the vortex shedding in the cylinder wake. *Phys. Rev. Lett.* **113** (8), 084501. [57](#)
- [17] MANTIČ-LUGO, VLADISLAV, ARRATIA, CRISTÓBAL & GALLAIRE, FRANÇOIS 2015 A self-consistent model for the saturation dynamics of the vortex shedding around the mean flow in the unstable cylinder wake. *Phys. Fluids* **27** (7), 074103. [57](#)
- [18] MELIGA, PHILIPPE 2017 Harmonics generation and the mechanics of saturation in flow over an open cavity: a second-order self-consistent description. *J. Fluid Mech.* **826**, 503–521. [57](#)
- [19] MITTAL, S. 2008 Global linear stability analysis of time-averaged flows. *Int. J. Numer. Meth. Fluids* **58** (1), 111–118. [57](#)
- [20] NOACK, B. R., AFANASIEV, K., MORZYŃSKI, M., TADMOR, G. & THIELE, F. 2003 A hierarchy of low-dimensional models for the transient and post-transient cylinder wake. *J. Fluid Mech.* **497**, 335–363. [57](#)
- [21] NORE, CAROLINE, TUCKERMAN, LAURETTE S, DAUBE, OLIVIER & XIN, SHIHE 2003 The 1:2 mode interaction in exactly counter-rotating von Kármán swirling flow. *J. Fluid Mech.* **477**, 51–88. [66](#), [68](#)
- [22] PIER, BENOÎT 2002 On the frequency selection of finite-amplitude vortex shedding in the cylinder wake. *J. Fluid Mech.* **458**, 407–417. [57](#)
- [23] PINTER, A, LÜCKE, M & HOFFMANN, C 2006 Competition between traveling fluid waves of left and right spiral vortices and their different amplitude combinations. *Phys. Rev. Lett.* **96** (4), 044506. [58](#), [59](#), [60](#), [61](#), [65](#)
- [24] PINTER, A, LÜCKE, M & HOFFMANN, C 2008 Bifurcation of standing waves into a pair of oppositely traveling waves with oscillating amplitudes caused by a three-mode interaction. *Phys. Rev. E* **78** (1), 015304(R). [58](#), [59](#), [60](#), [65](#)
- [25] PINTER, A, LÜCKE, M & HOFFMANN, C 2008 Wave-number dependence of the transitions between traveling and standing vortex waves and their mixed states in the Taylor-Couette system. *Phys. Rev. E* **78** (1), 017303. [58](#), [59](#), [60](#), [65](#)
- [26] SIPP, DENIS & LEBEDEV, ANTON 2007 Global stability of base and mean flows: a general approach and its applications to cylinder and open cavity flows. *J. Fluid Mech.* **593**, 333–358. [57](#)

- [27] TAGG, R., EDWARDS, W. S., SWINNEY, H. L. & MARCUS, P. S. 1989 Nonlinear standing waves in Couette-Taylor flow. *Phys. Rev. A* **39** (7), 3734. [58](#)
- [28] TURTON, S. E., TUCKERMAN, L. S. & BARKLEY, D. 2015 Prediction of frequencies in thermosolutal convection from mean flows. *Phys. Rev. E* **91** (4), 043009. [58](#), [61](#), [65](#)

Chapter 5

Frequency prediction from exact or self-consistent meanflows

Yacine Bengana¹ and Laurette S. Tuckerman¹

¹Laboratoire de Physique et Mécanique des Milieux Hétérogènes (PMMH), CNRS; ESPCI Paris, PSL Research University; Sorbonne Université; Univ. Paris Diderot, France

To be submitted to *Physical Review Fluids*

The self-consistent model developed by Mantič-Lugo *et al.* [9] describes the nonlinear process of amplitude saturation of supercritical flows and predicts accurately the nonlinear frequency, the amplitude and the mean fields. This model is formed by the mean flow governing equation and the linearized Navier-Stokes equation, coupled via the Reynolds stress by the leading mode. This model is assumed to be valid for supercritical flows for which the RZIF property is verified. The self-consistent model is applied to the thermosolutal convection for which a supercritical Hopf bifurcation gives rise to two branches: the standing waves and the traveling waves. This model is solved by means of a full Newton method. Although the RZIF property is verified for the traveling waves, the self-consistent model reproduces the nonlinear frequency only very near the onset of the bifurcation. The assumption that the nonlinear interaction (Reynolds stress) arising from the leading mode suffices to reproduce the nonlinear mean field and frequency is not valid in this case. By considering higher orders in the Reynolds stress term, we are able to reproduce the nonlinear frequency, the amplitude, and the mean fields.

5.1 Introduction

Periodic emission or translation of vortical structures is an intriguing and important nonlinear phenomenon observed in fluid flows in many different configurations. The amplitude and frequency are two essential characteristics of these time-periodic systems. Usually, these are obtained either by experiment or by solving the full Navier-Stokes equations via a direct numerical simulation.

The first step in understanding a nonlinear problem is linear stability analysis about its

equilibrium solution. This analysis shows whether an infinitesimal perturbation to the base flow grows or decays exponentially i.e whether the equilibrium solution is stable or unstable. This analysis is also used to locate the threshold of the bifurcation, at which the growth rate is equal to zero. The periodic oscillations originate from a supercritical Hopf bifurcation and linear stability analysis predicts the nonlinear frequency in the vicinity of the threshold [4]. Far from the threshold, linear analysis no longer predicts the frequency because the nonlinear interactions can no longer be neglected.

In many cases, linearization about the time-averaged field [1, 13, 14, 16, 20] yields the nonlinear frequency as the imaginary part of the eigenvalue of the leading eigenmode. Moreover, the growth rate, which is the real part of the eigenvalue, is nearly zero, showing that the mean flow is marginally stable, as had been previously suggested [6] in the context of turbulent shear flow. We emphasize that this result, which has been named RZIF in [20], is a match and not a prediction. It requires the mean flow, which must be determined by either experiment or direct numerical simulation. However, the RZIF property confirms the importance of the mean flow. As stated in, e.g. [3, 17, 18], the mean flow is essential, first for understanding the selection of the frequency of the nonlinear system and also as a factor in the theoretical development of reduced models, which is common in turbulent flow modeling.

At the early stage of the instability, the mean flow is identical to the base flow. As the perturbation grows, it introduces a distortion of the mean flow via the nonlinear interaction (Reynolds stress). The perturbation amplitude continues to grow until it is saturated by nonlinear interactions. The mean flow corresponding to this final saturated state is marginally stable. This process of amplitude saturation has been described in [11, 17]. Reduced models may help to understand the physical mechanisms of nonlinear systems. The reduction in numbers of degrees of freedom makes them easy to manipulate and less expensive to solve. However, these reduced models must be validated before they can be used in applications.

The self-consistent model (SCM) developed by Mantič-Lugo *et al.* [9] on the cylinder wake combines the mean flow equation and the equation obtained by linearizing about the mean flow. The mean flow equation is approximated by assuming that only the leading eigenmode of the linearized equation is important in creating the distortion of the mean flow. This assumption is based on the temporal spectrum of the cylinder wake that is dominated by the fundamental frequency. Therefore the Reynolds stress term, which is the source of the nonlinearities, is reduced to the leading mode. The amplitude of the mode is then chosen such that the growth rate of the linear problem is zero. For the cylinder wake, the results obtained by these coupled equations match the mean flow and the nonlinear frequency. The model describes the evolution of the amplitude of the mode as the distortion grows.

In this paper, we investigate the self-consistent model for the traveling wave branch in thermosolutal convection, for which RZIF is satisfied [20]. We will show that, for this case, the self-consistent model fails to predict the frequency or the mean flow. Higher order terms contributing to the Reynolds stress are necessary to reproduce the mean flow to sufficient accuracy. We have thus shown that satisfaction of the RZIF property does not necessarily imply the validity of the self-consistent model.

The procedure used in [10] to solve the self-consistent model is economical but not robust. The second-order generalization is more accurate, but its formulation in [12] is complicated. We will show that the full Newton method, as carried out in [2], is efficient in solving this system of equations and is feasible even at fifth order.

5.2 Definition of the problem

5.2.1 Thermosolutal convection

Thermosolutal convection is produced by temperature and concentration differences $\Delta\Theta$ and ΔC imposed on plates separated by a height h . We consider a two-dimensional configuration governed by the Boussinesq approximation, meaning that only the density appearing in the buoyancy term varies and depends linearly on temperature and concentration, with thermal and solutal volume expansion coefficients β_T and β_C . The properties of the fluid such as the kinematic viscosity ν , thermal and solutal diffusivities κ_T and κ_C are assumed to be constant. We use the scales h , $\Delta\Theta$, ΔC and the thermal diffusion time h^2/κ_T to nondimensionalize the variables. As the configuration is two-dimensional, we represent velocity by a streamfunction Ψ . In the conductive state, the flow is at rest and Θ and C vary linearly with z via diffusion. The coupled non-dimensional governing equations are written as

$$\partial_t \Theta - \mathcal{J}[\Psi, \Theta] = \nabla^2 \Theta + \partial_x \Psi, \quad (5.1a)$$

$$\partial_t C - \mathcal{J}[\Psi, C] = L \nabla^2 C + \partial_x \Psi, \quad (5.1b)$$

$$\partial_t \nabla^2 \Psi - \mathcal{J}[\Psi, \nabla^2 \Psi] = Pr[\nabla^4 \Psi + \partial_x(R_T \Theta + R_S C)]. \quad (5.1c)$$

where the streamfunction Ψ , temperature Θ and concentration C are deviations from the conductive state. We recall that the vorticity is equal to $-\nabla^2 \Psi$. The vorticity form of equation (5.1c) has been used to eliminate the pressure gradient from the momentum equation.

Equations (5.1) contains four dimensionless parameters:

$$Pr = \frac{\nu}{\kappa_T}, \quad L = \frac{\kappa_S}{\kappa_T}, \quad R_T = \frac{\beta_T g \Delta \Theta h^3}{\nu \kappa_T}, \quad R_S = \frac{\beta_S g \Delta C h^3}{\nu \kappa_T} \quad (5.2)$$

The Prandtl number Pr is the ratio of viscosity to thermal diffusion, and L is the ratio of solutal to thermal diffusivity. (Note that the parameter L defined above was called the Lewis number in [19, 20], but is in fact the inverse of the Lewis number.) These parameters can also be considered to measure the ratio of the thickness of the viscous and solutal boundary layers to the thermal boundary layer. Thermal and solutal gradients are measured by the thermal and solutal Rayleigh numbers R_T and R_S . The Poisson bracket is defined by

$$\mathcal{J}[f, g] = \partial_z f \partial_x g - \partial_x f \partial_z g \quad (5.3)$$

We note that if either f or g is independent of x , then $\mathcal{J}[f, g] = 0$. For simplicity and clarity, we write equations (5.1) in compact form

$$\partial_t U = \mathcal{L}U + \mathcal{N}(U, U) \quad (5.4)$$

where $U \equiv (\Theta, C, \nabla^2 \Psi)^T$, \mathcal{L} is the operator grouping linear diffusive terms and \mathcal{N} corresponds to advective terms. Opposite signs for R_S and R_T mean that temperature gradient is destabilizing and the concentration gradient is stabilizing or *vice versa*. This is necessary for the occurrence of a Hopf bifurcation. Branches of traveling waves (TW) and standing waves (SW) are generated by a Hopf bifurcation in a system with translation and reflexion symmetry $O(2)$ as shown in [5].

The boundary conditions are as follows:

- The temperature and concentration deviations are zero on the plates at $z = 0, 1$

$$T = C = 0 \quad \text{on } z = 0, 1 \quad (5.5)$$

- Imposing zero tangential stress leads to free-slip conditions at $z = 0, 1$

$$\partial_{zz} \Psi = 0 \quad \text{on } z = 0, 1 \quad (5.6)$$

This unrealistic boundary condition simplifies the problem but does not alter the behavior qualitatively near the threshold.

- No horizontal flux

$$\int_0^1 -\partial_z \Psi(x, z) dz = \Psi(x, 0) - \Psi(x, 1) = 0 \quad (5.7)$$

Ψ is defined up to an additive constant. Choosing this arbitrary constant to be $\Psi(x, z = 0) = 0$, we obtain

$$\Psi(x, 0) = \Psi(x, 1) = 0 \quad (5.8)$$

- Periodic boundary conditions in the horizontal direction

$$U(x + \lambda, z) = U(x, z) \quad (5.9)$$

For the pure thermal convection problem $R_S = 0$, Rayleigh [15] calculated a stationary bifurcation with a critical Rayleigh number that is a function of the wavenumber k ,

$$Ra_0 = \frac{(k^2 + \pi^2)^3}{k^2} \quad (5.10)$$

We fix the wavenumber to $k = \pi/\sqrt{2}$ which minimizes equation (5.10) and for which the critical Rayleigh number of the stationary bifurcation is $Ra_0 = 657.5$. We set the streamwise length of the domain to $\lambda = 2\pi/k = 2\sqrt{2}$ and define the reduced Rayleigh number as

$$r = \frac{Ra_T}{Ra_0} \quad (5.11)$$

The presence of a solutal gradient introduces a solutal Rayleigh number. The principal physical effect induced by the concentration gradient is the Soret effect controlled by the

separation parameter,

$$S = \frac{Ra_S}{Ra_T} \quad (5.12)$$

We carry out our study over the range of reduced Rayleigh number $r \in [2.06, 3]$. As in [20], we fix the Prandtl number at $Pr = 10$, the inverse L of the Lewis number $L = 0.1$ and the Soret number to $S = -0.5$.

5.2.2 Numerical methods

We present the numerical methods used for studying thermosolutal convection. The code has been developed in [20] and a synoptic view is given in figure 5.13, which describes a time integration code for the governing equations. Newton's method is implemented by transforming the time integration code with the method developed in [7]. We developed our own Newton method to solve the SCM model.

Spatial discretization

The spatial discretization uses a pseudo-spectral code. The periodic field $U(x, z, t)$ is decomposed in a Fourier-sine basis as

$$U(x, z, t) = \sum_{m,n} \hat{U}_{mn}(t) e^{imkx} \sin(n\pi z) \quad (5.13)$$

The two-dimensional Fourier transform brings the field represented on the physical space grid to the spectral representation (5.13). We differentiate in the spectral domain and we transform into the grid space (physical domain) to carry out the nonlinear Poisson bracket operations. The spatial resolution is $N_x \times N_z = 8 \times 8$, which is sufficient to describe the behavior in this periodic/free-slip configuration in our parameter range. In what follows, we will use hats and indices on U to denote features other than the wavenumbers in (5.13).

Time discretization

The time evolution is carried out by means of a mixed scheme. The diffusive term ∇^2 is evolved by the implicit Euler method. The convective terms, i.e. the Poisson brackets and the $\partial_x \Psi$ that remain are evolved with an explicit Euler method [20]. The time-discretized version of the governing equations (5.1) are

$$\Theta^{n+1} = (1 - \Delta t \nabla^2)^{-1} (\Delta t (-\mathcal{J}[\Psi, \Theta]^n + \partial_x \Psi^n) + \Theta^n) \quad (5.14a)$$

$$C^{n+1} = (1 - \Delta t Le \nabla^2)^{-1} (\Delta t (-\mathcal{J}[\Psi, C]^n + \partial_x \Psi^n) + C^n) \quad (5.14b)$$

$$\begin{aligned} \nabla^2 \Psi^{n+1} = & (1 - \Delta t Pr \nabla^2)^{-1} (\Delta t (-\mathcal{J}[\Psi, \nabla^2 \Psi]^n \\ & + Pr(Ra_T \partial_x \Theta^n + Ra_S \partial_x C^n)) + \nabla^2 \Psi^n) \end{aligned} \quad (5.14c)$$

The standing waves are unstable and are therefore computed by forcing the reflexion symmetry. The traveling waves have been computed with Newton's method by transforming the time-stepping code, as described in [20]. The time-stepping code is used to provide an initial guess for the traveling waves for the Newton method. The time-stepping method is summarized in figure 5.13 in the appendix.

5.2.3 Linear stability analysis

We present in this section the equations governing linear stability analysis about the conductive state, as well as the equations governing linearization about the mean field.

Linearization about the conductive state

Linear stability analysis consists of studying the evolution of an infinitesimal perturbation from an equilibrium state, in this case the conductive state. The linearized problem is written as

$$\partial_t u' = \mathcal{L}u' \quad (5.15)$$

where the infinitesimal time-dependent perturbations $u' = [\tau, c, \nabla^2 \psi]$ are of the form $u'(x, z, t) = \tilde{u}(x, z)e^{\lambda t}$, with \tilde{u} the eigenvector and λ its eigenvalue. \mathcal{L} is the linearized operator containing in this case only the right hand side of equations (5.1). Equation (5.15) then becomes

$$(\sigma + i\omega)\tilde{u} = \mathcal{L}\tilde{u} \quad (5.16)$$

As our study concerns a Hopf bifurcation from the conductive state, the eigenvalue $\lambda = \sigma + i\omega$ of the operator \mathcal{L} is complex and its real part σ crosses the marginal stability axis.

Linearization about the time averaged field

We consider the Reynolds decomposition $U = \bar{U} + u'$, with u' the perturbations and \bar{U} the temporal average of the traveling wave fields defined by

$$\bar{U}(x, z) = \frac{1}{T} \int_{t=0}^T U(x, z, t) dt \quad (5.17)$$

Substituting the Reynolds decomposition into the governing equations (5.4) we obtain

$$\partial_t u' = \mathcal{L}\bar{U} + \mathcal{L}u' + \mathcal{N}(\bar{U}, \bar{U}) + \mathcal{N}(u', \bar{U}) + \mathcal{N}(\bar{U}, u') + \mathcal{N}(u', u') \quad (5.18)$$

The temporal average of equations (5.18) gives the equations obeyed by the mean fields

$$0 = \mathcal{L}\bar{U} + \mathcal{N}(\bar{U}, \bar{U}) + \overline{\mathcal{N}(u', u')} \quad (5.19)$$

where $\overline{\mathcal{N}(u', u')}$ is the nonlinear interaction term called Reynolds stress. This term can be viewed as an external forcing in order for the mean field to be a stationary solution. Indeed the mean field is not a steady solution of the system (5.1). The mean fields are computed from nonlinear simulations because equation (5.19) is not a closed system. Subtracting equations (5.19) from (5.18) we obtain the fluctuation equations

$$\partial_t u' = -\mathcal{L}_{\bar{U}}(u') - \mathcal{N}(u', u') + \overline{\mathcal{N}(u', u')} \quad (5.20)$$

where

$$\mathcal{L}_{\bar{U}}u' \equiv \mathcal{L}u' + \mathcal{N}(\bar{U}, u') + \mathcal{N}(u', \bar{U}) \quad (5.21)$$

Equations (5.19) and (5.20) are the cornerstone of the linearization about the mean fields [1, 13, 14, 16, 20] and of the self-consistent model developed in [9] and described in section 5.4.

The RZIF procedure calls for neglecting the nonlinear self-interactions from equations (5.20). We then obtain the governing equations of the linear stability analysis about the mean

$$\partial_t u' = \mathcal{L}_{\bar{U}}(u') \quad (5.22)$$

Since (5.22) is linear in u' and homogeneous in t , its solutions are again of the form $u'(x, z, t) = e^{(\sigma + i\omega)t} \tilde{u}(x, z)$, leading again to the eigenproblem

$$(\sigma + i\omega) \tilde{u} = \mathcal{L}_{\bar{U}} \tilde{u} \quad (5.23)$$

For the traveling waves, the frequency ω obtained by the linearization about the conductive state deviates substantially from the nonlinear frequency, whereas that obtained by the linearization about the mean field matches it almost exactly. Moreover the growth rate σ is very close to the marginal stability axis. This property of the mean fields and linear stability analysis was named RZIF in [20] meaning that the real part of the eigenvalue is nearly zero and the imaginary part of the eigenvalue matches the nonlinear frequency.

In contrast, the self-consistent model is constructed as a closed system of equations (5.19) and (5.23) by making the further assumption that the nonlinear interaction term of equation (5.19) can be truncated to include only the leading eigenmode of (5.23). That is, \bar{U} is defined by solving (5.19) and (5.23) rather than calculated by taking the mean (5.17) of the full evolution equations (5.4). Thus, the mean flow and the nonlinear frequency are approximated without time integration. A detailed explanation of the SCM is given in section 5.4.

5.3 RZIF using fields from DNS

5.3.1 Overview

Our study follows that of [20]. To make it self-contained, we have reproduced the traveling waves and the linear stability analysis about the base and mean fields. Figure 5.1(a) shows the evolution of the field components over one temporal period spaced by a quarter of a period. The temperature Θ is in phase opposition with concentration C and the streamfunction Ψ . Figure 5.1(b) shows the mean fields, which are homogenous in the horizontal direction. Figure 5.1(c) shows the results of linear stability analysis about the conductive and mean fields compared to the exact nonlinear frequency of the traveling waves. All frequencies match at the threshold $r_c = 2.06$ [20] as they must for a supercritical Hopf bifurcation, but only the frequency about the mean field follows the nonlinear frequency when we increase the Rayleigh number. The imaginary part of the eigenvalue ω obtained by linearization about the mean field matches almost exactly the nonlinear frequency. In contrast, the frequency obtained by linearizing about the conductive base state and shown as triangles diverges completely from the nonlinear frequency. The real part of the eigenvalue shows the growth rate which indicates whether the field about which

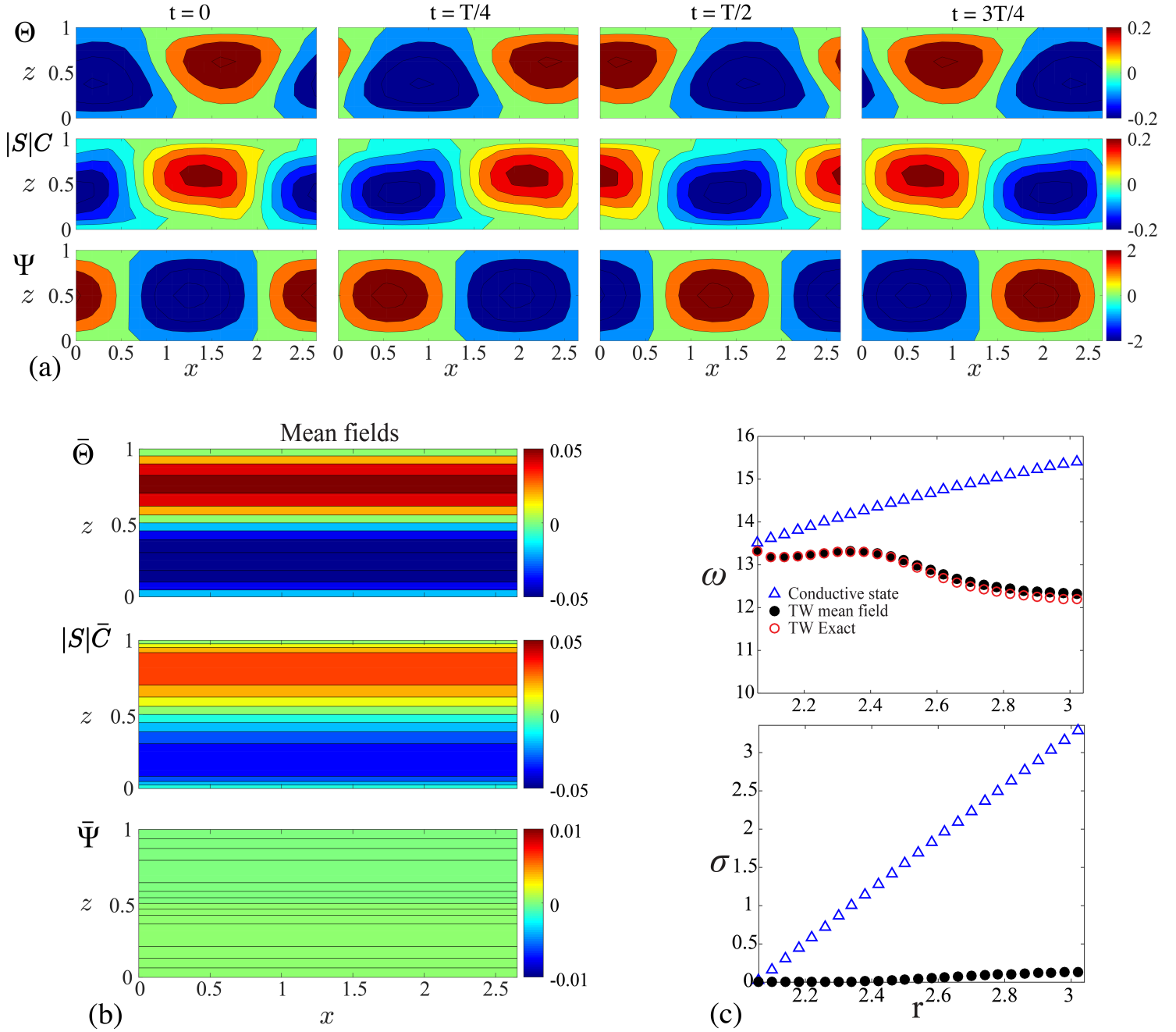


Figure 5.1 – (a) Evolution of traveling waves over a period T for temperature Θ , concentration $|S|C$ and the streamfunction Ψ for $r = 2.5$, $L = 0.1$, $S = -0.5$, $Pr = 10$. (b) Mean fields of $\bar{\Theta}$, $|S|\bar{C}$ and $\bar{\Psi}$. The horizontal invariance of the temporal mean fields in x is a consequence of the equivalence of time and space translation for traveling waves. (c) Exact nonlinear frequencies ω of TW (\circ) as well as frequencies and growth rates σ obtained by linearization about the base (Δ) and mean fields (\bullet) as a function of r . The frequencies about mean fields (\bullet) and the exact frequencies (\circ) match almost perfectly; moreover the growth rate about the mean field collapses onto the marginal stability axis $\sigma = 0$. Adapted from [20].

we linearize is stable or not. As already demonstrated from nonlinear simulation, the base flow is unstable as shown by the positive growth rate $\sigma > 0$. The growth rate about the mean field is near the marginal stability axis $\sigma = 0$. Therefore the TW satisfies the RZIF property. This property was reported for the first time by Barkley [1] for the Bénard-von Kármán vortex street that can be viewed approximately as a traveling wave modulated

in the x direction. In figure 5.1(c), the frequency about the mean field separates slightly from the exact frequency for $r > 2.5$. The growth rate also separates from the marginal stability axis.

5.3.2 Fourier decomposition and eigenvectors

The RZIF procedure does not merely approximate the nonlinear frequencies via the eigenvalues but also approximates the temporal Fourier coefficients via the eigenvectors. To understand this, we turn to the argument given by Turton *et al.* [20] based on the temporal Fourier decomposition to explain the RZIF property. The Fourier decomposition of a periodic solution is written as

$$U = \bar{U} + \sum_{n \neq 0} \hat{u}_n e^{in\omega t} \quad (5.24)$$

where $\hat{u}_{-n} = \hat{u}_n^*$. We substitute (5.24) into the governing equations and separate the resulting terms of different frequencies. The term $n = 0$ is the governing equation of the mean field. From equation (5.1) we have

$$0 = \mathcal{L}\bar{U} + \underbrace{\mathcal{N}(\bar{U}, \bar{U}) + \sum_{m \neq 0} \mathcal{N}(\hat{u}_m, \hat{u}_{-m})}_{(i)} \quad (5.25)$$

The Fourier coefficients \hat{u}_n satisfy the equation

$$in\omega \hat{u}_n = \underbrace{\mathcal{L}\hat{u}_n + \mathcal{N}(\bar{U}, \hat{u}_n) + \mathcal{N}(\hat{u}_n, \bar{U})}_{(ii)} + \underbrace{\sum_{m \neq 0, n} \mathcal{N}(\hat{u}_m, \hat{u}_{n-m})}_{(iii)} \quad (5.26)$$

The nonlinear term (i) appearing in equation (5.25) is the Reynolds stress. This term is responsible for the distortion and production of the mean field. The Reynolds stress could be seen as an external force needed for the mean field to satisfy the stationary equations as suggested by Barkley [1]. The term (ii) in equation (5.26) is the linear operator about the mean field. As stated by Turton *et al.* [20] if the higher order Fourier coefficients are negligible compared to the fundamental mode, then higher harmonic interactions can be neglected (iii). Thus linearization about the mean field leads to an eigenvalue problem with $\sigma = 0$. This means that if the time trace has only a single frequency, equation (5.26) for $n = 1$ leads to the RZIF property:

$$i\omega \hat{u}_1 = \mathcal{L}\hat{u}_1 + \mathcal{N}(\bar{U}, \hat{u}_1) + \mathcal{N}(\hat{u}_1, \bar{U}) = \mathcal{L}_{\bar{U}} \hat{u}_1 \quad (5.27)$$

This argument shows that RZIF implies the equality of the first temporal Fourier coefficient of $U(t)$ and the eigenvector of $\mathcal{L}_{\bar{U}}$.

We wish to test the validity of this in our system, where

$$U(x, z, t) = \bar{U}(x, z) + \sum_{n \neq 0} \hat{u}_n(x, z) e^{in\omega t} \quad (5.28)$$

Figure 5.2(a,b) show the real and imaginary part of the normalized first Fourier coefficient

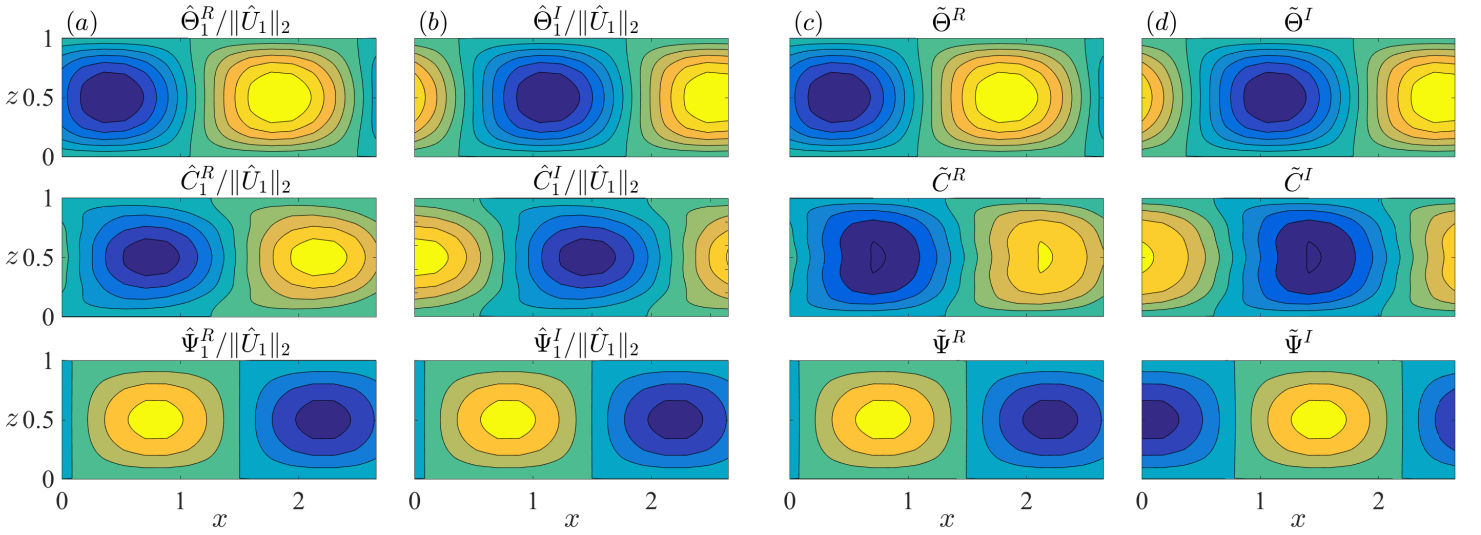


Figure 5.2 – Column (a): real part of the normalized first Fourier coefficient of temperature $\hat{\Theta}_1^R/\|\hat{U}_1\|_2$, concentration $\hat{C}_1^R/\|\hat{U}_1\|_2$ and the streamfunction $\hat{\Psi}_1^R/\|\hat{U}_1\|_2$. Column (b): imaginary part of the normalized first Fourier coefficient, $\hat{\Theta}_1^I/\|\hat{U}_1\|_2$, $\hat{C}_1^I/\|\hat{U}_1\|_2$ and $\hat{\Psi}_1^I/\|\hat{U}_1\|_2$. (c,d) show the eigenvectors obtained by linearization about the mean fields. Columns (c): real part of the leading eigenvector, $\tilde{\Theta}_1^R$, \tilde{C}_1^R and $\tilde{\Psi}_1^R$. Columns (d): imaginary part of the leading eigenvector, $\tilde{\Theta}_1^I$, \tilde{C}_1^I and $\tilde{\Psi}_1^I$. Those results are obtained for $r = 2.5$, $L = 0.1$, $S = -0.5$, $Pr = 10$. We observe the typical quarter phase shift of traveling waves shown in figure 5.1.

\hat{u}_1 for the reduced Rayleigh number $r = 2.5$. We observe that the temperature is in phase opposition with the concentration and the streamfunction, which is consistent with the nonlinear fields shown in figure 5.1(a). The quarter phase shift between the real (column a) and imaginary part (column b) is identical to the time translation of nonlinear fields shown in figure 5.1(a) and typical of traveling waves. From the mean fields \bar{U} , we determine the leading eigenvector \tilde{u}_1 via (5.23), again for reduced Rayleigh number $r = 2.5$. The real and imaginary parts of those eigenvectors are shown in figures 5.2(c,d). These are very close to the normalized Fourier coefficients in figure 5.2(a,b) described previously. A slight difference is noted for the concentration field. For traveling waves, because of the horizontal translation symmetry, neither the temporal Fourier coefficients nor the eigenvectors are uniquely defined, but we have chosen the combinations and phases that provide the best match to the traveling waves.

We now wish to compare the Fourier coefficients over our entire range of reduced Rayleigh number r . To do so, we extract the one-dimensional z -profiles of \hat{u} and \tilde{u} as follows. The displacement of a traveling wave in the horizontal direction is equivalent to time translation as shown in figure 5.1(a). (This property permits us to compute the traveling waves by Newton's method.) Therefore to calculate the temporal mean field and the temporal Fourier coefficients of the traveling waves, we can use an instantaneous spatial Fourier transform in the x direction

$$U(x, z) = \bar{U}(z) + \sum_{n \neq 0} \hat{u}_n(z) e^{inkx} \quad (5.29)$$

Because \bar{U} is independent of z , so is the operator $\mathcal{L}_{\bar{U}}$ and its eigenmodes are of trigonometric

form, for example:

$$[\tilde{\tau}(z) \cos(kx), \tilde{c}(z) \cos(kx), \tilde{\psi}(z) \sin(kx)] \quad (5.30a)$$

$$[\tilde{\tau}(z) \sin(kx), \tilde{c}(z) \sin(kx), \tilde{\psi}(z) \cos(kx)] \quad (5.30b)$$

We computed the traveling waves over a range of reduced Rayleigh number r and calculated their first Fourier coefficients \hat{u} from the spatial Fourier decomposition (5.29). We also linearized about the mean fields \bar{U} and computed the eigenvectors \tilde{u} . In order to compare $\hat{u}(z)$ and $\tilde{u}(z)$ over the entire range of r values, rather than comparing profiles for each value of r , we combine these one-dimensional functions into two-dimensional representations $\hat{u}(r, z)$ and $\tilde{u}(r, z)$ where at $r = r^*$,

$$\hat{u}(r = r^*, z) = \tilde{u}(z) \quad (5.31)$$

Figure 5.3 shows the contours of these two-dimensional functions $\tilde{u}(r, z)$ and $\hat{u}(r, z)$ constructed from the leading eigenvectors $\tilde{u}(z)$ (dashed curves) and from the normalized Fourier coefficients $\hat{u}(z)$ (bold curves). The Fourier coefficients of temperature and streamfunction match the eigenvectors from the linearization about the mean fields. The concentration fields match only very near the threshold and diverge drastically when we increase the Rayleigh number. Therefore though the linear analysis about the mean fields matches the nonlinear frequencies, it does less well in matching all the fields of thermosolutal convection. Note that the divergence of the eigenvectors from the Fourier coefficients is significant from $r > 2.5$, as it is for the frequency shown in figure 5.1(c).

5.3.3 Approximating the mean flow

In the self-consistent model of [9], the distortion of the mean field is assumed to be caused only by the leading mode. In this section, we will determine how many modes are necessary to create the true mean field and therefore to satisfy the RZIF property.

The mean fields \bar{U} of traveling waves are necessarily homogeneous in the horizontal direction as shown in figure 5.1(b). For x -independent fields, the Poisson bracket (5.3) which corresponds to $\mathcal{N}(\bar{U}, \bar{U})$ vanishes and equation (5.25) is reduced to

$$0 = \partial_{zz} \bar{U} + \sum_{m \neq 0}^N \mathcal{N}(\hat{u}_m, \hat{u}_{-m}) \quad (5.32)$$

Thus the mean field satisfies

$$\bar{U} = -\partial_{zz}^{-1} \sum_{m \neq 0}^N \mathcal{N}(\hat{u}_m, \hat{u}_{-m}) \quad (5.33)$$

with N the total number of Fourier coefficients. If we consider all temporal Fourier coefficients \hat{u}_m taken from a direct numerical simulation, solution \bar{U} of equation (5.33) is the exact mean field. We define \bar{U} to be the field obtained by truncating (5.33):

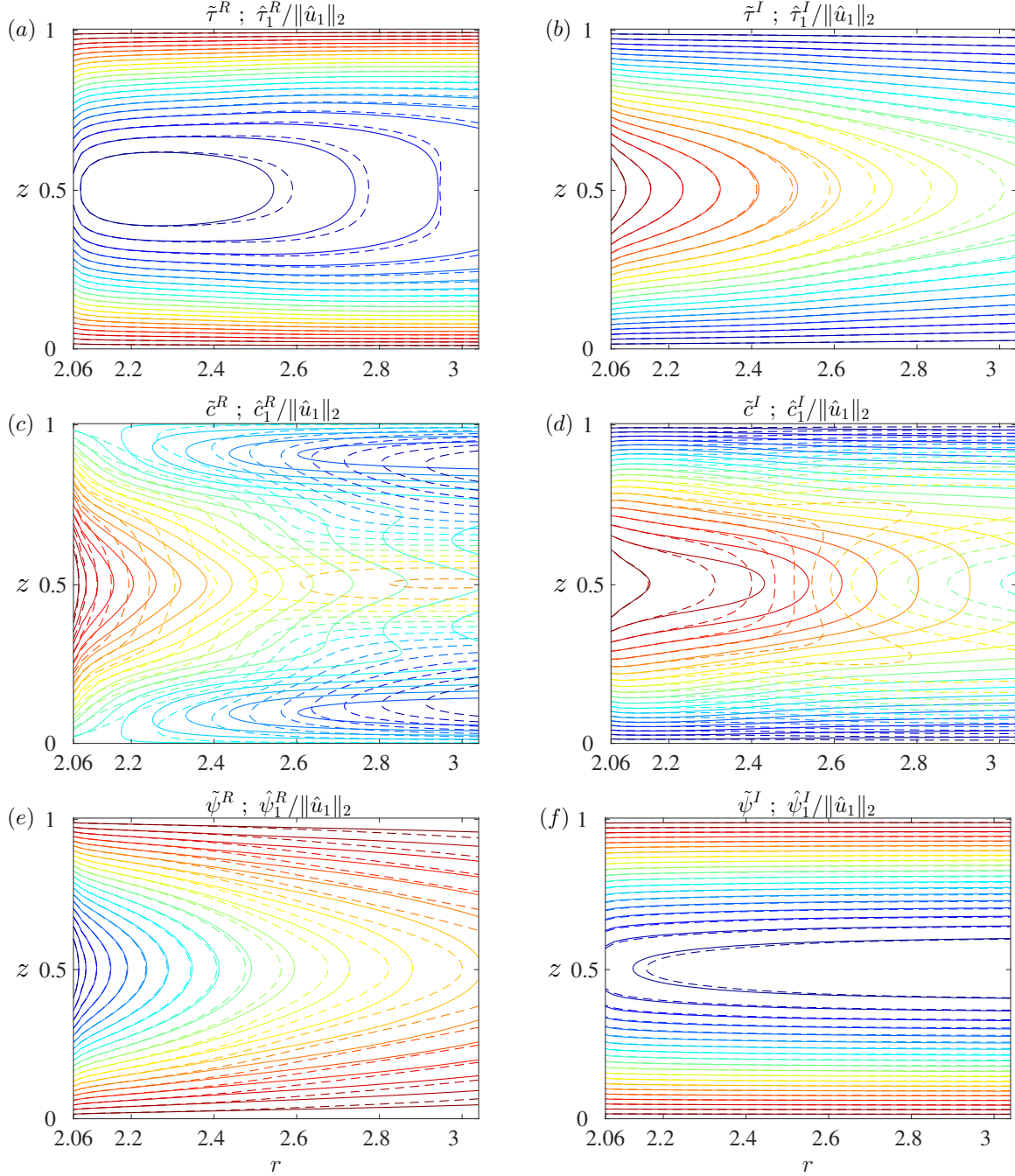


Figure 5.3 – Contours of functions $\tilde{u}(r, z)$ constructed from the real and imaginary parts of eigenvectors (dashed curves) obtained by linearization about the mean fields and functions $\hat{u}(r, z)$ constructed from the real and imaginary parts of the normalized Fourier coefficients (solid curves). (a, c, e) Contours of functions obtained from the real parts of the eigenvectors $\tilde{\tau}^R$, \tilde{c}^R , $\tilde{\psi}^R$ and from the real parts of the normalized Fourier coefficients $\hat{\tau}_1^R/\|\hat{u}_1\|_2$, $\hat{c}_1^R/\|\hat{u}_1\|_2$, $\hat{\psi}_1^R/\|\hat{u}_1\|_2$. (b, d, f) Contours of functions obtained from the imaginary parts of eigenvectors $\tilde{\tau}^I$, \tilde{c}^I , $\tilde{\psi}^I$ and from the imaginary parts of the normalized Fourier coefficients $\hat{\tau}_1^I/\|\hat{u}_1\|_2$, $\hat{c}_1^I/\|\hat{u}_1\|_2$, $\hat{\psi}_1^I/\|\hat{u}_1\|_2$. Fourier coefficients and the leading eigenvectors start to diverge from one other essentially at $r > 2.4$ and for $z \in [0.3, 0.7]$. (a, b) The temperature and the streamfunction match better than the (c, d) concentration. Indeed, the imaginary part of the concentration matches the Fourier coefficient only close to the threshold, while the real parts diverge even close to the threshold.

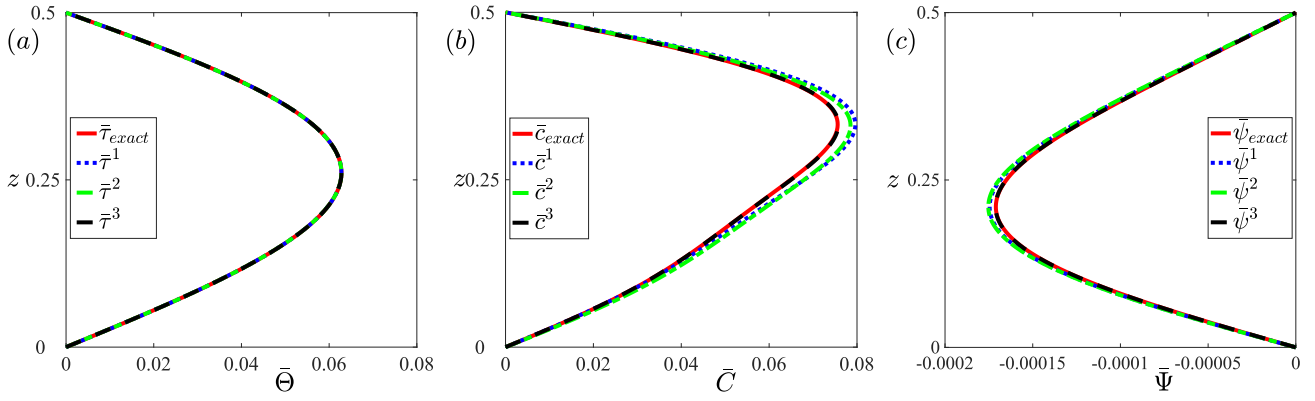


Figure 5.4 – Mean field approximation of (a) temperature, (b) concentration and (c) streamfunction at $r = 2.5$. The exact mean fields are shown as red bold line, the mean fields truncated at first order as the dotted curve, truncated at second order by the green dashed line and truncated at the third order by the black dashed line.

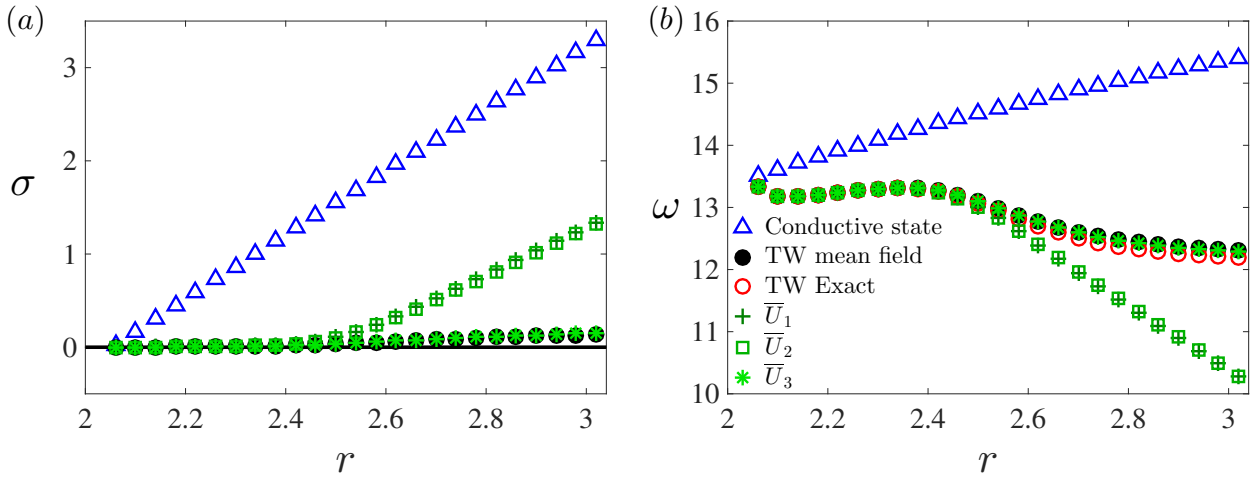


Figure 5.5 – (a) Growth rate and (b) frequency as a function of Rayleigh number for TW. (b) Exact frequencies are shown by (\circ) . Linearization about the base and mean flows are represented by (Δ) and (\bullet) . The results of linearization about the truncated mean fields \bar{U}_1 , \bar{U}_2 and \bar{U}_3 are shown by $(+)$, (\square) and $(*)$.

$$\bar{U}_K = -\partial_{zz}^{-1} \sum_{m \neq 0}^K \mathcal{N}(\hat{u}_m, \hat{u}_{-m}) \quad (5.34)$$

(This use of the subscript will only apply in this section.)

We approximate the mean fields by truncating the series in (5.34) at order $N = 1$, $N = 2$ and $N = 3$. Figure 5.4 compares the approximated mean fields with the exact mean field. The temperature is accurately reproduced by the first term whereas the concentration and streamfunction require the first three terms in order to match the exact mean field to the point where they are visually indistinguishable. This result is consistent with that of Turton *et al.* [20]. They showed peaked spectra for the temperature field of traveling waves implying that the higher harmonics contribute little to the mean field, whereas those of the concentration and streamfunction are not as highly peaked.

We now linearize about the truncated mean fields to study the dependence on truncation

level of the accuracy of the estimated nonlinear frequencies. Figure 5.5 shows the same results as figure 5.1(c) but also includes the results of linearization about the truncated mean fields \bar{U}_1 , \bar{U}_2 and \bar{U}_3 . Figure 5.5(b) shows that the frequency obtained by linearization about the first order mean field (plus signs) matches the frequency obtained about the full mean field until $r = 2.5$ and diverges abruptly from it for $r > 2.5$. The growth rate shown in figure 5.5(a) also deviates from the marginal stability axis $\sigma = 0$ (bold line) at $r = 2.5$. It is important to point out that reconstructing the mean field only by the first Fourier coefficient increases the initial difference already present between the exact nonlinear frequency and that obtained by linearization about the exact mean field. The frequency about the third-order mean field (stars) matches perfectly that calculated from the full mean field and therefore matches the nonlinear frequency. Moreover, the very small growth rate matches that of the full mean field. We conclude that the third order mean field \bar{U}_3 is sufficient for the system to satisfy the RZIF property. The second Fourier coefficient has almost no effect on the truncated mean field (figures 5.5(b-c)) nor on the frequency and growth rate. Moreover, if we consider only the first and third coefficients and neglect the second Fourier coefficient, the change in the mean field and in the eigenvalues (stars) is not significant. Nevertheless, we have

$$\| \mathcal{N}(\hat{u}_1, \hat{u}_{-1}) \| = 7.19 \quad \| \mathcal{N}(\hat{u}_2, \hat{u}_{-2}) \| = 0.057 \quad \| \mathcal{N}(\hat{u}_3, \hat{u}_{-3}) \| = 0.035$$

i.e. $\| \mathcal{N}(\hat{u}_2, \hat{u}_{-2}) \|$ is greater than $\| \mathcal{N}(\hat{u}_3, \hat{u}_{-3}) \|$. This result suggests that the amplitudes of the modes for $n > 1$ are not the only relevant point in the construction of the true mean field.

For completeness, we exhibit the Fourier coefficients \hat{u}_n themselves. The Fourier coefficients obtained over our range of reduced Rayleigh number are represented as contours of the two-dimensional functions $\hat{u}_n(r, z)$, defined as before in (5.31). Figure 5.6 shows contours of these functions obtained from the real parts of the first three Fourier coefficients. As suggested in the discussion of figures 5.4 and 5.5, there is an obvious resemblance between the first and third Fourier coefficient. The imaginary parts of the Fourier coefficients (not shown) also present the same resemblance.

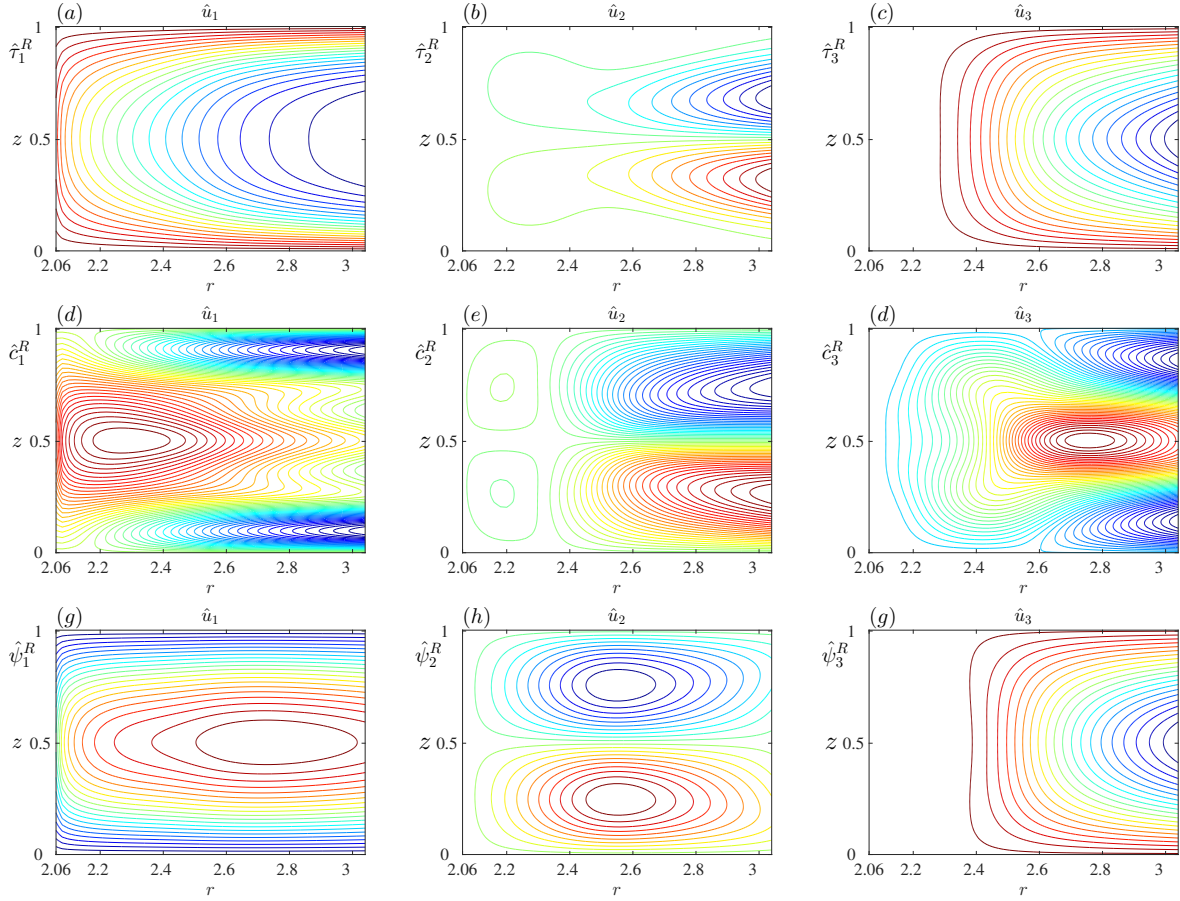


Figure 5.6 – Contours of functions $\hat{u}_n(r, z)$ constructed from the real parts of the three first Fourier coefficients. (a,d,g) show the function constructed from the first Fourier coefficient \hat{u}_1 , (b,e,h) from the second Fourier coefficient \hat{u}_2 and (c,f,i) from the third Fourier coefficient \hat{u}_3 . (a-c) shows the temperature fields. (d-f) concentration. (g-i) the streamfunction. We observe the resemblance between the first and the third Fourier coefficients.

5.4 Self-consistent model

5.4.1 Decoupled model

While the idea that linearization about the mean flow reproduces properties of the nonlinear Bénard–von Kármán vortex street is intriguing, it is not predictive because a full direct numerical simulation (DNS) must be carried out. In contrast, Mantič-Lugo *et al.* [9] have developed an approach, the self-consistent model (SCM) which does not rely on a DNS. The key hypothesis is that the most unstable leading eigenmode suffices for the mean field distortion. Consequently, the Reynolds stress term (i) contributing to the mean field in equation (5.25) contains only the leading mode. Neglecting the higher harmonic interactions (iii) from (5.26) reduces this equation to an eigenvalue problem about the mean field. The following equations form the SCM

$$0 = \mathcal{L}\bar{U} + \mathcal{N}(\bar{U}, \bar{U}) + \mathcal{N}(U_1, U_{-1}) + \mathcal{N}(U_{-1}, U_1) \quad (5.35a)$$

$$(\sigma + i\omega)U_1 = \mathcal{L}_{\bar{U}}U_1 \quad (5.35b)$$

$$\|U_1\| = A \quad (5.35c)$$

$$\sigma = 0 \quad (5.35d)$$

with U_1 the leading eigenmode and U_{-1} its complex conjugate, A the amplitude of the mode and $\mathcal{L}_{\bar{U}}U_1$ the linear operator defined, as usual, by

$$\mathcal{L}_{\bar{U}}U_1 = \mathcal{L}U_1 + \mathcal{N}(\bar{U}, U_1) + \mathcal{N}(U_1, \bar{U})$$

(Here, we have used U_1 rather than \hat{u}_1 to denote the leading eigenmode in order to prepare for presenting our solution method for (5.35) via Newton's method in section 5.4.2.) Thus, according to (5.35), \bar{U} , U_1 , ω , and A are defined such that $\sigma = 0$. The question is whether this yields correct values, in particular for the mean field \bar{U} and the frequency ω .

In [10], system (5.35) is solved by an iterative algorithm that decouples (5.35a) and (5.35b) as follows. The amplitude A is fixed. Initially the base field is used in (5.35b) and Mantič-Lugo *et al.* [10] compute the eigenvector U_1 and eigenvalue $\sigma + i\omega$ by solving the eigenproblem (5.35b). (It is for this reason that σ cannot immediately be set to zero, despite (5.35d). When (5.35b) is solved as an eigenproblem, the eigenvalue will in general have a non-zero real part.) The eigenvector is then given norm A and substituted into the mean field governing equation (5.35a), which is solved by Newton's method. The new value of \bar{U} is substituted into (5.35b), leading to a new value of U_1 . The process is continued until convergence, yielding values of \bar{U} , U_1 , σ , and ω for each value of A . The final values chosen for \bar{U} , U_1 , ω and A are those for which $\sigma(A) = 0$. For more details see [10] and [8].

System (5.35) has the advantage of describing the amplitude saturation process, mimicking the evolution of A in time, discussed in [11, 21]. The unstable base field solution extracts energy from the perturbations, which grow until they saturate. By neglecting higher harmonics, the SCM computes the mean field, the nonlinear frequency and the nonlinear mode with its amplitude A without time integration. Mantič-Lugo *et al.* [10] accurately reproduce the results of Barkley [1] for the cylinder wake up to $Re = 120$.

5.4.2 Full Newton method for SCM

From an algorithmic perspective, problems of convergence for high Re have been reported in solving this system by the algorithm described above. A relaxation factor and a different normalization of the nonlinear term in equation (5.35a) have been necessary to ensure convergence; details about the algorithm can be found in [8]. We have been unable to use the algorithm of [10] to solve the SCM for the traveling wave branch of the thermosolutal convection. Indeed, we have been able to solve the system only very close to the threshold r_c ; beyond 2% from r_c we no longer converge. Therefore we implemented a full Newton method to solve (5.35). Very recently Andrea Fani *et al.* [2] also applied a full Newton method to solve the SCM for the acoustic generation from the Bénard—von Kármán vortex street.

Here we present the Newton method developed to solve the system of equations that compose the SCM, which is equivalent to system (5.35). This system contains four unknowns with three fields which are the mean field \bar{U} , the real part U_1^r and imaginary part U_1^i of the leading eigenmode U_1 and the scalar unknown Ω . We recall that the traveling wave mean fields are homogeneous in the streamwise direction and the term $\mathcal{N}(\bar{U}, \bar{U})$ corresponding to the Poisson bracket vanishes from equation (5.35a). Separating equation (5.35b) into real and imaginary parts, the SCM is written as

$$0 = \mathcal{L}\bar{U} + \mathcal{N}(U_1, U_{-1}) + \mathcal{N}(U_{-1}, U_1) \quad (5.36a)$$

$$0 = -\Omega U_1^i - \mathcal{L}_{\bar{U}} U_1^r \quad (5.36b)$$

$$0 = \Omega U_1^r - \mathcal{L}_{\bar{U}} U_1^i \quad (5.36c)$$

$$0 = U_1^i(z = 1/2) \quad (5.36d)$$

where

$$\mathcal{L}_{\bar{U}} U_1^r \equiv \mathcal{L} U_1^r + \mathcal{N}(\bar{U}, U_1^r) + \mathcal{N}(U_1^r, \bar{U})$$

$$\mathcal{L}_{\bar{U}} U_1^i \equiv \mathcal{L} U_1^i + \mathcal{N}(\bar{U}, U_1^i) + \mathcal{N}(U_1^i, \bar{U})$$

Because Ω is treated as a scalar unknown, the imposition of phase condition (5.36d) is required to close the system of equations. As presented in section 5.4.1, Mantič-Lugo *et al.* [10] solved the SCM equations (5.35) as a decoupled problem. The mean governing equation (5.35a) is solved for \bar{U} by Newton's method and the linear equation (5.35b) is solved for U_1 , σ and Ω as an eigenvalue problem by diagonalization. In that formulation, the presence of a growth rate σ in system (5.35) cannot be avoided. Moreover, the amplitude A of the leading mode must be imposed as an external parameter because the amplitude of an eigenvector is arbitrary. In contrast, with the full Newton method we set σ to 0 and remove it as a variable because we solve the SCM as a coupled problem. Moreover, the amplitude A of the mode is not present explicitly in the system (5.36) because it is included in U_1 . The fact that we do not normalize U_1 allows the trivial solution $U_1 = 0$ to be possible choice for the system, which must be avoided. In practice, we start the simulation with an initial guess obtained by Mantič-Lugo *et al.* [10] algorithm that converges near the threshold. We avoid the trivial solution $U_1 = 0$ by considering the mode U_1 with its amplitude. By varying the reduced Rayleigh number r by small intervals, the method converges to the solution $[\bar{U}, U_1, \Omega]$. System (5.36) merely describes a robust

method of solving the SCM (5.35). As is the case for [10] the mean field \bar{U} , mode U_1 with its amplitude and the frequency Ω are obtained from (5.36) without time integration.

Newton's method consists of solving $F(U) = 0$ where $U = [\bar{U}, U_1^r, U_1^i, \Omega]$ and $F(U)$ is the RHS of (5.36). We approximate $F(U + u)$ by a Taylor expansion at first order

$$F(U + u) = F(U) + DF(U)u \quad (5.38)$$

with $u = [\bar{u}, u_1^r, u_1^i, \omega]$ and solve the linear system

$$DF(U)u = F(U) \quad (5.39a)$$

$$U = U - u \quad (5.39b)$$

where $DF(U)$ is the Jacobian matrix and u the decrement applied to U . The details of equation (5.39) for system (5.36) are

$$\begin{aligned} & -(\mathcal{L}\bar{u} + [N(U^R, u^R) + N(u^R, U^R) + N(U^I, u^I) + N(u^I, U^I)]) = \\ & \mathcal{L}\bar{U} + [N(U^R, U^R) + N(U^I, U^I)] \end{aligned} \quad (5.40a)$$

$$\begin{aligned} & -(\Omega u^I + \omega U^I + (\mathcal{L} - k^2)u^R + N(\bar{U}, u^R) + N(u^R, \bar{U}) + N(\bar{u}, U^R) + N(U^R, \bar{u})) = \\ & \Omega U^I + (\mathcal{L} - k^2)U^R + N(\bar{U}, U^R) + N(U^R, \bar{U}) \end{aligned} \quad (5.40b)$$

$$\begin{aligned} & -(-\Omega u^R - \omega U^R + (\mathcal{L} - k^2)u^I + N(\bar{U}, u^I) + N(u^I, \bar{U}) + N(\bar{u}, U^I) + N(U^I, \bar{u})) = \\ & -\Omega U^R + (\mathcal{L} - k^2)U^I + N(\bar{U}, U^I) + N(U^I, \bar{U}) \end{aligned} \quad (5.40c)$$

$$-u^I(z = 1/2) = U^I(z = 1/2) \quad (5.40d)$$

We summarize the algorithm in figure 5.14 in the appendix.

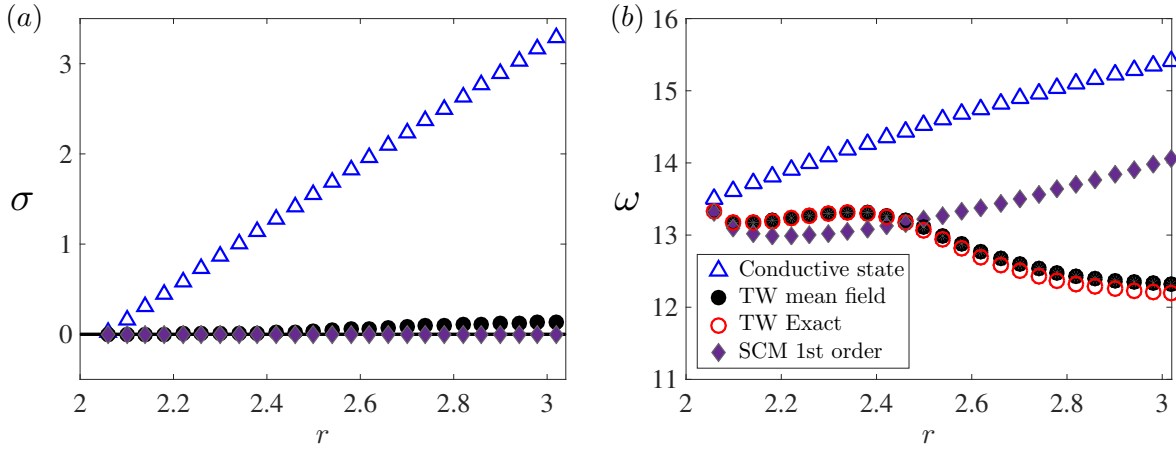


Figure 5.7 – (a) Growth rate, (b) Frequency as a function of Rayleigh number. Exact frequencies are shown by open circles (\circ). Frequencies and growth rates obtained by linearization about the base and full mean field are represented by triangles (\triangle) and solid circles (\bullet). Frequencies predicted by the SCM at first order are shown by diamonds (\blacklozenge).

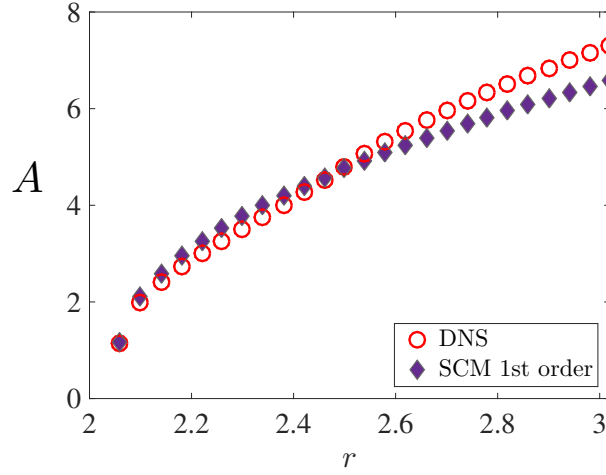


Figure 5.8 – Amplitude of the first mode computed by the self-consistent model at 1st order, compared to the fundamental Fourier coefficient amplitude.

5.4.3 First-order SCM

We present in this section the result of the self-consistent model (5.35). Figure 5.7 shows the frequency resulting from linearization about the exact mean flow (dots), that about the conductive base state (triangles), the exact frequency of the traveling waves (circles) and the results of the SCM (diamonds). In this method, $\sigma = 0$ by construction, as shown in figure 5.7(a). Although the RZIF property is satisfied for the traveling waves, we observe in figure 5.7(b) that the frequency given by the SCM at first order matches the nonlinear frequency only very close to the threshold. Therefore, the SCM fails to predict the nonlinear frequency.

Figure 5.8 shows the amplitude A computed with the SCM and the nonlinear amplitude of the fundamental Fourier coefficient. As was the case for the frequency shown in figure 5.7(b), both the value and the slope of the amplitude match those of the nonlinear amplitude near the threshold and deviate from them for $r > r_c$.

This case provides a counterexample to the SCM, showing that the RZIF property does not

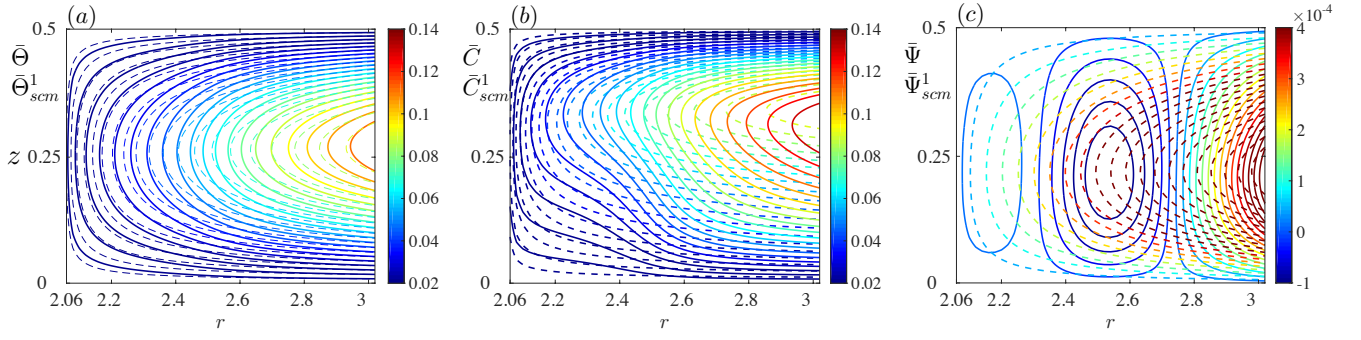


Figure 5.9 – Contours of functions $\bar{U}(r, z)$ and $\bar{U}^1_{SCM}(r, z)$ constructed from the exact mean fields (bold curves) and from the mean field calculated by SCM at first order (dashed curves). (a) Temperature, (b) concentration and (c) streamfunction. We observe that the SCM mean fields do not match the exact mean fields. The streamfunctions have very small amplitudes and very different spatial forms.

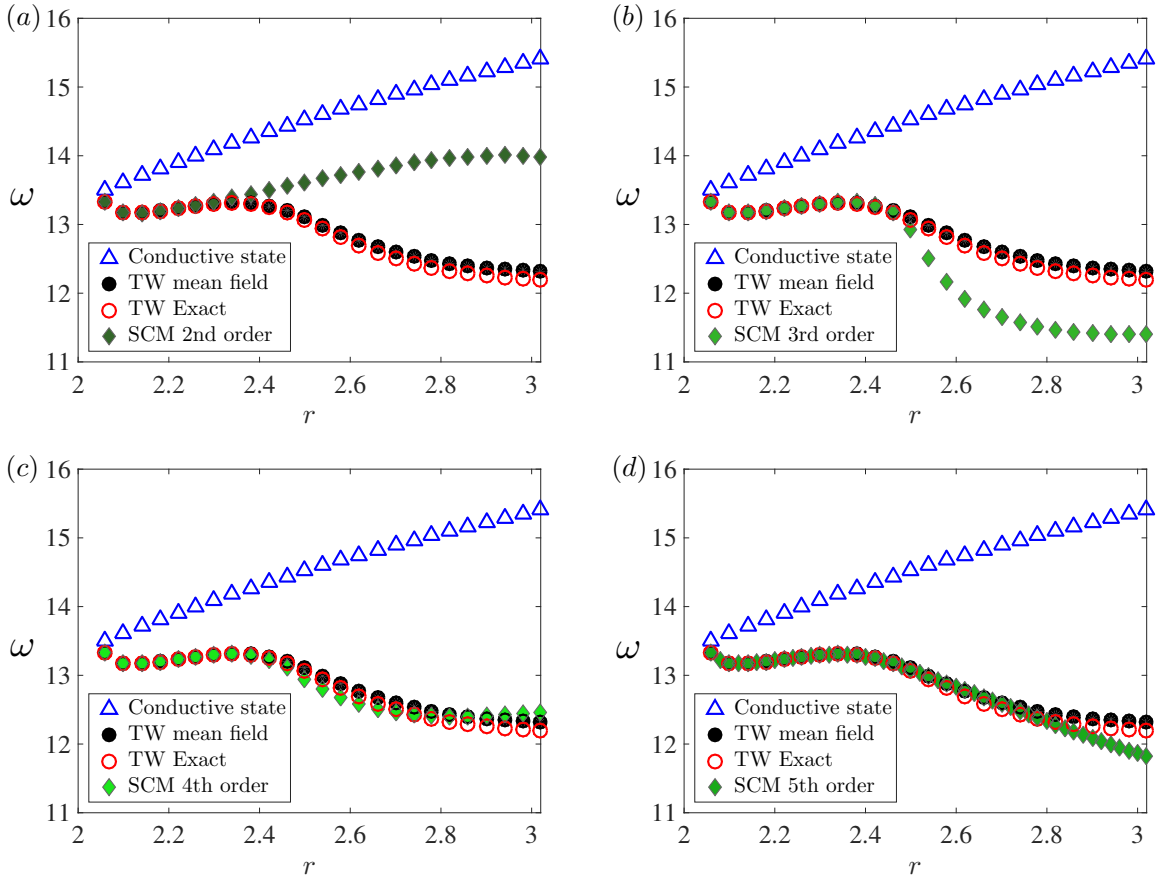


Figure 5.10 – Frequency as a function of Rayleigh number. Exact frequencies are shown by open circles (\circ). Frequencies obtained by linearization about the base and mean field are represented by triangles (\triangle) and solid circles (\bullet). Frequencies predicted by the SCM are shown by diamonds : (a) second order (\blacklozenge), (b) third order (\blacklozenge), (c) fourth order (\blacklozenge) and (d) fifth order (\blacklozenge)

necessarily imply the validity of SCM. The assumption that only the leading eigenmode contributes significantly to the distortion of the mean field does not hold. This result is supported by that of section 5.3.3, which showed that the three first modes must be included to recover the mean flow.

As was the case before, the mean field \bar{U} is independent of x , while U^R and U^I consist

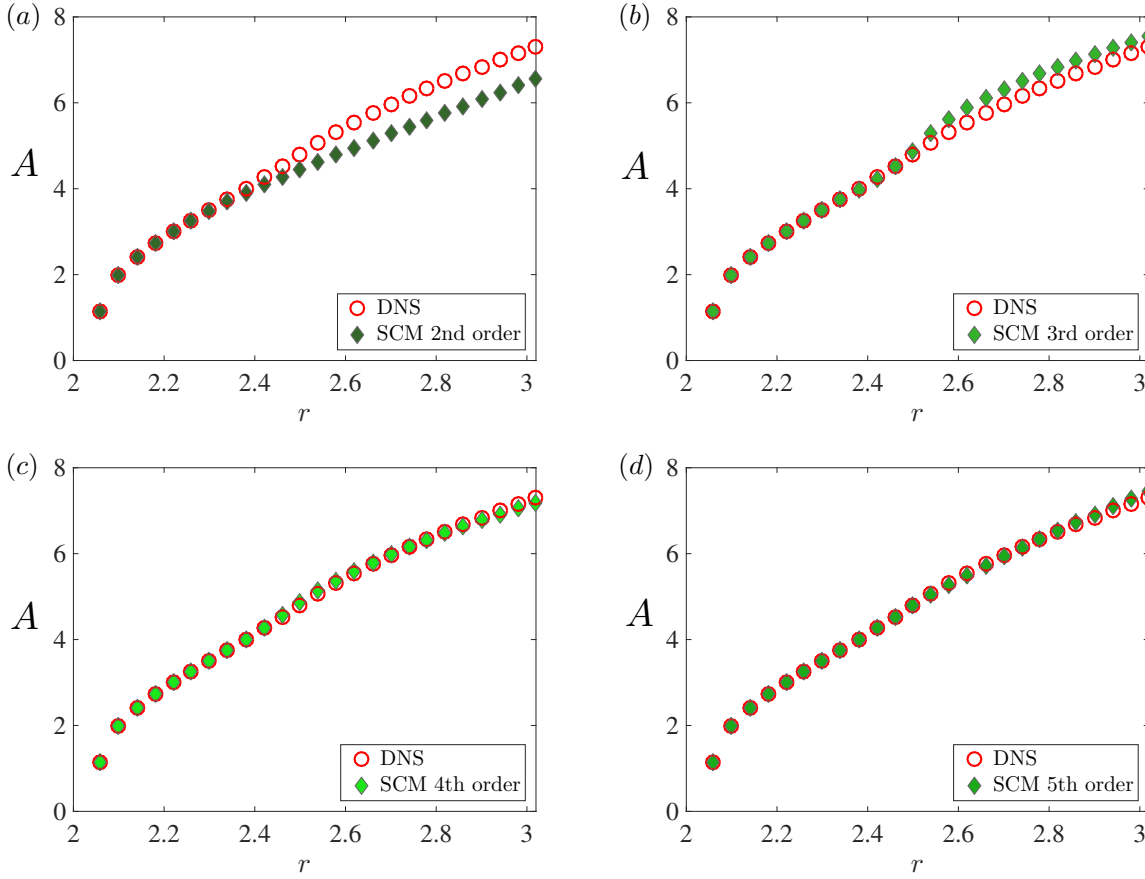


Figure 5.11 – Amplitude of the first mode computed by the self-consistent model at 2nd, 3rd, 4th and 5th order, compared with the fundamental Fourier coefficient amplitudes.

of profiles in z multiplied by trigonometric factors e^{ikx} or $\cos(kx)$, $\sin(kx)$. In order to compare these profiles over our entire Rayleigh-number range, as we did in figures 5.3 and 5.6, we construct two-dimensional functions of r and z out of the profiles \bar{U} , $U_1^R(z)$ and $U_1^I(z)$ obtained from SCM and from our full numerical values. Figure 5.9 compares the mean fields obtained by the first order SCM (dashed curves) with the exact mean fields (solid curves). We observe that the prediction of the temperature mean field shown in figure 5.9(a) is quite good. In contrast, the concentration and the streamfunction do not match the exact mean fields. Therefore, the self-consistent model fails to predict the nonlinear frequency and the mean field.

5.4.4 Higher-order SCM

Meliga [12] considered the second order in the SCM model in order to predict the nonlinear frequency and calculate the mean flow of the open cavity. In this section, we investigate the generalized SCM by considering successively higher orders in the terms (i) and (iii) of equations (5.25) and (5.26).

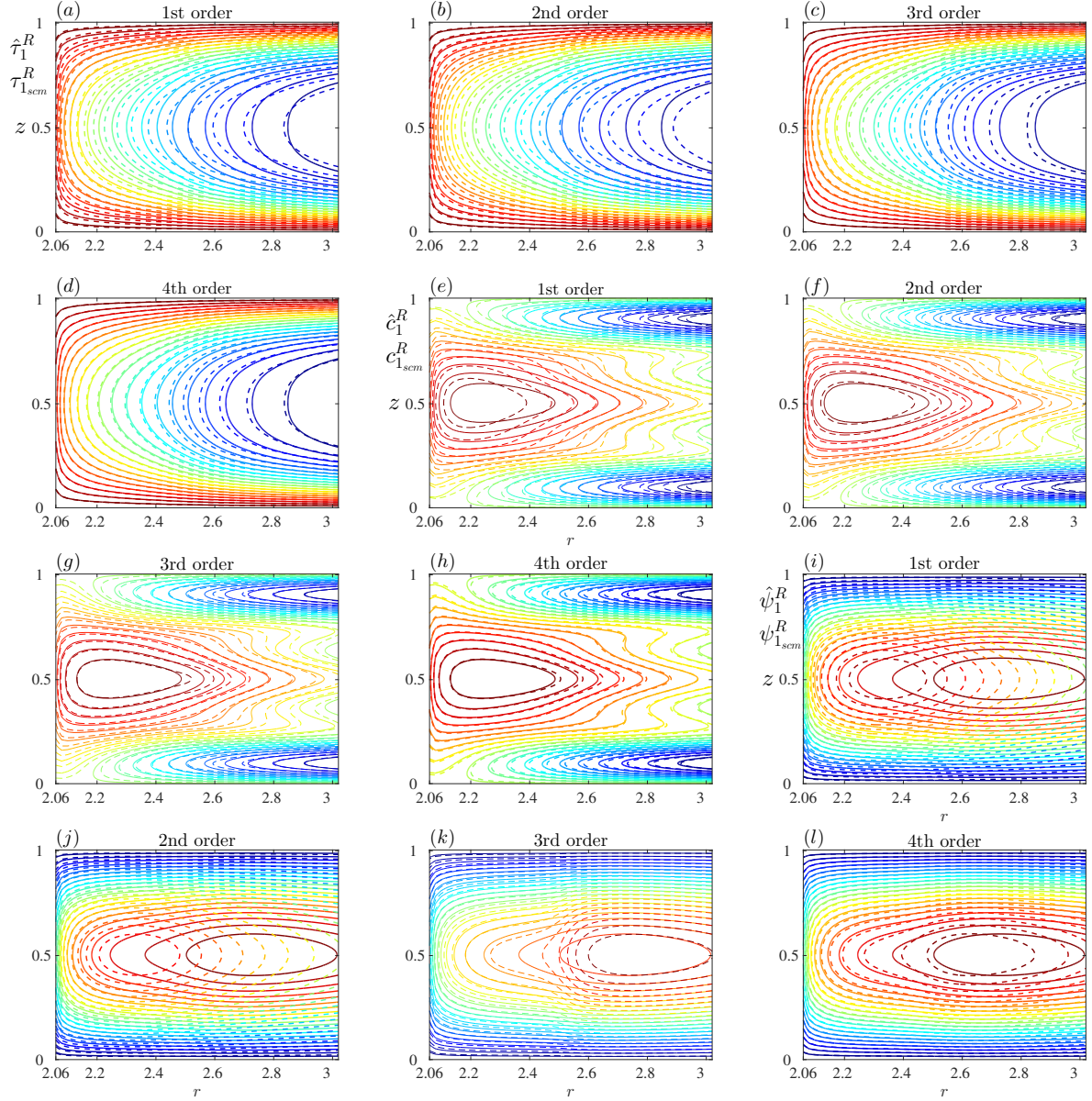


Figure 5.12 – Contours of the function $\hat{u}_1(r, z)$ constructed from the real part of the first Fourier coefficient (bold curves) and $\hat{u}_{SCM}(r, z)$ constructed from the real part of first mode obtained by SCM (dashed curves) at (a, e, i) 1st, (b, f, j) 2nd, (c, g, k) 3rd and (d, h, l) 4th order. (a-d) Shows the temperature fields, (e-h) concentration and (i-l) streamfunction. We observe clearly that the modes are better resolved when we increase the SCM order. Nevertheless, we note that even at the 4th order we do not reproduce perfectly the exact nonlinear modes

We present the system of equations corresponding to the fifth order:

$$0 = \mathcal{L}\bar{U} + \mathcal{N}(\bar{U}, \bar{U}) + \mathcal{N}(u_1, u_{-1}) + \mathcal{N}(u_2, u_{-2}) + \mathcal{N}(u_3, u_{-3}) + \mathcal{N}(u_4, u_{-4}) + \mathcal{N}(u_5, u_{-5}) \quad (5.41a)$$

$$i\omega u_1 = \mathcal{L}\bar{U}u_1 + \mathcal{N}(u_2, u_{-1}) + \mathcal{N}(u_{-1}, u_2) + \mathcal{N}(u_3, u_{-2}) + \mathcal{N}(u_{-2}, u_3) + \mathcal{N}(u_4, u_{-3}) + \mathcal{N}(u_{-3}, u_4) + \mathcal{N}(u_5, u_{-4}) + \mathcal{N}(u_{-4}, u_5) \quad (5.41b)$$

$$2i\omega u_2 = \mathcal{L}\bar{U}u_2 + \mathcal{N}(u_1, u_1) + \mathcal{N}(u_3, u_{-1}) + \mathcal{N}(u_{-1}, u_3) + \mathcal{N}(u_4, u_{-2}) + \mathcal{N}(u_{-2}, u_4) + \mathcal{N}(u_5, u_{-3}) + \mathcal{N}(u_{-3}, u_5) \quad (5.41c)$$

$$3i\omega u_3 = \mathcal{L}\bar{U}u_3 + \mathcal{N}(u_1, u_2) + \mathcal{N}(u_2, u_1) + \mathcal{N}(u_4, u_{-1}) + \mathcal{N}(u_{-1}, u_4) + \mathcal{N}(u_5, u_{-2}) + \mathcal{N}(u_{-2}, u_5) \quad (5.41d)$$

$$4i\omega u_4 = \mathcal{L}\bar{U}u_4 + \mathcal{N}(u_2, u_2) + \mathcal{N}(u_1, u_3) + \mathcal{N}(u_3, u_1) + \mathcal{N}(u_5, u_{-1}) + \mathcal{N}(u_{-1}, u_5) \quad (5.41e)$$

$$5i\omega u_5 = \mathcal{L}\bar{U}u_5 + \mathcal{N}(u_1, u_4) + \mathcal{N}(u_4, u_1) + \mathcal{N}(u_2, u_3) + \mathcal{N}(u_3, u_2) \quad (5.41f)$$

We added to the initial problem (5.35) four unknowns u_2, u_3, u_4, u_5 and four equations. We solve system (5.41) sequentially, including first u_2 , then u_3 , then u_4 and finally u_5 . Each of these successive systems are solved by a full Newton method.

Figure 5.10 shows the frequencies predicted by the higher order SCMs. We observe in figure 5.10(a-b) that by including the second and third order we improve the prediction of the frequency until $r = 2.4$ and deviate as we increase the reduced Rayleigh number. Figure 5.10(c) shows that even though the fourth order greatly improves the frequency prediction, it is not as precise as that of the exact mean field. Figure 5.10(d) shows that the frequency obtained from the SCM at fifth order gives almost a perfect match with the nonlinear frequency until $r \approx 2.8$ and deviates as we increase r . We recall that a full calculation in our case includes the eight modes of our horizontal spatial resolution $N_x = 8$.

Figure 5.11 shows the amplitude of the first mode u_1 obtained by the SCM and that of Fourier coefficient \hat{u}_1 . It is clear that the amplitude of u_1 is better predicted than the frequency. Indeed the amplitude obtained by the SCM at fourth and fifth order matches almost exactly that of Fourier coefficient \hat{u}_1 as shown in figure 5.11(c-d).

Figures 5.12 show the contours of the function $\hat{u}_1(r, z)$ representing the real part of the first Fourier coefficient compared to the leading mode obtained by the SCM at different orders. We observe that the first modes are quite well predicted at 4th order by the SCM; the 5th order (not shown) improved only very slightly the results of the 4th order SCM. It is obvious that we have to take account the eight orders to have an exact match between the first Fourier coefficient and the mode obtained by SCM.

5.5 Discussion

Thermosolutal convection presents a supercritical Hopf bifurcation that gives rise to two solutions, traveling waves, and standing waves. First, we have reproduced the results of Turton *et al.* [20]. We have computed the full nonlinear solution of the traveling waves. Then, we have carried out a linear stability analysis about the mean field of this solution and about the conductive state. The frequency (imaginary part of the eigenvalue) obtained by linearization about the mean field matches the nonlinear frequency; moreover, the growth rate (real part of the eigenvalue) is close to zero, showing that the mean field is marginally stable. Therefore, the traveling waves satisfies the RZIF property [20]. In contrast, the base field is unstable with a positive growth rate and the imaginary part of the eigenvalue deviates from the nonlinear frequency right after the threshold.

We then reconstructed the mean flow by considering successively the first, second and the third Fourier coefficients computed from the full nonlinear solution. The mean field is accurately reproduced by considering these three first Fourier coefficients. We have carried out linear stability analysis about the three approximations of the mean field and we have found that the frequency obtained about the mean field reconstructed from the first Fourier coefficient, matches the nonlinear frequency only for $r \in [2.06, 2.5]$ and the growth rate is nearly zero over the same range of reduced Rayleigh number. For $r > 2.5$ the frequency deviates from the nonlinear frequency and the growth rate leaves the marginal stability axis. The mean field reconstructed by considering both the first and the second Fourier coefficients does not improve the results. In contrast, the frequency obtained from the linearization about the mean field constructed from the three first Fourier coefficients matches the frequency obtained about the exact mean field over the entire range of Rayleigh number $r \in [2.06, 3]$ and the growth rate is nearly zero. These results already indicate that the self-consistent model will fail to reproduce the nonlinear results.

The self-consistent model developed in [9] couples the mean flow governing equation and the linearized Navier-Stokes equation through the Reynolds stress exerted by the leading eigenmode. It was assumed in [9] that for flows where the RZIF property is satisfied, the SCM reproduces features of the nonlinear dynamics such as the frequency, the amplitude, and the mean fields. We have shown that this assumption is not valid. Indeed, even the exact leading mode (first Fourier coefficient) does not suffice to reproduce the mean field.

We have implemented a full Newton method in order to avoid the convergence difficulties shown by the algorithm of [9]. We have found that for the traveling waves, the SCM predicts the nonlinear features only very near the threshold. To solve the SCM far from the threshold, we have also extended the SCM to take account successively of high orders in the Reynolds stress, which successively improved the predictions. At the fifth order, the amplitude of the leading mode is well predicted but the frequency starts to deviate from the nonlinear frequency for $r > 2.8$, suggesting that at high Rayleigh number we need to consider even higher orders.

5.6 Appendix

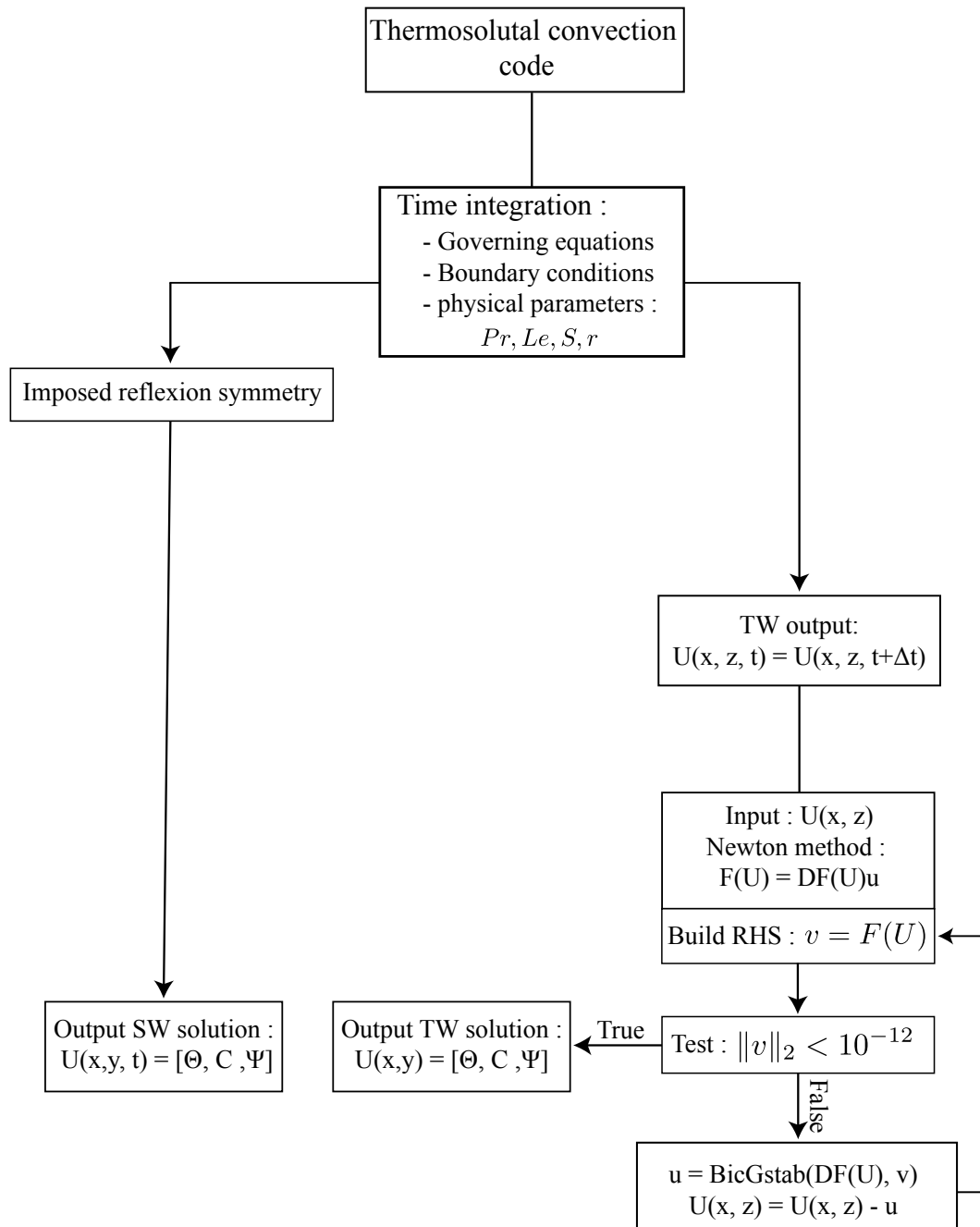


Figure 5.13 – Synoptic view of the time integration code.

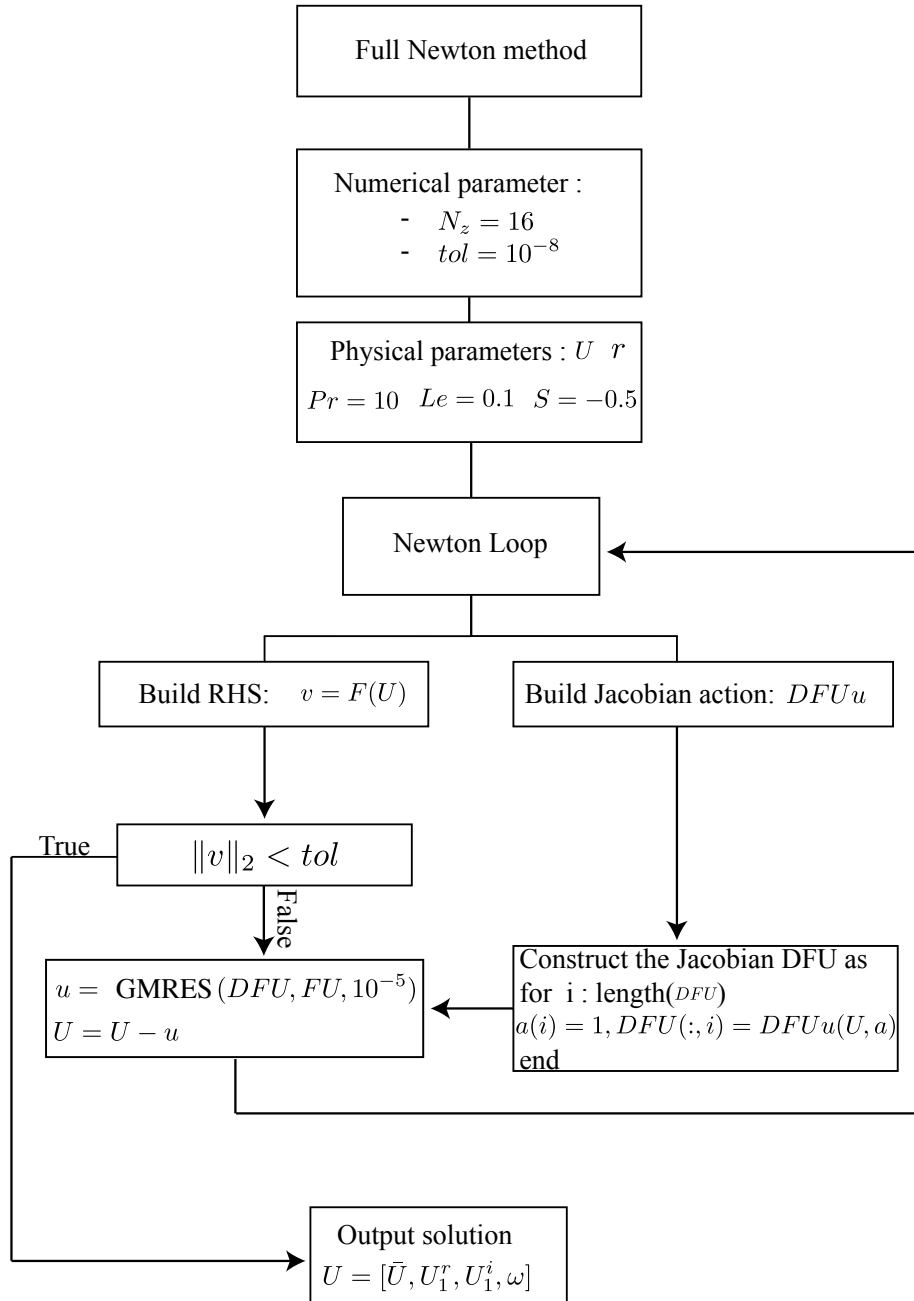


Figure 5.14 – Synoptic view of the full Newton method code.

Bibliography

- [1] BARKLEY, D 2006 Linear analysis of the cylinder wake mean flow. *EPL (Europhys. Lett.)* **75** (5), 750. [75](#), [80](#), [81](#), [82](#), [89](#)
- [2] FANI, A, CITRO, V, GIANNETTI, F & AUTERI, F 2018 Computation of the bluff-body sound generation by a self-consistent mean flow formulation. *Phys. Fluids* **30** (3), 036102. [76](#), [90](#)
- [3] HAMMOND, DA & REDEKOPP, LG 1997 Global dynamics of symmetric and asymmetric wakes. *J. Fluid Mech.* **331**, 231–260. [75](#)
- [4] JACKSON, CP 1987 A finite-element study of the onset of vortex shedding in flow past variously shaped bodies. *J. Fluid Mech.* **182**, 23–45. [75](#)
- [5] KNOBLOCH, E 1986 Oscillatory convection in binary mixtures. *Phys. Rev. A* **34** (2), 1538. [77](#)
- [6] MALKUS, WVR 1956 Outline of a theory of turbulent shear flow. *J. Fluid Mech.* **1** (5), 521–539. [75](#)
- [7] MAMUN, CHOWDHURY K & TUCKERMAN, LAURETTE S 1995 Asymmetry and hopf bifurcation in spherical couette flow. *Phys. Fluids* **7** (1), 80–91. [78](#)
- [8] MANTIČ LUGO, VLADISLAV 2015 Too big to grow self-consistent model for nonlinear saturation in open shear flows. PhD thesis, Ecole Polytechnique Fédérale de Lausanne, Lausanne. [89](#), [90](#)
- [9] MANTIČ-LUGO, VLADISLAV, ARRATIA, CRISTÓBAL & GALLAIRE, FRANÇOIS 2014 Self-consistent mean flow description of the nonlinear saturation of the vortex shedding in the cylinder wake. *Phys. Rev. Lett.* **113** (8), 084501. [74](#), [75](#), [80](#), [84](#), [89](#), [97](#)
- [10] MANTIČ-LUGO, VLADISLAV, ARRATIA, CRISTÓBAL & GALLAIRE, FRANÇOIS 2015 A self-consistent model for the saturation dynamics of the vortex shedding around the mean flow in the unstable cylinder wake. *Phys. Fluids* **27** (7), 074103. [76](#), [89](#), [90](#), [91](#)
- [11] MAUREL, A, PAGNEUX, V & WESFREID, JE 1995 Mean-flow correction as non-linear saturation mechanism. *Europhys. Lett.* **32** (3), 217. [75](#), [89](#)
- [12] MELIGA, PHILIPPE 2017 Harmonics generation and the mechanics of saturation in flow over an open cavity: a second-order self-consistent description. *J. Fluid Mech.* **826**, 503–521. [76](#), [94](#)

- [13] MITTAL, SANJAY 2008 Global linear stability analysis of time-averaged flows. *Int. J. Numer. Meth. Fluids* **58** (1), 111–118. [75](#), [80](#)
- [14] PIER, BENOÎT 2002 On the frequency selection of finite-amplitude vortex shedding in the cylinder wake. *J. Fluid Mech.* **458**, 407–417. [75](#), [80](#)
- [15] RAYLEIGH, LORD 1916 On convection currents in a horizontal layer of fluid, when the higher temperature is on the under side. *Philos. Mag.* **32** (192), 529–546. [77](#)
- [16] SIPP, DENIS & LEBEDEV, ANTON 2007 Global stability of base and mean flows: a general approach and its applications to cylinder and open cavity flows. *J. Fluid Mech.* **593**, 333–358. [75](#), [80](#)
- [17] STUART, JOHN TREVOR 1958 On the non-linear mechanics of hydrodynamic stability. *J. Fluid Mech.* **4** (1), 1–21. [75](#)
- [18] TRIANTAFYLLOU, GEORGE S, TRIANTAFYLLOU, MICHAEL S & CHRYSSOSTOMIDIS, C 1986 On the formation of vortex streets behind stationary cylinders. *J. Fluid Mech.* **170**, 461–477. [75](#)
- [19] TUCKERMAN, LAURETTE S 2001 Thermosolutal and binary fluid convection as a 2×2 matrix problem. *Physica D* **156** (3-4), 325–363. [76](#)
- [20] TURTON, SAM E, TUCKERMAN, LAURETTE S & BARKLEY, DWIGHT 2015 Prediction of frequencies in thermosolutal convection from mean flows. *Phys. Rev. E* **91** (4), 043009. [75](#), [76](#), [78](#), [80](#), [81](#), [82](#), [86](#), [97](#)
- [21] ZIELINSKA, BJA, GOUJON-DURAND, S, DUSEK, J & WESFREID, JE 1997 Strongly nonlinear effect in unstable wakes. *Phys. Rev. Lett.* **79** (20), 3893. [89](#)

Chapter 6

Preliminary studies

We describe in this chapter two preliminary studies, the first on the lid-driven cavity flow and the second on the Bénard prism.

6.1 Lid-driven cavity flow

We have studied the dynamics of an incompressible flow in a two-dimensional lid-driven square cavity. We have computed the nonlinear dynamics, the temporal spectra, and the Fourier modes. By a linear stability analysis, we localized the threshold of the Hopf bifurcation. The growth rate σ , which is the real part of the eigenvalue λ , crosses the marginal stability axis at $Re = 8018.2$ which is in very good agreement with Fortin *et al.* [9], Botella & Peyret [7], Auteri *et al.* [1] and Bruneau & Saad [8]. As in Barkley [3], Turton *et al.* [14] and for the open cavity presented in Chapter 3, we have investigated the linear analysis of the mean flow of the lid-driven cavity. We observed that the growth rate is close to zero, showing the marginal stability of the lid-driven cavity mean flow and that the imaginary part of the eigenvalue matches the nonlinear frequency. We have therefore added a new configuration for which the RZIF property is satisfied.

This is a preliminary study to prepare to test the self-consistent model of Mantič-Lugo *et al.* [13] on this geometry by using a full Newton method.

6.1.1 Problem

We present the dynamics of the incompressible flow in a two-dimensional lid-driven square cavity. We impose a horizontal velocity ($u = -1, v = 0$) at the upper wall and we impose a no-slip boundary condition ($u = 0, v = 0$) at the other walls. Therefore, the flow is generated by the shear of the lid displacement as shown by the configuration in figure 3.1. As in Botella & Peyret [7] and Auteri *et al.* [1], the lid moves towards the left. (The flow is by reflection symmetry equivalent to that caused by the lid moving to the right as in Goodrich *et al.* [10]). The discontinuity in the boundary conditions between the moving lid and the static vertical walls causes the singularities at upper corners of the cavity. Indeed, the discontinuity in the horizontal velocity implies infinite pressure and vorticity as shown by Botella & Peyret [7]. This singularity does not play a major role in the dynamics of the flow and it is mainly a numerical problem for spectral methods. Accordingly, we have not regularized the singularities in this current study.

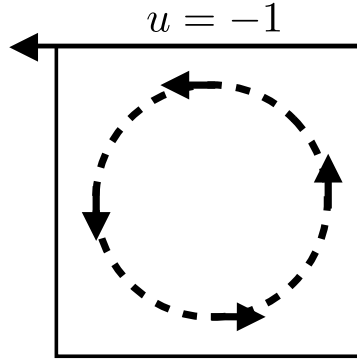


Figure 6.1 – Geometry of our study. At the upper wall, a uniform unit velocity ($u = -1$; $v = 0$) is imposed. On the other walls, we impose a no-slip boundary condition ($u = 0$; $v = 0$).

The nonlinear problem is governed by the two-dimensional incompressible Navier-Stokes equations. The linear problems about the base and mean flow are governed by the linearized Navier-Stokes equations. These procedures and governing equations have been presented for the shear-driven open cavity flow in Chapter 3, for Taylor-Couette flow in Chapter 4 and for thermosolutal convection in Chapter 5. Therefore in this chapter, we will only present the results.

6.1.2 Numerical simulation and validation

Numerical method

This study has been carried out with FreeFEM++ software developed by Hecht [11] written in C^{++} as its name indicates. This software is based on finite elements for spatial discretization for solving partial differential equations, more specifically the Taylor-Hood elements with a polynomial element of order one P_1 for the pressure p and of order two $[P2, P2]$ for the velocity fields $[u, v]$. The time is discretized by a Characteristics-Galerkin method; see for example Azañez *et al.* [2] and Benítez & Bermúdez [6]. The stationary solution is computed by a Newton-Raphson method. The linear problem is also solved in FreeFEM as a generalized eigenvalue problem with the shift-invert method using the ARPACK library.

Comparison with literature

The validation of the results consists first of all in verifying that the calculated solution is independent of the mesh resolution. Secondly the accuracy is validated by comparing the solution with the results of Auteri *et al.* [1]. The computation time of the stationary solution (base flow) is much smaller than that of the temporal integration. Therefore, the mesh convergence and the accuracy have been checked on the stationary solution and also on eigenvalues obtained for different Re by the linear stability analysis about the base flow as shown in figure 6.3.

The accuracy of the solution has been verified on the streamwise and vertical velocities at the cavity midplane. Figure 6.2(a,b) compares the evolution of the velocity $u(0.5, y)$ and $v(x, 0.5)$ for $Re = 1000$ with the results of Auteri *et al.* [1]. The solution that we computed

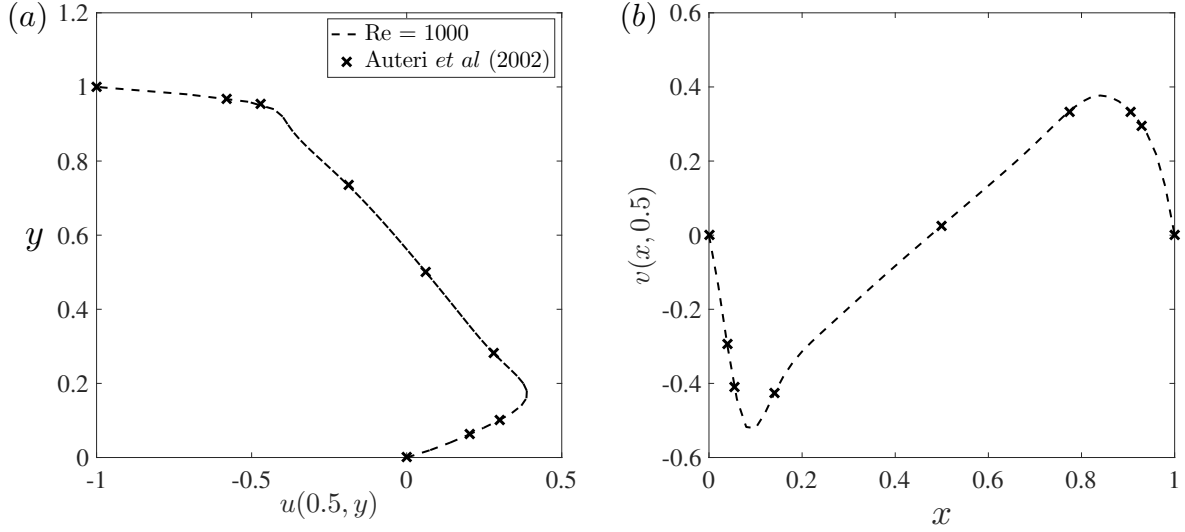


Figure 6.2 – Comparison of (a) $u_{\max}(0.5, y)$ and (b) $v_{\max}(x, 0.5)$ of the stationary solution obtained by using the mesh at 48039 $n_{d.o.f}$ with the results of Auteri *et al.* [1] for $Re = 1000$. We observe that even though the mesh is not very fine, we obtain very good agreement with Auteri *et al.* [1], who used finite differences for space discretisation with a structured mesh resolution of 1024×1024 .

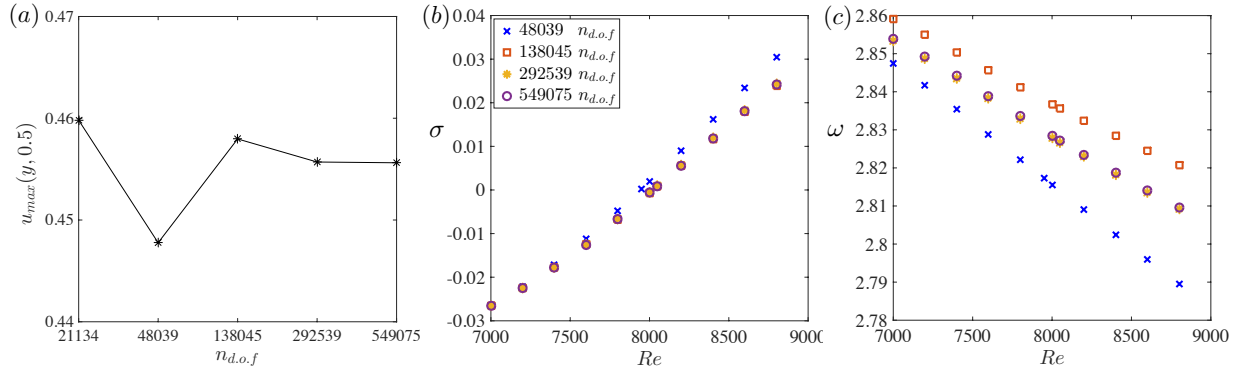


Figure 6.3 – (a) Maximal velocity $u_{\max}(0.5, y)$ maximized over y at $x = 0.5$ and $Re = 9000$ for different mesh resolutions. The solution is independent of the resolution with 292539 degrees of freedom ($n_{d.o.f}$). (b) Growth rate $\sigma = \Re(\lambda)$ obtained by linear stability analysis about the base flow as a function of Re and for different mesh resolutions. We observe that the growth rate is independent of the resolution starting with 138045 $n_{d.o.f}$. (c) The frequency $\omega = \Im(\lambda)$ is more sensitive to the mesh resolution than the growth rate. Indeed, the frequency is approximately independent of the mesh when the mesh attains 292539 $n_{d.o.f}$ cf. Tab 6.1.

is indistinguishable from that of Auteri *et al.* [1] even though we used a relatively coarse mesh with 48039 $n_{d.o.f}$.

In the next section, we will study the dependence of the solution on the mesh resolution.

Mesh refinement

The different mesh resolutions tested and the thresholds Re_c of the first Hopf bifurcation obtained for each mesh resolution are listed in Table 6.1.

Figure 6.3(a) shows the evolution of the maximum of the horizontal velocity $u_{max} = \max(u(0.5, y))$ in the vertical direction at the center of the cavity and $Re = 9000$ for different unstructured meshes. We observe that the solution begins to be independent of the mesh resolution from 292539 $n_{d.o.f}$. The results of the linear stability analysis about the base flow for the different meshes are presented in figures 6.3(b-c). Figure 6.3(b) shows that the growth rate σ is not very sensitive to the mesh resolution and thus the threshold of the bifurcation is not significantly impacted as shown by table 6.1. Figure 6.3(c) shows that the frequency ω is on the other hand, quite sensitive to the mesh resolution.

mesh	triangles	vertices	$n_{d.o.f}$ [u v p]	Re_c
I	4598	2388	21134	x
II	10528	5397	48039	7943.455
III	30426	15439	138045	8022.002
IV	64633	32655	292539	8018.271
V	72210	121516	549075	8018.272

Table 6.1 – Summary of the meshes tested, with u, v the streamwise and vertical velocities respectively, and p the pressure field. Thresholds are obtained for the different meshes by linear interpolation of the growth rates shown in figure 6.3(b). The threshold converges at mesh IV.

In this preliminary study, we will use the mesh with a resolution of 48039 $n_{d.o.f}$, which corresponds to mesh II in table 6.1. For our definitive study, we will increase the resolution and use mesh IV to study the self-consistent model applied in this geometry.

6.1.3 Results

Nonlinear dynamics

The flow is produced by the shearing of the cavity lid displacement. The stationary stable flow (base flow) at low Reynolds number consists of a global recirculation that is reflection symmetric with respect to the vertical midplane and attached by the shear layer to the moving lid as showed by Kawaguti [12]. This recirculation is surrounded by a shear boundary layer developing on the other walls. This stationary solution becomes unstable at high Reynolds number. The breaking of the reflection symmetry occurs through a Hopf bifurcation at the threshold $Re_c = 7943.4$. This threshold is calculated from linear stability analysis about the base flow by linear interpolation of the growth rates, which is in good agreement with the result of Auteri *et al.* [1]. The 0.9% difference is due to the coarse mesh. Indeed, the difference between the threshold obtained with the highly resolved mesh V shown in table 6.1 with that of Auteri *et al.* [1] is only 10^{-4} . For $Re > Re_c$ the base flow exists but is unstable. The perturbation moves from the base state to a time-periodic state as shown by the time trace of the velocity $u(x_1, y_1)$ at $(x_1, y_1) = (0.7, 0.87)$ in figure 6.5(a). In figure 6.4 we show the streamfunction fluctuations ψ' of the time-periodic flow at $Re = 8400$ over a period T spaced by quarter of a period. The flow consists of five counter-rotating vortices attached to the right wall, and originates from a shear instability. These vortices are stretched and entrained by the shear layer that develops just below the moving lid and rotates within the cavity following by inertia the global recirculation. The vortices in figure 6.4 rotate in a counterclockwise sense because the lid moves to the left. We observe also the correspondence between the quarter period and the quarter spatial phase shift typical of traveling waves.

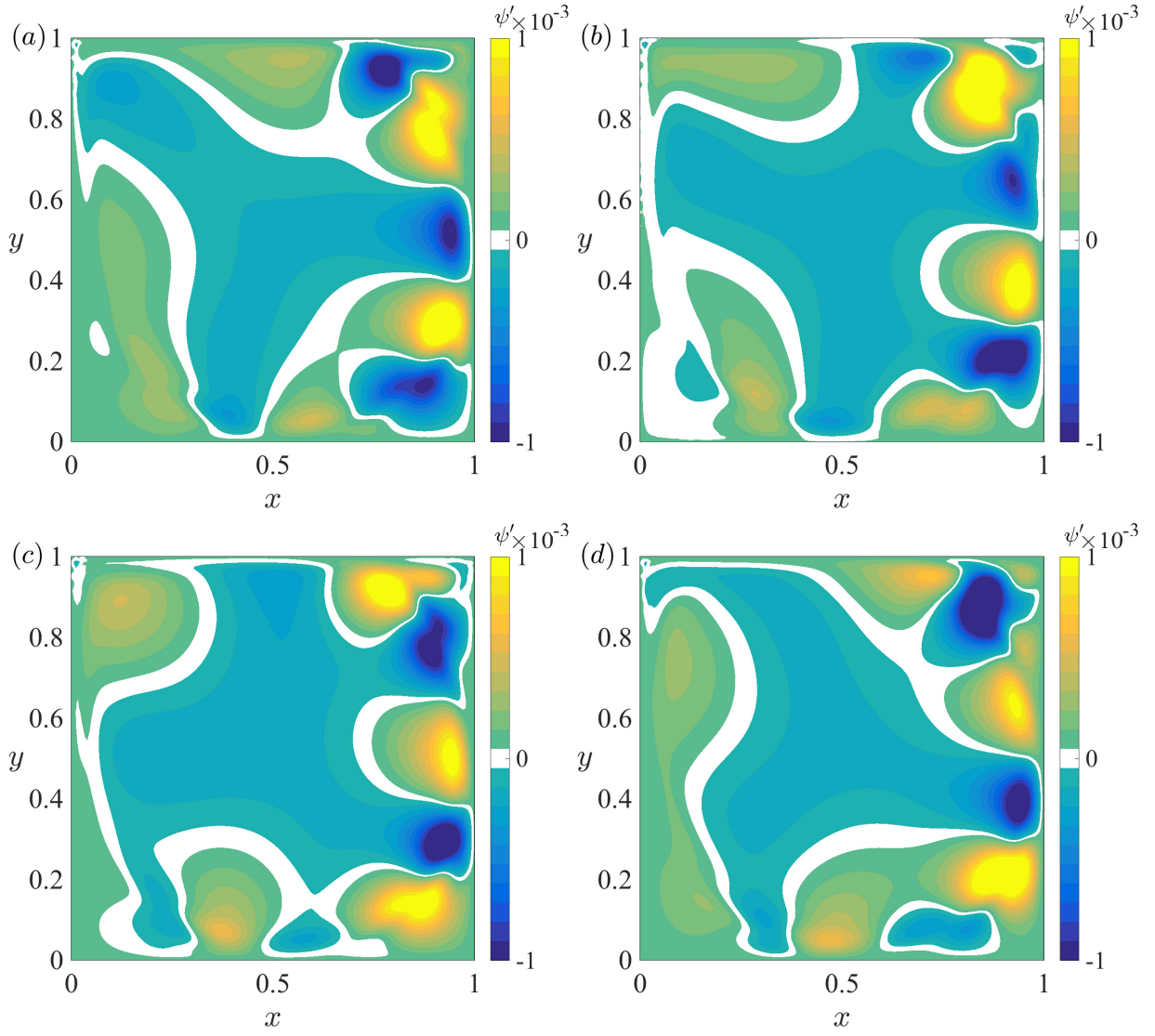


Figure 6.4 – Streamfunction fluctuations ($\psi' = \psi - \bar{\psi}$) over one period for $Re = 8400$. (a) $t = 0$, (b) $\frac{T}{4}$, (c) $\frac{T}{2}$, (d) $\frac{3T}{4}$. We observe the counter clockwise displacement of the structures similar to traveling waves.

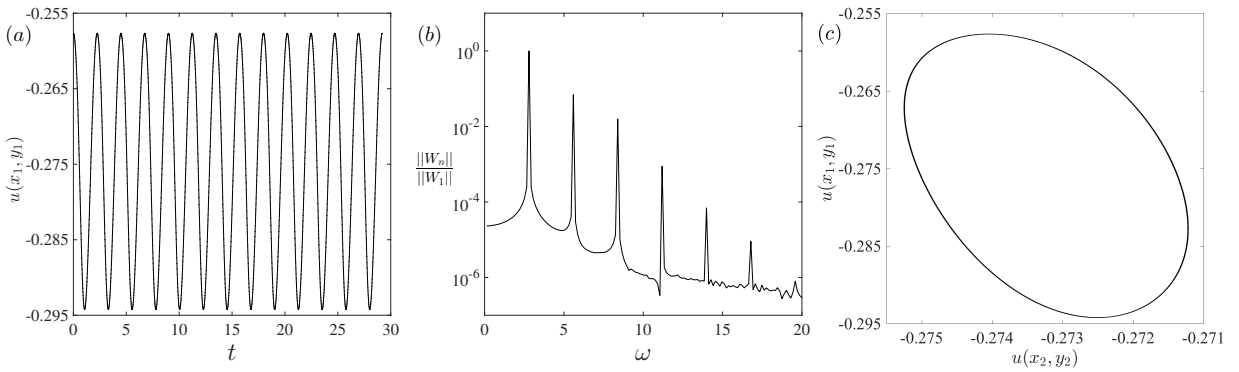


Figure 6.5 – For $Re = 8400$, (a) time series of streamwise velocities at $(x_1, y_1) = (0.7, 0.87)$. (b) Temporal spectrum of the horizontal velocity normalized by the fundamental frequency. (c) Phase portrait with streamwise velocity $U(x_1 = 0.7, y_1 = 0.87)$ and $U(x_2 = 0.25, y_2 = 0.85)$, showing the limit cycle produced by the Hopf bifurcation.

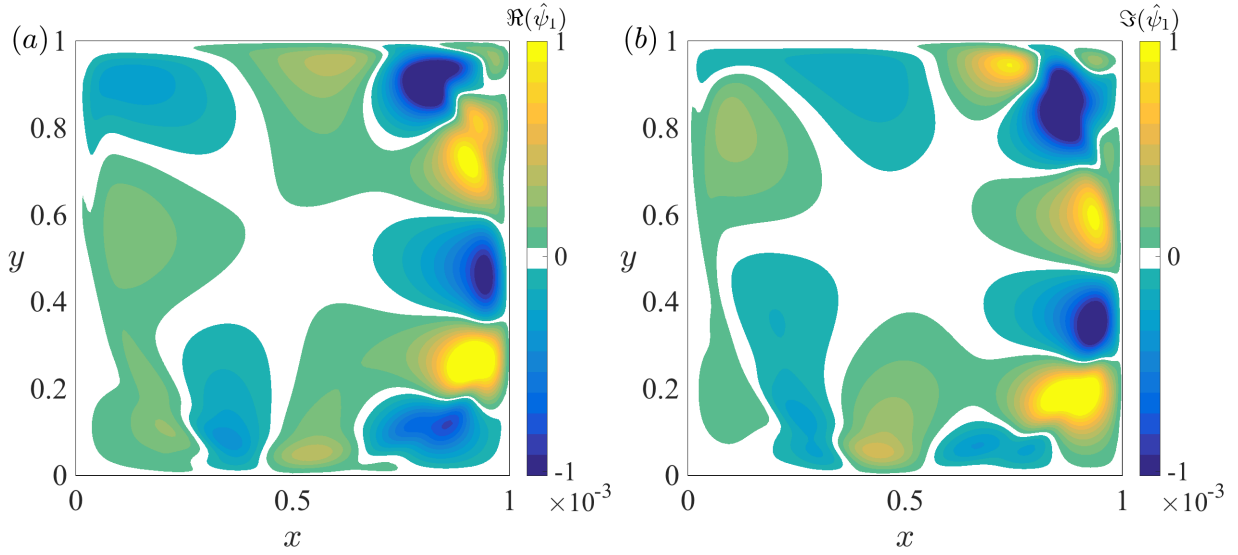


Figure 6.6 – (a) Real $\Re(\hat{\psi}_1)$ and (b) imaginary $\Im(\hat{\psi}_1)$ parts of the first Fourier coefficient of the streamfunction at $Re = 8400$. We observe the typical phase shift between the real and imaginary part, similar to that observed in figure 6.4.

Figure 6.5(b) shows the temporal spectrum of the horizontal velocity normalized by the fundamental frequency. We observe that the second harmonic is not negligible. Figure 6.5(c) shows the phase portrait exhibiting the limit cycle typical of a Hopf bifurcation.

Figures 6.6(a,b) show the real and imaginary part of the first temporal Fourier coefficient of the streamfunction at $Re = 8400$. This Fourier coefficient is very similar to the streamfunction fluctuations shown in figure 6.4 but at a different phase.

The phase shift between the real and imaginary part is in a clockwise sense, the opposite to that shown in figure 6.4, which can be shown to be as expected.

Linear stability analysis about the base and mean flow

In Figure 6.7 we show the results obtained by linear stability analysis about the base flow and by linearization about the mean flow. Figure 6.7(a) shows the zero crossing of the growth rate σ obtained about the base flow (crosses). This indicates that the base flow is unstable and locates at the same time the Hopf bifurcation threshold at $Re_c = 7943.4$. Figure 6.7(b) shows that the frequency ω obtained from linear stability analysis about the base flow matches the nonlinear frequency (stars) at the threshold and diverge from it when increasing the Reynolds number. Whereas the frequency obtained by linearization about the mean flow matches exactly the nonlinear frequency near the threshold and deviates only slightly when increasing the Re . In addition, the growth rate obtained about the mean flow is very close to zero. This result confirms that the RZIF property is satisfied in this case.

The base flow at $Re = 8400$ (figure 6.8(b)) presents a primary recirculation at the center of the cavity with secondary recirculations on the corners. The mean flow computed from the nonlinear simulation is very similar to the base flow as shown by the very small distortion in figure 6.8(b). Figure 3.11 shows the leading eigenvector obtained about the base flow at $Re = 8400$ (a,b) and that obtained by linearization about the mean flow (c,d). These eigenvectors are qualitatively similar to the first Fourier coefficient but with

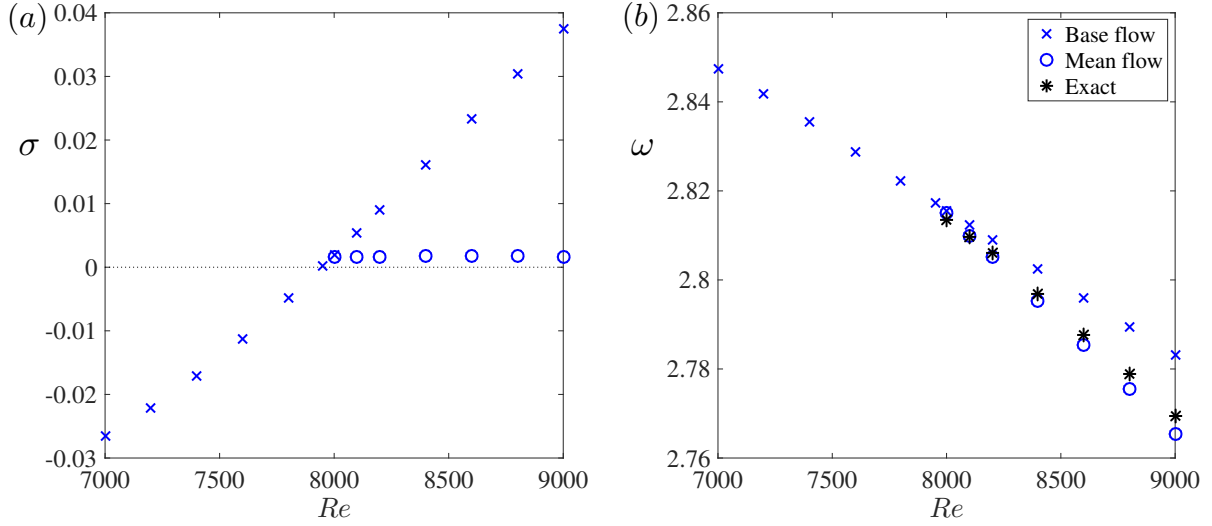


Figure 6.7 – Eigenvalues $\lambda = \sigma + i\omega$ obtained by linearization about the base flow (crosses) and mean flow (circles). The exact frequency is shown by stars. (a) Growth rates σ . (b) Frequency ω . The growth rates about the mean flow are nearly zero and the frequency obtained by linearization about the mean flow is very close to the exact nonlinear frequency.

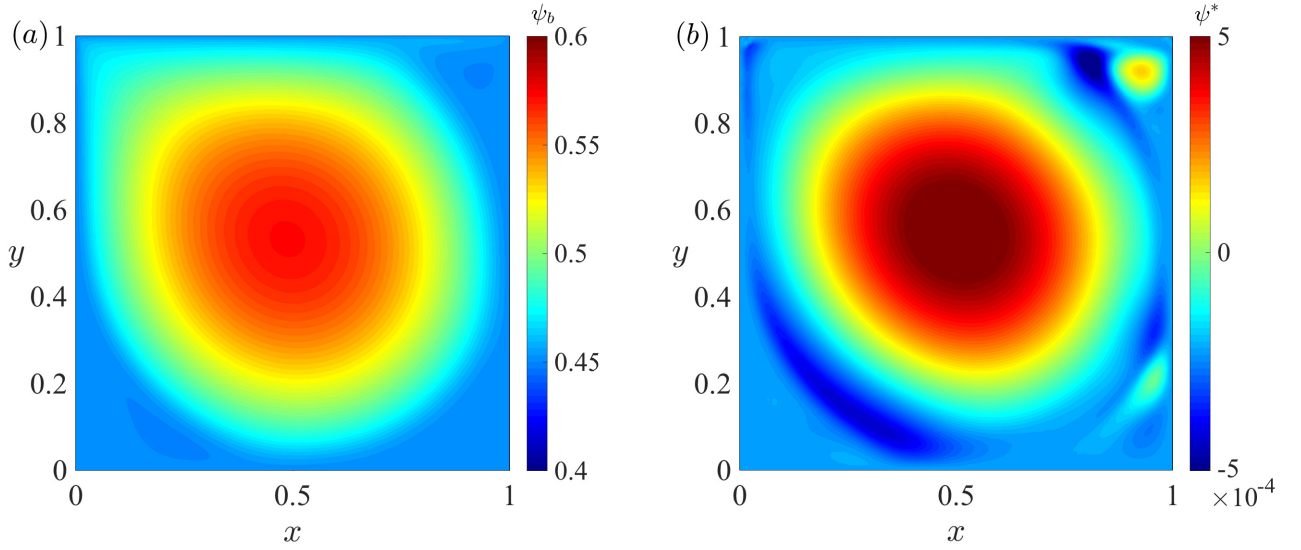


Figure 6.8 – (a) Stationary solution (base flow) of streamfunction ψ_b . (b) Distortion ($\psi^* = \psi_b - \bar{\psi}$) at $Re = 8400$. The mean flow $\bar{\psi}$ and the base flow are almost identical as shown by the distortion scale.

different phases. Quantitatively the eigenvectors could not be compared to the first Fourier coefficient as linear stability analysis does not enable to compute amplitudes of the modes.

Portions of the eigenvalue spectra obtained about the base flow for different Re are shown in figure 6.10. Figure 6.10 shows that other Hopf bifurcations occur for $Re > 8600$. Figure 6.11 shows the full spectra obtained about the mean flow. The growth rate of the leading eigenmode is almost on the marginal stability axis throughout the entire range $Re \in [8000, 9000]$. Moreover, the unstable modes that appear at $Re > 8600$ in figure 6.10 are not present in figure 6.11.

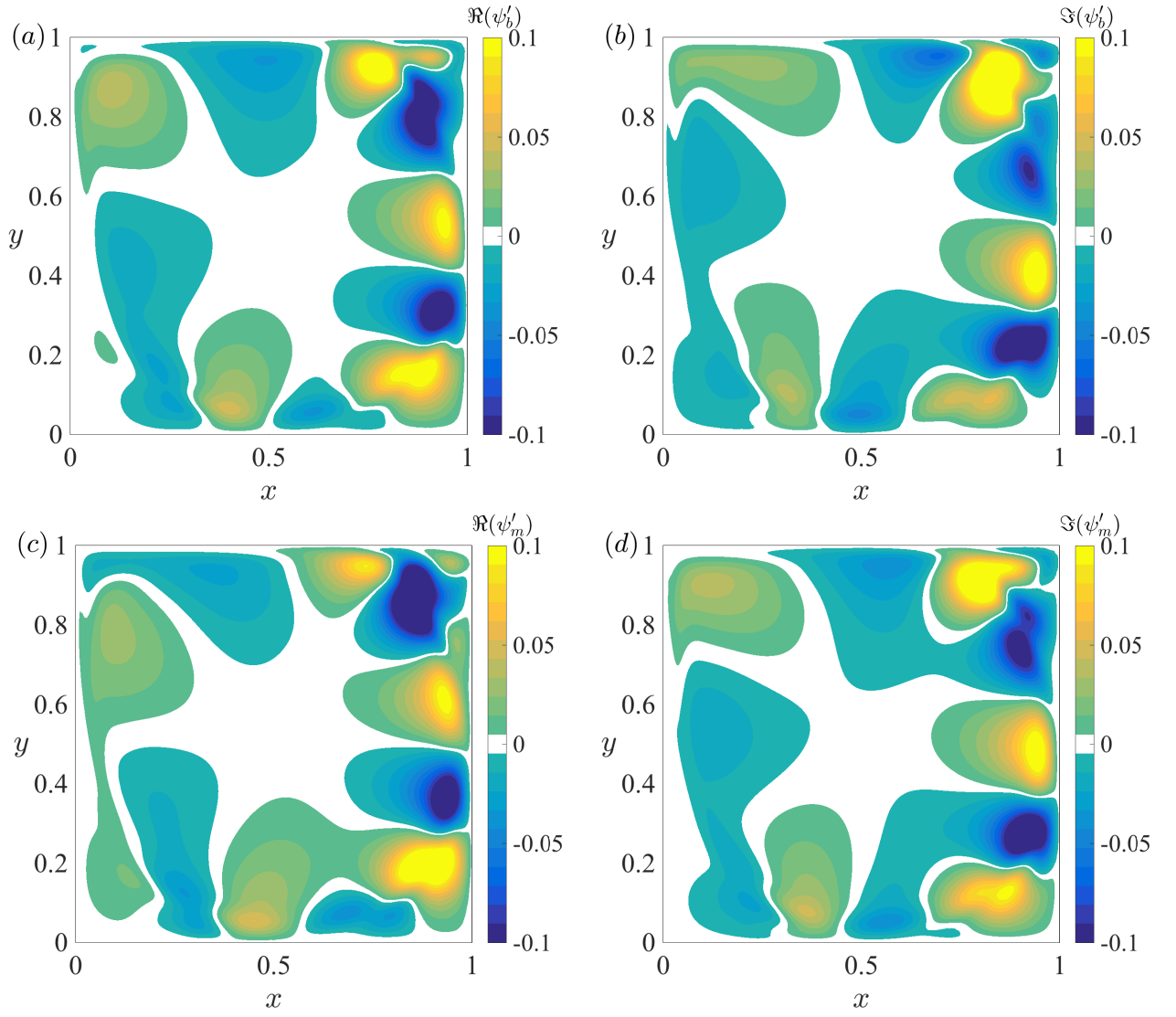


Figure 6.9 – Streamfunction of the real and imaginary parts of the leading unstable eigenmodes about the base flow (a,b) and mean flow (c,d) at $Re = 8400$.

6.1.4 Conclusion

In this study, we have validated our simulation with respect to the literature. We have described briefly the dynamics of lid-driven cavity flow. Importantly, we have confirmed by means of linear stability analysis about the base flow and linearization about the mean flow that the RZIF property is satisfied in this configuration.

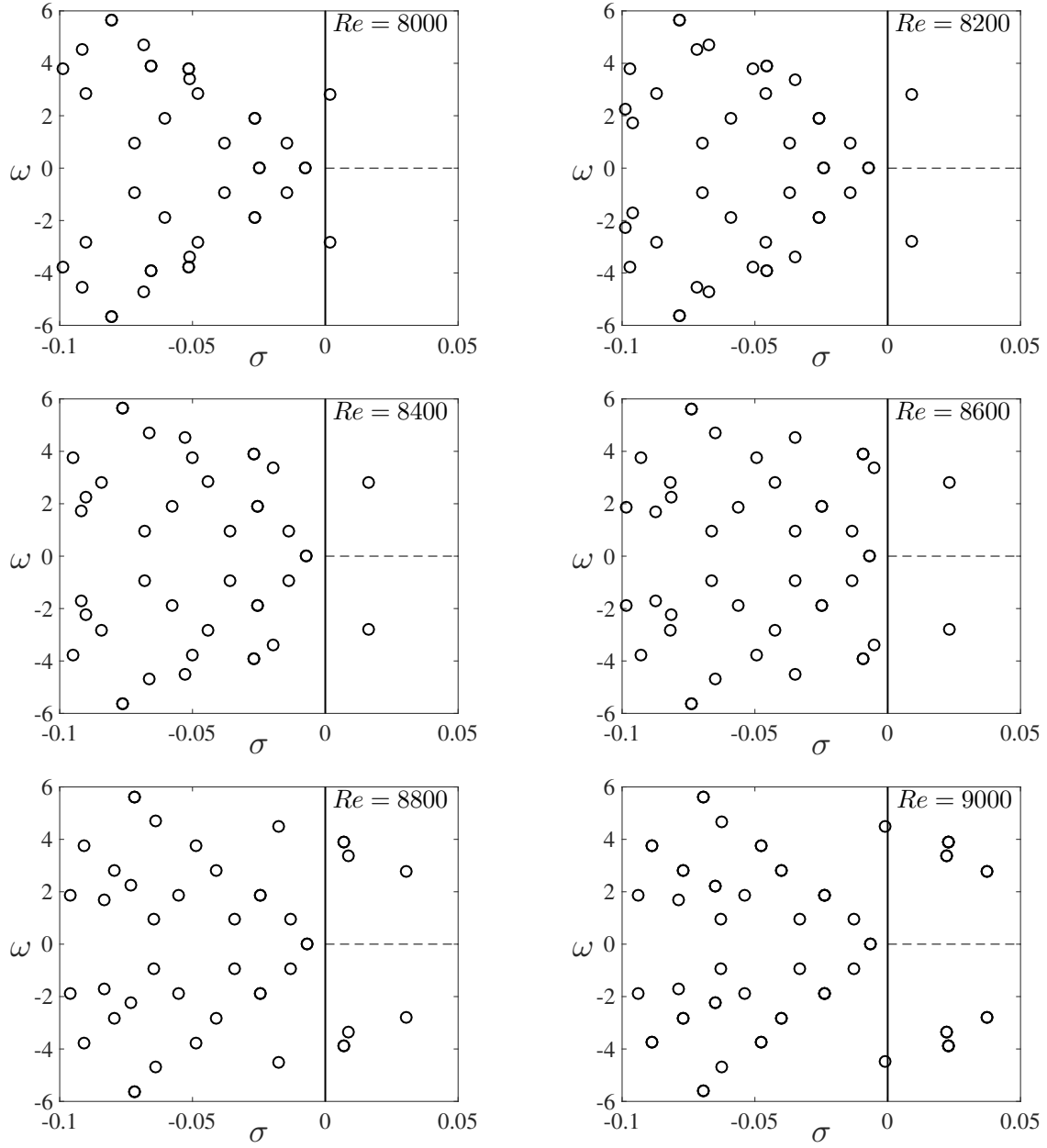


Figure 6.10 – Full eigenvalue spectrum for different Re , obtained by linearization about the base flow.

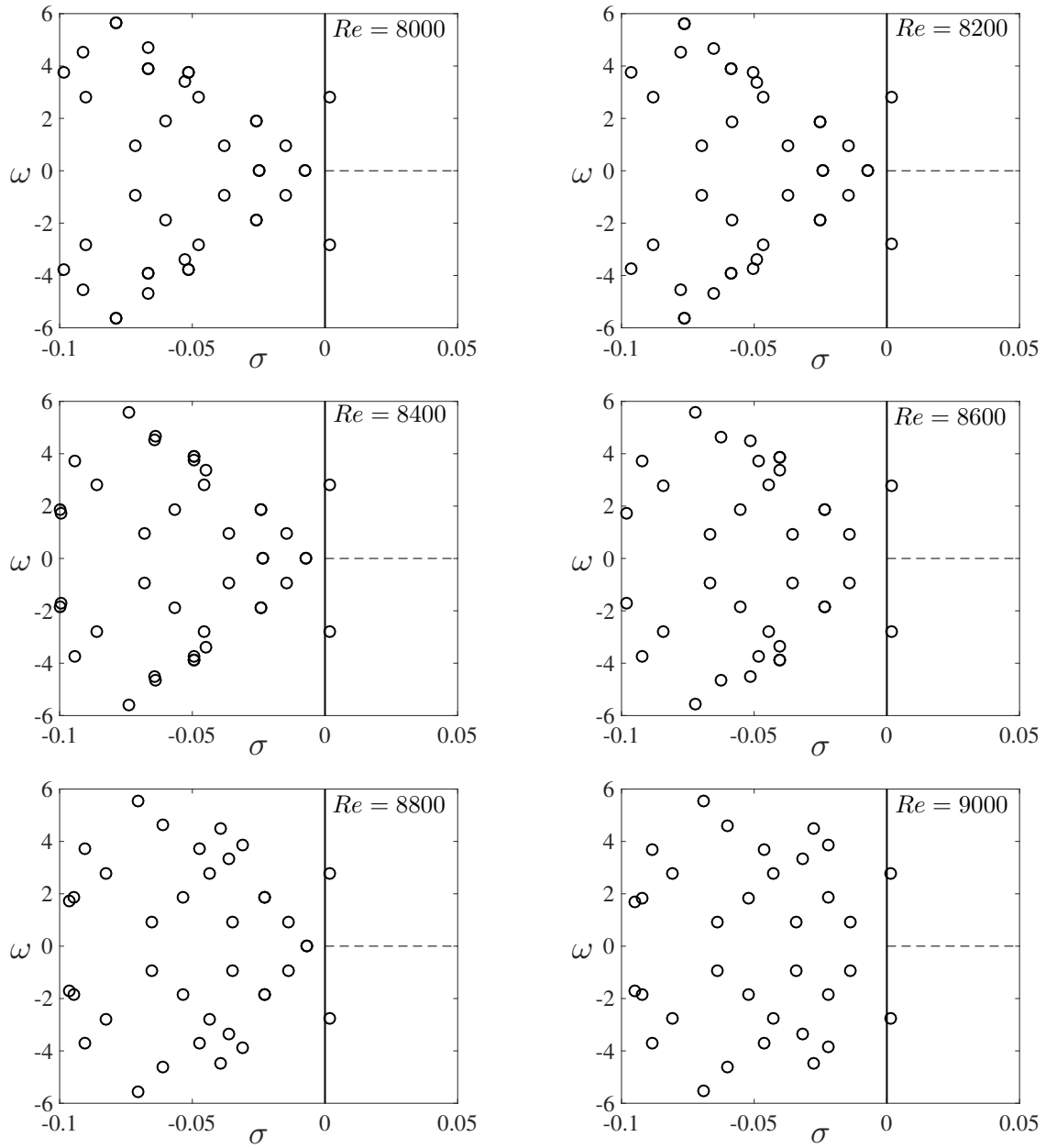


Figure 6.11 – Full eigenvalue spectrum for different Re , obtained by linearization about the mean flow.

6.2 Stability analysis of the Bénard arrow

J. E. Wesfreid, Y. Bengana

Henri Bénard (1874-1939) began the systematic experimental study of two hydrodynamic systems: the thermal convection of fluids heated from below and the periodic vortex shedding behind a bluff body in a flow. Using optical methods, he discovered the spatial pattern or cellular organization of this kind of fluid motion [4, 15, 16].

Motivated by his experience in optical methods in hydrodynamics, Bénard built a water tank in which a rectangular elongated obstacle with a pointed upstream shape, is displaced, producing a deformation in the free surface. He associated this deformation with the presence of vortices in the fluid and he reported that he “was surprised to discover two splendid lines of alternate vortices...” [1]. Bénard performed systematic experiments using these elongated bodies, for which the aspect ratio L/D of these obstacles varied between 2.5 and 40. where L is the length of the body in the flow direction and D its transversal width. He observed that the wavelength λ (the distance between successive vortices in one line) grew with the transversal dimension D and did not depend on the longitudinal dimension L . The wavelength also increased with the viscosity ν of the fluid but not, as a first approximation, with the velocity U of the obstacle.

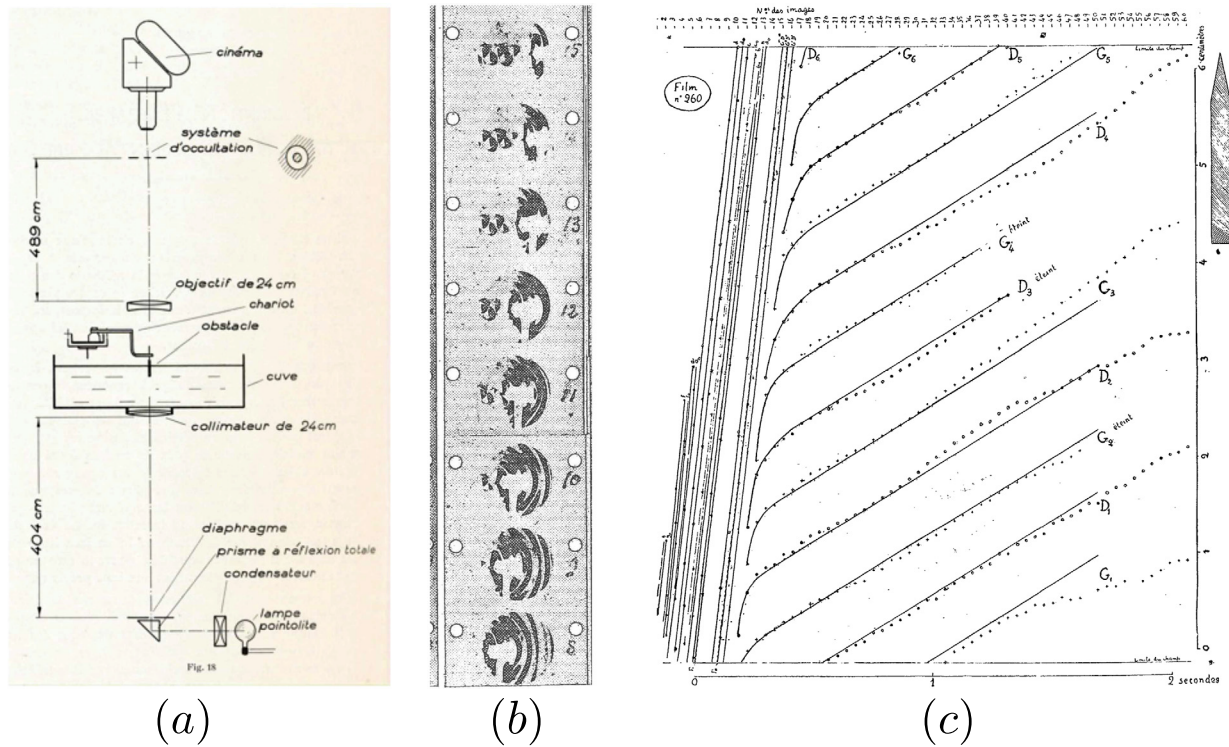


Figure 6.12 – (a) Scheme of experimental apparatus, with the water tank and optical system for the cinematograph (here in the version of the facility that was installed in Paris in 1930); (b) sequence from the original films showing images of the vortex shedding during the motion of the body to the right. In image 8, ripples of the fluid surface around the body are observed. In image 10, on the left, a first vortex appears within the field of vision and in image 15, when the body leaves the field, the two lines of alternating vortices clearly appear; (c) spatio-temporal plot of each vortex displacement motion. On the left hand side is plotted the displacement of the bluff body. The difference of slopes gives the phase velocity of the shedding. From [5].

Although a large literature exists on the theoretical prediction of these parameters in the

case of vortex shedding behind a circular cylinder, no previous study has until now been carried out for the prismatic geometry used by Bénard to discover and to measure the alternating rows of the vortex street. In the next section we describe our theoretical and numerical study of this problem.

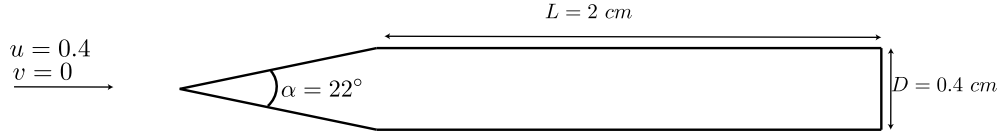


Figure 6.13 – Geometry of our study. Uniform unit velocity ($u = -1$; $v = 0$) is imposed at the upstream. we impose a no-slip boundary condition ($u = 0$; $v = 0$) on all walls.

In order to find predictions of the exact value of the observed frequency in the experiments, linear stability calculations must be performed which take into account the nonlinear modified mean flow profile $\bar{U}(x, y)$ around the bluff body which induces the vortex shedding. The velocity fluctuations and quadratic nonlinearities of the Navier-Stokes equations governing the flows generate a distortion of this average flow profile around the obstacle. As a consequence, its instability depends on this self-regeneration. Therefore, the first step for this theoretical analysis is to estimate the mean flow around the body. This can be done from experimental measures or by direct numerical simulation (DNS). The geometry of the bluff body used in our calculations is one of the cases treated by Bénard (see figure 6.13), more specifically that for which $L = 2$ cm and $D = 0.4$ cm with an angle of 22° in the upstream extremity. We have used FreeFem++ Hecht [11] with the same methods for time integration, steady state solving and stability analysis as for the lid-driven cavity. Our domain is $[-25, 50] \times [-20, 20]$ with the point of the arrow located at the origin. The mesh has 174 000 degrees of freedom.

From these base and mean flow profiles we can observe the change of the time-averaged recirculation length, which grows with Reynolds number. When the flow is unsteady, the recirculation length of the mean flow is smaller than that of the corresponding base flow due to the nonlinear modification of the mean flow. This behaviour has also been observed numerically and experimentally in similar configurations, such as trapezoidal and circular cylinders, e.g [3].

We have studied the stability of both the base and time-averaged mean flow profiles. We observe in figure 6.15 that the growth rate for the equations linearized about the base state is positive, whereas when the governing equations are linearized about the time-averaged profile produced by vortex shedding, the growth rate is zero.

In addition, we display the values of the frequency obtained by the nonlinear numerical simulation (DNS) and the original experimental results of Bénard for one series of measurements performed on the prismatic body of $L = 4$ cm and $D = 0.2$ cm. Only the linear stability calculation about the time-averaged mean flow agrees very well with the DNS results. In addition, there is agreement with the values obtained 110 years ago by Bénard.

It was necessary to wait nearly eighty years to understand the frequency dependence or similarity law arising from a hydrodynamic supercritical Hopf bifurcation such as the vortex shedding behind bluff bodies.

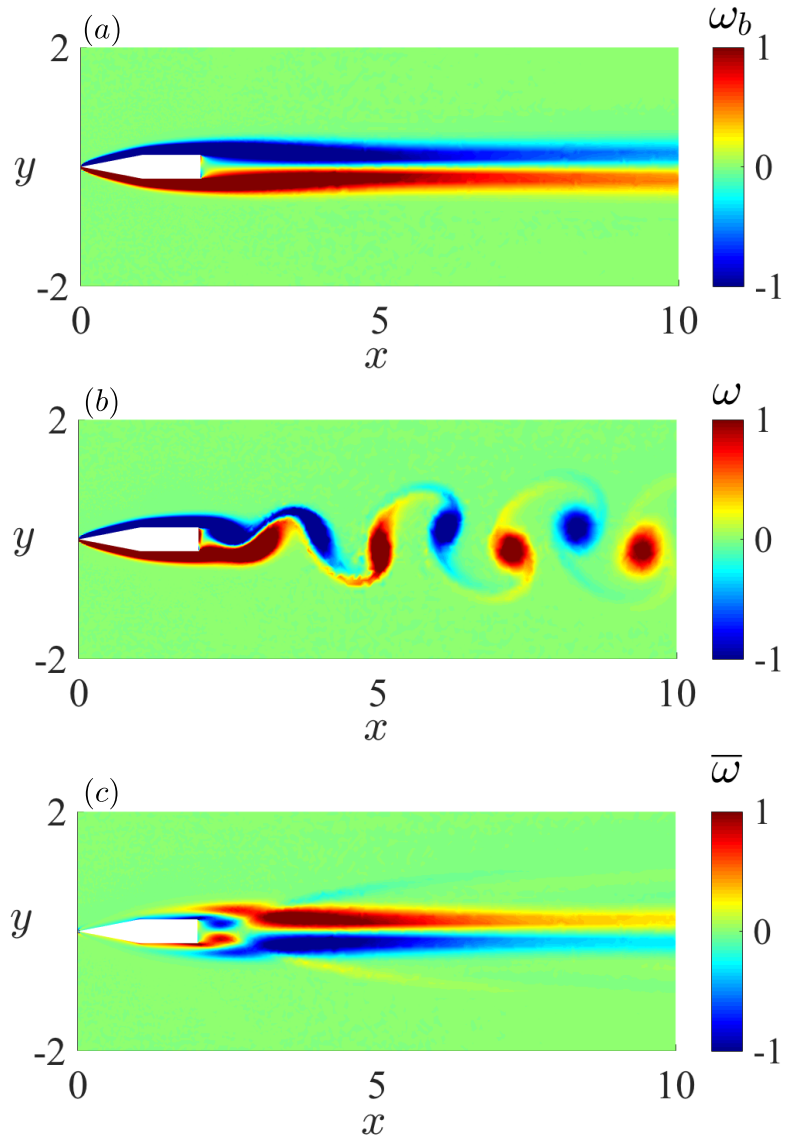


Figure 6.14 – Vorticity field at $Re = 200$. (a) Base flow, (b) instantaneous vorticity and (c) temporal mean flow. We show only the central part of our computational domain, which is $[-25, 50] \times [-40, 40]$.

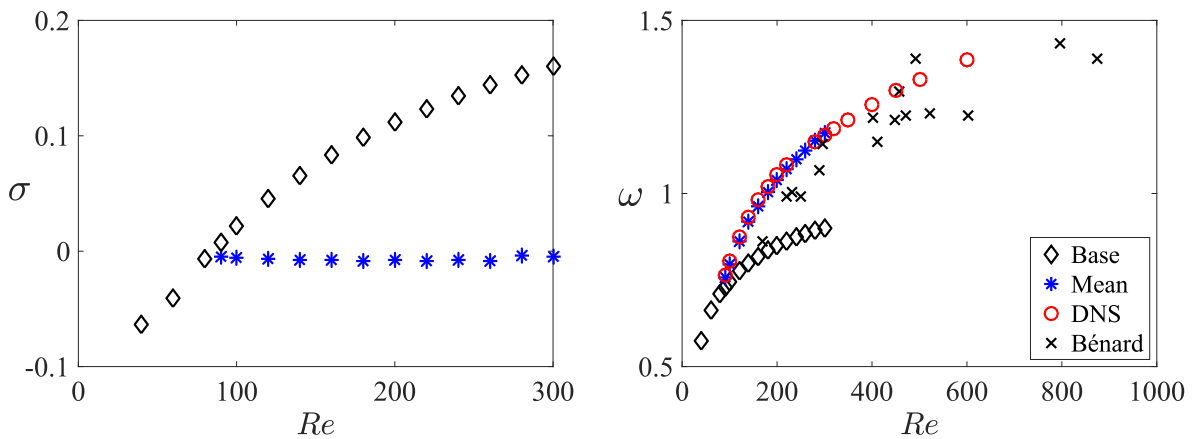


Figure 6.15 – (a) Growth rate (real part of the eigen value) and (b) frequency (imaginary part of the eigenvalue). The results obtained by linear stability analysis about the base flow are shown with diamonds. The results obtained by the linearization about the mean flow are shown with stars. The nonlinear frequency obtained from DNS is shown with circles and that obtained by Bénard is shown with crosses.

Bibliography

- [1] AUTERI, FRANCO, PAROLINI, NICOLA & QUARTAPELLE, L 2002 Numerical investigation on the stability of singular driven cavity flow. *J. Comput. Phys.* **183** (1), 1–25. [102](#), [103](#), [104](#), [105](#)
- [2] AZAÏEZ, MEJDI, DEVILLE, MICHEL & MUND, ERNEST H 2011 *Éléments finis pour les fluides incompressibles*. PPUR Presses polytechniques. [103](#)
- [3] BARKLEY, D 2006 Linear analysis of the cylinder wake mean flow. *EPL (Europhys. Lett.)* **75** (5), 750. [102](#), [113](#)
- [4] BÉNARD, HENRI 1901 *Les tourbillons cellulaires dans une nappe liquide propageant de la chaleur par convection: en régime permanent*. Gauthier-Villars. [112](#)
- [5] BÉNARD, HENRI 1926 *Titres et travaux scientifiques*. Librairie Louis Arnette. [112](#)
- [6] BENÍTEZ, M. & BERMÚDEZ, A. 2011 A second order characteristics finite element scheme for natural convection problems. *J. Comput. Appl. Math.* **235** (11), 3270 – 3284. [103](#)
- [7] BOTELLA, O & PEYRET, R 1998 Benchmark spectral results on the lid-driven cavity flow. *Computers & Fluids* **27** (4), 421–433. [102](#)
- [8] BRUNEAU, CHARLES-HENRI & SAAD, MAZEN 2006 The 2d lid-driven cavity problem revisited. *Computers & Fluids* **35** (3), 326–348. [102](#)
- [9] FORTIN, A, JARDAK, M, GERVAIS, JJ & PIERRE, R 1997 Localization of hopf bifurcations in fluid flow problems. *Int. J. Numer. Meth. Fluids* **24** (11), 1185–1210. [102](#)
- [10] GOODRICH, JOHN W, GUSTAFSON, KARL & HALASI, KADOSA 1990 Hopf bifurcation in the driven cavity. *J. Comput. Phys.* **90** (1), 219–261. [102](#)
- [11] HECHT, F. 2012 New development in FreeFem++. *J. Numer. Math.* **20** (3-4), 251–265. [103](#), [113](#)
- [12] KAWAGUTI, MITUTOSI 1961 Numerical solution of the Navier-Stokes equations for the flow in a two-dimensional cavity. *JPSJ* **16** (11), 2307–2315. [105](#)
- [13] MANTIČ-LUGO, VLADISLAV, ARRATIA, CRISTÓBAL & GALLAIRE, FRANÇOIS 2014 Self-consistent mean flow description of the nonlinear saturation of the vortex shedding in the cylinder wake. *Phys. Rev. Lett.* **113** (8), 084501. [102](#)

- [14] TURTON, SAM E, TUCKERMAN, LAURETTE S & BARKLEY, DWIGHT 2015 Prediction of frequencies in thermosolutal convection from mean flows. *Phys. Rev. E* **91** (4), 043009. [102](#)
- [15] WESFREID, J.E. 2010 Scientific Biography of Henri Bénard. In *Dynamics of Spatio-Temporal Cellular Structures: Henri Bénard Centenary Review* (ed. I.Mutabazi, J.E. Wesfreid & E. Guyon). Springer. [112](#)
- [16] WESFREID, JOSÉ EDUARDO 2017 Henri Bénard: Thermal convection and vortex shedding. *Cr Mécanique* **345** (7), 446–466. [112](#)

Chapter 7

Conclusion and perspectives

Each chapter of this manuscript has its own conclusion. We will summarize the results here as an overall conclusion and propose some perspectives.

Within this thesis, we have studied various flows undergoing oscillations through a Hopf bifurcation: open shear-driven square cavity flow, Taylor-Couette flow, thermosolutal convection and also two preliminary studies (the lid-driven cavity flow and the flow around a prismatic object). The central line of this thesis is the ability of a linear analysis to give information about nonlinear flows such as the frequency. In most cases, classic linear stability analysis about the base flow fails to predict the nonlinear frequency. However, linearization about the time-averaged mean flow predicts the nonlinear frequency for most flows even though the mean flow is not an equilibrium solution of the Navier-Stokes equations. Barkley [1] found that linearization about the mean flow of a cylinder gives a growth rate near zero indicating that the mean flow is marginally stable. This property has been named RZIF, meaning that the real part of the eigenvalue is near zero and the imaginary part is near the nonlinear frequency.

We carried out direct numerical simulations to study the nonlinear dynamics of the flow in the shear-driven cavity over the range of $Re = [4000, 5000]$. We constructed the full bifurcation diagram which shows two successive Hopf bifurcations leading to limit cycles each of which exhibits a different frequency and a different numbers of structures in the mixing layer region. There is a range of Reynolds number where these two limit cycles coexist and are separated by a quasiperiodic state. We approximated the unstable quasiperiodic state by using the edge state technique. We then studied its Fourier spectrum for different Reynolds numbers showing that it is a nonlinear combination of the two limit cycles. We also carried out a Floquet analysis that confirmed the results obtained from the DNS.

The second goal of this study is to understand which information of the nonlinear dynamics could be obtained from a linear analysis around the base and mean flow. For the open shear-driven cavity, the linear analysis about the stationary solution gives a quite good prediction of the nonlinear frequency, but linearization about the mean flow gives a better prediction. Moreover, the growth rate has been significantly damped and therefore approaches the marginal axis. For the cavity, it is the geometry that drives the frequency selection and therefore the nonlinear interactions do not play a significant role. This is the

reason for which the linear stability about the base flow gives a good prediction.

Since in this problem, there are two limit cycles, the eigenvalue spectrum obtained from linear stability analysis about the mean flow shows a mode that corresponds to the other limit cycle and *vice versa*. These eigenmodes indicate qualitatively the same stability behavior as the limit cycles with respect to one other: as the Reynolds number is increased, the real part of one eigenvalue decreases from positive to negative for the limit cycle which undergoes stabilization via a secondary bifurcation and increases from negative to positive for the limit cycle which undergoes a destabilization. As this behavior is only qualitative, it is important to further analyze other hydrodynamic flows and it is necessary to bring more theoretical understanding in order to clarify if it is a systematic behavior. The generalization of the mean flow analysis to the quasiperiodic state would be also an interesting perspective to pursue after this work.

The RZIF property has been validated on various examples: cylinder wake, open shear-driven square cavity flow, lid-driven cavity flow, flow around a prismatic object. However, satisfaction of the RZIF property by the mean flow is not systematic for all nonlinear flows undergoing a Hopf bifurcation. Turton *et al.* [4] studied thermosolutal convection which is governed by a thermal and solutal gradient. This problem undergoes a supercritical Hopf bifurcation which in the presence of $O(2)$ symmetry gives rise to two solutions: traveling and the standing waves. The linear stability analysis around the conductive state fails to predict the nonlinear frequency. Linearization about the mean of the traveling waves gives almost exactly the nonlinear frequency and the growth rate matches the marginal stability axis. However, linearization about the mean flow fails completely for the standing waves. One explanation about why it works, based on the Fourier spectra, has been proposed. Turton *et al.* [4] argued that satisfaction of the RZIF property is justified by its peaked spectrum and the failure of the standing waves by its broad spectrum.

To confirm or invalidate this result we sought to investigate another pair of hydrodynamic traveling and standing waves. In counter-rotating Taylor-Couette flow, traveling and standing waves exist respectively in the form of spirals traveling upwards and downwards and ribbons. The ribbons are standing waves in the axial direction i.e. equal superpositions of axially-upwards and axially-downwards traveling waves. Linearization about the mean flow of these two branches shows that the RZIF property is valid for both of them. It appears that the spectrum of the spirals and ribbons are both peaked as is the case for the traveling waves in thermosolutal convection problem.

During this work, we have discovered two heteroclinic cycles, one non-axisymmetric and the other axisymmetric. Both cycles share the same saddles, which are axisymmetric states containing two axially stacked pairs of vortices. By computing the growth rate of approach to (departure from) one saddle state, we have been able to clarify the linear dynamics leading to this two heteroclinic cycles. These successive cycles are not documented and will be investigated in depth in the future.

Mantič-Lugo *et al.* [2] assumed that in the case of RZIF only the first leading mode contributes to the mean flow distortion. From this assumption, they developed the self-consistent model (SCM) to describe the amplitude saturation process without time integration. This model is a coupled system consisting of the mean flow equation and the linearized Navier-Stokes equations. The Reynolds stress term in the mean flow equation

is truncated at first order. They assumed that this model is valid for flows that satisfy the RZIF property as was shown successfully for the cylinder wake. We point out that the self-consistent model is similar to the harmonic balance of McMullen *et al.* [3] but considered from a different viewpoint. In fact, they considered the mean flow equation and the linearized Navier-Stokes equation which explains the presence of a growth rate, which is not present in harmonic balance of McMullen *et al.* [3] as it is a Fourier approach. The SCM model fails to predict the nonlinear frequency, the mean flow and the amplitudes of the modes in the case of the traveling waves of thermosolutal convection. We have extended this model by considering the system of equations up to the fifth order to match the nonlinear results. Therefore, the satisfaction of RZIF does not imply the validity of SCM but if the SCM is verified, RZIF should be satisfied.

During this thesis we were motivated by the RZIF property. We have shown that up to now only standing waves in thermosolutal convection oppose clearly the universality of the RZIF property. A better theoretical understanding of this property is still missing which prevents the determination of a robust criterion of its validity. The definition of such criterion is an important open question for the future.

Bibliography

- [1] BARKLEY, D 2006 Linear analysis of the cylinder wake mean flow. *EPL (Europhys. Lett.)* **75** (5), 750. [117](#)
- [2] MANTIČ-LUGO, VLADISLAV, ARRATIA, CRISTÓBAL & GALLAIRE, FRANÇOIS 2014 Self-consistent mean flow description of the nonlinear saturation of the vortex shedding in the cylinder wake. *Phys. Rev. Lett.* **113** (8), 084501. [118](#)
- [3] MCMULLEN, MATTHEW, JAMESON, ANTONY & ALONSO, JUAN 2006 Demonstration of nonlinear frequency domain methods. *AIAA J.* **44** (7), 1428–1435. [119](#)
- [4] TURTON, SAM E, TUCKERMAN, LAURETTE S & BARKLEY, DWIGHT 2015 Prediction of frequencies in thermosolutal convection from mean flows. *Phys. Rev. E* **91** (4), 043009. [118](#)

Résumé

Les écoulements fluides jouent un rôle important dans de nombreux phénomènes naturels ainsi que dans de nombreux secteurs industriels. On s'intéresse dans cette thèse aux écoulements instationnaires oscillants provenant d'une bifurcation de Hopf.

L'écoulement affleurant une cavité carrée ouverte présente deux cycles limites séparés par un état quasi-périodique instable. Nous avons décrit en détail ce scénario au moyen de simulations numériques directes, de l'analyse de stabilité linéaire et de l'analyse de Floquet. La bifurcation de Hopf dans la géométrie de Taylor-Couette donne naissance à deux solutions, les spirales (ondes progressives) et les rubans (ondes stationnaires dans la direction axiale). Nous avons découvert que la branche des rubans est suivie de deux cycles hétéroclines consécutifs avec deux états axisymétriques comme point d'ancrage.

L'analyse de stabilité linéaire autour des solutions stationnaires permet d'obtenir le seuil de bifurcation. Une autre approche, est la linéarisation autour du champ moyen. Cette approche permet d'obtenir des fréquences très proches des fréquences non linéaires et montre dans la plupart des cas un taux de croissance proche de zéro. Nous avons montré que les spirales, les rubans, la cavité entraînée ainsi que l'écoulement autour d'un objet prismatique vérifient cette propriété.

Dans la convection thermosolutale, la linéarisation autour du champ moyen des ondes stationnaires ne permet pas d'obtenir les fréquences non linéaires et le taux de croissance est loin d'être zéro, par contre pour les ondes progressives cette propriété est pleinement satisfaite. Nous avons étudié la validité d'un modèle auto-cohérent dans le cas de ces ondes progressives. En effet, si l'écoulement vérifie la propriété du champ moyen, ce modèle est supposé calculer le champ moyen, la fréquence non linéaire ainsi que l'amplitude. Ce modèle est constitué de l'équation gouvernant le champ moyen couplé avec l'équation linéarisée au travers le mode le plus instable et des contraintes de Reynolds. Nous avons montré que dans le cas des ondes progressives ce modèle permet de prédire la fréquence non linéaire seulement très proche du seuil. La prédiction est améliorée significativement en considérant les ordres supérieurs dans le terme des contraintes de Reynolds.

Mots Clés

Analyse de stabilité linéaire, dynamique non linéaire, champ de base et moyen, cycles hétéroclines

Abstract

Fluid flows play an important role in many natural phenomena as well as in many industrial applications. In this thesis, we are interested in oscillating flows origins from a Hopf bifurcation.

The open shear-driven square cavity has two limit cycles separated by an unsteady quasi-periodic state. We have described this scenario in detail by using direct numerical simulations, linear stability analysis, and Floquet analysis. The Hopf bifurcation in Taylor-Couette flow gives rise to two solutions, spirals (traveling waves) and ribbons (standing waves in the axial direction). We discovered that the ribbons branch is followed by two consecutive heteroclinic cycles connecting two pairs of axisymmetric vortices. We studied in detail these two heteroclinic cycles.

The linear stability analysis about the stationary solution is used to compute the threshold of the bifurcations. Another approach is the linearization about the mean field. This approach gives frequencies very close to that of the nonlinear system and shows in most cases a nearly zero growth rate. We have shown that spirals, ribbons, the lid-driven cavity and the flow around a prismatic object verify this property.

In the thermosolutal convection, the frequencies obtained by the linearization about the mean field of the standing waves do not match the nonlinear frequencies and the growth rate is far from zero, on the other hand for the traveling waves this property is fully satisfied. We studied the validity of a self-consistent model in the case of the traveling waves. The self-consistent model consists of the mean field governing equation coupled with the linearized Navier-Stokes equation through the most unstable mode and the Reynolds stress term. This model calculates the mean field, the nonlinear frequency, and the amplitude without time integration. The self-consistent model is assumed to be valid for flows that satisfy the property of the mean field. We have shown that in this case, this model predicts the nonlinear frequency only very close to the threshold. We have improved significantly the predictions by considering higher orders in the Reynolds stress term.

Keywords

Linear stability analysis, nonlinear dynamics, base and mean field, heteroclinic cycles

